

POLITECNICO DI TORINO

Master's Degree
in Nanotechnologies for ICT

Master's Degree Thesis

Investigation of Metal/Organic Interfaces for Organic and Molecular Electronics



Supervisors

Prof. Mariagrazia Graziano
Prof. Gianluca Piccinini
Prof. Maciej Krzywiecki
Dr. Yuri Ardesi
M. Eng. Fabrizio Mo

Candidate

Giacomo Agnesod

Academic Year 2022-2023

*To my family and closest friends
Who made all this possible
And to me*

Summary

The investigation of the interface between metal substrate and adsorbed organic molecules is of primary interest in organic and molecular electronics research. The electronic properties of the devices are affected by the interface interaction, thus determining the efficiency and functionality of the device. This work consists of the study of metal phthalocyanines, respectively CoPc, ZnPc, and MgPc, deposited through thermal evaporation PVD on a polycrystalline gold substrate, following a step-wise method to investigate both monolayer and thin films. The samples are analyzed by photoemission spectroscopy (XPS and UPS). Where available, the experimental results are compared to *ab initio* simulations in the density functional theory framework of idealized systems, that consider an Au(111) surface. Particular attention is dedicated to the self-organization of the organic monolayer, obtained through a geometry optimization that simulates the relaxation processes, and on the calculation of the electron density, that is connected to the intensity and direction of the interface charge transfer. From the gathered results, it is demonstrated that the combination of both XPS and UPS analysis is mandatory for the complete investigation of the metal/organic interface, providing both qualitative and quantitative outcomes. The reduction of the work function due to adsorption is mainly attributed to the pushback effect and the ionization potential, which are directly measured with UPS, thus defining the energy band diagram at the interface. From the energy shifts of the characteristic peaks, it is demonstrated that no chemical bonds are built between metal and molecules, nevertheless, a bi-directional charge transfer mechanism occurs for CoPc. Therefore, the central metal atom of the molecule affects the interaction. The evolution of carbon satellite peaks proves the self-organization of the phthalocyanines in the multi-layer, composed of stacks of molecules with aligned benzene rings that generate resonance effects. The non-linear reduction of the Au_{4f} peak intensity at the initial deposition stages, can be attributed to the transition from a sub-monolayer film to a full coverage of the gold surface. This aspect is particularly relevant for the fabrication of monolayers and ultrathin structures, that also better reflect the simulated ideal systems. Finally, the calculations of the transmission spectrum and the IV characteristic denote completely different conductive properties between the laying down and the standing configurations. The obtained results highlight the importance of precisely controlling the deposition process to obtain the desired interface properties. Moreover, a good match with theoretical simulation results is obtained when a full coverage of the metal surface is achieved. Future works might focus on the investigation of the fabrication to improve the interface properties control against the process variations, for reliable electronic device productions.

Acknowledgements

I'd like to express my gratitude to Professor Maciej Krzywiecki, who generously provided knowledge and expertise during the whole experimental activities conducted in collaboration with the ESpeFuM Laboratory's Group of the Politechnika Śląska in Gliwice (Poland). Special thanks to Aleksandra Przybyła who ran all the photoemission spectroscopy analyses, and to Justyna Juszczak-Synowiec for introducing me into atomic force microscopy. Thanks should also go to Fabrizio Mo, with whom I conducted parallel activities, and shared AFM and STM images, and for the guidance in the DFT calculations.

Contents

List of Tables	9
List of Figures	11
1 Introduction	17
I First part	21
2 Metal phthalocyanines	23
2.1 Molecular structure and properties	23
2.2 Crystal structure	24
3 Surface and interface physics	27
3.1 Bulk material electronic structure	27
3.1.1 Band diagram of a solid	27
3.1.2 Bulk states	29
3.1.3 Surface states	30
3.2 Molecular energy spectrum	34
3.2.1 Organic semiconductor	35
3.3 Metal-organic interface	36
3.3.1 Induced density of interface states	38
3.3.2 Metal-molecule band diagram at equilibrium	39
3.3.3 Conduction at the nanoscale	41
4 Electronic structure	43
4.1 Generic system Hamiltonian	43
4.2 Born-Oppenheimer approximation	44
4.3 Hartree model	45
4.4 Hartree-Fock model	46
4.5 Self Consistent Field	48
5 Density functional theory	51
5.1 Introduction to atomistic simulators	51
5.2 DFT method	52

5.2.1	Kohn-Sham Hamiltonian	53
5.2.2	Exchange-correlation functional	54
5.2.3	Basis sets	55
5.2.4	Van der Waals correction	56
6	Technological background	61
6.1	Physical vapor deposition	61
6.1.1	Classification of PVD	61
6.1.2	Vapor-surface interaction	62
6.1.3	Growth modes and film qualities	65
6.1.4	Thermal PVD experimental setup	67
6.2	Photoemission spectroscopy	70
6.2.1	Electrons-photons interaction in solids	71
6.2.2	Photoelectric effect	71
6.2.3	Three-step model	72
6.2.4	XPS and UPS experimental setup	74
6.2.5	XPS data analysis	79
6.2.6	Peak fitting	81
6.2.7	Quantitative analysis	85
6.2.8	UPS data analysis	88
II	Second part	91
7	Sample preparation	93
7.1	Gold substrate	93
7.2	Phthalocyanine deposition	96
8	Photoemission analysis results	101
8.1	Gold substrate analysis	102
8.1.1	XPS results	102
8.1.2	UPS results	105
8.1.3	Effects of the annealing	106
8.2	CoPc on polycrystalline Au	111
8.2.1	Qualitative analysis	112
8.2.2	Quantitative analysis	118
8.3	ZnPc on polycrystalline Au	121
8.3.1	Qualitative analysis	121
8.3.2	Quantitative analysis	128
8.4	MgPc on polycrystalline Au	133
8.4.1	Qualitative analysis	133
8.4.2	Quantitative analysis	139
8.5	Conclusions	146

9	Simulation results	151
9.1	Geometry optimization	152
9.1.1	Methodology	152
9.1.2	Monolayer organization	155
9.1.3	Adsorption energy	160
9.2	Analyses	164
9.2.1	Molecular energy spectrum	164
9.2.2	Charge transfer	169
9.3	Thin film and bi-layer analysis	175
9.3.1	Geometry optimization	176
9.3.2	Charge transfer analysis	177
9.4	Transport properties	180
9.4.1	Device structure	180
9.4.2	Transmission spectrum and current	181
9.5	Conclusion	185
10	Summary and conclusion	189

List of Tables

6.1	Pressure, molecular density, and mean free path of the particles for the different vacuum levels.	69
6.2	Bragg's angle of a quartz crystal (1010) monochromator for different x-ray sources.	76
6.3	Energy and orbitals of the XPS peaks of some of the most common elements.	80
6.4	Electron quantum numbers.	81
6.5	Spin-orbit splitting and peak intensity ratio.	83
7.1	Total thickness of the organic thin film at each deposition step for the three samples.	98
8.1	Au/CoPc work function and work function shift at each deposition step. . .	117
8.2	Energy features of the HOMO level of a CoPc thin film.	118
8.3	Au/ZnPc UPS results. The value indicated by (*) is the offset of the Fermi level measured from the UPS of step 0. All the values are referred to the zero energy of the detector. The missing data are due to the low signal. . .	128
8.4	Parameters used for the calculation of the overlayer thickness.	132
8.5	Au/MgPc UPS results. The value indicated by (*) is the offset of the Fermi level measured from the UPS of step 0. All the values are referred to as the zero energy of the detector. The missing data are due to the low signal.	140
8.6	Parameters used for the calculation of the overlayer thickness.	143
8.7	Most relevant quantities to build the energy band diagram at the interface. In order: the work function of the bare gold surface, the shift of the work function after the adsorption, and the edge of the HOMO level, which coincides with the energy barrier.	149
9.1	Employed FHI pseudopotentials for the specific element. For gold DZP is used for the geometry optimization and the analysis, whereas SZP is for the device calculations.	155
9.2	Geometry optimization data: "Z1" and "Z2" are between the central metal atom and the gold surface (Z1) or the molecular plane (Z2) respectively. ΔE is the energy difference between the configurations. The angles in parenthesis refer to the fully optimized final structures.	160
9.3	Adsorption energy E_{ads} of the three metal phthalocyanine on polycrystalline gold evaluated for the best configuration.	163

9.4	Calculation of the charge localized in different regions of the system. The charge of the adsorbed molecules is compared with the isolated one to highlight the distribution of the excess charge upon adsorption.	174
9.5	Charge distribution in a ZnPc bi-layer deposited on Au(111) surface calculated for different atomic sets.	180

List of Figures

2.1	Model of a metal phthalocyanine structure obtained with <i>Avogadro</i> . The different colors indicate the elements, in particular: H in white, C in grey, N in blue, and the central metal atom, which can be Co, Mg, or Zn, in orange.	24
2.2	Metal phthalocyanine α -, β - and η - configurations.	26
3.1	Energy band diagram as a function of the lattice interatomic distance.	28
3.2	Approximation of the cadmium telluride electronic structure calculated through local empirical pseudopotential model.	30
3.3	One-dimensional model of the potential energy across a metal surface.	31
3.4	Surface state of a metal, showing a periodic behavior in the bulk and an exponential decay above the surface.	32
3.5	Localized surface state of a semiconductor, showing an exponential decay of the wavefunction both above and below the surface.	33
3.6	Band diagram of an organic semiconductor showing the broadening of the HOMO and LUMO and the most relevant energy quantities. The dashed lines highlight the electronic structure of the single molecule.	34
3.7	Continuous IDIS with a non-negligible density of states in the forbidden gap vs. the discrete molecular electronic structure. The CNL is shifted with respect to the original Fermi level.	39
3.8	Qualitative scheme of the metal/molecule interface band diagram evolution.	40
3.9	Qualitative representation of the transport in molecular devices. The source electrons with an energy E within the bias window, set by the applied voltage, can be transferred to the drain with a probability equal to $T(E)$	41
6.1	Schematic of the different processes that take place at the surface involving the gas particles.	63
6.2	Qualitative plot of the physisorption potential energy. The substrate surface is at $z = 0$ and z_0 indicates the adsorption distance, E_B is the negative adsorption energy.	65
6.3	Plot of the adsorption potential energy considering both physisorption and chemisorption. E_b indicates the energy barrier that the adsorbate must overcome to reach the most stable state.	66
6.4	Schematic of the conformal and non-conformal thin film deposition.	67

6.5	Schematic of a thermal PVD setup. The crucible is inserted into the resistive heater, the sample is hosted upside down, exactly above the source, with the shutter in between, and the microbalance is aligned to the sample.	68
6.6	Picture of the crucible stage and the thermocouple filament.	70
6.7	Schematic of the photoelectric effect.	72
6.8	Schematic of the photoelectron excitation of a core level and a valence band electron (left). Propagation of the photoelectron through the material in case of no scattering event (A), and scattering with other particles losing information on the BE (B).	74
6.9	Schematic of the XPS instrumental setup.	75
6.10	Schematic of the X-ray diffraction interference, showing the optical path difference of $2 \cdot d \cdot \sin \theta$.	76
6.11	Energy level alignment between the sample and the detector.	78
6.12	XPS full spectrum. The dark area is the background contribution generated by the Au_{4f} peak.	79
6.13	Qualitative UPS spectrum of a sample before and after the deposition of molecules highlighting how to measure the most relevant quantities.	88
7.1	Picture of the organic deposition chamber.	97
8.1	Full survey spectrum of the bare gold surface of Au/CoPc, before the deposition of the organic molecules, showing the atomic percentages of the elements composing the substrate.	103
8.2	XPS local peaks of gold, oxygen, carbon, and silicon measured from the bare gold surface of the substrate.	104
8.3	AFM images of the gold surface taken in the non-contact mode of the topography and phase. The sample belongs to Fabrizio Mo.	105
8.4	Plots of the cut-off energy (left) and Fermi edge (right) of the bare gold substrate of the first sample measured through UPS, the calculated values are $\phi_{Au} = 4.52$ eV and $E_F = 0.16$ eV.	106
8.5	XPS full survey spectrum of the bare gold substrate after annealing at 700°C for 40 s.	107
8.6	Local XPS spectrum of the main peaks of the annealed substrate at 700°C for 40 s, in particular: Au_{4f} , O_{1s} , C_{1s} , and Si_{2p} .	109
8.7	Plots of the electron affinity (left) and the valence band (right) of the oxidized surface of the annealed sample obtained through UPS.	110
8.8	Pictures of the gold substrate after a 2 s annealing process, showing a gradual damage of the surface taken with the AFM camera. The bottom-right image refers to a 40 s annealed sample.	111
8.9	Gold Au_{4f} and oxygen O_{1s} peaks of the Au/CoPc sample measured after each deposition step.	113
8.10	Au/CoPc carbon C_{1s} peaks, on the left the overlay of the spectra after each deposition step, while on the right the zoom of the carbon peak fitting for the last step, with an expected $d = 2$ nm.	114
8.11	Nitrogen N_{1s} and cobalt Co_{2p} peaks of the Au/CoPc sample measured after each deposition step.	116

8.12	XPS survey of AuCoPc after step 4, at the maximum amount of deposited material. In the legend are collected the atomic percentage estimates of the different elements present at the surface.	118
8.13	Estimate of the CoPc overlayer thickness through the Lambert-Beer law by using three different approximations of the electron mean free path.	119
8.14	Gold Au_{4f} and oxygen O_{1s} peaks of the Au/ZnPc sample measured after each deposition step, indicating the expected thickness of the layer.	122
8.15	Carbon C_{1s} peak measured from the bare gold substrate. The signal originates from the adventitious carbon adsorbed at the surface that resisted the ion beam etching.	123
8.16	Carbon C_{1s} peaks of the Au/ZnPc sample measured after each deposition step.	124
8.17	Carbon C_{1s} peak of Au/ZnPc after the final deposition step.	126
8.18	HOMO overlay and Thin film valence band.	127
8.19	Full survey spectrum of Au/ZnPc before (top) and after (bottom) the deposition process. The first spectrum is plotted up to 730 eV since no characteristic peaks are detected for higher BE.	129
8.20	Nitrogen N_{1s} and zinc Zn_{2p} (primary) peaks of the Au/ZnPc sample measured after each deposition step.	130
8.21	Comparison of the estimation results of the ZnPc overlayer thickness obtained through different methods and by considering different XPS signals.	131
8.22	Gold Au_{4f} and oxygen O_{1s} peaks of the Au/MgPc sample measured after each deposition step.	134
8.23	Carbon C_{1s} peaks of the Au/MgPc sample measured after each deposition step.	135
8.24	Carbon C_{1s} peak of Au/MgPc after the final deposition step.	137
8.25	Nitrogen N_{1s} and magnesium Mg_{1s} peaks of the Au/CoPc sample measured after each deposition step.	138
8.26	HOMO overlay and Thin film valence band.	139
8.27	Full survey spectrum of Au/MgPc before (top) and after (bottom) the deposition process.	141
8.28	Comparison of the estimation results of the MgPc overlayer thickness obtained through different methods and by using different XPS signals.	142
8.29	AFM image of the MgPc organic thin film edge. From the profiles measured across the edge, the measured final thickness is of 6 nm rather than the expected 10.5 nm.	143
8.30	Topography and phase of a 3 nm thick cluster of MgPc deposited on gold. The sample belongs to Fabrizio Mo.	144
8.31	STM images of the MgPc thin film deposited on polycrystalline gold, showing a large number of grains. The left image belongs to Fabrizio Mo's sample.	145
8.32	I-V characteristic and density of states calculated in six different points of the Au/MgPc sample. The first plot shows the uncovered gold surface, whereas the second plot is obtained from the organic thin film.	147
8.33	Band diagrams of the three samples, the energies are obtained from the XPS and UPS measurements.	148

9.1	Representation of the supercell used in the simulations. The molecule is place at the 0° rotation configuration. The gold (111) lattice vectors of the surface are indicated by the dashed black lines.	153
9.2	Animations of the relaxation process of ZnPc (15°) and gold substrate from the lateral and vertical view.	156
9.3	Animations of the relaxation processes of a ZnPc that involve the rotation of the molecule around the central metal atom as a consequence of the intermolecular interactions. Initially, the ZnPc has a -30° rotation angle, which is reduced to -20° in the relaxed structure.	158
9.4	Lateral and vertical view of the fully relaxed Au/CoPc (top) and MgPc (bottom) in their respective best configuration (-12° and 15°).	159
9.5	structure of the Au/benzene adsorption	161
9.6	Representation of the molecular arrangement of the phthalocyanine monolayer that exploits the symmetry of the molecules. The two configurations have similar energies.	163
9.7	Molecular energy spectrum of the three molecules. the blue refers to the gas phase, calculated in both bulk and molecular configuration, and the orange is the projection of the DOS on the molecule after the adsorption.	166
9.8	Comparison between the calculations and the photoemission measurements. On the left are plotted the valence bands of the Au/MPc vs. XPS, whereas on the right are plotted the PDOS vs. UPS.	168
9.9	Electron difference density of the three structures (Au/CoPc, Au/MgPc, and Au/ZnPc) with isovalue 0.05 (purple) and -0.05 (blue).	170
9.10	Profile of the electron density difference along the z-direction.	171
9.11	Representation of the Mulliken population on the three-dimensional model of the three interfaces, the scheme color indicates the charge, thus the positively charged atoms are in red, and the negatively charged in blue.	173
9.12	Animation and final configuration of the four cobalt phthalocyanine stack geometry optimization. The result is similar to the α and η configurations, with a tilting angle of 22.85° and molecular separation of 3.45 \AA	177
9.13	Animations of the geometry optimization from the lateral and vertical perspective of the bi-layer structure. In the picture are indicated the most relevant geometry parameters of the final structure.	178
9.14	Molecular energy spectrum of the ZnPc bi-layer highlighting the splitting of the states caused by the interface interaction with the adsorbed molecule, indicated by the red curve (ZnPc 1).	179
9.15	Representation of the device configuration of the three molecular structures. In order: CoPc, ZnPc, and ZnPc bi-layer, in each system the gold tip is close to the central metal atom, but not exactly on top.	182
9.16	Transmission spectra of the three molecular devices for 11 bias voltages between 0V and 1V. The red part of the curves identifies the portion of the spectrum that is included in the bias window, thus that effectively contributes to the drain current.	183
9.17	I-V characteristic of the three molecular devices.	184

9.18 Transmission pathways of CoPc (violet) and ZnPc (orange) devices. The blue and the green arrows refer respectively to the forward and the backward electron transmission. The size of the arrow indicates the probability density. 186

Chapter 1

Introduction

The constant need for computing capacity combined with improvements in technology drove the development of the transistor to a constant downsizing that allowed it to accommodate more devices and different functional blocks in a single chip. The large amount of transistors that can be integrated into a chip exceeds one billion, this outstanding goal was possible thanks to the CMOS logic [1]. The scaling along the decades followed Moore's law, introduced by Gordon Moore in 1965, which stated that every 18 months, the number of transistors that can be stored in a chip doubled [2]. The increasing packing density, bring also other advantages, like the higher speed of the circuit and performances and the reduction of the power dissipation of the single device. However, the total power consumption of such complex chips can be very high, indeed, the great challenge of nowadays devices, is the reduction of the power dissipation and interconnection bandwidth [3, 4]. The scaling process is not only a technological issue since, at this scale, even the basic operating principles are different with respect to the large MOSFETs. Non-ideal effects rise, like Short Channel Effect (SCE), Drain Induced Barrier Lowering (DIBL), threshold voltage roll-off, and other [3], that required new device design to be overcome, leading to the FinFET [3, 4].

Nowadays, the scaling has reached the nanometric scale, where quantum mechanical effects are dominant, like the quantum confinement and the tunneling effect through the gate dielectric [3]. The scaling is reaching a fundamental limit: the channel length of the FinFET is comparable with the de Broglie wavelength of an electron at room temperature, where the probability of direct tunneling from source to drain is so high that will be impossible to switch off the transistor [3]. A further reduction, exploiting the same technology is physically unsustainable, for this reason completely new technologies have been proposed and studied, going "Beyond CMOS", where innovative devices, supported also by new computing paradigms, are investigated [4]. In recent decades, the use of molecules for the development of electronic devices has become increasingly important. Organic electronics has already some applications in different fields, like organic light-emitting displays (OLED) [5] in optoelectronics, thin film transistors [6] in electronics, and organic photovoltaic cells (OPV) [5, 7], chemical sensors [8] and other. Nevertheless, molecules are also exploited in the so-called molecular electronics, an innovative technology that employs a single molecule, or a small group of molecules, as the active region of the

device [9, 10, 11]. Replace the channel of a FET with a molecule is the ultimate scaling of the device since molecules are the fundamental components of compound materials [9]. The simple structure of a molecular FET consists of a molecule bonded with the source and the drain contacts and suspended above a substrate that works as a gate dielectric, which has the major advantage of being compatible with silicon technology [12]. Moreover, it is possible to manipulate single molecules and exploit self-assembling deposition techniques to provide large-scale production and reduce the costs [11, 12]. Even though the current level of fabrication of such molecular devices is affected by a huge process variability and low throughput [10, 11, 12]. The molecular transistor can, ideally, overcome the CMOS capabilities, since the shorter channel and the small current involved make the device faster and, also, reduce the power consumption. The fabrication drawbacks and the low $I_{\text{ON}}/I_{\text{OFF}}$ ratio of the molecular transistor make this new technology unable to surpass the current one in the near future [10, 11, 12]. However, technological compatibility can lead to the integration of molecular devices for complementary applications. In the field of molecular electronics, the interaction between the molecules and the metal electrodes is crucial in determining the properties of the system [13, 14]. The investigation of the complex phenomena that act at the surface and at the hetero-interface between adsorbed molecules and metal substrates is a fundamental step toward the knowledge of the physical and chemical properties of the combined system. Thus, the interface between the metal electrode and molecule strongly affects the performance of the device, therefore, an area of the device that can be potentially exploited to control and improve its capabilities [13, 14]. A comprehensive description of the metal-molecule interface interaction is a challenging task since both electrostatic and pure quantum mechanical effects are involved. Moreover, such an interface can provide a charge transfer between the two species, that has a huge impact on the properties of the organic thin film, which, in turn, can be exploited to improve and engineer the performances of the organic electronic device [15, 16].

This work is focused on the investigation of the interactions that occur between a gold substrate and the adsorbed π -conjugates molecules, moreover, the physical and chemical properties of the deposited thin film are analyzed, proving also a discussion on the layer morphology. The employed molecules belong to the family of transition metal phthalocyanines [17, 18], which are characterized by a central transition metal atom that provides interesting properties to the molecule, such as a magnetic moment or, in some cases, an electric dipole. Moreover, these molecules have to huge advantage of being sufficiently resistant to heat, light, oxygen, and moisture [17, 19, 20]. Indeed, they are already used for some applications in optoelectronics, organic photovoltaic cells, and even in organic spintronics [21, 22, 23, 24]. By the experimental analysis, the relationships between the structure and the electronic properties of metal/organic interfaces are investigated. To this aim, theoretical calculations at the Density Functional Theory (DFT) level are presented for some system configurations and compared to experimental results where available.

The thesis is structured in two parts, the first part aims to provide a basic introduction to the electronic structure of the interface between a metal substrate and the adsorbed molecule (3.3) as intended in the literature. Moreover, chapter 4 is meant to provide a very basic background on the quantum mechanical formalism that describes the electronic structure in solid. Whereas chapter 5 is conceived to provide an introduction of the Density Functional Theory (DFT) formalism which is the one adopted by the commercial

simulator tool (*Quantum ATK*) used in this work for the simulation of the metal-molecule interfaces. Finally, in chapter 6, the last one of the first part, an overview of the deposition and analysis techniques employed during the fabrication and investigation of the samples is presented, with a focus on the fundamental physical principles on which they are based. In particular, the Physical Vapor deposition (PVD) is discussed in section 6.1) whereas the X-ray Photoemission Spectroscopy (XPS) and the Ultraviolet Photoemission Spectroscopy (UPS) are presented in section 6.2, with an additional section dedicated to the peak fitting.

The second part is the core of the thesis, where the fabrication procedure is presented and the experimental data, acquired with the photoemission spectroscopies, are discussed and compared with the *ab initio* simulation results and the literature. The three investigated samples are made by gold-coated silicon substrates which undergo a sequence of deposition steps, where CoPc, ZnPc, and MgPc are respectively deposited through PVD. The details of the substrate preparation and the deposition methodology are presented in chapter 7. After each deposition step, the samples are moved to the analysis chamber where the photoemission spectroscopies (UPS and XPS) are conducted. With a step process, we are able to investigate the properties of the as a function of the organic layer thickness. The gathered results are discussed in chapter 8. In particular, for very thin layers, the physical and chemical properties of the metal/organic interface are extracted, with a focus on the interface charge transfer. On the contrary, information on the morphology and the organization of the organic molecules emerge from the analysis of the thicker layer. The three samples are compared in order to highlight the influence of the central metal atom on the properties of the device. In chapter 9 the simulation results based on the DFT method are discussed and compared with the experimental results. The goal of the simulation is to support the experiments, therefore the focus is on both the morphology of the adsorbed monolayer and the charge transfer at the interface. The three samples are modeled by the respective ideal structure composed of a substrate and a single adsorbed molecule. Nevertheless, despite the huge approximation, the obtained results match the photoemission experiments, and furthermore, they provide a deeper investigation of the charge transfer mechanisms. Finally, an initial investigation of the conduction properties of the metal phthalocyanine is conducted, focused only on the calculation of the transmission spectrum.

Part I

First part

Chapter 2

Metal phthalocyanines

2.1 Molecular structure and properties

The molecules under study belong to the family of the transition metal phthalocyanines (MPc). As shown in figure 2.1, phthalocyanines are large, planar carbon-based molecules, with D_{4h} point symmetry, characterized by a macrocyclic structure, which means that the molecule shows a large ring-shaped structure [17, 18]. The ring is made of four pyrrole groups with the nitrogen pointing towards its center and connected to each other by four extra nitrogen atoms, for a total of 8 nitrogen atoms. Each of the pyrrole is connected to a peripheral phenyl ring which lacks two hydrogen atoms. The peculiarity of the metal phthalocyanines is the presence of a transition metal, located at the exact center of the molecule, bonded through covalent bonds to the nitrogen atoms of the pyrrole groups. The particular shape and the presence of phenyl and pyrrole groups make the MPCs π -conjugated molecules, which means that they are conductive, so they can be exploited as active material in organic electronic devices and molecular electronics [25].

Metal phthalocyanines are widely used and investigated as organic semiconducting material due to their promising electrical and optical properties, chemical and thermal stability, and resistance to moisture and oxygen contamination, other than a large variability and tuning of the properties [17, 19, 20]. The large amount of different metals that can be hosted by a phthalocyanine ion allows an extra degree of freedom for the tuning of the physical and chemical properties of the molecule. Moreover, the presence of the benzene rings allows the functionalization of the molecule by replacing the hydrogen atoms with other interesting active groups. For example, by replacing the hydrogen atoms with fluor atoms the electrical properties of the molecule change completely, moving from a p-type organic semiconductor to a n-type one, thus radically modifying the transport properties of the device [20, 26]. The electric and magnetic properties of the MPc do not only depend on the valence electrons and on the spin of the central metal atom but also on the bonds that are established between the metal and the phthalocyanine ion since they modify the shape of the metal orbitals [27, 28].

Normally, MPCs are non-polar molecules due to their planar structure, however, three-dimensional MPCs can be produced, as, for example, GaClPc or TiOPc that are characterized by an additional non-metal atom (Cl and O respectively) located out of the molecular plane and directly bonded to the central metal atom [29, 30, 20]. These molecules, due to their particular shape, exhibit an electrical dipole orthogonal to the molecular plane, thus showing completely different electrical properties. However, this work is focused on the investigation of cobalt (CoPc), zinc (ZnPc), and magnesium (MgPc) phthalocyanines [18, 22, 31, 23, 32, 19], three planar MPCs with no particular functionalization, in order to compare the influence of the central metal on the properties of the organic thin film and also, to keep the structure as simple as possible to make the simulations faster and easier.

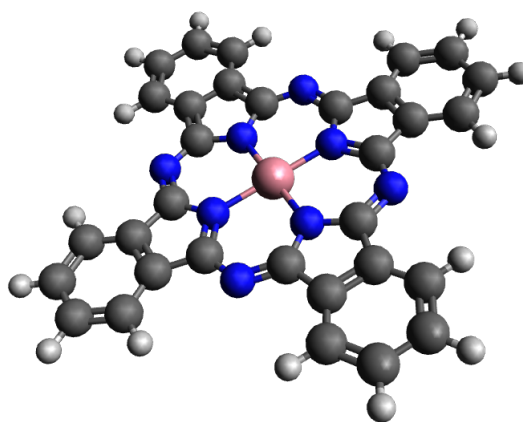


Figure 2.1. Model of a metal phthalocyanine structure obtained with *Avogadro*. The different colors indicate the elements, in particular: H in white, C in grey, N in blue, and the central metal atom, which can be Co, Mg, or Zn, in orange.

2.2 Crystal structure

A technologically interesting feature of MPc is that they are classified as self-assembled molecules [20, 33]. It is a particular type of deposition process where the adsorbed molecules, due to the established interactions among the components (mainly non-covalent interactions) allow the spontaneous formation of layers characterized by an organized structure, without any sort of external action. In static-self assembly, while the system is relaxing to thermodynamic equilibrium, the establishment of an organized layer is the configuration that minimizes the energy, thus the most stable and most probable. The non-covalent interactions between the molecules act on a local level, as a consequence, a nanostructure is built on its own [20].

The organization of the molecules is not limited to the first adsorbed layer, indeed, the successively deposited layers follow the same pattern: the phthalocyanine molecules

align themselves, forming linear chains of stacked molecules, as a result, the thin film is characterized by a sequence of organized molecular pillars that respect the same pattern of the self-assembled monolayer [20, 34, 23, 35, 36]. From former studies found in literature [31, 36], it is demonstrated that the thickness of the deposited thin film plays a determinant role in the overall molecular organization. In the case of a monolayer, or a very thin film made of few layers, the adsorbed molecules lay horizontally over the substrate, in other words, all the layers are parallel to the surface. On the other hand, in the case of a thicker layer, or bulk, the molecules are subjected to a reorganization in order to reduce the energy of the system: they are tilted by an angle with respect to the column axis. The molecules are still planar, so no deformation of the intramolecular bonds occurs, however, the van der Waals interactions between the molecules are responsible for the inclination. Nevertheless, the columnar structure is preserved, the film is still made by a periodic pattern of molecular pillars obtained by the vertical alignment of the central metal atom of the MPCs. Even if the exact arrangement of the molecule may depend on the central metal atom, for example by slightly changing the distance between the molecules of the same column, the spacing between the column, and the rotation angles, three main structures are proposed by the literature [35, 34, 20], namely α -, β - and η - configurations, as shown in figure 2.2. They differ on the tilting angle between the molecules and the horizontal plane, which, in turn, affects the inclination of the adjacent columns with respect to the chain axis, indeed, for both β - and η - configurations they are facing in the opposite direction, generating the so-called herringbone structure, while the α -phase shows a brick-stone structure, with columns sharing the same orientation. The stacking angle has also repercussions in the crystal lattice vectors, by changing the relative rotation angle and position of the adjacent molecules of the same layer, and also on the magnetic properties of the organic material, since they are strictly related to the stacking of the molecular π -system. A thin film of MgPc can be ferromagnetic or anti-ferromagnetic depending on the arrangement [37].

The growth of a deposited thin film with a specific phase is a challenging technological task that depends on the deposition technique and the set of adopted parameters, which are the substrate temperature, the pressure in the deposition chamber, and the deposition rate. A β -arrangement of CoPc can be obtained by heating the substrate during the evaporation over 300°C, providing enough energy to turn on the transition from the α -phase, that was previously grown at room temperature [17]. For the ZnPc the transition from α to β phase occurs at a temperature of 220°C [23], whereas for CuPc the temperature is slightly lower (210°C) [35]. Other information on the principles of the deposition for organic molecules and how to control the morphology of the deposited layer are presented in chapter 6.1.

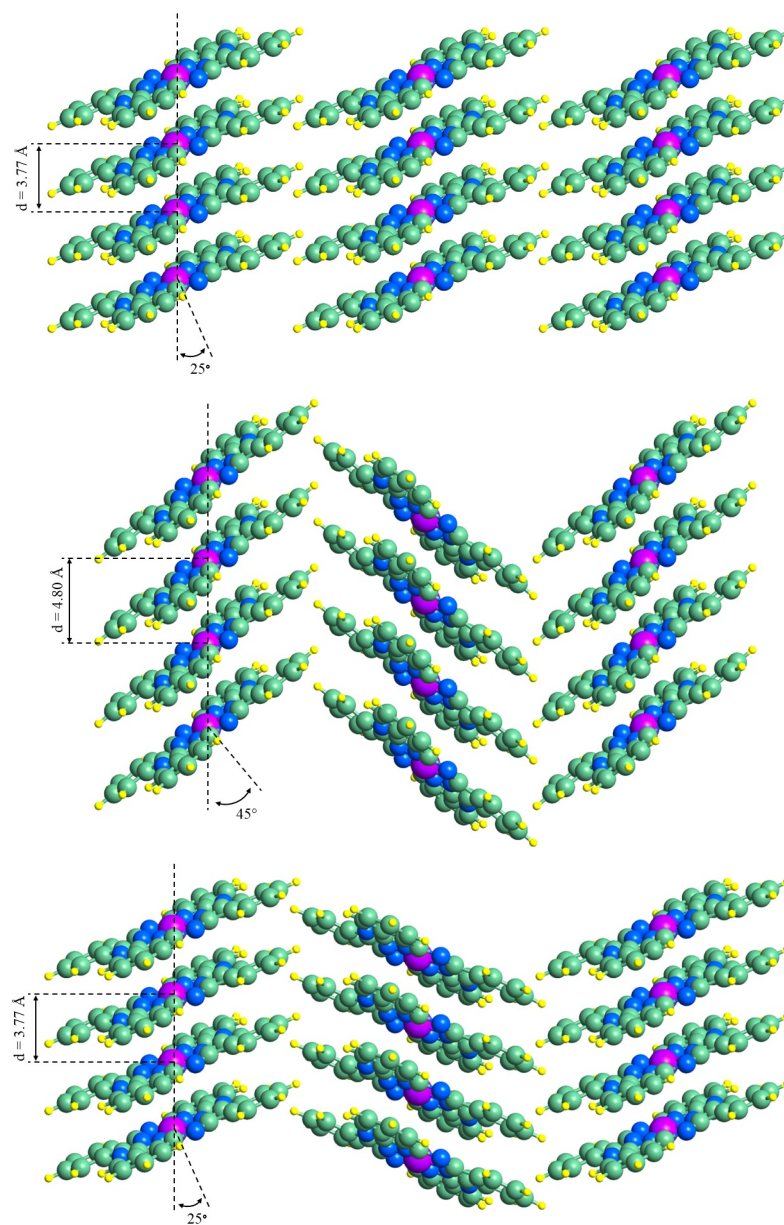


Figure 2.2. Metal phthalocyanine α -, β - and η - configurations.

Chapter 3

Surface and interface physics

Before presenting the interesting phenomena that occur at the interface between a metal substrate and an adsorbed molecule, it could be useful to spend a few words describing the electronic structure of the components involved in the interaction, in order to provide the basic physics background, so that the reader can better understand the following discussion and comprehend the conclusions. Differently from metal surface physics and the molecular electronic structure, which are well-established concepts in literature [38, 39], the interface between a metal and a molecule is still under study. A general model that describes this interaction is not yet available, however, in literature [13, 40, 16], some attempt models have been proposed. The interface interaction is a fascinating topic that deserves further investigation since has a huge impact on the properties of the molecular device, therefore, a component that has the potential to be engineered.

3.1 Bulk material electronic structure

3.1.1 Band diagram of a solid

In solid-state physics, the so-called electronic band structure identifies the range of energies that the electrons of a solid are allowed or forbidden to occupy. The band structure of a material is of central importance since it determines the electronic and optical properties. The origin of the bands lies in a quantum mechanical interaction between the electron waves of a periodic crystal lattice. In a solid, the atoms are kept closely packed together by the chemical bonds, the kinetic energy of every atom is limited and the number of atoms of a macroscopic bulk solid is in the order of the Avogadro number $N = 6.022 \cdot 10^{23}$. The electrons of a single isolated atom occupy the discrete energy atomic orbitals. When more atoms interact to form a molecule, a split of the atomic energy levels happens due to Pauli's exclusion principle. The number of molecular orbitals is proportional to the number of atoms. Since a solid is made of N atoms, the number of states is extremely large and the energy spacing between them tends to zero, causing the formation of the continuous energy bands. However, some energy intervals lack energy states, which means that an electron of that solid cannot have those specific energies, forming "band gaps". The

most important one is the energy gap that separates the valence band from the conduction band of a solid, at thermodynamic equilibrium, the former is filled by electrons and the latter is empty. The band gap is responsible for the majority of the optical and electronic properties of the solid, indeed it is the reference for the classification of materials according to the electric conduction. Electrons can be transferred between these two bands by means of the carrier generation and recombination processes. Figure 3.1 shows the splitting of the atomic orbitals and the formation of the bands as a function of the distance between the atoms of the solid that, in turn, is responsible for the interactions between the electron wavefunctions.

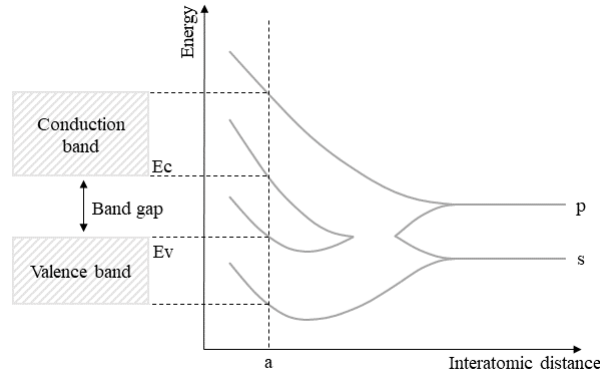


Figure 3.1. Energy band diagram as a function of the lattice interatomic distance.

According to the picture, there are solids that have no band gap, there is no separation between the valence and conduction band. Those materials belong to the class of metals. They are characterized by a partially filled band regardless of the temperature, which provides a very high conductivity. Semiconductors and insulators, on the other hand, have a valence band and a conduction band separated by an energy gap. The distinction lies in the extent of the band gap, in a semiconductor, it is short with a couple of electronvolts maximum, whereas an insulator has a much larger band gap, making the conduction very difficult.

The Density of States (DOS) of a system describes the number of electronic states per unit of volume and energy. For a three-dimensional bulk material, the density of states has the following form:

$$D(E) = \frac{V}{2\pi^2} \left(\frac{2m}{\hbar^2} \right)^{3/2} E^{1/2}$$

where m is the electron mass, \hbar is the Planck constant. The square root dependence on the energy makes the DOS parabolic in the reciprocal space, moreover, close to the valence band and conduction band edges, the DOS is zero. However, the number of occupied states per unit volume at a given energy for a system at equilibrium is obtained by the product of the DOS and the probability distribution function. For electrons, the Fermi-Dirac probability distribution function (3.1) must be used, it identifies the probability

that a fermion occupies a state at a specific energy.

$$f_{FD}(E) = \frac{1}{\exp\left(\frac{E-E_F}{k_B T}\right) + 1} \quad (3.1)$$

The Fermi level (E_F) in the previous equation is by definition the energy at which the Fermi function is equal to $f_{FD}(E_F) = 1/2$. Moreover, at a temperature of 0 K, the Fermi function assumes a step shape, with a probability of 1 that a state at energy below the Fermi level is occupied, and a zero probability that an energy state above the Fermi level is filled. However, at ambient temperature, around 300 K, the edges of the Fermi function are smoother, with a non-zero probability that some states above the Fermi level are occupied by electrons. In these terms, metals are characterized by a Fermi level in between an energy band, whereas for insulators and semiconductors, it lies in the energy band gap. Moreover, since a semiconductor has a short band gap, some electrons are hosted in the conduction band at room temperature, showing better transport properties with respect to the insulator. In semiconductors, the Fermi level provides information on the distribution of free charges in the valence band (holes) and conduction band (electrons). An intrinsic semiconductor has the Fermi level at the middle of the band gap, thus, the populations of free carriers in the bands are equal. By the doping process is possible to unbalance the two populations, if the number of free electrons is larger than the number of holes, the Fermi level is close to the conduction band edge, and vice-versa. The Fermi level is also a key quantity in describing the interaction between different materials: while reaching the equilibrium, a charge transfer at the interfaces acts in order to align the Fermi level of the components.

3.1.2 Bulk states

A more complete explanation of the origin of the band structure is obtained by considering the periodicity of the crystal lattice [38]. For a periodic system, the Schrödinger equation, which describes the state of the electrons, assumes solutions in the form of Bloch functions:

$$\psi_{nk}(\vec{r}) = e^{i\vec{k}_n \cdot \vec{r}} u_{nk}(\vec{r}) \quad (3.2)$$

where \vec{k} is the electron wavevector related to the particle's direction motion, n is the index of the band and \vec{r} identifies the position in the three-dimensional space. For an electron in a perfect crystal, the energy eigenstates are Bloch states that have the same periodicity of the crystal structure identified by the function $u_{nk}(\vec{r})$, such that $u_{nk}(\vec{r} + \vec{R}) = u_{nk}(\vec{r})$, where \vec{R} is the real space lattice vector. Therefore, the Bloch function can be rewritten in the following way:

$$\psi(\vec{r} + \vec{R}) = e^{i\vec{k} \cdot \vec{R}} \psi(\vec{r})$$

Normally, the plot of the band structure of a solid is expressed by the dispersion relation between the wavevector of the electrons and the electron energy, having information on both the energy and the state of motion. Figure 3.2 represents the band structure of cadmium telluride, calculated through an empirical pseudopotential method [41], showing the dispersion curves as a function of the wavevector. Due to the periodicity and the

symmetry of the crystalline lattice, only some specific directions of the k-space should be plotted in order to have a full description of the system, the directions connect the high symmetry points (Γ , K , X , W ...) of the Brillouin zone [38]. A complete description of the band structure is not necessary for the purpose of this thesis, however, one has to know that from the band structure can be extracted important information on the electronic and optical properties of the material.

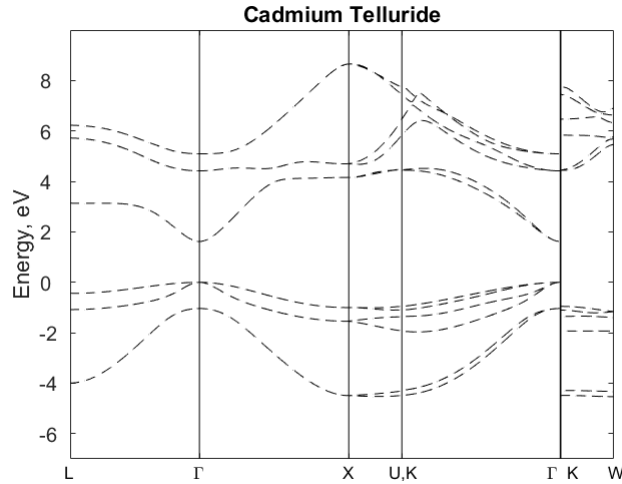


Figure 3.2. Approximation of the cadmium telluride electronic structure calculated through local empirical pseudopotential model.

3.1.3 Surface states

The surface of a material is the sharp transition between the solid and the vacuum. The atoms at the surface of a solid material have fewer neighboring atoms with respect to all the other atoms inside the bulk. As a consequence, they show some dangling bonds, and, according to that, the electronic structure close to the surface is markedly different. In particular, the different potential at the surface causes the generation of new electronic states, the so-called surface states, in which wavefunctions are restricted to the surface [39]. These states are like reminiscences of the isolated atom states. Since the electronic structure is different, the surface electronic properties differ from the 3D bulk material. The local distortion of the distribution of the electronic charge induced by the surface modifies some characteristics of the material, like the work function, the contact potential, surface reactivity, and all those phenomena that remove electrons from the solid, like thermionic and photoelectric effects [39].

Surface states of a metal

The surface can be modeled, in a simplified way, as a one-dimensional semi-infinite chain of identical and periodically arranged atoms. The potential energy of such a structure is depicted in figure 3.3. At the surface, represented by the end of the chain, the potential jumps abruptly to the vacuum level (this is an oversimplification of any real surface) [39].

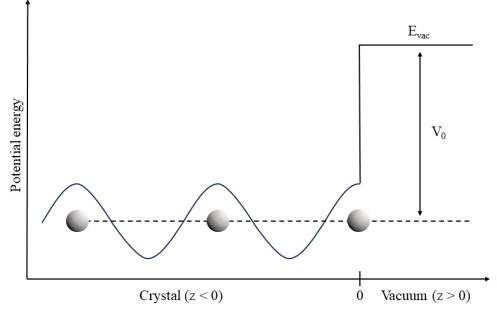


Figure 3.3. One-dimensional model of the potential energy across a metal surface.

The states of the system are obtained by solving the steady-state Schrodinger equation, with a periodic potential of the following form: at $z_0 = 0$ there is the surface, below the solid and above the vacuum, moreover, the chain is periodic, so the bulk potential has a periodic shape, with the periodicity of the lattice.

$$\left[-\frac{\hbar^2}{2m} \frac{d^2}{dz^2} + V(z) \right] \Psi(z) = E\Psi(z)$$

$$\begin{cases} V(z) = P\delta(z + la) & z < 0 \\ V(z) = V_0 & z > 0 \end{cases}$$

The solution of the equation is obtained by separating the domain in bulk ($z < 0$) and vacuum ($z > 0$) regions, the piecewise-defined function is obtained by imposing the usual condition of continuity of the wavefunction and its first-order derivative at the surface ($z = 0$), in other terms, the two components of the wavefunction must be matched at the surface. Since the potential inside the material is infinite and periodic, the solutions have the form of Bloch waves (3.2), on the contrary, on the vacuum side, the wavefunction cannot diverge and it does not contain any complex term [39]. So, to have continuity, the bulk wavefunction must be a superposition of an incoming and a reflected Bloch wave, a standing wave. The electron wavefunction has the following expression:

$$\begin{cases} \Psi_{in}(z) = Ae^{ikz}u_k + Be^{-ikz}u_{-k} & z < 0 \\ \Psi_{out}(z) = Ce^{-\sqrt{\frac{2m}{\hbar^2}(V_0-E)}z} & z > 0 \end{cases}$$

The term under the square root is a real quantity since E is the energy of the electrons which is lower than the vacuum potential V_0 because the electrons are confined in the

solid. The shape of the surface states at a metal surface is therefore represented in figure 3.4: they are characterized by a periodic standing Bloch wave inside the crystal with an exponentially decaying tail on the vacuum side. It can be demonstrated that the equation is fulfilled by every possible allowed electron energy of the bulk state, within the energy bands. This means that the bulk states of a metal are just slightly perturbed by the surface, indeed, the decaying tail allows the non-zero probability of having an electron outside the crystal, bounded to the surface, as a consequence, there is a lack of negative charge density just below the surface, resulting in the formation of a surface dipole layer [39].

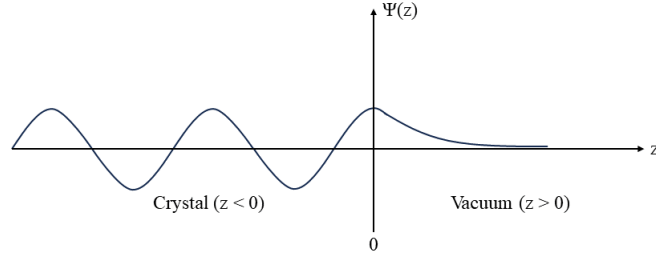


Figure 3.4. Surface state of a metal, showing a periodic behavior in the bulk and an exponential decay above the surface.

The surface dipole has a huge effect on the electronic properties of the surface, it is responsible for the perturbation of the surface potential which leads to the change in the metalwork function. The surface dipole is characteristic of the surface, it depends of course on the material, but also on the crystallographic phase that the surface exposes [42]. The work function is the key quantity, in the band diagram of electronic devices, to describe the metal, as a matter of fact, the UPS analysis is conducted in order to determine the work function of the device.

Surface states of a semiconductor

For the purposes of this thesis, the discussion on the surface states can be restricted to the metal case, however, for the sake of completeness, a brief presentation of the surface states in a semiconductor is provided in the following since the surface states introduced new electron energy states within the semiconductor band gap. The model is similar to the previous one (3.3): a semi-infinite chain of equally spaced atoms, however, in this case, the shape of the potential inside the material is a cosine function, whereas, on the vacuum side, the potential is constant to the V_0 [39].

$$\begin{cases} V(z) = V [\exp(i\frac{2\pi z}{a}) + \exp(-i\frac{2\pi z}{a})] = 2V \cos(\frac{2\pi}{a} z) & z < 0 \\ V(z) = V_0 & z > 0 \end{cases}$$

The solutions of the Schrodinger equation are obtained by imposing, once again, the condition of continuity of the zero and first-order derivative of the piecewise-defined function

at the surface. As well as the metal, all the bulk energy states, defined by the energy bands of the crystal, are allowed solutions, the shape of those states, indeed, is identical to the former metal case. However, additional surface state solutions became possible, by considering a complex wave vector $k_{\perp} = -iq$ inside the crystal, since the lattice is no longer infinite, and the periodic boundary conditions do not have to be satisfied. The allowed solutions of the system have the following expression:

$$\begin{cases} \Psi_{in} = e^{qz}u(z) & z < 0 \\ \Psi_{out} = e^{-\alpha z} & z > 0 \end{cases}$$

The matching conditions are achieved only by a single energy value α , which lies in the forbidden band gap. The wavefunction of the surface state is characterized by the exponentially decaying tail towards the vacuum and by an oscillating function that vanishes going deeper in the bulk, as shown in figure 3.5 [39]. In conclusion, the additional surface state is localized at the surface, in a region of few angstroms. The surface state wavefunction of a three-dimensional crystal is:

$$\Psi(\vec{r}) = u_{k_{\parallel}}(\vec{r}_{\parallel})e^{ik_{\parallel}\vec{r}_{\parallel}}e^{qz}$$

where $k_{\parallel} = (k_x, k_y)$ is the wavevector of the Bloch wave parallel to the surface, which is real since the surface is assumed to be periodic and infinite along those directions. A single surface state is obtained with a characteristic energy for each possible k_{\parallel} . The surface states are less separated in energy with respect to the bulk states, they are a sort of reminiscence of the isolated atom atomic orbitals. The density of surface states is in the order of $N_{ss} = 10^{15} \text{ cm}^{-2}$, which corresponds to the density of exposed atoms at the surface, several orders lower than the bulk DOS. It is evident that the existence of the surface states in the energy band gap of a semiconductor has important effects on its electronic and optical properties, which can be exploited in applications [39]. The complete representation of both bulk states and surface states is obtained through the projected bulk band structure [39].

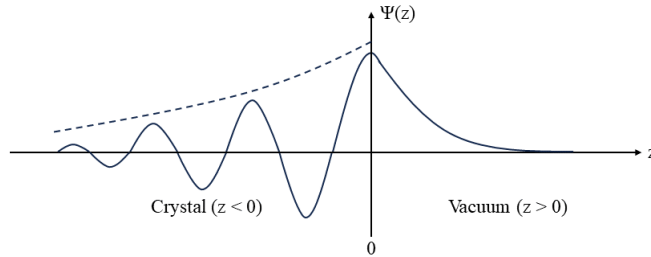


Figure 3.5. Localized surface state of a semiconductor, showing an exponential decay of the wavefunction both above and below the surface.

3.2 Molecular energy spectrum

Different from a solid material, the molecule is made of a limited number of atoms kept together with chemical intermolecular interactions. From a quantum mechanical point of view, a molecule is seen as a quantum dot, since the electrons are confined in all three directions of the space, within the extension of the molecule [43]. The density of states of a zero-dimensional structure consists of a series of Dirac delta functions. A way to compute the electronic structure of a molecule is through the Linear Combination of Atomic Orbitals (LCAO) [44, 45], the obtained result is that the molecules are characterized by a set of discrete energy levels associated with the molecular orbitals. Among all the discrete electronic states, normally, only two of them are considered, since of major importance in determining the electrical and optical properties of the molecule: namely the HOMO (Highest Occupied Molecular State) and LUMO (Lowest Unoccupied Molecular State). As the name suggests, at thermodynamic equilibrium, the electrons can occupy the states up to the HOMO level included, whereas, the states above the HOMO are all empty. Another very important quantity is the energy separation between these two levels, the so-called HOMO-LUMO gap (HLG), which acts as the band gap of a semiconductor. The probability distribution function follows the Fermi-Dirac statistics, as a matter of fact, the Fermi level is within the HLG, moreover, every orbital can host at maximum two electrons of opposite spin, due to the Pauli's exclusion principle [43]. Other quantities can be extracted from the molecular band diagram: the Ionisation Potential (IP) is defined as the energy difference between the vacuum level and the Fermi level, while the Electron Affinity (EA) is the energy distance between the vacuum level and the LUMO. A generic molecular structure diagram, where all the previously mentioned quantities are exhibited, is shown in figure 3.6.

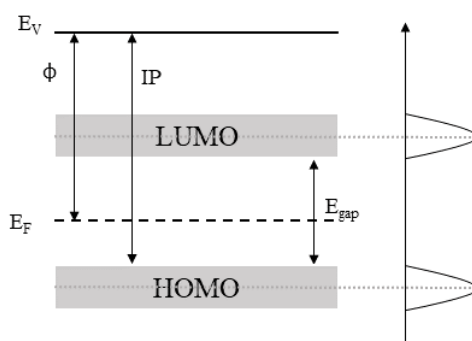


Figure 3.6. Band diagram of an organic semiconductor showing the broadening of the HOMO and LUMO and the most relevant energy quantities. The dashed lines highlight the electronic structure of the single molecule.

3.2.1 Organic semiconductor

An organic semiconductor is made of carbon-based molecules that are usually bonded to oxygen, hydrogen, and nitrogen. There are different classes of organic semiconductors according to the disorder of the molecules, the smaller the molecules, the higher the degree of order, and, in some cases, a crystalline structure can be achieved. The molecules act like space-localized energy states, however, due to the disordered arrangement of the molecules and the thermal noise, the molecular energy states are not defined by the same energy. Molecular orbitals are scattered into a "valence band" like and "conduction band" like a set of states, respectively rising from the HOMO and LUMO of the single molecules, as shown in figure 3.6. The density of states in such bands can be approximately described by a Gaussian distribution. Thus, the HOMO and LUMO states are broadened into narrow Gaussian peaks which are encoded the degree of disorder of the organic semiconductor. As a matter of fact, the full-width half maximum (FWHM) of the peak shrinks with the order [25]. Usually, the band gap of organic semiconductors is quite large, indeed, the absorption is in the visible range. The arrangement of free molecules in a layer brings other effects on the band structure. Due to the formation of narrow bands, IP and EA are defined based on the band edges, thus the former is reduced and the latter is increased, as a consequence, the energy gap is shrunk with respect to the isolated molecule. In addition, the geometry relaxation of a crystalline organic semiconductor stabilizes the system, and screening mechanisms between molecules can occur, reducing IP and increasing EA once more. Moreover, surface dipoles may arise from polar bonds. The effect is a rigid shift of the energy levels with respect to the vacuum level, without affecting the energy band gap of the material [25].

A key characteristic in defining the transport properties of an organic semiconductor is the presence or not of delocalized states, molecular orbitals that extend over the whole molecule. The carbon atoms of organic molecules can be subjected to the hybridization process that generates hybrid orbitals. By mixing one s-type orbital with a p-type one, two sp hybrid orbitals are formed. The sp^2 -orbitals consist of three co-planar sp -orbitals oriented at 120° from one to another and a remaining, out of the plane, p_z -orbital. The intermolecular bonds, involving the carbon atoms, that constitute the molecule can be of two types, the strong σ -bonds are between an s atomic orbital and a carbon sp hybrid orbital, whereas, the weak π -bonds are between p_z atomic orbitals of adjacent carbon atoms. The π bonds induce electronic states that are delocalized over the molecule. The double bond between two carbon atoms consists of a σ -bond plus an additional π -bond. A conjugated polymer is an organic macromolecule characterized by a backbone of alternating single and double bonds between adjacent carbon atoms. The overlapping p_z -orbitals allow the creation of a system of delocalized electrons, that provide interesting optical and electronic properties. In large molecules, the delocalization can be restricted to a small region of the molecules, involving a bunch of atoms, forming a conjugation site with a local delocalization. indeed, a long polymer chain is characterized by a series of conjugation sites. The organic semiconductor is made by a set of energy states distributed in energy and space, which correspond to the conjugated sites. Thus, the charge transport is completely different with respect to the crystal semiconductor framework. The electrons and holes can jump between conjugation sites thanks to the "hopping" process [46]. A

simple, yet overcome, representation of the hopping process is provided by the Miller-Abrahams (MA) model [47] which defines the transition probability (3.2.1) between two states entirely based on tunneling processes, where each state is defined by a position and an energy. The jump is then thermally activated.

$$W_{ij}(R_{ij}, \Delta E_{ji}) = \nu_0 e^{-2\gamma|R_{ij}|} e^{-\frac{\Delta E_{ji}}{k_B T}}$$

$R_{\{i,j\}}$ is the distance between the two states, whereas $\Delta_{\{j,i\}} = E_j - E_i$ is the energy separation between the final and initial state. ν_0 is just a normalization factor and γ is a tunneling parameter that takes into account the wavefunction overlapping between close states. The probability decreases with the distance in both energy and space between two states. Moreover, the previous equation is valid only for upward transitions, when $E_j > E_i$, whereas, for all the downward jumps, the probability is always $W_{\{ij\}} = 1$, independently from energy difference and displacement. The MA model is not predictive, its parameters must be fitted with experiments. However, it provides an effective way to visualize and qualitatively describe the hopping process. The interested reader can find a better analysis of hopping provided by the Marcus Model of the transition probability in [48].

3.3 Metal-organic interface

For an organic device, the interfaces between the components determine the transport properties, thus, the performances of the device, how the energy bands align while reaching the thermodynamic equilibrium and the possible creation of energy barriers define the charge transfer and the injection efficiency. The majority of organic devices use metallic electrodes, indeed, the metal/organic contacts have been intensively investigated in the last years, providing some models for the alignment of the electronic structures of the components. Due to the superposition of several electrostatic and quantum mechanical factors, like the presence of dipoles at the surfaces, a charge transfer between the components, chemical reactions, and others, the metal/organic interface does not behave like a Schottky barrier, on the contrary, it is characterized by unique features. Moreover, from a technological point of view, the morphological properties of the deposited organic layer and its crystalline organization are controlled by the interface interactions [16, 19, 28]. When two solids are put in contact, the thermodynamic equilibrium is reached when the Fermi levels are aligned, to achieve this goal, a charge transfer occurs at the junction. This simplistic model does not take into account the presence of dipolar layers at the interface that completely modify the electronic landscape at the interface. The possible origin of the dipoles is still under study, however, some interpretation is provided by the literature [16, 28, 40] and presented in the following. The most evident effect of the interface dipole is the change of the work function, but also other physical observables are altered, like the molecular energy levels and tunneling currents. Nevertheless, all the measurable quantities are affected simultaneously by different mechanisms, therefore, trying to identify the single effects is a challenging task. To describe the real charge rearrangement, it is necessary to solve the Poisson equation of the system, however, for the purposes of this work is sufficient to provide a qualitative introduction of the main factors.

Pauli pushback effect

Also known as the "pillow" effect, the Pauli pushback is present whenever a molecule is physisorbed on a metal substrate. The metal is characterized by a surface dipole which defines, with the Fermi level, the work function. When a molecule is adsorbed, a repulsive force, between the electrons of the molecule and the metal ones, "push" the metal surface electrons "back" inside the metal bulk. As a consequence, the surface dipolar layer of the metal is reduced, which, in turn, results in a reduction of the metal work function (at the surface). The adsorption of molecules causes a charge rearrangement of the metal electron cloud. The repulsion has a quantum mechanical nature: when approaching, the molecular orbitals overlap with the metal wavefunctions, but this is avoided by the orthogonalization of the orbitals imposed by the Pauli principle. The pillow does not form a new dipole, it just reshapes the already existing metal surface dipole, the reduction of the work function is indicated by $\Delta\phi_{PB}$ and can reach 1 eV. The variation of the metal work function depends on the metal and molecule polarizability.

Screening

If the Pauli effect acts on the metal side of the interface, as soon as the molecule is adsorbed, the induced rearrangement of the free electrons at the metal surface screens the intermolecular interactions of the molecule. As a result, the molecular charges find a new configuration that is energetically convenient. Therefore, the screening has an impact on the molecular electronic structure: the orbitals are reshaped and, as a consequence of the adsorption, the electronic states have lower energy. This also reduces the HOMO-LUMO gap, which defines the electronic and optical properties of the organic layer. A simple explanation of this behavior can be found in the relationship between the size of a quantum well and the energies of its modes, which are inversely proportional to the size of the well. Indeed, the screening softens the molecular interactions, thus, the electrons are less confined and the orbitals have a larger extension, resulting in a lower energy. Another phenomenon that contributes to the change in the molecular electronic structure is the relaxation of the molecules during the adsorption, which can affect the interatomic distances and so the orbital energies, as a result, the IP and EA of the organic layer are modified.

Charge transfer

The coupling between the molecular orbitals and the metal wavefunctions which is responsible for the charge rearrangement, leads to the formation of hybrid states at the surface. As a consequence, the molecular states are broadened, and the intensity of such an effect depends on the coupling between the wavefunctions. In order to reach the thermodynamic equilibrium, the molecular states up to the Fermi level must be filled, which means that the positions of the broadened HOMO and LUMO determine the eventuality and the direction of the charge transfer across the interface. Indeed, it is not strange that after the interaction, the broadening of electronic states crosses the Fermi level, allowing the transfer of charge. If the LUMO expands below E_F , electrons are moving from the metal to the molecule, and an upward shift of the vacuum level occurs, the opposite happens if

the HOMO is above E_F , the molecule loose negative charge resulting in a downshift of the vacuum level. The charge transfer will introduce a bond dipole density that follows the Helmholtz equation, which has to be summed to the pushback effect.

$$\Delta\phi_{CT} = \frac{\mu_{CT}}{\epsilon_0 A}$$

The amount of net charge transferred is typically a non-integer value. However, a secondary effect of charging a molecule is the rearrangement of the electronic states: adding (or removing) an electron to (from) a molecule will shift the energy level up (down). The shift of the molecular orbitals may unbalance the system, in the sense that, in this intermediate configuration, an excess (or deficiency) of electrons can be hosted in the molecule, leading to a second charge transfer, that, once again, causes a shift in the energy levels. This is repeated until the thermodynamic equilibrium is reached.

3.3.1 Induced density of interface states

The IDIS model [40, 49, 28] is an alternative to the previous phenomena to describe the charge transfer at metal-organic interfaces. It describes interfaces characterized by weak hybridization of the molecular orbitals with the metal wavefunctions. During the adsorption, the metal surface state tails tunnel into the band gap of the molecule, which leads to a shift and broadening of the organic material energy levels and the formation of hybrid states into the band gap. As a result, the initially discrete molecular electronic structure is transformed into a continuous density of states characterized by a non-negligible DOS within the energy gap, the so-called "induced density of interface states" that gives the name to the model. According to the model, the effect of the interaction is enclosed in the change of the molecular electronic structure. In figure 3.7 are superimposed the discrete and the continuous DOS of a generic molecule.

The IDIS defines the charge transfer at the interface. The alignment of the band structures is referred to as the Charge Neutrality Level (CNL), a sort of Fermi level of the IDIS that is obtained by integrating the induced DOS of the molecule until a point that matches the number of electrons of the isolated and neutral molecule (3.7). Therefore, the position of the CNL and the metal work function with respect to the vacuum level determines the direction and the intensity of the charge transfer: if CNL is above ϕ_M the electrons move from the molecule to the metal (donor molecule), the opposite behavior if CNL is below ϕ_M (acceptor molecule).

$$N = \sum_i Z_i = \int_{-\infty}^{CNL} \rho_{IDIS} dE$$

The charge transfer induces a dipole at the interface (Δ) that can be calculated by introducing the slope factor S ($0 < S < 1$) that represents the deviation of the interface with respect to the Schottky limit, indicating the dependence of the interface Fermi level on the metal work function, thus, the strength of the interaction.

$$S = \frac{dE_F}{d\phi_M} = \frac{1}{1 + 4\pi e^2 D(E_F) dA}$$

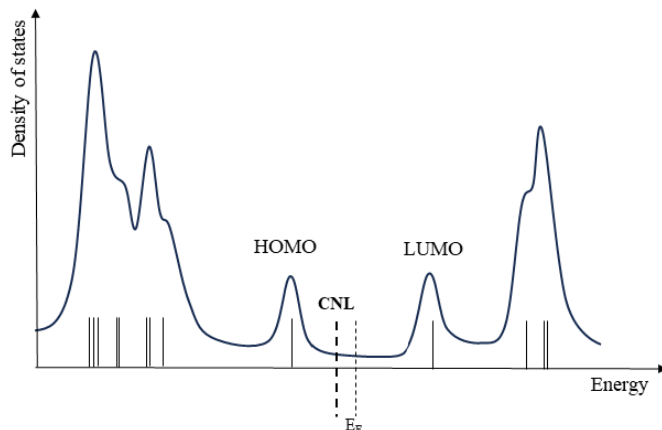


Figure 3.7. Continuous IDIS with a non-negligible density of states in the forbidden gap vs. the discrete molecular electronic structure. The CNL is shifted with respect to the original Fermi level.

The slope parameter can be obtained from the IDIS, as shown in the previous formula: $D(E_F)$ is the density of states of the molecule at the Fermi level, d the adsorption distance, and A the unit cell size. Finally, the position of the Fermi level and the induced surface dipole Δ are calculated.

$$E_F - CNL = S(\phi_M - CNL) \quad \Delta = (1 - S)(\phi_M - CNL)$$

3.3.2 Metal-molecule band diagram at equilibrium

This section discusses the band diagram of the metal-molecule interface as it evolves during the interaction, by decomposing the complex phenomenon through the previously introduced factors one at a time, in order to highlight the single effects [29, 50]. However, with this separation, we are approximating the description of the phenomenon, since, in reality, all the effects happen simultaneously and they interfere with each other.

In the initial configuration, when metal and molecule are far from each other, no interaction occurs, the equilibrium condition is reached by aligning the vacuum level of both materials (3.8a). As the distance between the metal and molecule becomes shorter, the molecular orbitals and the metal wavefunctions start to spatially overlap and the interaction begins. The trivial equilibrium condition obtained by aligning the Fermi level of the metal and molecule cannot be employed. The first phenomenon to consider is the Pauli pushback (3.8b) that reduces the work function of the metal at the surface of $\Delta\phi_{PB}$, caused by the shrinking of the metal surface dipole due to the quantum mechanical repulsion with the molecule. Moreover, also the molecule feels the dipole at the surface, as a consequence, the electronic structure of the molecule is rigidly downshifted of a quantity $\Delta\phi_{PB}$. Figure 3.8c points out the changes in the molecular electronic structure, focusing, for simplicity, only on the HOMO and LUMO levels. The reorganization of the molecular

energy levels is caused by the screening performed by the surface charge rearrangement. As a consequence, the HOMO-LUMO gap is reduced. Then, the coupling between the molecular orbitals and the metal bands causes the broadening of the molecular states (3.8d). In this scenario, depending on the intensities of the previous factors, may happen, as shown in figure 3.8e that some molecular states allow a transfer of charge with the metal (empty LUMO below E_F , or occupied HOMO above E_F). To reach the thermodynamic equilibrium, the molecular states must be filled up to the Fermi level, the charge transfer will introduce a dipole at the surface $\Delta\phi_{CT}$ that shifts, according to the direction of the charge transfer, the work function of the molecule. However, the molecular states are very sensible to the addition (removal) of charge to (from) the molecule, hence, the energy levels are shifted again. Finally, the equilibrium condition is reached (3.8f). This simple model takes into account only a few phenomena, many others, like the distortion of the molecule geometry, chemical bonds, or molecular dipoles, can deeply modify the interface band structure. In conclusion, the adsorption modifies the work function and the energy of the molecular orbitals, respectively by $\Delta\phi$ and $\Delta\epsilon$, where V_S is the energy shift due to the screening effect and V_{CT} the one due to the charge transfer.

$$\Delta\phi = \Delta\phi_{PB} + \Delta\phi_{CT}$$

$$\Delta\epsilon = \Delta\phi_{PB} + \Delta\phi_{CT} + V_S + V_{CT}$$

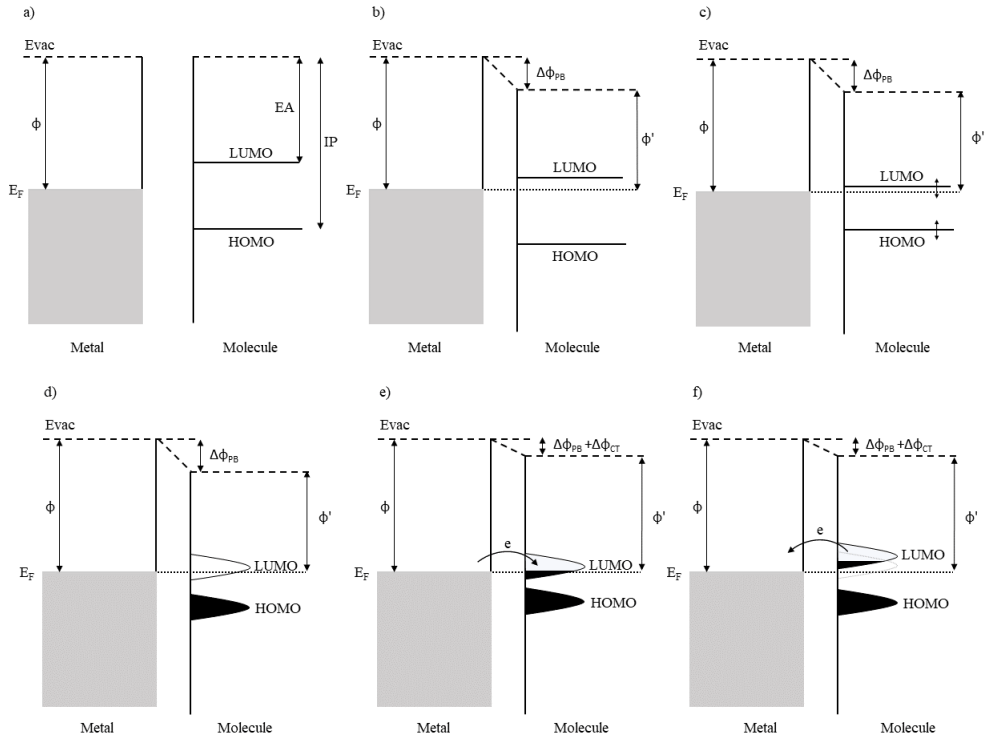


Figure 3.8. Qualitative scheme of the metal/molecule interface band diagram evolution.

3.3.3 Conduction at the nanoscale

Finally, this section presents the very basic information concerning quantum conduction involving zero-dimensional systems (quantum dots), which is fundamental for the transport properties in molecular devices. The aim is to provide a simple qualitative description of the conduction mechanism, with a particular focus on the importance of the so-called transmission function. The reason is that the results, presented in chapter 9.4 are not sufficient to provide a comprehensive analysis of the phthalocyanine transport properties, thus the discussion of the most essential aspects is sufficient. The rigorous description of the quantum transport is based on the Non-Equilibrium Green's Function (NEGF) formalism. An introduction to this topic is provided in [51], which is a suitable reference material for interested readers who are not familiar with neither the second quantization formalism nor the many-body perturbation theory. Moreover, it presents the "toy model", which is an oversimplification of the transport through quantum dots, but it allows to define the Landauer-Büttiker formalism from which an equation of the electrical current is obtained, the so-called Landauer's equation 3.3.

$$I_{DS} = \frac{2q}{h} \int T(E) [f_{FD}(E, E_{FS}) - f_{FD}(E, E_{FD})] dE \quad (3.3)$$

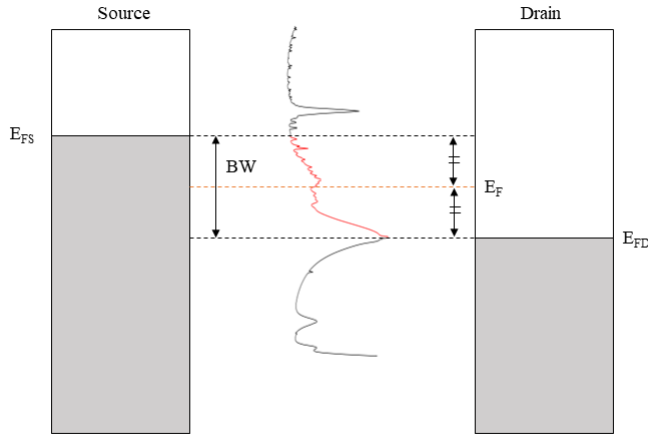


Figure 3.9. Qualitative representation of the transport in molecular devices. The source electrons with an energy E within the bias window, set by the applied voltage, can be transferred to the drain with a probability equal to $T(E)$.

The Landauer's equation is a fundamental formula for the calculation of the electric current between two electrodes, which encloses in just three terms the complexity of the quantum transport mediated by a quantum dot. In particular, the properties and the features of the molecular device (electrode-molecule-electrode) are described by the transmission function $T(E)$, which is a function of the energy E , and by the difference between the Fermi-Dirac functions of the source and drain evaluated at the energy E , respectively

$f_{FD}(E, E_{FS})$ and $f_{FD}(E, E_{FD})$. The transmission function basically defines the probability that an electron with a specific energy E can be transmitted from the source to the drain through the quantum dot. Each electron that is transmitted contributes to the drain electric current I_{DS} . The transmission function depends on the electronic properties of the molecule and on how it interacts with the electrodes. Moreover, it is also a function of the working conditions of the device, as the applied bias, thus it is a very complex function, but necessary to have a full picture of the device transport properties. On the other hand, the difference between the Fermi-Dirac functions in the Landauer's equation determines the "Bias window", which is defined by the applied bias voltage and sets the range of electron energies that may contribute to the current. If an electron has an energy E , included between $f_{FD}(E, E_{FS})$ and $f_{FD}(E, E_{FD})$, it can be transferred from the source to the drain, passing through the molecule with a probability equal to $T(E)$. Figure 3.9 shows a very simple model that qualitatively describes the transport in molecular devices, which does not consider many fundamental aspects of the process.

Chapter 4

Electronic structure

All the electronic properties of a system, like the charge distribution, the potentials, and the energies involved, can be extracted from the electronic structure [52]. According to quantum mechanics, a system is described through a Hamiltonian operator, from which the electronic states of the system are obtained by solving the steady-state Schrödinger equation: $\hat{H}\Psi = E\Psi$. Where \hat{H} is the Hamiltonian operator, Ψ is the many-body eigenfunction of the whole system and E is the energy. The solutions are the stationary states of the system. However, deriving the Hamiltonian of a system is not trivial, even for a small amount of atoms, the expression of the Hamiltonian is challenging to solve. The reference materials [45, 53] will provide a deeper description and discussion on the basics of quantum mechanics. The electronic structure corresponds to the state of motion of all the electrons of the considered system subjected to the electrostatic field created by the stationary nuclei [54]. In other terms, it consists of finding the eigenfunctions ϕ_i and their associated energies E_i of every state. For a molecular system, the wavefunction of the many-body system $\Psi(r_1, r_2, \dots, r_n)$ is the steady state of the entire molecule which defines all the molecular orbitals. The square modulus of the eigenfunctions $|\psi_i|^2$ identify the regions of space related to the probability of finding an electron, thus they describe the molecular orbitals of the system. Moreover, E_i are the energy levels associated with the orbitals. These quantities, which characterize the electronic structure of the molecule, are obtained by solving the steady-state Schrödinger equation.

4.1 Generic system Hamiltonian

The Hamiltonian operator is the quantum mechanical operator that represents the total energy of the system. The rigorous expression of the Hamiltonian of a generic system is obtained by the sum of the kinetic energies of every particle (nuclei and electrons) and a potential energy term that takes into account all the possible Coulombic interactions between every particle of the system, reported here.

$$\hat{H} = \hat{K} + \hat{U} = -\frac{\hbar^2}{2m}\Delta + V(\vec{r})$$

Where the terms \hat{K} and \hat{U} are respectively the kinetic energy and the potential energy operators. \hbar is the reduced Planck constant, and m is the mass of the particle. Both terms can be rewritten by considering the different components of the system. The kinetic operator can be split into two components referring separately to the kinetic energy operator of the N_n nuclei and the N_e electrons. This is allowed because the Laplacian operator Δ is linear, therefore, the superposition of effects can be applied. Whereas, the potential energy operator can be separated into three components according to the particles involved in the Coulombic interaction.

$$\hat{K} = \hat{K}_n + \hat{K}_e = - \sum_{j=1}^{N_n} \frac{\hbar^2}{2m_n} \Delta_{R_j} - \sum_{i=1}^{N_e} \frac{\hbar^2}{2m_e} \Delta_{r_i}$$

Where $\vec{R}_j = (x_j, y_j, z_j)$ and $\vec{r}_i = (x_i, y_i, z_i)$ are respectively the vectors of the coordinates of the nuclei and electrons. The potential energy operator corresponds to the potential energy and, as already anticipated, three components are individuated, as shown below. The first and last term are the contribution of the nuclei-nuclei and electrons-electrons repulsion, respectively, while the second one is the contribution due to the electrons-nuclei attraction.

$$V = V_{nn} + V_{ne} + V_{ee}$$

To summarize, the complete and generic expression of the Hamiltonian of a system is the following (4.1):

$$\hat{H} = - \sum_{j=1}^{N_n} \frac{\hbar^2}{2m_n} \Delta_{R_j} - \sum_{i=1}^{N_e} \frac{\hbar^2}{2m_e} \Delta_{r_i} + V_{nn} + V_{ne} + V_{ee} \quad (4.1)$$

Unfortunately, this expression of the Hamiltonian makes the solution of the Schrödinger equation impossible, because the number of variables is too large even for a system with few atoms. Some approximations of the model should be taken into account in order to reduce the complexity of the problem while providing an acceptable description of the system. In solid-state physics, the first approximation that is exploited is the so-called tight-binding approximation, which basically consists of dividing the system into ions and valence electrons rather than nuclei and electrons. The ions are made of the atomic nuclei plus the core electrons, which are strongly bound to their nucleus, and thus do not participate in the chemical interactions that constitute the solid. With this approximation, the number of electrons to be considered, and consequently, the number of variables, is heavily reduced.

4.2 Born-Oppenheimer approximation

The reason for this approximation [55] lies in the huge mass difference between the two species of the system, the nuclei, and the electrons. Since the kinetic energy of the nuclei (or ions) is due to thermal agitation, a rough estimation of the nuclei velocity can be obtained from the following equation.

$$\frac{1}{2} M v_n^2 \simeq \frac{3}{2} k_B T \quad v \simeq \sqrt{\frac{3k_B T}{M}}$$

The velocity difference between electrons and nuclei is around three orders of magnitude, this means that the electrons, being tens of thousands of times lighter than the nuclei, and so much faster, can quickly respond to any variation of the nuclei configuration. The electrons can restore an equilibrium condition almost instantaneously with respect to any small displacement of the ions. On the contrary, for any change in the electron cloud configuration, the ions will react very slowly, and, in the meantime, the electrons have already changed their configuration several times, thus, the ions are interacting with an average of the electron configurations. The Born-Oppenheimer approximation imposes that the electrons reach instantaneously an equilibrium condition for any nuclei configuration, and, on the other hand, the nuclei configuration depends on a time average of the electron one, which is constant in time. As a consequence, since the nuclei have fixed coordinates, their kinetic energy, and so the respective operator of the Hamiltonian, is null. In addition, the potential energy term related to the nuclei-nuclei interaction is neglected. This reduces the Hamiltonian of the system to the following one, where the nuclei are involved in V_{ne} only.

$$\hat{H} = \hat{K}_e + V_{ne}(\vec{r}_i, \vec{R}_j) + V_{ee}(\vec{r}_i, \vec{r}_k)$$

The problem is reduced to solve the steady-state Schrodinger equation (4.2) by considering the electronic Hamiltonian only, indeed, the wave function of the system is reduced to the many-body wave-function of the N_e electrons only, which depends on the electron coordinates as variables, whereas the nuclei positions are just parameters.

$$\hat{H}\psi(\vec{r}_1, \vec{r}_2, \dots, \vec{r}_{N_e}) = E\psi(\vec{r}_1, \vec{r}_2, \dots, \vec{r}_{N_e}) \quad (4.2)$$

In summary, with the Born-Oppenheimer approximation we get rid of two terms of the general Hamiltonian of a solid, but this is not sufficient to obtain a manageable description of the system, since the number of variables is still very high and, moreover, the potential energy term, which concerns the interaction between electrons, does not allow a solution. In the following, I will briefly present how V_{ee} is fitted [51]. Several methods have been developed, each taking a different approach to describing V_{ee} .

4.3 Hartree model

As already anticipated, the main problem in solving the many-body Schrödinger equation (4.1) relies on the V_{ee} term of the Hamiltonian. The full expression of this term takes into account all the possible Coulombic interactions between every couple of electrons of the system. Its expression is the following:

$$V_{ee}(\vec{r}_i, \vec{r}_j) = \frac{(-e^2)}{2} \sum_{i=1}^N \left[\sum_{j \neq i} \frac{1}{|\vec{r}_i - \vec{r}_j|} \right]$$

The Hartree assumption is that it is possible to decompose the many-body eigenfunction describing the whole electronic system as the product between N_e single-electron wave-functions, each one of them depends on the spatial coordinates of a single electron, as

shown below. This approximation of the wave function lies on the assumption that the electrons of the system are not interacting between them.

$$\Psi_{HAR} = \psi_1(\vec{r}_1)\psi_2(\vec{r}_2)\dots\psi_{N_e}(\vec{r}_{N_e}) \quad (4.3)$$

From the variational method, it can be demonstrated that, by assuming a wave function of this kind (that is factorized), the best solution of the system must satisfy the following expression of the Hamiltonian, where the many-body problem is moved to a set of N_e independent equations, one for each electron [53].

$$-\frac{\hbar^2}{2m_e}\Delta_i\psi_i + \hat{V}_{tot}(\vec{r}_i)\psi_i = \epsilon_i\psi_i$$

Where, as always, the first term represents the kinetic energy of the single electron, the term V_{tot} includes the two components of the Coulombic interactions between electron-nuclei and electron-electron, whereas ϵ_i is the eigenvalue of the wave function, which means the energy of the state identified by ψ_i . Now, it is convenient to have a close look at potential energy operator \hat{V}_{ee} applied to ψ_i , which can be written in the following way:

$$\hat{V}_{ee}(\vec{r}_i) = e^2 \sum_{j \neq i}^N \int \frac{|\psi_j(\vec{r}_j)|^2}{|\vec{r}_i - \vec{r}_j|} d\vec{r}_j$$

It is possible to simplify the expression by recalling that the charge density in \vec{r} , generated by the electron in the j-state, is $\rho_j(\vec{r}) = -e|\psi_j(\vec{r})|^2$. This allows us to rewrite the electron-electron potential energy by exploiting the charge density generated by the whole electronic structure, as equation 4.4 expresses. The meaning of this result is that the Coulombic potential that affects the single i-electron of the system is generated by the combination of all the other electrons of the system [53]. Moreover, if the system has a large number of electrons, the contribution of the single j-electron on the total charge density is very small, for this reason, it is acceptable to consider a unique charge density that involves all the electrons, even if that means considering a self-interaction between the j-electron and itself. In conclusion, a single potential term \hat{V}_{ee} is evaluated for every electron. Nevertheless, in order to correct the self-interaction of the i-electron with its contribution to the charge density, a corrective factor is introduced, that simply scales the strength of the interaction [51].

$$\hat{V}_{ee}(\vec{r}_i) = \frac{(N_e - 1)}{N_e}(-e) \int \frac{\rho(\vec{r})}{|\vec{r}_i - \vec{r}|} d\vec{r} \quad (4.4)$$

For the above-mentioned reasons, the Hartree model is said to be one-electron, since the problem that has to be solved depends on a single electron and it is valid for every electron of the system. Then to obtain the electronic structure, the states must be filled according to the probability defined by the Fermi distribution function.

4.4 Hartree-Fock model

Unfortunately, the Hartree model introduced in the previous chapter is not correct since it does not respect Pauli's exclusion principle that forces the impossibility of two fermions of

the same system to be described by the same set of quantum numbers. This assumption is reflected in the symmetry of the total many-body wavefunction of the system, which must be antisymmetric [52]. In other terms, it has to respect the following property:

$$\Psi(\vec{r}_1, \dots, \vec{r}_i, \dots, \vec{r}_j, \dots, \vec{r}_{N_e}) = -\Psi(\vec{r}_1, \dots, \vec{r}_j, \dots, \vec{r}_i, \dots, \vec{r}_{N_e})$$

The difference between the two wave functions is that two electrons are inverted: in the second one, the i -electron, which was originally in the state ψ_i , is now in the state ψ_j and vice versa. It is easy to demonstrate that the wavefunction used in the Hartree model does not satisfy this condition, indeed, it is symmetric. However, a suitable expression of the wave function can be obtained by exploiting a linear combination of the orbital products, which means that the many-body wavefunction of the system can still be factorized by the one-electron wavefunction, as demonstrated in the following.

Considering a two electrons system, the antisymmetric wavefunction is obtained by a linear combination of the product of the single electron orbitals, and the antisymmetry properties are easily verified:

$$\begin{aligned} \Psi(x_1, x_2) &= \frac{1}{\sqrt{2}} \{ \psi_1(x_1)\psi_2(x_2) - \psi_1(x_2)\psi_2(x_1) \} \\ -\Psi(x_2, x_1) &= -\frac{1}{\sqrt{2}} \{ \psi_1(x_2)\psi_2(x_1) - \psi_1(x_1)\psi_2(x_2) \} = \frac{1}{\sqrt{2}} \{ \psi_1(x_1)\psi_2(x_2) - \psi_1(x_2)\psi_2(x_1) \} \end{aligned}$$

A wave function of this kind respects Pauli's exclusion principle since it forbids having both electrons occupying the same quantum state simultaneously: if x_1 is equal to x_2 the total wavefunction is null. The new expression of the wavefunction can also be written in matrix form, it corresponds to the determinant of the matrix that has as elements the single-electron wavefunctions, normalized by adding the factor in front.

$$\Psi(x_1, x_2) = \frac{1}{\sqrt{2}} \begin{vmatrix} \psi_1(x_1) & \psi_1(x_2) \\ \psi_2(x_1) & \psi_2(x_2) \end{vmatrix}$$

This result can be generalized for a system of N_e electrons: the many-body wavefunction describing the whole electronic system is written as a linear combination (considering all possible permutations of the states) of single electron wavefunctions. Such wavefunction is obtained from the so-called "Slater determinant" defined from the matrix of the single electron states [52]. The Hartree-Fock model just introduces this correction to the total wavefunction, in other terms, the quantum mechanical nature and properties of the electrons are introduced in the model.

$$\Psi(\vec{r}_1, \vec{r}_2, \dots, \vec{r}_{N_e}) = \begin{vmatrix} \psi_1(\vec{r}_1) & \psi_1(\vec{r}_2) & \dots & \psi_1(\vec{r}_{N_e}) \\ \psi_2(\vec{r}_1) & \psi_2(\vec{r}_2) & \dots & \psi_2(\vec{r}_{N_e}) \\ \dots & \dots & \dots & \dots \\ \psi_{N_e}(\vec{r}_1) & \psi_{N_e}(\vec{r}_2) & \dots & \psi_{N_e}(\vec{r}_{N_e}) \end{vmatrix}$$

With this definition of the wavefunction, Pauli's exclusion principle is then satisfied, since if two electrons share the same quantum state in the same time instant, the determinant of the matrix is zero.

The main effect of this new expression of the wavefunction is the rise of an extra term in the Hamiltonian, a term that does not involve Coulombic interactions but depends on the quantum properties of the electrons. In the following, I will provide a short presentation of this contribution to the energy of the system. Like for the Hartree model, the Hartree-Fock model transforms the many-body wavefunction of the system into a set of N_e equations, where the wavefunction ψ_i refers to the state of the i -electron. The eigenproblem that has to be solved is the following:

$$-\frac{\hbar^2}{2m_e}\Delta_i\psi_i(\vec{r}_i) + \left[-e^2 \sum_{I=1}^{N_{ion}} \frac{Z_I}{|\vec{r}_i - \vec{R}_I|} + e^2 \sum_{j \neq i} \int \frac{|\psi_j(\vec{r}_j)|^2}{|\vec{r}_i - \vec{r}_j|} d\vec{r}_j \right] \psi_i(\vec{r}_i) +$$

$$-\delta_{i,j} \sum_{j \neq i} \int \frac{e^2}{|\vec{r}_i - \vec{r}_j|} \psi_j^*(\vec{r}_j) \psi_i(\vec{r}_j) \psi_j(\vec{r}_j) d\vec{r}_j = \epsilon_i \psi_i(\vec{r}_i)$$

Where the first line of the equation is exactly like the Hartree model. Thanks to the Born-Oppenheimer approximation the only-nuclei terms are neglected, the first term is the kinetic energy of the electrons, the second and third terms represent the Coulombic interaction between the electron-nuclei and electron-electrons respectively, whereas the last term of the left-hand side is the so-called "exchange-correlation" term, that rises due to the peculiar choice of the antisymmetric wave function [53]. Each one of these terms gives a different contribution to the energy of the system. In the exchange-correlation contribution is encoded the quantum nature of the electrons, which reduces the electrostatic repulsion, thus correcting the energy of the system, which is indeed lowered. The reason is that the electrons of the system are correlated, so they tend to avoid each other while moving, from a quantum mechanical point of view it means that the probability of having one electron in \vec{r}_1 and a second electron in \vec{r}_2 does not depends only on the charge density $\rho(\vec{r})$ in those points, but the presence of one electron reduces the probability to have another electron in the same region of space. Electrons with the same quantum number cannot occupy the same orbital, which means that they cannot be in the same region of space. The exchange-correlation energy is always negative because it reduces the repulsion between electrons since it forbids the superposition of the orbitals, resulting in a deformation of the orbital shapes, hence stabilizing the system.

4.5 Self Consistent Field

As previously said, the main issue with the solution of the Schrödinger equation considering the generic Hamiltonian (4.1) consists in how to handle the potential energy operator \hat{V}_{ee} that makes the number of variables unmanageable. The "Self Consistent Field" (SCF) method tries to find an approximation to this term, by applying an iterative approach [51]. The starting points are, as always, the Born-Oppenheimer approximation, in such a way we get rid of the pure nuclei terms (kinetic and electrostatic repulsion), and the idea to transform the many-body wavefunction, the one in 4.2, into a set of N_e decoupled single-electron equations. For this reason the potential V_{ee} is substituted with a suitable potential $V_{SCF}(\vec{r})$. The expression of $V_{SCF}(\vec{r})$ is very similar to the one proposed by

Hartree (4.4), it takes into account the Coulombic interaction between all electrons, but avoids the self-interaction between the i -electron with itself. Therefore, the potential depends on the electron density $n(\vec{r})$ obtained by considering all the electrons of the system. The electron density $n(\vec{r})$ is obtained by the sum over the occupied states of the square of the single-electron wavefunctions, in other terms:

$$n(\vec{r}) = \sum_{occ.i} |\psi_i(\vec{r})|^2$$

Where $|\psi_i(\vec{r})|^2$ refers to the probability of having the i -electron in \vec{r} . The charge density is strictly related to the electron density simply by multiplying the latter by the elementary charge e with a minus sign: $\rho(\vec{r}) = -e \cdot n(\vec{r})$, that appears in the Hartree expression of the single electron potential. So, the expression of $V_{SCF}(\vec{r})$ is the following, where the multiplicative factor is just a correction to avoid the self-interaction of each electron with its contribution to the electron density.

$$V_{SCF}(\vec{r}) = \frac{(N_e - 1)}{N_e} e^2 \int \frac{n(\vec{r}')}{|\vec{r} - \vec{r}'|} d\vec{r}' \quad (4.5)$$

This method is called self-consistent since the solution of the Schrödinger equation, expressed in terms of $V_{SCF}(\vec{r})$ to obtain the wavefunctions of the system, requires an iterative procedure, where at every step the potential $V_{SCF}(\vec{r})$ is updated until convergence is reached. The reason behind the loop is that the potential is a function of the electron density, which is obtained starting from the electron wavefunctions, which are the solution of the Schrödinger equation that contains $V_{SCF}(\vec{r})$. As shown in 4.5. The process flow is the following:

1. initial guess of the potential $V_{SCF}(\vec{r})$;
2. solve the steady state Schrödinger equation with $V_{SCF}(\vec{r})$ and obtain the eigenfunctions ψ_i and the eigenvalues E_i of the electronic system;
3. calculate the electron density $n(\vec{r})$ starting from the eigenfunctions ψ_i ;
4. calculate $V_{SCF}(\vec{r})$ from $n(\vec{r})$;
5. updates the new expression of the potential if it is significantly different from the previous one, according to some chosen tolerance, otherwise the calculation is converged.

Both Hartree and Hartree-Fock methods follow the SCF method. However, as already discussed in the Hartree-Fock model, 4.5 does not describe well the interaction, since the correlation between the electrons is not included. The main problem is that a close expression of V_{XC} does not exist, indeed, the several simulation methods developed to solve the electronic structure provide different descriptions of this term. This will be the topic of the next chapter on the "Density Functional Theory".

Chapter 5

Density functional theory

The DFT is a simulation method developed for the calculation of the electronic structure of atomic systems. However, before starting with a description of the method, it is recommended to provide a sort of classification of the several simulation methods and where the main differences lie [53, 56].

5.1 Introduction to atomistic simulators

The first huge distinction is between two categories of simulations: the *ab initio* methods and the semi-empirical ones. The former provides a solution of the many-body steady state Schrödinger equation where the only assumptions are the physical constants and the physical principles, avoiding any reference with any sort of experimental data or empirical evidence. On the contrary, the latter exploits the results obtained from experiments or from other *ab initio* simulations that are introduced as parameters in the description of the system. Even if the semi-empirical method could feel less accurate, in some cases, it can lead to better results, however, it is necessary that the parameters used fit well the system. The major drawback is that those parameters are specific to that system. The accuracy of a semi-empirical method strictly depends on the quality of the experimental data from which is based. Unfortunately, the majority of the system has no access to valid data from which to build the set of parameters, For this reason, *ab initio* methods are required. They are, for sure, much less efficient, but they work with almost any system, however, according to the system, it is necessary to choose the most suitable. The second big distinction consists in the type of variables that have to be found in the simulation. In the wavefunction-based method, those variables are, as suggested by the name, the wavefunctions of the electronic system. However, as demonstrated from the models presented in the previous chapters, the wavefunctions may be derived from the electron density $n(\vec{r})$. So, since the electron density and the wavefunctions are strictly related, it is possible to reformulate the problem in order to explicitly derive the electron density. Perturbation methods and variational methods, like Hartree-Fock, belong to the wavefunction-based models, whereas the density functional theory (DFT) is of the second type. The simulations performed in this work are all obtained through DFT calculations,

for this reason, in the next chapter, I will provide some key information on how the model works.

I have introduced the Hartree-Fock model because, in some sense, it sets the basis for all the different methods, for example, the semi-empirical ones tend to further approximate the Hartree-Fock model by introducing parameters to avoid the calculation of the electron-electron integral. Whereas the so-called "electron correlation methods" introduce an additional description of the exchange-correlation term, which is the main issue in obtaining accurate results [56]. One of the assumptions of the Hartree-Fock method is the absence of any sort of interactions between the electrons of the system, from this simplification it is possible to write the factorized wavefunction for the whole structure. This means that the motion of one electron is not affected by the dynamics of all the others. Therefore, in order to take into account the correlation of the electron motion, an additional term must be introduced to the model. The total wavefunction is just a superposition of the Hartree-Fock wavefunction plus a set of other many-body wavefunctions Ψ_i , as shown below.

$$\Psi_{tot} = \Psi_{HF} + \sum_i c_i \Psi_i$$

where Ψ_{HF} is obtained through the Slater determinant and c_i are suitable coefficients. Basically, the way by which these coefficients are calculated diversifies the correlation methods. The many-body wavefunctions Ψ_i can be represented as a superposition of basis functions, if the set of basis functions is infinite, the exact solution of the problem can be obtained, in other terms, the true wavefunction of the system is reconstructed [53]. This is the Fischer-Riesz theorem which states that the original wavefunction can be expressed by a Fourier transform on a complete basis set. So, it is also possible to demonstrate that by this approach, by improving the basis set, the method converges to the exact solution. Unfortunately, in a real system, the set size must be infinite, thus, no exact solution can be obtained. A trade-off between accuracy and efficiency is necessary to reduce the simulation time, for example by limiting the basis set. Finally, there are other methods called force-field methods that work in a completely different way: the unit of the model is the atoms, so there is no distinction between nuclei and electrons, and the driving force that governs the interactions is the second Newton's law. The system is essentially represented by balls and springs where atoms are characterized by different sizes, whereas different stiffness of the springs determines the strength of the bonds [53]. These methods are not interesting for the purpose of this work.

5.2 DFT method

The "pure" Density Functional Theory is an *ab initio* method whose target, as the name suggests, is the electron density of the system $n(\vec{r})$, by optimizing it all at once [53, 56]. Once again, the interaction between electrons is governed by a mean-field generated by the whole electronic cloud, represented by the electron density $n(\vec{r})$, where all the electrons are moving. Thus, mathematically, rather than solve a single many-body wavefunction, the problem is reduced to a system of N_e decoupled one-electron wavefunctions, where N_e is the number of non-interacting electrons. The solution is achieved by performing a

SCF loop. I called it "pure" since there is a distinction between the true DFT method found in literature and the one that I actually used to perform my simulations. For computational issues, the adopted DFT method is not completely *ab initio* since to speed up the simulations, it exploits also pseudo-potentials and other corrections that come from semi-empirical methods [57]. Further details are provided in the following. However, with the DFT a satisfying trade-off between accuracy and efficiency can be obtained, even for structures made by hundreds of atoms. The great advantage of using the DFT method, which strongly reduces the complexity of the system, is justified by Hohenberg-Kohn's theorem [58], which asserts that the energy of the electronic ground state is completely determined by the electron density. This allows us to describe the system through its own electron density $n(\vec{r})$, which is described by three spatial coordinates and the spin, for a total of 4 variables that do not depend on the number of electrons in the system. Whereas, a steady-state wavefunction of a system of N_e electrons is a function of $4N_e$ variables since every electron is described by three coordinates and the spin. Different systems have different electron densities and different ground states. There is a direct link between energy and electron density, identified by a functional [56]. Unfortunately, this functional is unknown, there is no analytic expression of it.

Before moving on, I want to spend a few words on what the "functional" mentioned before stands for, since this is one of the fundamental knowledge to understand how DFT works [53]. A function is an expression that generates a number from a set of variables x and it is indicated with $f(x)$, analogously, a functional is an expression that produces a number starting from a function, where the variables of the function are now parameters of the functional. It is indicated with $F[f]$, in square brackets. In the DFT the variables are the coordinates of the electrons, the functions are the electron density or the wavefunctions, while the energy, which depends on those functions, is the functional. Therefore, the properties of the many-body system can be determined through functionals.

It is demonstrated that the DFT method leads to reliable results, nevertheless, there are few cases for which the DFT should be avoided. DFT fails in describing weak interactions as the van der Waals interactions, in describing loosely bound electrons, and for some strong electron-electron interactions. The problem in these cases is that the adopted functional does not consider some interactions that, there, are dominant. Some corrections can be introduced in order to improve the description of the system and obtain better results. The goal of the DFT is to design *ad-hoc* functionals that are able to successfully connect the energy of the system with its electron density, in order to achieve accurate results [56].

5.2.1 Kohn-Sham Hamiltonian

The first idea was to express the Hamiltonian of the system as a functional of the electron density. The Born-Oppenheimer approximation is the initial point, so the Hamiltonian of the system, which expresses the total energy of the system, is composed of the kinetic energy of the electrons and the potential energy terms due to nucleus-electron and electron-electron interactions. In this framework, the exchange-correlation term is included in $V_{ee}[n]$. Notice that this description uses functionals instead of operators, also, it does not

depend on the electron wavefunctions.

$$H_{tot} = E_{tot} = K_e[n] + V_{ne}[n] + V_{ee}[n]$$

The solution to the problem is the electron density $n(\vec{r})$, a three coordinates function that does not depend on the size of the system. An exact solution could be obtained if the functionals were known, unfortunately, they are impossible to derive.

The DFT formalism used in the simulations moves a step back with respect to the "pure" DFT, in the sense that the electron wavefunctions (the orbitals) are re-introduced in the model [57, 59]. As a consequence, the kinetic energy of the system K_e must be calculated starting from this set of auxiliary orbitals, from which the evaluation of the electron density $n(\vec{r})$ is performed. With this assumption, accurate results can be obtained since the only unknown functional is the one related to the exchange-correlation contribution to the potential energy $V_{XC}[n]$, which is a small fraction of the total energy. However, the complexity of the system is increased from only three variables (the coordinates of the electron density) to $3N_e$ (the coordinates of each electron). The Kohn-Sham Hamiltonian [57], shown in 5.1 is very similar to the Hartree-Fock one, the expression of the kinetic energy is the same, the Coulombic potential energies are identical and there is the contribution of an additional term involving the correlation between electrons.

$$H_{KS}[n] = \sum_i^{N_e} \left[-\frac{\hbar^2}{2m_e} \Delta_i + V_{HF}[n(\vec{r}_i)] + V_{XC}[n] + V_{ext}(\vec{r}_i) \right] \quad (5.1)$$

In equation 5.1 the electron kinetic energy is evaluated for all the electrons in the system, indeed it depends on all the electron coordinates, the first term of the potential is the Coulombic one, related to the electrostatic interaction between the charges in the system, so it also depends on the electron coordinates. The exchange-correlation term, in which are encoded the quantum mechanical properties of the electrons (Pauli's exclusion principle), reduces the total energy of the system, by avoiding the superposition of electron orbitals. Therefore, stabilizing the whole system [53]. It is the unknown functional of the Hamiltonian. The last term is the potential energy coming from external applied electrostatic fields. Once again, the many-body Schrödinger equation can be decomposed into a system of one-electron equations that make the calculation manageable. The three potentials constitute the so-called effective potential V_{eff} of the Kohn-Sham DFT (KS-DFT) [57]. It depends on the electron density $n(\vec{r})$, which in turn, is obtained starting from the wavefunctions (the same used to solve the kinetic term) that depend on V_{eff} . This suggests that the KS-DFT must be solved self-consistently, starting from an initial guess of the electron density, then calculating the effective potential, solving the Kohn-Sham equation for the wavefunctions, rebuilding a new electron density, and repeating until convergence. At this point the issue is how to model the exchange-correlation functional, several DFT models have been developed, and the difference lies exactly in how this term is estimated [56].

5.2.2 Exchange-correlation functional

Here I want to present some of the functionals used in DFT. As already said, the difference between the DFT methods is how the exchange-correlation functional is implemented,

there is no a best functional, but according to the system characteristics, one has to choose the most suitable. However, it can be demonstrated that the exchange-correlation functional is unique for every system, but its expression does not exist [53]. The quality of the functional is determined by comparing the simulation results with the experimental evidence or with other higher-level calculators [53]. The most popular functional classes are presented here: the Local Density Approximation (LDA) assumes that the $n(\vec{r})$ behaves like a uniform electron density since it is slowly varying. This is the simplest description of $n(\vec{r})$ because the exchange-correlation potential at a certain position \vec{r} depends only on the value of the electron density at that position. Usually, LDA overestimates the strength of the bonds between atoms. An improvement is to consider the electron spin, obtaining in this way the LSDA functional. When considering strongly varying electron density, the former description fails in the representation, the Generalized Gradient Approximation (GGA) works much better [60]. Here the exchange-correlation potential at the position $n(\vec{r})$ depends on the electron density and on its local gradient at that point. In this sense, the model is semi-local. In general, with these functionals, the bond strength is underestimated.

$$E_{LDA}[n] = \int n(\vec{r})\epsilon_{LDA}(n(\vec{r}))d\vec{r}$$

$$E_{GGA}[n] = \int n(\vec{r})\epsilon_{GGA}(n(\vec{r}), \nabla n(\vec{r}))d\vec{r}$$

Meta-GGA functionals introduce in the methods the higher order derivatives of the electron density, the Laplacian, and so on, more term, higher the accuracy. The last class is the hybrid functionals where the exchange-correlation term is obtained by joining the Hartree-Fock exchange-correlation term with other *ab initio* or empirical results of E_{XC} . For example, a molecular system is well described by a hybrid functional, like B3LYP, indeed, it is the one used in the first geometry optimization of the molecules studied in this work.

5.2.3 Basis sets

According to the Linear Combination of Atomic Orbitals (LCAO) [45], as the name suggests, by linearly combining the atomic orbitals it is possible to build the molecular orbital. However, in every electronic structure calculator, functions like orbitals are obtained by considering a finite basis set made of known functions. As already mentioned, a function can always be expanded in its complete basis set, which are an infinite number of functions, making the simulation impossible. The approximation consists of considering just a finite set of basis functions, from which the molecular orbital will be built on.

$$\psi_i = \sum_{\alpha} c_{\alpha}\phi_{\alpha}$$

In the equation above, ψ_i is the molecular orbital built as a linear combination of the atomic orbitals ϕ_{α} . The accuracy of the description depends on the size of the basis set, by reducing the set the accuracy drops because the atoms are roughly represented, moreover, the type of basis functions is relevant. The most common functions used for an LCAO model are the Slater-type Type Orbitals (STO) and the Gaussian Type Orbitals

(GTO). Since they represent the atomic orbitals, they are centered on the atom. However, the main difference is in the behavior of the curve at the nucleus. GTO is obtained from a combination of more Gaussian curves, but its slope is zero at the center and does not give a correct representation of the atomic orbital near the nucleus. Whereas STO has a discontinuity in the derivative at the nucleus. In addition, GTO decays too fast, giving a poor description of the wave function tails. As a matter of fact, the combination of Gaussian is exploited to better represent the behavior of each basis set's function. Even though the GTO basis set looks worse, it is still used to reduce the complexity of the calculation because the integrals are easier to solve.

A further improvement to the basis function is obtained by doubling all the functions of the basis set through the , in such a way that the molecular orbitals can be built on a wider number of components, thus increasing its reliability to the real system. The LCAO model is suited for molecular structures; for a periodic system, obtained by imposing periodic boundary conditions to a supercell, a better choice is to directly use plane waves that are already functions of the whole system. This model is ideal for describing delocalized electron densities that are slowly varying in space, like a metal valence band. Furthermore, the plane waves can also be used to represent molecules, if they are placed in a sufficiently large supercell that avoids any sort of overlapping or interaction between adjacent molecules, however, to get such molecular plane wave the number of plane waves of the basis must be large, so the LCAO model is preferred. In conclusion, the type of adopted basis set strongly depends on the structure under calculation and must be selected correctly to avoid any unrealistic results.

5.2.4 Van der Waals correction

As previously mentioned, the DFT is not able to correctly consider the weak interactions between the electrons, because the energies involved are comparable to the calculation error allowed by the simulation. However, in many systems, like interfaces between metal surfaces and adsorbed organic molecules, this type of interaction can be crucial in the interaction of the two components and in the organization of the layer. As a matter of fact, as already said while talking about physisorption, the attraction forces that keep the adsorbed molecules close to the surface are indeed weak forces of van der Waals [20]. Since my work deals with such a type of structure, I need to spend a few words on how these weak interactions can be implemented in the DFT model and correct the energy of the system.

Intramolecular forces

In order to make a molecule, the valence electrons of the involved atoms must build some chemical bonds that keep the system stable. It is possible to distinguish different kinds of chemical bonds according to the electronegativity of the two atoms involved [61, 62]. The electronegativity can be considered as how likely an atom will attract the electron shared in a bond. Oxygen atoms, for example, are characterized by a high electronegativity, indeed they acquire electrons while making a bond with almost any other element. The type of chemical bonds in a molecule determines some of its physical and chemical properties. A

covalent bond is built between two atoms with large electronegativity, they both provide an electron to share with the other atom. Between identical atoms, the covalent bond is pure in the sense that the electrons are equally shared, but, if there is a difference in the electronegativity of the two atoms, the bond is polar, and the electrons have a larger probability of being closer to the most electronegative atom. It is also possible that more than one electron is shared, in this case, a double or triple bond is built. The higher the number of involved electrons, the stronger the bond. The typical length of a covalent bond is around 1-2Å. If the electronegativity difference is larger than 1.9, the stronger atom steals an electron from the other. As a result, they both become ions, and an electrostatic force is generated between them. Those intramolecular bonds have an energy of around 100 – 1000 kJ/mol.

Intermolecular forces

However, other interactions can exist between the molecules, these are the intermolecular bonds, which are weaker than the previous bonds and they are mainly generated by electrostatic interactions between permanent or induced dipoles [61, 62]. The stronger interatomic bond is the so-called hydrogen bond since it involves a hydrogen covalently bonded to a high electronegative atom, like oxygen. The polar covalent bond generates a permanent dipole with a positive charge close to the hydrogen atom which can attract or repel other dipoles. The energy of such bonds is around 20 – 50 kJ/mol, which is comparable to the error provided by a DFT simulation. On the other hand, the van der Waals forces exist between polar and non-polar molecules. Once again, they are electrostatic interactions, but the bonding energy is much smaller, around 0.1 – 10 kJ/mol.

Depending on the type of dipoles involved, three different van der Waals forces can be identified: Keesom's forces are interactions between permanent dipoles of molecules (weaker than the hydrogen bond case). Then, Debye's forces occur between a polar and a non-polar molecule. The former is characterized by a dipole that generates an electric field that induces a dipole in the non-polar adjacent molecule. As a result, the second molecule exhibits a temporary polarisation and establishes the bond. The last are London's forces, which are interactions between a fluctuating dipole and an induced one. The origin of these forces lies in the temporary localization of the charge in non-polar molecules, since, it is possible, that during the electron motion, the electronic charge became unbalanced, thus generating a fluctuating dipole that instantaneously can induce a dipole to another molecule or atom. Consequently, it changes its electronic configuration, which in some cases can also affect the inducing dipole. This force is larger for heavy atoms. All the van der Waals interactions are strongly affected by the distance between the involved dipoles and their intensity. Additional information on this topic can be found in [63]

Perturbation theory

Not all the intermolecular interactions are presented in the previous lines, for example, the ones involving ions. In any case, the important aspect is that all these forces are electrostatic so they can be described through the same model. Moreover, because of their origin, they are automatically accounted for in the system Hamiltonian equation,

and the solution of the steady-state Schrödinger equation already accounts for them. However, in simulations, the energy of such forces is so small that it is comparable to the error introduced by the DFT, so some corrections to the model are required. Since these interactions are weak, the involved energies are up to three orders of magnitude less than the covalent and ionic bonds, they can be analytically represented through the perturbation theory. According to the Moller-Plesset perturbation theory (MP), the wave function of the system and the energy can be expanded in a Taylor series where λ identifies the perturbation parameter, while the subscript of Ψ_i and E_i are the order of the perturbation [64]. The zero-order terms are related to the unperturbed system, the ground state of the Hartree-Fock equation. These expressions are used to solve the steady-state Schrödinger equation. In order to consider the intermolecular interactions, the expansion up to the second order is sufficient.

$$\Psi = \Psi_0 + \lambda^1\Psi_1 + \lambda^2\Psi_2 + \dots$$

$$E = E_0 + \lambda^1E_1 + \lambda^2E_2 + \dots$$

The computational cost of the correction increases with the number of atoms and the maximum order considered, which means that only a system with a small number of atoms, a maximum of 50 atoms, can be accurately represented.

For larger devices, the DFT method or a semi-empirical approach is preferred. Therefore, the supermolecular approach introduces in the DFT model a correction that includes the intermolecular forces in the description of the system that usually provides good results that can be compared with the perturbative ones [65]. The following corrections can be applied to the GGA functionals: the DFT-D correction exploits empirical methods to take into account the dispersive interactions, and in some cases, it gives better results than the perturbative approach. The interactions are modeled through a damped interatomic potential, moreover, some improvements are applied, like in Grimme-D2 and Grimme-D3, where the correction is less empirical, the parameters of the potential are calculated with *ab initio* methods and so the correction is more general and suited to a larger amount of system. This correction can be used for describing generic weak interactions, providing, generally, a more accurate description. Another correction is the vdW-DF, where the correction term is evaluated explicitly, without any empirical data, however, the computational cost is much larger than DFT-D and the accuracy is not substantially improved. Indeed, in this work, the DFT-D Grimme-D3 correction is the adopted one.

A further improvement in the description can be achieved with the counterpoise correction (CP) that works on the basis set that is used for describing the atoms in the system [66]. This correction tries to fix the so-called Basis Set Superposition Error (BSSE), that arises since a non-complete basis set is considered. The basis set used in the DFT is centered in the nuclei, this introduces an error due to the different overlap of the basis functions according to the nuclear geometry of the system, a system with more nuclei shows more overlapping of the basis function providing an improvement of the basis set, like if the basis set of one component helps to compensate the incomplete basis set of

the other components. Ideally, if the basis set is complete, the BSSE becomes zero, so the solution is to introduce in the model some ghost atoms described through their basis set, thus increasing the number of basis functions used. Adding more basis functions to a complete basis set will provide no improvement, so the idea is to add basis functions until the interaction energy does not change anymore. The energy of the BSSE correction, for a metal-molecule interface, can be calculated as:

$$E_{CP} = E_{metal}^* - E_{metal} + E_{molecule}^* - E_{molecule}$$

where the asterisk indicates the system including the ghost atoms. This correction, however, is only an estimation of the interactions that occur at the interface between the two components. The counterpoise correction will be always used in the simulations of this work, and the same for the van der Waals correction. It is crucial that all the simulations are consistent with the method applied, in order to make reliable comparisons.

Chapter 6

Technological background

6.1 Physical vapor deposition

Among all the thin film deposition techniques, the Physical Vapor Deposition (PVD) is the one used for the fabrication of the structures studied in this thesis. The properties of the deposited thin, like the crystalline structure or the coverage, film strictly depend on the adopted deposition technique and on the group of process parameters, like temperature, pressure, and deposition rate, that are set up. Moreover, according to the material that has to be deposited, organic molecules in my case, specific technologies are more suited than others, to avoid any damage to the source. The working principle of PVD techniques is to provide, to a source material in the solid phase, the energy sufficient to permit the single particles to leave the source, forming a vapor in the deposition chamber. Then, the vapor, after traveling in a vacuum, comes in contact with the cooler surface of the sample, on which it is deposited [67, 68]. The term "physical" states that there are no strong bonds or chemical reactions between the sample and the vapor, but that the molecules are adsorbed at the surface mainly due to weak Van der Waals interactions. Then, the film grows by the accumulation of molecules driven by the condensation processes [20, 39].

6.1.1 Classification of PVD

The PVD techniques are classified according to the physical process employed for the creation of the vapor phase. The big distinction is between evaporation and sputtering PVDs [67]. Concerning evaporation, the source is heated globally or locally and thanks to the thermal agitation, the particles are able to leave the solid. A further distinction, depending on the heating process, exists, namely thermal PVD and electron beam PVD. In both technologies the source is hosted in a crucible (of quartz or ceramic material), however, in the former, a coil rolls up around the crucible, providing heat to the source through the Joule effect. Therefore, in this way, both the crucible and the source are heated, causing the possible desorption of unwanted contamination from the crucible. The crucible material must be suitable for the evaporation temperature of the source. Thermal PVD is the most simple PVD technique, indeed, it requires relatively low power consumption with respect to other solutions. The second technique, on the other hand, exploits an

electron beam obtained from an electron gun, which, basically, consists of a hot filament that emits a stream of electrons through thermionic emission, focused and accelerated by an electric field. The beam is, then, deflected and focused on a millimetric spot of the source, through an applied magnetic field. The kinetic energy of the impinging electrons can be controlled by the accelerating voltage of the electron gun, the power can reach 10 kW. In such conditions, the source is locally heated, reaching temperatures around thousands of kelvin, whereas the crucible is kept cold, thus eliminating the evaporation of unwanted particles. However, the most used PVD technique is sputtering PVD. The sputtering process consists of bombarding a solid target with accelerated heavy particles of plasma so that the atoms of the target can be ejected from the surface. The plasma is a state of matter composed of ions, electrons, and neutral particles. To sputter a surface is necessary that the ions are heavy, in this way they can be accelerated by an electric field toward the target and easily dislodge the atoms. Argon is a suitable noble gas that, in addition, avoids any chemical interaction with the surface. Sputtering is useful for the deposition of compounds. To increase the efficiency of the sputtering process, some technological improvements to the technique have been developed, like magnetron or RF sputtering [68].

Thermal evaporation PVD is the deposition technique used for the fabrication of the samples analyzed in this thesis. This technique permits to evaporating of the source particles with the slowest possible energy, indeed, it allows the deposition of organic molecules, since the source is not damaged during the process. On the contrary, the energy provided by the e-beam and the sputtering process destroys the molecule structure. Moreover, the deposition rate, controlled by the temperature of the source and the pressure of the chamber, can vary a lot, allowing the deposition from very thin layers, such as the one required by this work, to thicker ones. The presence of a quartz microbalance inside the chamber, close to the sample, allows the in-situ control of the estimated thickness of the deposited layer. Lastly, the evaporation PVDs are compatible with the high vacuum conditions required by the experimental setup. A scheme of thermal PVD is shown in Figure 6.5.

6.1.2 Vapor-surface interaction

The properties of the deposited thin film strictly depend on the interaction between the vapor phase and the sample surface [20, 16]. The interaction, however, is governed by the condition of the atmosphere in which the deposition process is developing, which can be controlled by a bunch of macroscopic parameters, in particular: the temperature of the source, the pressure in the deposition chamber and the growth rate measured by a quartz crystal microbalance. Some physical quantities, that give further information on the entity of the interaction, can be defined. The impinging rate, defined by the Hertz-Knudsen law (6.1), expresses the number of molecules that impinge on a unit surface per unit time.

$$R = \frac{p}{\sqrt{2\pi mk_B T}} \quad (6.1)$$

Where p is the pressure, m is the mass of the gas molecules, T is the temperature, and k_B is the Boltzmann constant. The larger the value of R , the higher the number of molecules

that get in contact with the surface and that can be involved in the deposition process. This quantity is proportional to the pressure inside the chamber, which is related to the number of molecules and their momentum, and inversely proportional to the molar mass and the temperature of the gas, at a fixed pressure. The inverse of the impinging rate is the time between two subsequent impacts [39, 69].

Once the particles reach the surface, they may be involved in several scenarios, as depicted in figure 6.1. As a matter of fact, to have a deposition, it is not sufficient that the particles impinge on the surface, but an interaction is necessary. Some particles are captured by the surface, reducing the number of particles in the vapor phase, the others are reflected back. The sticking coefficient S , is expressed by the following equation:

$$S = \frac{N_{ads}}{N_{inc}} = \frac{N_{ads}}{RA\Delta t}$$

where N_{ads} is the number of adsorbed particles, whereas N_{inc} represents the number of incident particles that, in a time interval Δt impinges on an area A , then R is the impinging rate. S is defined as the probability that the vapor molecule is captured by the surface. Adsorption is the term used to indicate the process that bonds the particle to the surface. During the adsorption on a surface, the particle does not enter in the bulk of the substrate but it is deposited on top, at a distance which depends on the established bonds between the species. Nevertheless, the system is dynamic. The adsorption process is in contrast with the desorption, the inverse mechanism. The particles, after a certain time, can leave the surface and return to the vapor phase, as depicted in figure 6.1. Even in this case, a desorption rate, proportional to $\exp(-E_a/k_bT)$ can be defined, where E_a is the activation energy of the process, low temperature of the surface is necessary to reduce the desorption. At the thermodynamic equilibrium, the adsorption rate is balanced by the desorption rate [69].

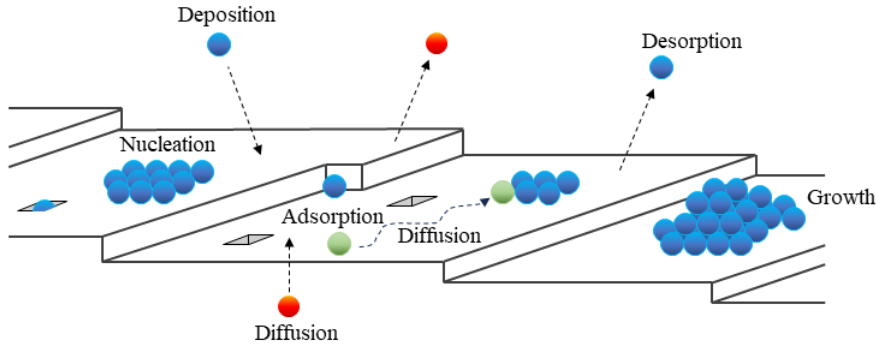


Figure 6.1. Schematic of the different processes that take place at the surface involving the gas particles.

The thermal agitation allows the diffusion of the adsorbed particles over the surface. Atoms and molecules can travel in order to find the best position, the one that minimizes the energy. The defects of the substrate surface behave as preferential sites for

the chemisorption of molecules, or, it is possible that several particles nucleate together, forming clusters that expand as the deposition goes on. The union of two nuclei is called coalescence, while the deposition over other adsorbed particles is condensation. The bonds between condensed particles are always lower than the adsorption bonds [69]. The diffusion is controlled by the temperature of the substrate: at higher temperatures, the particles have a higher probability of finding and arranging themselves in the best configuration. This is usually required in order to make an organized layer. However, the desorption rate increases. At very high temperatures, the molecules can be decomposed and the surface can be modified [69, 20]. Indeed, how the surface temperature affects the morphology and properties of a thin film is usually investigated. Depending on the type of bonds that the particles can establish with the surface, two processes are identified: physisorption and chemisorption [39, 69].

Physisorption

In this case, as the name suggests, the bonds between the adsorbates and surface are weak electrostatic interactions, mainly Van der Waals forces. As a consequence, the energy stored in the bond is low, around $E \approx 10\text{-}100$ meV, whereas the average distance between the particle and the surface is between $z_p \approx 3\text{-}10$ Å. Indeed, these bonds can be easily broken even by thermal agitation at room temperature. The electronic structure of the molecule is unchanged by the interaction. The model that describes a physisorbed atom is the one-dimensional oscillator that interacts with an image charge beneath the surface. The overall potential energy that establishes the interaction, expressed by equation 6.2, is obtained by the sum of an attractive and a repulsive term [69]. The former has its origin in the electrostatic force between the adsorbate and its image of opposite charge, whereas the latter is due to the overlapping of the molecular orbitals with the wavefunctions of the substrate.

$$V(z) \approx -\frac{1}{16\pi\epsilon_0} \frac{q^2 u^2}{(z - z_S)^3} \quad (6.2)$$

Where ϵ_0 is the vacuum dielectric constant, q is the image charge, u is the length of the particle dipole (nucleus-electron distance), and z_S is the solid surface. In figure 6.2 the energy of the free adatom at infinite distance is taken as a reference. While approaching the surface, the attractive term of the potential energy is dominant, indeed the energy is negative. Then, at a certain distance, indicated with z_0 , the curve shows a minimum of the energy, that indicates the equilibrium condition: the most stable and most probable distance between the physisorbed molecule and the surface. For shorter distances, the repulsive component becomes so strong that the energy has a steep rise up to infinity. This behavior represents the forbidden overlapping of the electron wavefunctions.

Chemisorption

In chemisorption, on the other hand, the bonds are strong, due to the establishment of chemical interactions between the molecules and the surface [39, 69]. As a consequence, differently from the physisorption, there is a significant modification of the electronic structure of the adsorbed molecule, that can affect the chemical properties of the organic

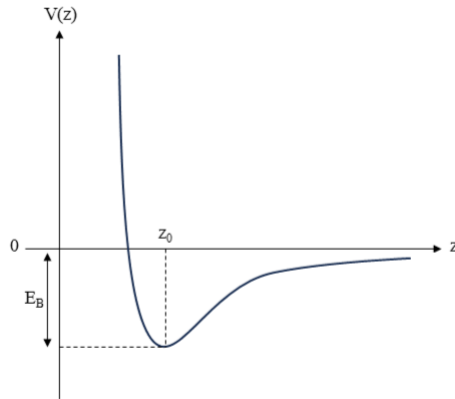


Figure 6.2. Qualitative plot of the physisorption potential energy. The substrate surface is at $z = 0$ and z_0 indicates the adsorption distance, E_B is the negative adsorption energy.

thin film. Once again, the potential energy is a function of the molecule-surface distance and it shows slight differences from the previous curve (6.2). The overall trend is the same, but in this case, due to stronger bonds, the minimum of the potential energy (E_B) is at a much deeper value, moreover, the distance between the molecule (z_c) and the surface is shorter. Typically, the average energy is higher than $E_B \approx 2 \text{ eV}$, and the distance can be between $z_c \approx 1 - 3 \text{ \AA}$, so that the thermal energy at room temperature is not sufficient to break the chemical bonds, in other words, a chemisorbed layer is much more resistant and it is preserved for a long time [69]. The majority of particles are subjected to both physical and chemical interactions, therefore, the potential energy curve can be obtained by the superposition effect of the separate processes (6.3). The curve is characterized by two minima, one is deep and close to the surface, which is related to the chemisorption, and the other, shallow and far, is due to the physisorption. Within the two minima, an energy barrier (E_b) arises, as a consequence, the molecule must have sufficient energy to overcome the potential barrier in order to be chemisorbed and form strong bonds with the surface.

6.1.3 Growth modes and film qualities

The growth process of a thin film can be described through three different models, that depend on the evolution of the organization of the adsorbed particles on the surface. It is the result of the balance between the interaction forces that act on the particles and on the surface. The growth modes are:

1. Layer-by-layer or Frank-Van der Merwe;
2. Island growth or Vollmer-Weber;
3. Layer plus island or Stranski-Krastanov.

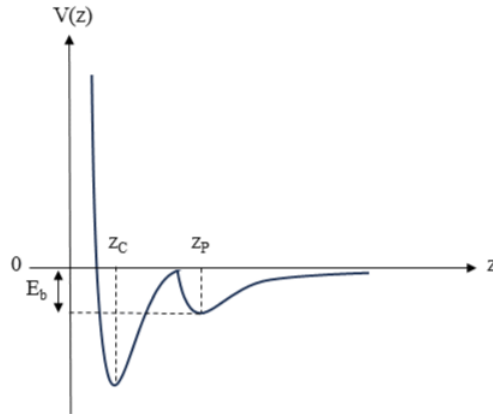


Figure 6.3. Plot of the adsorption potential energy considering both physisorption and chemisorption. E_b indicates the energy barrier that the adsorbate must overcome to reach the most stable state.

The first one refers, as the name suggests, to a deposition in which a new layer starts to be deposited after that the previous one is complete. This type of growth can be obtained when the interaction between the adatoms and the surface is stronger than the interaction between close adatoms. As a result, the thin film is characterized by a well-organized structure, indeed, a lattice can be easily achieved. However, the time required for this type of deposition is very long. The second method, on the contrary, consists of the creation of islands on the surface due to the nucleation of adatoms in some energetically favorable sites. Thus, the surface is not completely covered and the resulting layer is not uniform. By prolonging the deposition, the islands become higher and wider and, eventually, get in contact and they merge together. The final layer is characterized by a defective crystal lattice. This growth takes place when the interaction force between the particles is stronger than the one between the particles and the surface. The last case is a combination of the previous two, a first ordered layer is deposited, and then the growth continues with the formation of islands [20, 69, 39].

As already said, the crystalline structure of the deposited film is determined by the growth mode, but also by the lattice properties of the materials [16]. As a matter of fact, epitaxial growth, which means that the deposited layer has the same crystalline structure as the substrate, can only be achieved with the layer-by-layer mode, when the temperature of the substrate is kept high and the growth rate is very low [20]. If the previous conditions are satisfied, the result is a high-quality thin film with no grain boundaries. However, it is also possible to obtain an ordered and crystalline growth if the thin film and surface lattice constants are not matched. In this case, the process is well described by the layer plus island mode, typically a polycrystalline structure, characterized by lots of grain boundaries, is obtained. This is the case of metal deposition close to room temperature. The amorphous layer is characterized by the complete absence of a crystalline structure, but only a short-range ordering can be obtained. It is typical of insulators and organic thin

films [46]. The properties of the deposited thin film do not depend only on the interaction between the adatoms and the surface. As a matter of fact, the morphology of the surface plays a decisive role. The presence of defects is not the only aspect that affects the entity of the nucleation, but also the surface roughness and the possible presence of features and patterns on the surface have a strong impact on the uniformity of the thin film, as shown in figure 6.4. In order to have a deposited thin film that can perfectly reproduce the surface pattern, it is necessary that the deposition rate is the same at each point of the surface and in every direction. The deposition of a conformal layer is a challenging task, indeed, the morphology of the surface largely affects the growth rate. The more exposed regions, which are characterized by a larger acceptance angle, are subjected to a larger deposition, and there, the thickness of the film will be greater. Indeed, the acceptance angle defines the directions from which a particle can arrive and stick to the surface. Moreover, the flux density of the gas molecules directed on the surface is not uniform, but, for example in the thermal PVD, the particles are ejected radially from the source so that the deposition rate depends also on the emission angle. Moreover, the roughness or the pattern of the surface will shadow adjacent regions, where the deposition is almost null. In the case of a surface with high aspect-ratio features, like deep holes or pillars, it is very difficult to uniformly cover the walls or reach the deep bottom of the holes. All these factors set some limitations on the conformality of the final film grown with thermal PVD. Therefore, in order to reduce the imperfections and discontinuities of the thin film, it is convenient to heat the substrate, so that the adsorbed molecules or adatoms are not stuck, but they can diffuse and better cover the surface [20].

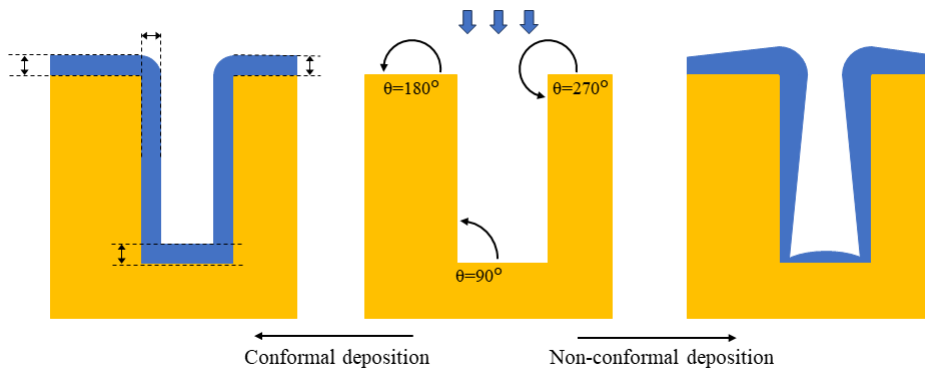


Figure 6.4. Schematic of the conformal and non-conformal thin film deposition.

6.1.4 Thermal PVD experimental setup

Here, the components of a thermal PVD setup are discussed and analyzed by referring, in particular, to the one that I used for the fabrication of the samples, which, indeed, is quite standard equipment. Figure 6.5 represents the general components required by a thermal PVD.

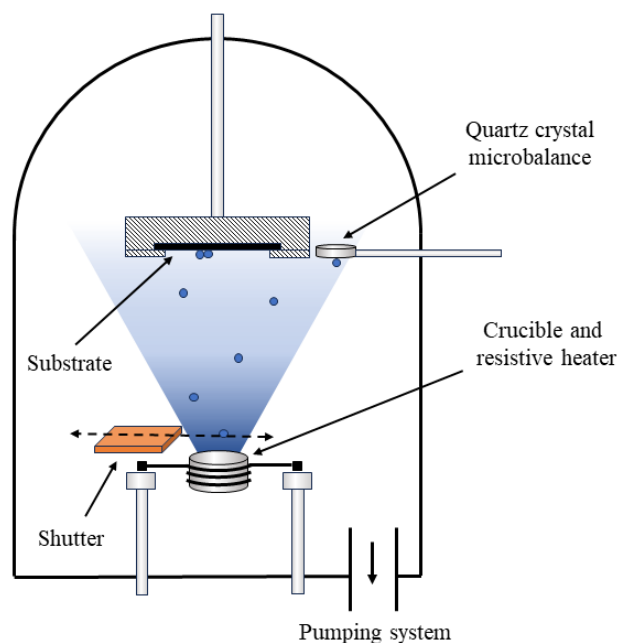


Figure 6.5. Schematic of a thermal PVD setup. The crucible is inserted into the resistive heater, the sample is hosted upside down, exactly above the source, with the shutter in between, and the microbalance is aligned to the sample.

Deposition chamber, source and shutter

The deposition process is performed inside a chamber where high vacuum (HV) conditions are maintained. The crucible is located at the bottom of the chamber, it is hosted on a support which also provides the connection with both the resistive heater and the thermocouple to measure the temperature of the source. The sample is placed upside down, with the surface directed toward the bottom of the chamber, exactly above the crucible in order to maximize the efficiency. The deposition rate is determined by the temperature of the source and the pressure in the chamber and, to improve the quality of the thin film, the deposition rate should be constant during the whole process. As already said, a major problem of thermal PVD is the desorption of contaminations from both the source, if not accurately purified, and from the crucible, which is connected to the employed resistive heating system. Therefore, in order to block the deposition of the unwanted particles while the source is heating up, a shutter is placed between the source and the sample. The shutter can be mechanically moved in order to cover the sample (or the source, depending on the system), thus avoiding the deposition, and, when the required deposition conditions are reached, it is opened. The shutter is necessary to stop the deposition when the wanted film thickness is reached, providing the timing control for the process. At that moment, the shutter must be closed quickly to block the evaporation flux, since the thermally controlled deposition rate cannot be abruptly interrupted.

Microbalance

The thickness of the deposited layer and the deposition rate are measured with a quartz crystal microbalance. Quartz is a piezoelectric material that is kept in oscillation to its resonance frequency by an AC voltage. In such a way the oscillation amplitude is maximized. The deposition of material on the quartz crystal reduces the resonance frequency, thus, by measuring the shift Δf , the excess mass and thus the film thickness can be determined. The accuracy reached by the microbalance is sub-Å, and the measurable order of magnitude of the deposition rate is of Å/s or even Å/min. However, in order to properly measure the thickness of the deposited layer, it is necessary to know the density and the acoustic impedance of the deposited material, quantities that are not always known. Moreover, the position of the microbalance must be as close as possible to the sample and aligned with the surface, so that the geometrical dependency of the deposition process is minimized and adjusted by a proper correction factor. The shutter must not cover or interfere with the microbalance, otherwise, the measurements are compromised.

Pressure and temperature

The high vacuum conditions are necessary for the evaporation techniques. Usually, a thermal PVD is performed at a pressure of about $p \approx 10^{-5}$ mbar. In such a way, the contaminations are reduced and the mean free path λ of the evaporated particles increases. With a long mean free path, the particles do not scatter or have interactions while traveling from the source to the surface, as a consequence, the deposition is directional, meaning that the evaporation flux is radial from the source. This may cause shadowing effects at the surface and reduce the conformality of the thin film [69]. The following table lists the energy ranges of the different levels of vacuum, by also indicating the respective number of molecules that impinge on a surface of 1 cm² and the average mean free path [70].

Table 6.1. Pressure, molecular density, and mean free path of the particles for the different vacuum levels.

Pressure Range	Pressure (mbar)	Molecules per cm ²	Mean Free Path
Low Vacuum	10 ³ – 10	10 ¹⁹ – 10 ¹⁶	6.6 10 ⁻⁶ – 6.6 10 ⁻³ cm
Medium Vacuum	10 – 10 ⁻³	10 ¹⁶ – 10 ¹³	6.6 10 ⁻³ – 6.6 cm
High Vacuum	10 ⁻³ – 10 ⁻⁷	10 ¹³ – 10 ⁹	6.6 cm – 660 m
Ultra-High Vacuum	10 ⁻⁷ – 10 ⁻¹²	10 ⁹ – 10 ⁴	660 m – 6.6 10 ⁴ km

The temperature of the source is measured with a thermocouple inserted in the crucible and in contact with the source. In thermal PVD the heater is a resistive filament rolled up around the crucible, that heats both the crucible and source through the Joule effect. The ramp of the temperature should be slow enough to avoid any reaction or damage to the source, in fact, if the temperature increases too fast, it is possible to burn the organic molecules and completely ruin the process. Moreover, after the deposition is concluded, the cooling of the source must be slow, to avoid the formation of molecular clusters. To improve the quality of the thin film, the sample can be heated as well [20]. In such a way the diffusion of the adsorbed particles is increased and the final film should show a better

organization. For this work, the samples are kept at a temperature of $T = 60^\circ\text{C}$ with the intent to increase a little bit the organization and the adsorption without damaging the surface.



Figure 6.6. Picture of the crucible stage and the thermocouple filament.

6.2 Photoemission spectroscopy

The main characterization tools used for the analysis of samples, which consist of molecular layers deposited on the metal substrate, are X-ray photoelectron spectroscopy (XPS) and ultraviolet photoelectron spectroscopy (UPS). The peculiar characteristic of these techniques is the investigation of the very surface of the materials [71, 72]. They are complementary techniques that can be performed in the same chamber, from which is possible to extract information on the electrical and optical properties and the composition of the sample. In particular, XPS is used to obtain information about the qualitative composition of the surface, about which elements the material is made of, and the chemical environment of the atoms, so that the chemical states of atoms can be defined. Moreover, the electronic structure and the density of states can be obtained. Whereas, with UPS the focus is on the valence band, from which are extracted fundamental electrical properties, like the work function and the energy of the molecular orbitals [71]. These techniques are widely used in the research field since they are considered non-destructive for the surface, in the sense that the surface is not heavily damaged during the analysis. However, depending on the material, some modifications of the surface could be possible, as a matter of fact, polymers, organic and soft materials can be degraded during the process, on the contrary, inorganic materials are much more resistant [71]. The working principle of the two techniques is the same, indeed, the only difference is the wavelength of the photon. Both are based on the photoelectric effect [71, 72], but the difference in the energy of the photon source determines the electronic states that can be involved during the interaction, thus the type of information that can be obtained. Moreover, the photon energy is also responsible for the surface sensitivity of XPS and UPS. The aim of this chapter is to provide a brief background on the physics behind the technology and then describe the main components of the experimental setup. Moreover, the intent is to provide the reader with the knowledge necessary to correctly interpret the XPS and UPS spectra discussed in

the second part of the thesis. That's why a basic guide for the peak fitting is also provided, mainly focused on the interpretation of the most important aspects and information that can be extracted from the photoemission spectrum.

6.2.1 Electrons-photons interaction in solids

It is known that the electronic structure of an atom is characterized by discrete states, each one of them associated with a unique energy. In solid state physics is common to distinguish the core electrons and valence electrons in order to simplify the description of the material. The former are the electrons that are strongly bonded to the nucleus of the atoms, the latter, on the other hand, are shared between atoms in order to form the bonds that constitute the material, providing stability to the solid [38]. When a photon impinges on a solid, its energy can be exchanged with the electrons of the material, so that the latter acquires energy and is promoted to an excited state. Usually, this excess of energy is dissipated by the scattering with other particles, however, if the provided energy is sufficient, the electron can escape from the atom [71]. These are the electrons of interest in the photoelectron spectroscopy. In order to have a transition from an initial to a final state, it is necessary that the former state is filled with an electron whereas the latter should be empty. The energy required to realize the transition must be equal to the energy difference between the states, it also means that the incident photon must carry the correct amount of energy to activate the transition. The quantum mechanical description of the transition between states is expressed by the Fermi golden rule (6.3), that is the probability of a particle, in this case, the electron, to have a transition from an initial to a final state [45].

$$W_{fi} = \frac{2\pi}{\hbar} \left| \Psi_f \hat{H}^* \Psi_i \right|^2 \delta(E_f - E_i - \hbar\omega) \quad (6.3)$$

Where Ψ_i and Ψ_f are respectively the wavefunctions of the initial and final state involved in the process, the Dirac delta term $\delta(E_f - E_i - \hbar\omega)$ keeps into account the energy constraint of the incident photon imposed by the energy conservation and the \hat{H}^* represents the perturbation of the equilibrium Hamiltonian of the solid due to the interaction with the external electromagnetic field carried by the photon. W_{fi} is just a term of the transition matrix that defines the scattering process: every cell of the matrix represents the probability of having a transition at a given energy between two specific states.

6.2.2 Photoelectric effect

In 1887 Heinrich Hertz noticed that electrons are emitted from a metal surface when exposed to a light source. Only in 1905 Albert Einstein provided a more complete explanation of this phenomenon. The experiment consisted of irradiating a solid metal sample with a known monochromatic light source and then measuring the emitted photoelectrons according to their kinetic energy and momentum. By knowing the work function of the metal, the binding energy of the emitted electron can be determined according to equation 6.4 [45, 71].

$$E_{kin} = h\nu - \Phi_m - E_B \quad (6.4)$$

Where Φ_m is the work function of the metal, whereas E_B is the binding energy of the electron before the interaction with the photon. The second is the quantity of interest since it carries information about the electronic state. By knowing the energy of the impinging photons, the work function of the material under study, and by measuring the kinetic energy of the photoemitted electrons, the binding energy is easily obtained. It is necessary that the energy of the photon beam is monochromatic to have an accurate measurement.

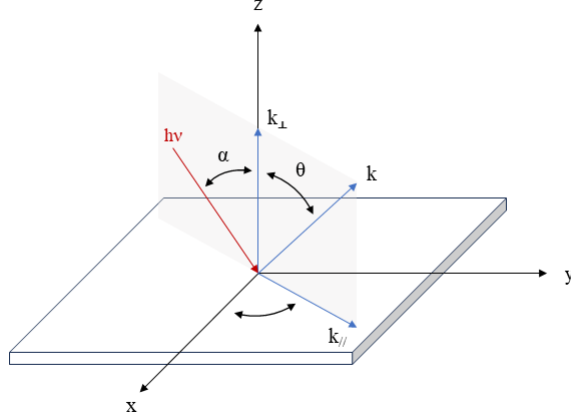


Figure 6.7. Schematic of the photoelectric effect.

The direction of propagation of the emitted electrons can be calculated by imposing the conservation laws of energy and momentum, as a result, the emission lies in the same plane as the incoming photon beam, whereas the magnitude of the emitted electron wave vector k_{em} is proportional to its kinetic energy as remarked in equation 6.5 [45].

$$k_{em} = \left(\frac{2mE_{kin}}{\hbar^2} \right)^{1/2} \quad (6.5)$$

6.2.3 Three-step model

To fully acknowledge the nature of this process, it is required a quantum mechanical approach, however, this is not necessary for the purpose of this work. A much simpler description of the interaction between the photons and the electrons in the material is provided by the three-step model [39]. Indeed, the process is approximated by the succession of three separate mechanisms.

1. Optical excitation of the electron from the initial to the final state.
2. Propagation of the excited electron to the surface.
3. Electron emission from the surface.

Optical excitation

The first process consists of the absorption of the impinging photons by the electrons of the sample. Due to this interaction, called scattering, energy is transferred from the photon to the electron which is promoted to an excited state. The absorption is a two-body process, which means that a single photon can excite only one electron. As said previously, to have a transition between two electronic states, the energy provided by the photon must be equal to the energy difference between the states, however, if the provided energy is much larger, the electron acquires enough energy to escape from the surface of the sample. The provided energy must be larger than the sum of the binding energy of the electron with its nucleus and the work function of the material. The excess energy is converted into kinetic energy, as shown in 6.4. In XPS the energy of the photons is sufficient to expel the core electrons, which are characterized by a well-defined binding energy, from the material. On the other hand, the photon energy in UPS is much lower and only the valence electrons can escape. These electrons belong to the valence band, there, the discrete states condense in a continuous energy band.

Propagation

The excitation of the electron is not sufficient for the measurement. In order to be expelled from the surface, thus reaching the detector, the electron must propagate from the scattering point, where the absorption took place, towards the surface. However, the electron, during this travel can be subjected to many scattering events, which consist of interactions with other particles, like electrons and nuclei. At every interaction, the electron loses energy. This means that in order to measure the true energy of the binding state, it is necessary that the electron does not scatter with anything. Depending on the kinetic energy of the photoemitted electron, the average distance that the electron can travel without any scattering is defined by the so-called Mean Free Path λ , which is a function of the electron energy only, and it is quite independent of the material where the electron is traveling. The curve has a minimum for 60 eV, however, up to 1000 eV the mean free path is around to 10 nm. This means that only the electrons that are excited at a distance from the surface lower than the mean free path (for a given energy) can be expelled from the surface without any further scattering mechanisms. So the measured kinetic energy corresponds to 6.4, which includes information on the binding energy of the electron before the photon absorption. All the electrons that are excited deeper in the sample can reach the surface, but their energy is not reliable to quantify the electron state and, indeed, they contribute to the background signal of the XPS spectrum, from which no information can be extracted. As already anticipated, the mean free path is responsible for the surface resolution of the XPS technique, indeed the meaningful signal comes from a few nanometers below the surface. For this reason, XPS and UPS are surface-sensitive.

Emission

The last step is the emission of the electrons from the surface and the propagation in the vacuum till the interaction with the detector. At the interface between the sample and the vacuum, the conservation of the wave-vector component parallel to the surface

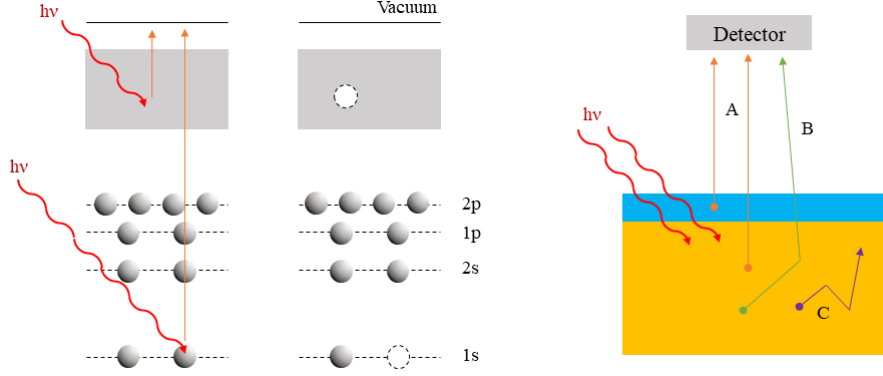


Figure 6.8. Schematic of the photoelectron excitation of a core level and a valence band electron (left). Propagation of the photoelectron through the material in case of no scattering event (A), and scattering with other particles losing information on the BE (B).

is required due to translational symmetry. This means that the $E(k_{\parallel})$ inside and outside the material must be the same, and that the emitted electrons carry information about the surface energy bands. It is possible to obtain angle-resolved spectrometers.

$$k_{\parallel} = \sqrt{\frac{2m}{\hbar^2} E_{kin}} \sin \theta \quad k_{\perp} = \sqrt{\frac{2m}{\hbar^2} E_{kin}} \cos \theta$$

6.2.4 XPS and UPS experimental setup

An XPS instrument is made of several components: an X-ray source, a sample stage, a series of extraction lenses, an analyzer, and a detector [71, 72]. The technological improvement of each part over the years, since 1969, when the first commercial XPS was produced by Siegbahn, allowed the XPS analysis to become an essential tool for the study of materials and surfaces. Indeed, it is widely used in different research fields. The analysis of the photoemitted electrons is performed in ultra-high vacuum (UHV) conditions [71], with pressure around $p \approx 10^{-9}$ mbar inside the chamber (table 6.1). Low pressure is required to avoid any scattering between the photoemitted electrons and the air molecules while traveling and being collected by the extraction lenses. However, for this purpose, a pressure around $p \approx 10^{-6}$ mbar is sufficient, the even higher vacuum is required to minimize the surface contamination, otherwise, in a few seconds, a thin contamination layer will completely cover the surface [71]. Figure 6.9 shows a schematic of the main components of the XPS instrument, which are presented in the following.

X-ray source

The X-rays are generated by bombarding a metallic anode with accelerated high-energy electrons emitted by a hot filament. The x-ray energy depends on the anode material,

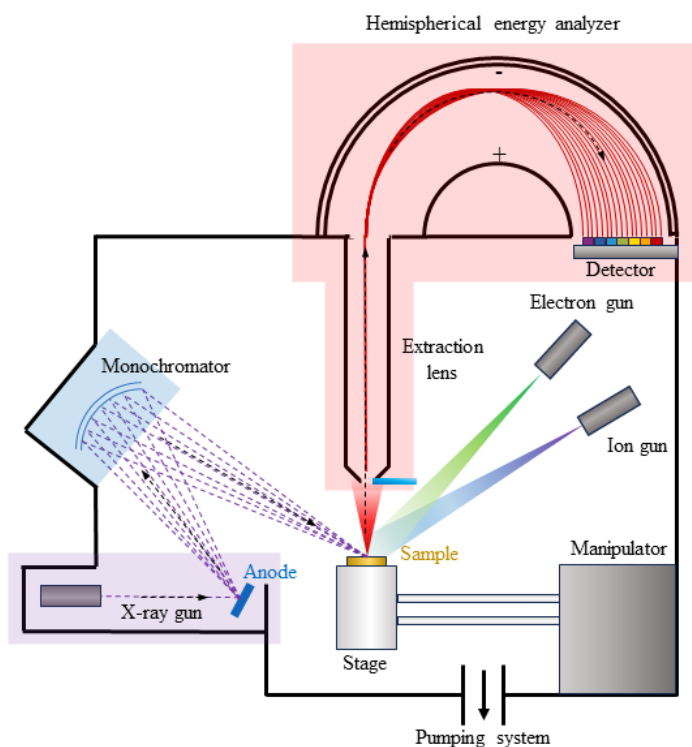


Figure 6.9. Schematic of the XPS instrumental setup.

whereas the intensity of the beam increases with the number and the energy of the electrons that collide with the anode. Only a small fraction of the power provides the generation of the x-ray beam, the remaining energy is converted into heat, thus, the anode must be cooled with water to avoid any damage to the source. The choice of the anode material has important consequences on the acquired spectrum. The energy of the beam identifies the characteristic peaks that can be analyzed, moreover, the higher the energy, the deeper the volume of interaction from which photoemitted electrons can be collected. The ionization cross-section, which measures the probability that an electron is extracted from an atom, decreases for high energy sources [71]. Finally, in the case of non-monochromatic sources, the characteristic line width will limit the resolution and the peaks will be broadened [71].

Common XPS instruments are equipped with a high-intensity twin anode x-ray source with both Mg and Al anodes that can be individually selected. They produce $K\alpha$ radiation lines at a energy of $E_{Mg} = 1253.6$ eV and $E_{Al} = 1486.6$ eV, respectively. Moreover, the natural line widths of the non-monochromatic radiations are 0.7 eV for the magnesium and 0.85 eV for the aluminum [71, 73]. Many instruments are also provided with a monochromator, for the Al source, consists of a quartz crystal positioned at a specific angle so that, by diffraction, it filters only the $K\alpha$ radiation, by removing any other x-ray

lines, and consequent satellite peaks, and Bremsstrahlung radiations. The monochromator works by constructive interference of the diffracted x-rays obtained by the interaction with the crystal, as shown in figure 6.10. The angle of incidence θ , defined as the angle between the beam propagation direction and the parallel crystal planes, coincides with the reflection angle. The optical path difference, introduced by reflection at different crystal planes, is a function of the lattice parameter d , which identifies the distance between adjacent planes, and the angle of incidence θ . In order to have constructive interference, the incoming x-ray wavelength must satisfy Bragg's law (6.6).

$$n \cdot \lambda = 2 \cdot d \cdot \sin(\theta) \quad (6.6)$$

Where the right-hand side is the optical path difference, and it must be an integer multiple of the x-ray wavelength. A quartz crystal positioned in its (1010) direction is characterized by a spacing $d = 4.255 \text{ \AA}$, according to that, a monochromator for the Al and Ag anode is built, by tuning the angle of incidence. On the other hand, for a Mg anode, no angle can fulfill Bragg's law. In table 6.2 are collected the Bragg's angle for the different x-ray sources. One can notice that, for the Ag anode, two angles are the solution of equation 6.6, and the second order angle (obtained for $n = 2$) is very close to the Al one [73].

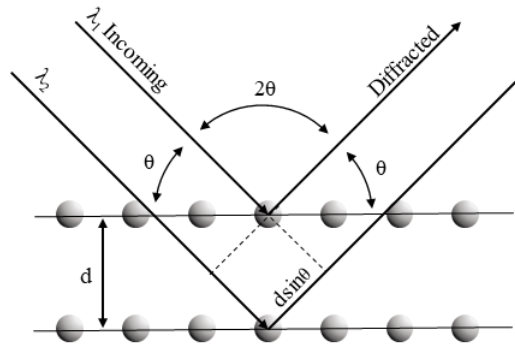


Figure 6.10. Schematic of the X-ray diffraction interference, showing the optical path difference of $2 \cdot d \cdot \sin \theta$.

Source	Energy (eV)	Wavelength (\AA)	Bragg's angle ($^\circ$)
Mg	1253.6	9.890	/
Al	1486.6	8.340	78.53
Ag	2984.3	4.155	9.22, 77.53

Table 6.2. Bragg's angle of a quartz crystal (1010) monochromator for different x-ray sources.

Moreover, it also decreases the line width of the source, as a matter of fact, when the monochromator is used, the line width for Al is reduced from 0.85 eV to approximately

0.2 eV [71], thus increasing the resolution of the measurement. The drawback of using a monochromator is the reduction of the x-ray flux directed towards the sample, however, the improvements in the electron collection and in the detector efficiency have compensated this problem [71]. The high x-ray intensity obtained with the source can be detrimental for some samples. The damages can be visible from the spectrum and they may consist in a broadening of the peaks during the exposition. Organic molecules are more susceptible to x-ray radiation with respect to metals and oxides [71].

Extraction lenses, analyzer, and detector

The photoemitted electrons are collected by the extraction lenses and directed toward the analyzer. The system of lenses defines the acceptance angle, which can be increased in order to improve the collection efficiency. It also allows the spot analysis, for those experiments where it is requested the study of a very small region of the sample [71]. In angle-resolved XPS, for example, a low acceptance angle is preferred [71].

Two analyzers were developed for the XPS, however, the concentric hemispherical analyzer is the most common since it provides better performances with respect to the cylindrical mirror analyzer, indeed it offers better resolution and throughput [71]. The concentric hemispherical analyzer is made by two hemispherical electrodes with radii R_1 and R_2 that form a cavity where the electrons, entering from a slit with a particular shape, are propagating. A proper voltage is applied to both electrodes, thus, the electrons are linearly dispersed depending on their kinetic energy. The electric field, expressed by equation 6.7, radially directed from the center of the spheres to the outside, bends the trajectory of the electrons with an intensity inverse proportional to the kinetic energy [74].

$$|\vec{E}(r)| = - \left[\frac{V_2 - V_1}{R_2 - R_1} \right] \cdot \frac{R_1 R_2}{r^2} \quad (6.7)$$

Where V indicates the applied voltage and the subscripts 1 and 2 refer to the inner and outer hemispheres respectively. Indeed, high-energy electrons will collide with the outer hemisphere, and low-energy electrons will collide with the inner one. Only the electrons with a specific kinetic energy are able to reach the detector at the end of the analyzer. This energy is the so-called pass energy. By changing the voltages applied to both electrodes, it is possible to tune the pass energy. Therefore, a scan over an energy interval can be obtained [74]. The energy resolution of the analyzer depends on many factors. The geometry of the analyzer is rather important since a better resolution is achieved for hemispheres with larger radii. Moreover, the kinetic energy of the electrons limits the resolution, with better results when the electrons have low energy [71]. Therefore, before entering the analyzer through the slit, the electrons are retarded by the extraction lenses of a quantity that coincides with the set pass energy. The energy resolution of the instrument is a function of the slit width W , the acceptance angle α , the pass energy, and the radius of the detected trajectory, as shown in the following equation:

$$\Delta E = E_P \left(\frac{W}{2R_P} + \alpha^2 \right)$$

An improvement of the resolution is obtained for lower pass energy, however, it also affects the throughput of the analysis, since fewer electrons are detected. As a matter of fact, for

survey scans a high pass energy is accepted, since there is no need for high resolution, but rather, high-intensity signals. On the contrary, to study single peaks, high resolution is required. The poor throughput is compensated by performing more scan iterations [71]. The detector, located at the end of the analyzer, collects only the electrons of a single kinetic energy defined by the pass energy. Often, multiple detectors are placed at the end of the analyzer to collect more electrons. For XPS, the detector is an electron multiplier, thus, for each collected electron, a stronger signal is generated.

In order to have a correct measurement of the electron kinetic energy, the sample and the spectrometer must be grounded in common, such that they have aligned Fermi levels and, more importantly, the photoelectron binding energy can be expressed as a function of the detector work function, independently on the sample work function. The band diagram is shown in figure 6.11 and the electron binding energy E_B assumes the following expression, where $h\nu$ is the x-ray energy, E_{kin}^{det} the photoelectron energy in the spectrometer and ϕ_{det} the detector work function.

$$E_B = h\nu - E_{kin}^{det} - \phi_{det}$$

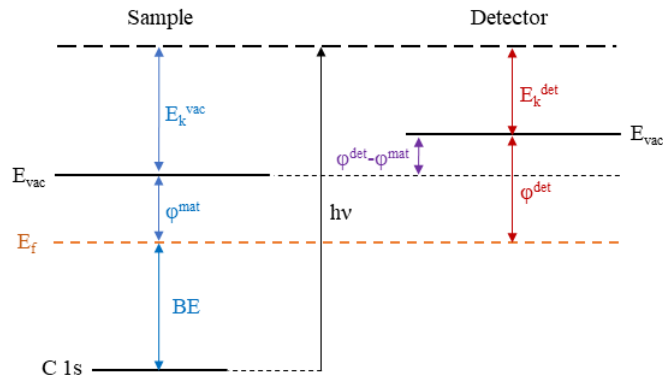


Figure 6.11. Energy level alignment between the sample and the detector.

Additional features

The chamber where the XPS is conducted is provided also with other features that can be used for further analysis or particular experiments. XPS systems are equipped with a sputtering gun which can be used to clean the surface, by removing the contaminations, and in particular the adventitious carbon layer, or to damage the surface on purpose. The heavy sputtering can be obtained with argon ions, whereas the more gentle sputter uses fullerene or gas cluster ion sources [71]. Since the working principle of UPS is identical to XPS, the same instrument is used, it is just required to introduce an ultraviolet radiation source. The most common UV sources are based on helium plasma. The light emission is generated by the exciting helium atoms so that the electrons are promoted to

a higher energy state. While relaxing, the excess energy is converted to UV radiation. Two emission lines are generated, HeI and HeII with energy 21.22 eV 40.8 eV respectively. The excitation of the helium atoms is obtained by pumping the gas with an electromagnetic field, producing a plasma made by ionized and excited He. The intensity of the UV emission is controlled by the pumping power, defined by the electromagnetic field, and by the pressure of the gas. Moreover, the sample stage can be provided for heating and cooling systems. With a resistive heater, the temperature of the sample can reach and even exceed 500 °C, whereas by cooling with liquid nitrogen a sample temperature below –100 °C can be achieved.

6.2.5 XPS data analysis

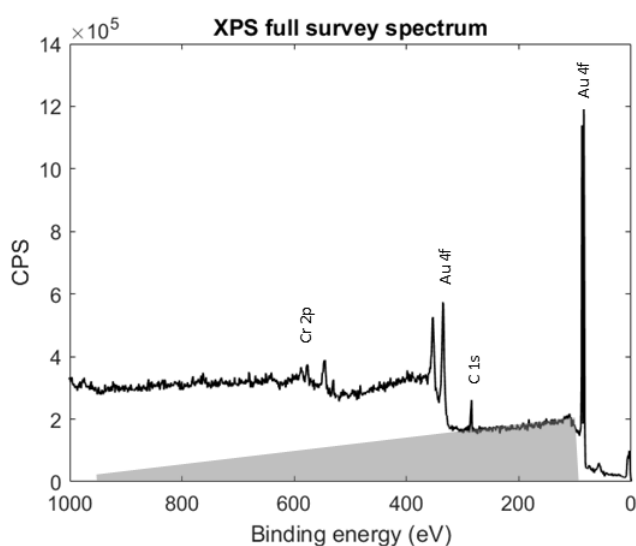


Figure 6.12. XPS full spectrum. The dark area is the background contribution generated by the Au_{4f} peak.

In this section, I will discuss the possible information that can be extracted from an XPS spectrum and how to evaluate it. Figure 6.12 depicts a typical energy spectrum obtained from an XPS analysis, the spectrum shows the counts per second of the number of electrons that are collected by the detector for a given energy, or, alternatively, the intensity of the signal of the detector. The abscissa of the spectrum is the energy expressed in electronvolt, it can be either the binding energy of the electron states before the interaction with the photon, or the kinetic energy of the electron in the vacuum, after the emission from the surface. Knowing the energy of the monochromatic photon source, we can move from one scale to the other. Typically an XPS spectrum is plotted with respect to the binding energy so that from left to right, the binding energy is reduced, which means that are firstly measured the emitted electrons that were strongly bonded to

their nucleus, and last are the ones belonging to the valence band. On the contrary, in the UPS spectrum, it is convenient to plot the intensity with respect to the kinetic energy, in order to directly get information of the material work function.

The XPS spectrum is composed of the superposition of intensity peaks centered at a specific energy with a background signal that extends for all the energy ranges. The peak height provides information on the amount of electrons that are emitted from the sample and collected by the detector at the particular energy, which, in turn, indicates the element from which the electron comes. As a matter of fact, a preliminary study of the energy positions of the peaks gives information on the elements present at the surface of the sample, whereas the intensity of the peak tells the number of elements at the surface [75]. This is because every element is characterized by a set of core electrons with well-defined binding energies, for example, a peak at 284 eV refers to the emission of electrons from the 1s orbital of a carbon atom, whereas a peak around 530 eV indicates the presence of oxygen at the surface. Every orbital of each element can emit electrons, however, there is always a main peak that refers to the most reactive orbital, indeed, during the analysis, for each element, only the main peak is considered. In table 6.3 are collected the binding energies and the respective orbitals of the main peaks for the most common elements [76, 77].

Table 6.3. Energy and orbitals of the XPS peaks of some of the most common elements.

Element	BE (eV)	Orbital
Carbon	284.8	1s
Oxygen	531-533	1s
Silicon	99.4	2p
Gold	84.0	4f

In quantum mechanics, the electron states are described by a series of quantum numbers that give the name and define different properties of the orbitals. They are collected in table 6.4. In order to have an idea of the meaning of the quantum numbers, a one-electron model is considered, the simplest is the hydrogen atom [45]. The principal quantum number n can assume discrete values and it is associated with the total energy of the electron. For the hydrogen atom, the electron binding energy is inversely proportional to the square of n (6.8). By increasing n the energy of the electron increases and also the distance from the nucleus. Electronic states with equal n belong to the same electronic shell, with reference to Bohr's model of the atom. The number of the orbital name refers to the electronic shell.

$$E_n = \frac{-13.6 \text{ eV}}{n^2}, \quad n = 1, 2, \dots \quad (6.8)$$

On the other hand, the letter in the orbital name is associated with the value of the second quantum number l , which indicates the electron angular L momentum defined by equation 6.9. The values that the second quantum number can assume depend on n (6.4), moreover, according to the value of l , the electron orbitals are indicated by the letters s , p , d and f , respectively when $l = 0, 1, 2, 3$. The letter defines, also, the shape of the orbital,

for example, s -orbitals are spherical, whereas p -orbitals have a dumbbell shape.

$$\hat{L}^2\Psi = \hbar^2l(l+1)\Psi \quad (6.9)$$

The number of electrons hosted in a sub-shell is $2(2l+1)$, this is because the third quantum number m_l and the spin m_s of the electrons break the degeneracy. m_l identifies the different orbitals within each sub-shell and it is associated with the component of the angular momentum along the z -axis. Each orbital can host up to two electrons with opposite spin. By the combination of these four quantum numbers, the state of each electron of the atom is defined.

Table 6.4. Electron quantum numbers.

Name	Symbol	Values
Principal quantum number	n	$1, \dots, n$
Azimuthal quantum number	l	$0, \dots, n-1$
Magnetic quantum number	m_l	$-l, \dots, 0, \dots, l$
Spin	m_s	$-1/2, 1/2$

6.2.6 Peak fitting

The analysis of an XPS spectrum consists in identifying the energy regions where useful signals are recorded and then, decomposing the overall signal into a suitable number of peaks through the peak fitting. If the sample composition is unknown, a general rule is to employ the smallest number of curves for the fitting, in the case of a known sample, it can be necessary to fix the position and/or other parameters of the fitting curves. Through the peak fitting, we are able to determine the composition of the analyzed sample by comparing the results with the characteristic electron binding energies for the specific orbitals that can be found in the XPS database [76, 77], thus determining the element and the type of bond in which it is involved. Furthermore, a quantitative analysis is possible by comparing the intensities of the peaks.

Background noise

Before proceeding with the fitting, it is necessary to remove the background noise. The noise signal covers all the energy range. Several aspects contribute to the noise, one of them is the detection of all the photoemitted electrons that undergo additional inelastic scattering events while traveling through the surface. By scattering, they lose part of their kinetic energy, and, as a consequence, they are collected at higher binding energy. For this reason, the background signal increases in intensity for higher binding energies, since every core level with lower energy may contribute to the background noise (6.12). Those electrons do not carry any useful information about the electronic states of the surface, indeed, this signal must be considered and removed during the analysis. There are several background types, however, for the majority of cases analyzed in this work, the "Shirley" background is the adopted one [75, 78].

Full width half maximum

Usually, the peaks can be Gaussian and Lorentzian curves or sum or product of them. From the parameters of the fitted curves, a huge amount of information, about the surface, can be extracted. As already said, from the position of the peaks, each of them associated with a specific binding energy, the composition of the surface is obtained, by determining the elements present at the surface. Moreover, the width of the peaks is the result of different aspects, including some technological limits like the width of the X-ray quasi-monochromatic source or the pass energy of the detector, but also physical phenomena like the core-hole lifetime broadening or the superposition of very close peaks. However, from the full width half maximum (FWHM) of every single peak, important considerations of the crystalline structure and the overall organization of the surface can be gathered. A large FWHM means that the shape of the peak is very broad over a large interval of energy, which means that the electronic state has itself a broadening, mainly caused by the disorder and imperfections. On the contrary, if the peak is sharp, the electrons emitted from that specific state have very similar energies, thus the layer presents an organized structure. As a matter of fact, while analyzing the gold substrate signal of our samples, from the FWHM of the main peak we deduced that it could show a polycrystalline structure, which was then confirmed by the atomic force microscopy (AFM) 8.3. By focusing on the deposited organic layer, thus on the signals coming from the organic molecules, the formation of an organized structure is suggested by the reduction of the FWHM of the carbon C_{1s} during each deposition step.

Peak asymmetry in metals

The shape of the peak can lead to a wrong fitting of the signal and a misinterpretation of the data. Concerning the analysis of metals, symmetric bell-shaped curves, like the Gaussian-Lorentzian functions, are not a suitable fit. This is because the photoemitted electrons can undergo successive electronic excitations that can deform the profile of the curve, thus leading to asymmetry. An asymmetric peak is characterized by a tail that extends toward high binding energy. They can be the result of several effects like the overlapping of several peaks, the excitation of vibrational modes, or the formation of electron-hole couples. Metals are characterized by an unfilled conduction band, therefore, the empty states can host electrons that were previously subjected to shake-up processes and then, interact with a photon and be emitted. This reduction of the kinetic energy is the origin of the tail [79, 71]. On the other hand, for insulating materials, like the majority of oxides and molecules, there is no continuum between filled and empty states, thus a symmetric peak is observed.

Spin-orbit interaction

Each electronic state is associated with a specific peak in the XPS spectrum, however, this is true only for the electrons hosted in s -orbitals, for all the other electrons in p , s , and f orbitals, each peak is always split in two as a consequence of the spin-orbit interaction between the electrons and the atom core. It is a relativistic effect between the spin of the electron and the rotation of the electron around the nucleus [45]. As a matter of

fact, the total angular momentum j of an electron is obtained by the sum of the second quantum number and the spin $j = |l + s|$. As a matter of fact, for the s -orbitals l is equal to zero since it has a spherical shape, thus the total angular momentum is equal to $j = 1/2$ and it is unique. On the contrary, for all the other orbitals, the total angular momentum has two possible values that are collected in table 6.5 [77]. The split in the angular momentum is also reflected in the electron energy, thus, generating coupled XPS peaks for non- s -orbitals.

Table 6.5. Spin-orbit splitting and peak intensity ratio.

Orbital	l	j	Area ratio
s	0	1/2	/
p	1	1/2, 3/2	1:2
d	2	3/2, 5/2	2:3
f	3	5/2, 7/2	3:4

Therefore, the electrons of the same sub-shell may have two different energies, however, the number of electrons that share the same energy is fixed, thus, in the XPS spectrum, the ratio between the intensities of the main peak and the secondary peak is fixed. The ratio is obtained through equation 6.10. For example, a p -orbital is characterized by a ratio of 1/2, which corresponds to 2 electrons hosted in the state $p_{1/2}$ and 4 electrons in the state $p_{3/2}$ [77].

$$\frac{I_1}{I_2} = \frac{2j_1 + 1}{2j_2 + 1} \quad (6.10)$$

The main peak is associated with the electrons with higher total angular momentum and they are always at lower binding energies. Moreover, the energy shift between the two peaks is characteristic of the orbital and it can be calculated through the following equation.

$$\Delta E = \frac{\beta(n, l)}{2} (j(j + 1) - l(l + 1) - s(s + 1))$$

$$\beta(n, l) = Z^4 \frac{\mu_0}{4\pi} g_s \mu_b^2 \frac{1}{n^3 \alpha^3 l(l + 1/2)(l + 1)}$$

Where μ_B is the Bohr magneton, g_s is the electron-spin g-factor which can be approximated to $g_s = 2.0023... \simeq 2$, α is the Bohr radius and Z is the atomic number of the element. The energy shift between the main and secondary peak is constant, for example, between the two peaks of Au_{4f} the energy shift is always $\Delta E = 3.7$ eV.

Satellite peaks

The presence of satellite peaks in an XPS spectrum can be attributed to several physical phenomena and interactions between particles that can lead to a reduction of the kinetic energy of the photoemitted electrons [71, 79]. These mechanisms include:

1. Shake-up and shake-off satellite peaks arise as a consequence of the interaction between the photoemitted electron and the valence band. The emission of the electron causes a sudden lack of the effective charge of the atom. The ejected electron can interact with valence electrons, thus energy is transferred and the valence electron is excited to a higher energy level (shake it up). As a consequence, the photoemitted electron loses kinetic energy and then it is recorded to a higher binding energy value. Shake-up satellites are characterized by distinct peaks at a few eV above (BE scale) the core level. In the second case, the valence electron is also ejected from the atom, as a consequence the energy dissipation is larger and the resulting peak has a broadened shape. In some cases, it is not distinguishable from the background noise.
2. Auger electron emission is another effect obtained when an X-ray beam is directed at a sample. The Auger effect consists of a three-particle process that takes place in ionized atoms. After the photoemission of a core electron, the relaxation of a high-energy electron can fill the empty core level. The excess of energy obtained by this relaxation can be simultaneously transferred to another electron (the Auger electron), which, in turn, is expelled from the atom. As a result, distinct peaks are recorded on the XPS spectrum at specific binding energies.
3. Plasmons are created by the collective oscillations of the valence band electrons in a solid. The absorption of X-ray photons can excite plasmons at the surface, and, after their relaxation, electrons are photoemitted at higher binding energy, generating a satellite peak. The energy shift to the core peak is characteristic of the material.

Chemical shift

The most important information that can be extracted from an XPS spectrum is the chemical state of the atoms. As previously said, the energies of the electronic states are specific for each element, however, the formation of chemical bonds with other atoms changes the electronic environment close to the atom, which is reflected in a shift of the binding energies of the core levels. The energy shift, caused by the particular chemical state, can reach a few electronvolts, a quantity that can be easily detected by the XPS analysis. The binding energy is a measure of the chemical environment of the atom, thus it is correlated to the electronic density, indeed, by decreasing the electron density close to an atom (like in the C-O bond, where the shared electron is closer to the oxygen since it has a larger electronegativity) the binding energy is increased. The opposite behavior if the chemical state increases the electron density of the atom. The majority of the possible configurations of each element are collected in databases [76, 77], which means that the position of a peak can be easily connected to the chemical state. However, the binding energies collected in table 6.3 refer to the most common configuration. Moreover, when a molecule with a known composition is analyzed, the intensities of the different peaks of the same element, associated with different chemical states, should reproduce the proportion of the molecule [79, 71]. For example, the phthalocyanine molecule is composed of 32 carbon atoms, 24 of which are involved in the benzene ring, while the other 8 are bonded to two nitrogen atoms, this 3:1 ratio is also measured in the XPS spectrum and, indeed, the peak associated with the C-N bond is more or less one-third of the main peak. Since

the chemical shift identifies a chemical bond, it is possible to determine the interaction between an adsorbed molecule and the substrate. If the molecules are chemisorbed at the surface, the energy of the peak of the substrate should shift towards higher binding energies. On the other hand, if while depositing, the peak of the substrate is fixed at the same position, the interaction with the adsorbate is not sufficiently strong to modify the chemical state of the surface, thus no chemical bonds are built.

Adventitious carbons

Almost every sample, after exposure to the atmosphere, has on its surface a non-negligible and detectable thin layer of adventitious carbon contamination. Even the shortest contact with air generates this unwanted layer, which is made by a variety of hydrocarbons, mainly short-chain, or even polymers. These molecules are made by both single and double bonds with oxygen, thus, the respective peaks are individuated in the spectrum. The adventitious carbons make the analysis of the carbon atom signal much more complicated since the detection of carbon-based materials or molecules is superimposed on the contamination. As a matter of fact, it is necessary to clean the sample before an XPS analysis, by using chemicals or more performing ion beam etching. However, for the analysis of the deposited layer, it is always convenient to take a survey of the bare substrate surface in order to have a reference that sets the adventitious carbon signals, and then proceed with the deposition. While fitting the adventitious carbon signal, usually three main components are individuated: C-C, C-O-C, and O-C=O. The first one is the one at lower binding energy and, normally, it is set to a value of $BE = 284.8$ eV. However, since the adventitious carbon is loosely bound to the surface, they are very sensible to the electrostatic environment at the surface. As a matter of fact, the interface dipole, discussed in the previous chapter, that rises as a consequence of the adsorption of molecules on a metal surface, changes the work function of the material. The binding energy of the C-C component of the adventitious carbon can be determined by the following experimental equation.

$$BE_{C-C,adv} = 289.58 \text{ eV} - \phi_m$$

Where ϕ_m is the work function of the metal substrate. Indeed, if it is reduced by the presence of adsorbed molecules, the binding energy of the adventitious carbon is shifted towards higher binding energies, and consequently, all the other peaks are rigidly moved, keeping the same energy distance from the C-C peak.

6.2.7 Quantitative analysis

By comparing the intensities of two or more peaks, it is possible to obtain quantitative information about the amount of material at the surface of the sample. The comparison is not limited to peaks of the same spectrum but can be carried out also between the same set of peaks belonging to different spectra. To quantify the XPS spectra it is necessary to consider the Relative Sensitivity Factor (RSF) characteristic of each element, which takes into account the different effective ionization volumes of each element. The RSF basically represents the intensity of the peak relative to another, it is expressed in relation to a reference and can be calculated from theory or derived through experimental results.

Once the set of RSF of each element is known, the amount of material at the surface can be estimated by dividing the peak intensity by the RSF [75]. Moreover, it is also possible to quantify the thickness of a deposited layer onto a substrate, by comparing the intensities of the substrate element signals measured before and after the deposition. By covering the substrate with another material, the intensity of the respective peak will be inevitably reduced. The reason for that is the fixed thickness of the investigation volume defined by the mean free path λ , which is independent of the material where the electrons are traveling, but is a function of the electron kinetic energy only [39].

All the methods for the overlayer thickness estimation are based on some assumptions, which are the exponential decay of the electron intensity with respect to the distance traveled through a material, the substrate must be flat, the thickness of the overlayer must be uniform and that the electrons have the same effective attenuation length, independently from their kinetic energy [71]. A first rough estimation of the thickness of a deposited layer can be obtained by inverting the Lambert-Beer equation. Actually, depending on the employed signal two variants are possible, the first one exploits the signal of the substrate, which reduces as the deposited layer gets thicker, on the contrary, the second one refers directly to the intensity of the overlayer peaks (6.11). However, the results are reliable only for thick films, where the substrate surface is completely and uniformly covered, in fact, this method is not suited for ultrathin films.

$$\frac{I_s}{I_{s_\infty}} = \exp\left[-\frac{d}{\lambda_s \cdot \cos \theta}\right] \quad \frac{I_o}{I_{o_\infty}} = 1 - \exp\left[-\frac{d}{\lambda_o \cdot \cos \theta}\right] \quad (6.11)$$

For the first equation, the one referred on the substrate, I_s and I_{s_∞} are the peak intensities of the substrate element, respectively after and before the deposition, d is the thickness of the deposited thin film, the quantity we are interested in, λ_s is the mean free path of the electrons evaluated at the kinetic energy corresponding to the binding energy of the peak and θ is the emission angle between the surface and the detector. The second equation has the same quantities, but all refer to the most relevant elements of the deposited material, usually carbon. Since the thickness is obtained by a ratio between peak intensities, any systematic error that acts on both measures is canceled out. However, the estimate of d hugely depends on the interpolation curve used for the mean free path. There are several analytic models and tools that can be adopted: equation 6.12 is universal, therefore it depends on the kinetic energy of the photoemitted electron only, the Seah and Dench equation (6.13) is specific since it also includes the density ρ of the deposited material. However, the best value of λ is obtained by the TPP-2M calculation that exploits the Tanuma, Powell, and Penn algorithm [80].

$$\lambda(E_{kin}) = 143 \cdot E_{kin}^{-2} + 0.054 \cdot E_{kin}^{-1/2} \quad (6.12)$$

$$\lambda(E_{kin}, \rho) = \frac{49 \cdot E_{kin}^{-2} + 0.11 \cdot E_{kin}^{-1/2}}{\rho} \quad (6.13)$$

Moreover, the second major problem is connected to the reference signals I_{s_∞} and I_{o_∞} , which must be measured from a sufficiently thick layer. For the substrate, it is usually sufficient to compare the measurement with the reference spectra generally taken before the deposition. However, for the other case, a good reference is not always accessible.

Alternatives to the Lambert-Beer-based equations have been proposed. A popular method for the evaluation of silicon oxide has been developed by Hill and al. equation in 6.14 [81, 82]. This method combines the intensities of the organic and substrate signals, thus completely avoiding the necessity of a reference, and allowing the estimation of the layer thickness from just one spectrum. The equation can be extended to several types of deposited materials by using the correct effective attenuation length (EAL). The experimentally calculated attenuation length is a correction of the theoretical electron mean free path that takes into account the elastic scattering of the photoemitted electrons. EAL values can differ depending on the XPS application, the instrumental configuration, and the polarization of the employed X-rays [83]. However, they are often used interchangeably in a loosely defined manner [84].

$$d = -\lambda_{EAL} \cos(\theta) \ln \left(1 + \frac{I_o/S_o}{I_s/S_s} \right) \quad (6.14)$$

Where λ_{EAL} is the experimental effective attenuation length of the cation or metal photoelectrons, I_o , and I_s are respectively the measured peak intensities of the deposited layer and the substrate that are corrected by considering the respective sensitivity factors (RSF) S_o and S_s and θ is the emission angle measured with respect the surface normal. By considering both substrate and deposited film signals the common instrumental errors are canceled, moreover, an eventual uniform overlayer deposited on the thin film after the atmosphere exposure has no effect on the measurements and it works with both thin and large depositions. However, the Hill equation considers a unique EAL for both substrate and film photoelectrons, thus assuming that their kinetic energies are almost the same, as a result, the number of applications is limited, being able to provide accurate results for specific samples, like silicon and its native oxide. By considering different EALs, the equation to solve becomes much more complex, as shown in 6.15. A graphical solution of the complete model is provided by the *Thickogram* [82].

$$\ln \left(\frac{I_o/S_o}{I_s/S_s} \right) - \left[\left(\frac{E_o}{E_s} \right)^{0.75} - \frac{1}{2} \right] \frac{d}{\lambda_o \cos \theta} - \ln 2 = \ln \sinh \left(\frac{d}{2\lambda_o \cos \theta} \right) \quad (6.15)$$

Where the attenuation lengths of the photoelectrons generated within the substrate and the deposited film, λ_s and λ_o , are related to the kinetic energies of the respective XPS peaks E_s and E_o through the following equation. This approximation provides good results for $E > 100$ eV, in case of low atomic number deposited materials, and for $E > 500$ eV for any material. Usually, the energy ratio is even more accurate since it allows for neglect of the material dependency of EAL [82].

$$\frac{\lambda_o}{\lambda_s} = \left(\frac{E_o}{E_s} \right)^{0.75}$$

Finally, the last method is an empirical formula that approximates equation 6.15, which depends on peak intensities of both substrate and organic layer and on the EAL [75]. The results discussed in the second part of this thesis are calculated with this method, providing a good match with the measurements conducted with the AFM, even if the

mean free path is used other than the EAL.

$$d = \cos \theta \frac{A_{o,s}^{2.2} \ln A_{o,s} L_{s,o}^{0.95} L_{o,o}^{0.05} + 2A_{o,s} L_{s,o}^{0.42} L_{o,o}^{0.58}}{A_{o,s}^{2.2} + 1.9} \quad (6.16)$$

Where $A_{o,s} = (I_o \cdot I_{s\infty}) / (I_{o\infty} \cdot I_s)$ depends on the peak intensities whereas $L_{s,o}$ and $L_{o,o}$ are the effective attenuation lengths of the electrons emitted by the substrate and the organic layer that travel through the organic layer respectively.

6.2.8 UPS data analysis

The difference between XPS and UPS lies in the energy of the photons directed towards the surface. Often two sources are used: HeI and HeII, with energy of 21.22 eV and 40.8 eV respectively [71]. As a consequence of the low energy source, the UPS investigates the valence electronic structure of the very sample surface, providing information on fundamental electronic quantities, like the work function and the HOMO level of the molecules. In figure 6.13 are displayed the UPS spectrum of the gold substrate before and after the deposition of the organic material (respectively top and bottom). Both spectra are plotted referring to the binding energy as the x-axis, in addition, they are aligned by pinning the Fermi level ($E_f = 0$ eV), which is used as an energy reference.

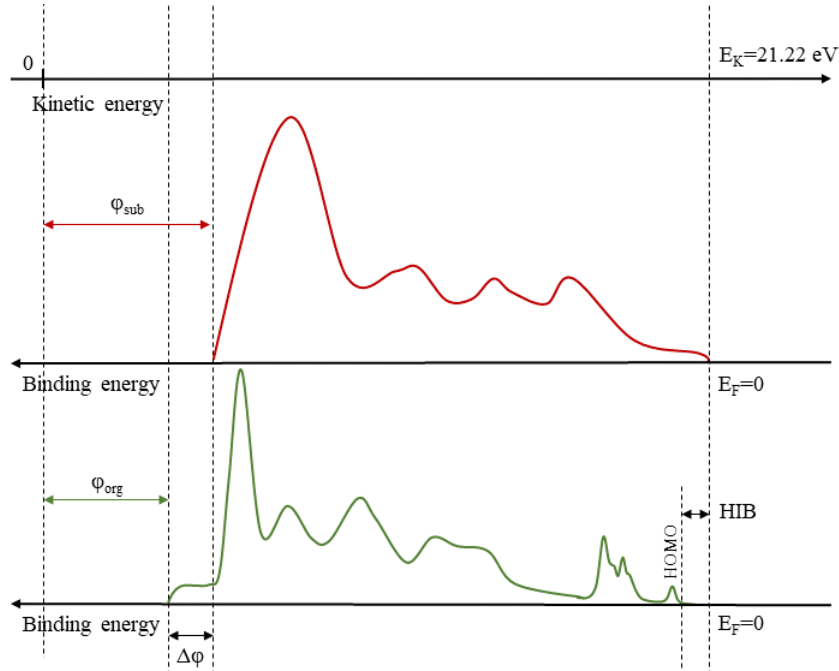


Figure 6.13. Qualitative UPS spectrum of a sample before and after the deposition of molecules highlighting how to measure the most relevant quantities.

Work function

The work function determines the amount of energy necessary to remove an electron from the material, an essential quantity to characterize a metal. In order to extract the work function from a UPS spectrum, if the plot is referring to the binding energy x-axis, one has to measure the high binding energy cut-off and the energy of the photon beam must be known. The high binding energy cut-off is determined by a linear fit of the curve, above this value (at higher BE) the spectrum is almost zero, and no electrons are emitted from the sample. The value of the work function is simply obtained by subtracting the energy cut-off from the photon energy.

$$\phi = h\nu - E_{cut-off}$$

Alternatively, the work function can be directly extracted from the spectrum, by plotting the curve with respect to the electron kinetic energy rather than the binding energy. In this way, the Fermi edge coincides with the photon radiation energy (21.22 eV), whereas the cut-off is exactly the work function. Indeed, according to the photoelectric effect, electrons with an energy lower than the work function ϕ are not able to escape from the sample surface, whereas, when the energy transfer is higher than ϕ the excess energy is completely converted in kinetic energy, the one detected. As a matter of fact, for a metal sample, the electrons at the Fermi edge are expelled with a kinetic energy equal to the energy of the photon radiation. By comparing the plots in figure 6.13, the cut-off is shifted after the deposition of the organic material. The shift of the work function is an expected effect caused mainly by the Pauli pushback effect [16], as explained in section 3.3. Indeed, comparing the two cut-offs, the dipole Δ at the interface between the metal and the adsorbed layer can be measured. Usually, after the deposition, the work function is reduced. Moreover, the value of the work function is useful also for the analysis of the XPS spectrum, since it fixes the peak energies of the adventitious carbon, necessary to avoid a misinterpretation of the carbon signal.

HOMO energy level

The HOMO level of a deposited organic layer arises when the layer thickness is sufficiently large. The HOMO peak is fitted by a Gaussian-Lorentzian symmetrical curve by considering, usually, a Tougaard-type background [75]. As for any XPS peak, the shape and the parameters of the fitting curve provide information on the deposited layer. Nevertheless, there are some peculiarities. Contrary to XPS, the relevant energy of the HOMO peak is its on-set, not the energy of the maximum. The reason is that the organic layer presents a certain amount of imperfections and disorder, thus the energy of the HOMO is sensitive to the local chemical environment. As a consequence, the HOMO peak is a superposition of several peaks which makes the value of the maximum completely unreliable. The FWHM of the HOMO peak reflects the arrangement and the organization of the deposited organic layer. The narrower the peak, the higher the ordering of the molecules. Moreover, when comparing experimental results and simulations, the interesting quantity is once again the on-set of the broadened HOMO peak obtained with the computation. The on-set of the HOMO is directly obtained with a linear fit of the curve, by plotting the UPS spectrum with respect to the binding energy.

Part II
Second part

Chapter 7

Sample preparation

The samples under study consist of three different thin films of metal phthalocyanine deposited through thermal evaporation PVD on a gold substrate. The molecules differ just in the central metal atom, which could be magnesium, cobalt, or zinc. In this chapter, I present how the samples have been prepared, in particular, how the deposition process has been conducted. However, since the quality and properties of the thin film severely depend on the substrate, the first section refers to the very initial preparation of the substrate, before its introduction in the vacuum chamber, where both deposition and photoemission analysis are conducted. This part of the process could appear trivial, but in reality, it is crucial for the realization of good samples from which meaningful results can be extracted and discussed. Then, the deposition process is presented, by specifically showing the procedure we have followed for the realization of the thin films, by also discussing some technological issues that may be encountered during the deposition of organic materials.

7.1 Gold substrate

All three samples analyzed in this work are made by the same type of substrate which consists of a gold-covered silicon wafer. The gold shows a polycrystalline structure, indeed the surface is very rough, and the average thickness of the thin film is around $t_{Au} = 20$ nm. Between the gold layer and the silicon wafer, a chromium adhesion layer was deposited, this film is very thin, and a couple of nanometers are sufficient since it has just a structural role by favoring the sputtering deposition of gold. The silicon wafer underneath the chromium is covered by a very thin native silicon oxide layer of a couple of nanometers, which is a consequence of the air exposure during the fabrication. In any case, differently from the chromium layer, the innate oxide has no effect on the photoemission results, indeed it is not detected by the XPS analysis. Each sample is obtained by cutting the wafer with a diamond blade, the final samples have a rectangular shape and a surface area of around $A = 0.5$ cm². The samples are small so that it is possible to host two samples on the same holder, and the photoemission analysis is performed on a small spot of 1 mm², indeed, large samples are not required. Moreover, the rectangular shape allows a good clamping

of the sample to the holder, by allowing a sufficient exposure of gold, where the molecules will be deposited.

Double solvent cleaning

Before the mounting on the sample holder, each sample has been cleaned with chemical solvents in an ultrasonic bath. The process consists of a sequence of three baths with a different solvent, each of them lasting around 15 min. The first one is acetone, followed by isopropanol and then the samples are washed with a distilled water rinse. For every step, the liquid is poured into a specific glass container, then the samples are immersed in the liquid and introduced into an ultrasonic tank, which is filled with sufficient water so that the glass container is suspended and the samples are shaking. The double solvent cleaning in acetone and isopropanol effectively removes organic residues and oils that appear on every surface. Unfortunately, solvents may leave their own residues on the surface, indeed, the second bath in isopropanol successfully removes the leftover acetone. After the de-ionized water rinse, the samples are stored in a fourth glass container where the residual water is removed by blowing nitrogen. Finally, the samples are introduced in a heater, where they are heated at a temperature of $T = 110^{\circ}\text{C}$ in low vacuum conditions at $p = 300$ mbar for at least one hour so that the water can evaporate and being removed from the chamber.

PTS sample holder

The instrumentation is adapted for the PTS sample holder [73]. The size of the sample and its shape, other than the range of materials that can be mounted, are determined by the type of sample holder and by how the holder is transported between the different chambers of the UHV system. The PTS standard is equipped with electrical contacts, so that a BIAS can be applied to the sample, for example during the UPS analysis, and also with heating and cooling contacts in combination with a thermocouple. The PTS sample holder has very delicate components which can be easily damaged, a special care during the operations is required. Moreover, since the deposition of organic molecules with thermal PVD involves all the surfaces inside the deposition chamber, some of the delicate parts of the PTS holder can be damaged during the process. To face this problem, the holder is covered with an aluminium foil that exceeds of few millimeters of the perimeter of the holder, in order to not interfere the transportation. However, it is necessary that the aluminum foil does not electrically short-cut the holder connection so that a BIAS cannot be applied. The aluminum foil does not affect the analysis and the deposition, besides, it provides very good protection for the sample holder. The clamping of the samples and the aluminum foil to the holder is obtained through the screws and the short bars so that they cover the least amount of the sample surface. In some cases, it could be necessary to use a conductive carbon adhesive double-sided tape to better fix the sample to the aluminum foil. The sample must not move while transporting the holder between the different chambers and, moreover, during the deposition, the sample is turned upside-down.

Once the sample is clamped with the holder, protected by the aluminum foil, the holder

can be introduced into the vacuum system through the loading chamber. All the different chambers, namely the loading chamber, the analysis chamber, where the photoemission spectroscopy is conducted, the organic deposition chamber, and the storage are all interconnected through the distribution chamber, provided with a UFO transfer mechanism [73]. In order to transfer the holder, without damaging the sample and the instruments, it is necessary that the pressure of the two chambers is comparable. The pressure in the analysis chamber is always kept at $p = 10^{-9}$ mbar, whereas in the deposition chamber, the pressure is around $p = 10^{-7}$ mbar. This means that the sample cannot be immediately used, but some hours are required to reduce the pressure in the loading chamber. On the subsequent day of the loading, the sample can be moved to another chamber.

Ion beam etching

The last preliminary step, before the deposition of the molecules, is a further cleaning of the sample surface through an argon ion beam. The same chamber where the photoemission spectroscopy is performed is also equipped with an argon ion beam etching system. The argon ions are generated by the source and then accelerated through a grid toward the substrate. The ion beam strikes the sample with a wanted direction angle with respect to the surface, providing a very uniform etching of the surface over a quite large spot with a diameter around 4 mm. Since the etching is purely physical, there is no chemical selectivity, in any case, there are materials that are more resistant to the milling process. The etch rate depends on the material, but also on the angle of incidence of the beam and of course on the intensity of the beam itself. The ion etching is performed in order to eliminate all the residual contaminations that the double solvent cleaning failed to remove. Therefore, the argon ion etching lasts for ten minutes with an applied voltage of 2.5 kV in such a way we are able to successfully remove the adventitious carbon and reduce the damage to the gold surface to the minimum.

Immediately after the ion beam etching, the sample is ready for the first photoemission spectroscopy, which is conducted in the same chamber. The analysis is restricted to a very small area of a few millimeters of the diameter of the cleaned surface, where the photon beam is directed and focused. The position of the sample inside the chamber is recorded, so that always the same spot is analyzed during the next photoemission steps, after the depositions. A full XPS survey over the whole energy range (up to $E_B = 1486.6$ eV) and the single peak spectra of the most relevant elements, like gold ($E_B = 84.0$ eV), carbon ($E_B = 284.8$ eV), oxygen ($E_B = 531$ eV) and silicon ($E_B = 99.4$ eV), are recorded (table 6.3). These data are used as references, in particular, the presence of contaminations at the surface is extracted from the adventitious carbon peaks, whereas the silicon peak is expected to be comparable to the background noise. On the other hand, from the UPS spectrum, the work function and Fermi edge of the bare gold substrate are obtained, which will be compared with the results after the deposition steps. A complete analysis of the bare gold spectrum is provided in chapter 8.1.

Annealing

Two out of three samples, MgPc and ZnPc, are subjected to a rapid thermal annealing step right before mounting on the sample holder. The aim of the annealing is to change the crystalline structure of the gold substrate, by turning it from polycrystalline to a [111] surface. Indeed, the rapid thermal annealing drives the rearrangement of the atoms towards a uniform lattice structure, thus reducing the roughness of the surface, which is one of the major responsible for the uniformity of the deposited organic layer (6.1.3). However, in order to obtain the desired surface crystal orientation of the gold, the sample must be subjected to a very specific temperature for the exact amount of time, slight variations of the process parameters can completely alter the resulting structure. In addition, a sample with a known crystal structure is required since it can be better reproduced with the software simulation tool, in such a way, the simulation results are more reliable.

The adopted annealing technique consists of burning the sample, after the double solvent cleaning process, with the flame of a Bunsen burner, then waiting until it is cooled down. The color of the flame is an indicator of the temperature, as a matter of fact, the sample is vertically introduced in the region of the flame with the wanted temperature of $T = 700^\circ\text{C}$ for a couple of seconds. However, due to the very poor control of the process, the variability of the annealing temperature is so high that the result gold structure is unpredictable. Moreover, since the sample is moved inside the flame and then removed, the annealing time is not constant for the whole surface, some regions have been annealed for a longer time. As a matter of fact, the intensity of the annealing is not uniform all over the sample, and a gradient effect is obtained. Figure 8.8 shows the images taken with the optical camera of the AFM microscope, which are better analyzed in the next chapter. As a consequence of the annealing, circular-shaped features, similar to bumps, arise at the surface. The size and the density of those features increase with the annealing intensity, indeed there is a gradient in the concentration, from a region where the surface is just flat gold to a region completely damaged by the annealing. The origin of the bumps can be related to the reorganization of the gold atoms with the consequent exposure of the silicon substrate. Moreover, a reaction between silicon and gold cannot be excluded, resulting in a mixture of the two materials and in heavy damage to the gold surface. The main reason is that this process is suited for bulk samples, in this case, the thickness of the gold layer is too thin, thus, the temperature and the time required to have the wanted crystal structure must be redefined.

Finally, all the XPS and UPS analyses are conducted on a spot where the damage of the annealing is minimal. The evidence of that is the absence of a silicon peak in the XPS spectrum, which excludes the mix between silicon and gold, instead, the surface is made of gold only. The different XPS results of a heavily damaged surface and an only gold surface are analyzed in chapter 8.1.

7.2 Phthalocyanine deposition

The organic layers of metal phthalocyanine are deposited through thermal evaporation PVD of the molecules, which are in the form of powder. The organic preparation chamber is shown in picture 7.1, where are visible the different components: the evaporator, the

vacuum gauge, the quartz crystal microbalance, the turbo molecular pump connection, the shutter, and the manipulator. A background of the technology is provided in chapter 6.1, where the main components are presented in detail. On the other hand, the aim of this chapter is to illustrate how the phthalocyanine deposition is conducted for the sample studied in this work.



Figure 7.1. Picture of the organic deposition chamber.

Methodology

The deposition of the organic thin film is performed in steps. At each step, a controlled amount of material is deposited, and then the sample is transferred to the analysis chamber where the photoemission spectra are obtained. After that, the sample returns to the deposition chamber for the successive deposition. The process is repeated a certain number of times. In such a way, it is possible to study the evolution of the deposition process and the physical/chemical properties of the thin film as a function of its thickness. From a very thin layer, information on how the molecules behave with the gold surface and the properties at the interface can be obtained, whereas, thicker layers provide information on

the molecule organization. The sample never leaves the vacuum conditions and it is taken out from the system only after the photoemission analysis of the last deposition step.

In the specific, this work studies three samples that differ in the type of deposited phthalocyanine, whereas the methodology is always the same. At each deposition step, a very thin layer of 0.5 nm is deposited. This thickness corresponds to a couple of monolayers [20] and it can be controlled by the quartz microbalance. However, for the last steps, the amount of deposited material is increased, so that the morphological features of the organic layer could be highlighted. In table 7.1 are collected the total thicknesses of the deposited layers at each step. The values represent the expected amount of material deposited which is measured by a microbalance, the real layer thickness can be estimated by a quantitative analysis of the XPS spectra or directly measured by taking an AFM image of a deposition edge, where the sample surface was covered by the clamping bars. CoPc was the first sample under study and, because of technical complications, only a few steps were fulfilled. For the successive samples, the process efficiency was improved and, as a result, more steps were performed.

Table 7.1. Total thickness of the organic thin film at each deposition step for the three samples.

Step	Au/CoPc (nm)	Au/ZnPc (nm)	Au/MgPc (nm)
1	0.5	0.5	0.5
2	1.0	1.0	1.0
3	1.5	1.5	1.5
4	2.0	2.0	2.0
5		2.5	2.5
6		3.0	3.0
7		6.0	4.5
8			7.5
9			10.5

In thermal evaporation PVD, the source contained in the crucible is heated by the Joule effect up to the evaporation temperature in a chamber with high vacuum conditions. The evaporation temperature of the different phthalocyanine molecules depends on the central metal atom, however, the evaporation temperature is close to $T_{eb} \approx 350^\circ\text{C}$, at the pressure inside the deposition chamber, which is in the order of $p \approx 10^{-6}$ mbar.

Since the heating of the source is obtained through a resistive heater, the temperature of the source is a function of the current flowing in the wire and the applied voltage. However, these values are not directly controlled by the operator, which can only set the maximum power generated by the heater and transferred to the source. The deposition system used for this work allows to programming of the source temperature ramp which is then followed by the PID control system. In such a way it is possible to precisely set the heating rate of the source, which must be slow enough to avoid any alteration or damage of the organic molecules. As a matter of fact, the heating of the source up to the evaporation temperature is a time-consuming process. During the whole process, the pressure inside the chamber and the temperature must be monitored to avoid any strange

behavior. The temperature of the source is constantly measured during the whole process, thanks to a thermocouple located inside the crucible, in direct contact with the source. In any case, the most important quantity of the process is the deposition rate measured by the quartz microbalance, which is the indicator of the amount of deposited material per time interval. The deposition rate defines the quality of the thin film, better results are obtained if the rate is kept as low as possible and constant during the deposition. As a matter of fact, during evaporation, it is necessary that the current is stable and that the pressure and temperature are constantly controlled. Since the thickness of the deposited layer is of 0.5 nm per step, the deposition rate must not exceed 0.03 Å/s. A deposition rate of 0.01 Å/s is optimal, however, it is challenging to keep stable at such a low rate, because even small fluctuations are detrimental.

During all the deposition steps of the ZnPc and MgPc samples, the temperature of the substrate is kept at 60 °C. As already explained in chapter 6.1.3, by heating the surface, the adsorbed molecules have more kinetic energy and they can diffuse easily over the surface, thus reaching the optimal position. Therefore, the self-organization of the organic layer is favored. A temperature of 60 °C is sufficient to provide a slight improvement of the deposition process, without any sort of alteration of the surface structure. A deep study of the deposition film quality and organization as a function of the substrate temperature, and how the organic film reacts to different annealing temperatures could be interesting topics for future works.

Deposition rate control

In order to have a stable deposition rate a direct control of the experimental parameters is necessary. The system is provided by a PID control that tunes the current flowing in the heater such that the temperature of the source T_S matches the temperature set by the ramp T_{set} . In addition, the only other parameter that can be controlled is the maximum power supplied by the heater, through the power limit. A stable deposition is obtained when the current is stable, this condition can be achieved by having a T_{set} much higher than the evaporation temperature. This is because of the PID control system, which causes an oscillatory behavior of the temperature, and so of the current, when T_S is close to T_{set} . This happens because spikes of current increase the temperature of the source above T_{set} , and then, the current drops in order to reduce the temperature, and the cycle repeats. The amplitude of the oscillations is proportional to the power limit since the intensity of the spikes is larger for a high limit. However, when T_{set} is much higher than the evaporation temperature, the set value is never reached and the power limit is fixed to a value that allows a deposition rate of 0.03 Å/s. However, without any adjustment of the power limit, the temperature of the source will slowly drop, indeed, it is necessary that the operator gradually increases the limit in order to compensate for the temperature drop and keep the deposition rate stable. In those conditions, the inertia of the system is large, thus any variation of the power limit requires some time to have an effect, and the operator must act in advance.

Additional comments

Before the deposition, the source must be carefully treated in order to be purified from all the impurities and contaminations that are present in the powder. After the load of the evaporator (that hosts the crucible containing the source) in the deposition chamber, the vacuum must be restored. The turbo molecular pump is switched on and the whole chamber is heated. The heating of the chamber is necessary for the desorption of the particles from the walls and to avoid any adsorption on the inner surfaces. After this step, the purification of the source consists of slowly heating the source to favor the desorption of unwanted molecules and the evaporation of water. During the process is necessary that the pressure inside the chamber is kept below $p < 10^{-5}$ mbar so that all the contaminations are efficiently removed from the chamber.

After the deposition, when the wanted amount of material has been deposited, the source is slowly cooled down. It is very important that both the heating and the cooling rates are slow in order to avoid any alteration or damage of the source, therefore, compromising the whole process. For example, a fast heating rate can burn the source, causing the formation of a solid clump of molecules inside the crucible that blocks the evaporation. Whereas, during the cooling of the source, there is the possibility of the formation of a cluster of molecules, if it is not sufficiently slow.

Chapter 8

Photoemission analysis results

In this chapter are discussed the experimental results obtained through the photoemission spectroscopy techniques, XPS and UPS, of the three samples presented in the previous chapter. The general XPS and UPS equipment are presented in chapter 6.2, which also provides a physical background on the techniques and a guideline on how to interpret the spectra in order to extract both a qualitative and a quantitative analysis of the sample. The XPS and UPS are conducted in the same vacuum chamber with a controlled pressure of 5×10^{-10} mbar. The ultra-high vacuum conditions are crucial for the photoemission analysis, to avoid any interaction between the photoemitted electrons and the atmosphere, with a consequent loss of the information. The X-ray gun is based on a AlK_{α} source equipped with a monochromator that improves the resolution. Thus the emitted photons have a unique energy of 1486.6 eV, which allows the investigation of a suitable energy range that includes the main peaks of the elements of our interest. The excitation voltage and the beam current are set to 12.0 kV and 10.0 mA respectively, as a result, the x-ray power is of 120 W. For the UPS analysis, the ultraviolet beam is generated by a helium plasma, thus the emitted photons have the characteristic energy of 21.22 eV. The intensity of the beam is controlled by the current, which is set at 100 mA coupled to a voltage of 1.0 kV. In the same chamber, before the analysis, the samples undergo non-focused argon ion beam sputtering that impinges on a surface of $4 \times 3 \text{ mm}^2$ for 10 minutes. The voltage is set to 2.5 kV to reduce the gold surface damage. More information on the components can be found in the manuals ([73]).

All the operations on the photoemission spectra and the fitting of the peaks are executed with *CasaXPS* software. The plots presented in the following are directly extracted from the software. The peak fitting is performed by using Gaussian and Lorentzian sum (SGL) curves in combination with a Shirley background. Whereas, for UPS, several backgrounds are employed depending on the calculation. To fit the HOMO peak, Tougaard's background and SGL are exploited, on the other hand, to measure the energy cut-off and the HOMO onset, the edge background is required. The photoemission data did not require any serious manipulation, indeed, no corrections of the peak energies were applied. For very low peak intensities, a soft smoothing of the data was necessary to better distinguish the peak from the background noise.

8.1 Gold substrate analysis

The very first photoemission analysis of the sample surface is carried out right after the ion beam cleaning of the surface. The reason is to record, for each sample, information on the structure of the surface and on the amount of contaminations that have not been successfully removed by the cleaning procedure. Moreover, it is necessary to have a substrate reference in order to study how the deposition of organic molecules will affect the physical and chemical properties of the device. As a matter of fact, the effects of the interactions that occur at the metal-organic interface can be discussed and evaluated by comparing the spectrum taken before and after the deposition.

All three substrates consist of a silicon wafer covered with a thin layer of gold, the metal deposition was obtained through sputtering. The complete XPS survey of the gold surface is shown in figure 8.1 (actually, a full spectrum covers energies from 0 eV to 1406.8 eV, however, above 650 eV no interesting features are detected). It refers to the first sample substrate, which is then covered with cobalt phthalocyanine. Since the three substrates are very similar, the majority of the following considerations are shared with the other employed gold substrates. However, the main differences lie in the number of contaminations that are still adsorbed, and in the effects of the rapid thermal annealing (RTA), which modified the structure of the surface. In any case, from the photoemission analysis results, the RTA process, applied to Au/ZnPc and Au/MgPc, results almost negligible (at least in the analyzed region), with only slight variations in the intensities of some peaks, that do not compromise the analysis. An extended analysis of the effect of the annealing is provided in section 8.1.3.

8.1.1 XPS results

From the complete spectrum depicted in figure 8.1 the chemical composition of the surface is obtained, showing the elements within the top tens of nanometers (10 nm – 20 nm) of the surface. As expected the predominant signal comes from gold, the main peak at a binding energy of $Au_{4f} = 84.00$ eV is followed by additional clearly visible peaks, in particular Au_{4d} and Au_{4p} at a binding energy of 334 eV and 546 eV respectively. All those peaks are split in two due to spin-orbit interaction, the value of the binding energy refers to the main one. The energy positions of the peaks perfectly match the values expected in literature [77, 76]. Other elements that are visible from the survey are oxygen, with the main peak at $O_{1s} = 531$ eV and chromium at $Cr_{2p} = 577$ eV. Those peaks are the result of the effects that the 2 nm chromium adhesion layer has on the structure of the gold layer. As a matter of fact, the adhesion layer and the gold are not well separated, but, the chromium atoms inter-diffuse within the first few nanometers of gold forming a Cr-Au alloy. The typical crystal structure of a gold layer deposited on chromium is polycrystalline, however, it is demonstrated that the majority of grains have a [111] crystal orientation [85]. In addition, the adhesion layer is partially oxidized, since chromium is a very reactive element, and, during the e-beam deposition, it may easily react with the water and oxygen present at the silicon surface. The evidence of chromium oxidation is demonstrated by the binding energy of the Cr_{2p} peak, which is equal to 576.7 eV, proper of the Cr-O bond of Cr_2O_3 [85]. This also partially explains the presence of a high oxygen signal. As a matter of fact,

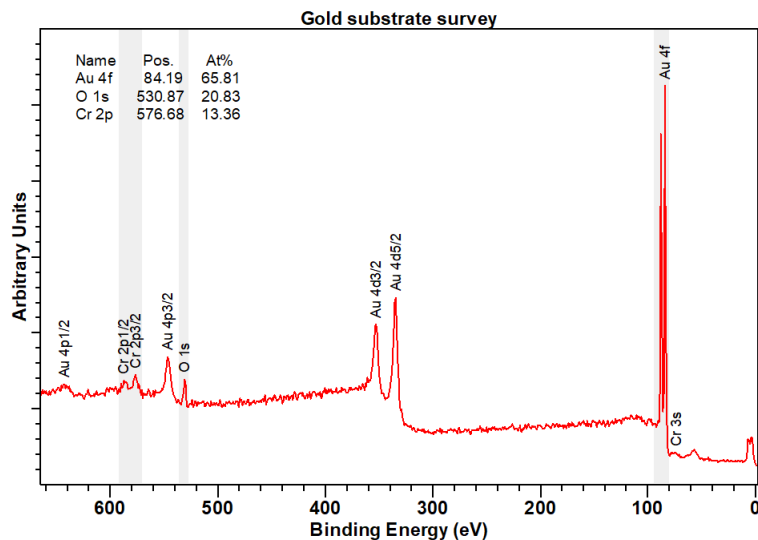


Figure 8.1. Full survey spectrum of the bare gold surface of Au/CoPc, before the deposition of the organic molecules, showing the atomic percentages of the elements composing the substrate.

the atomic percentages of chromium and oxygen are close to the 2:3 characteristic of the oxide. The appearance of those two peaks, in particular the chromium one, evidences the very low thickness of the gold layer, which should be around 20 nm as average. Otherwise, in the case of a thicker layer, the photoemitted electrons of the inter-diffused chromium atoms are not able to travel through the gold without any scattering event. Thus they are incapable of preserving the information of their binding energy and forming the peak. On the other hand, the complete spectrum in figure 8.1 shows only a short carbon peak proving the almost absence of contaminations. Finally, as expected, the silicon peak is comparable with the background noise, as shown in the respective graph in figure 8.2, (the silicon peak belongs to the second substrate, where ZnPc is deposited). The very short silicon peak is another indicator of the thickness of the gold layer, for the same reason as the chromium peak.

Information concerning the structure of the gold layer is extracted from the peak fitting components of the gold Au_{4f} . The positions of both peaks are matched with the expected results obtained from the literature [77, 76]: the main one at 83.90 eV is followed by the secondary peak at 87.57 eV as a consequence of the spin-orbit splitting. As a matter of fact, the energy difference is close to the expected $\Delta = 3.7$ eV. The intensity ratio between the two peaks is in accord with the theoretical value in table 6.5, with a second peak intensity equal to the 75% of the main one. The full-width-half-maximum (FWHM) of both peaks is close to 0.67 eV, which is an indicator of the crystallographic order of the gold surface. A very narrow peak is measured when the surface has a unique crystallographic orientation, with a FWHM lower than 0.5 eV. On the other hand, when the layer is amorphous, the peak is broadened over a larger energy interval. The reason is that in an amorphous

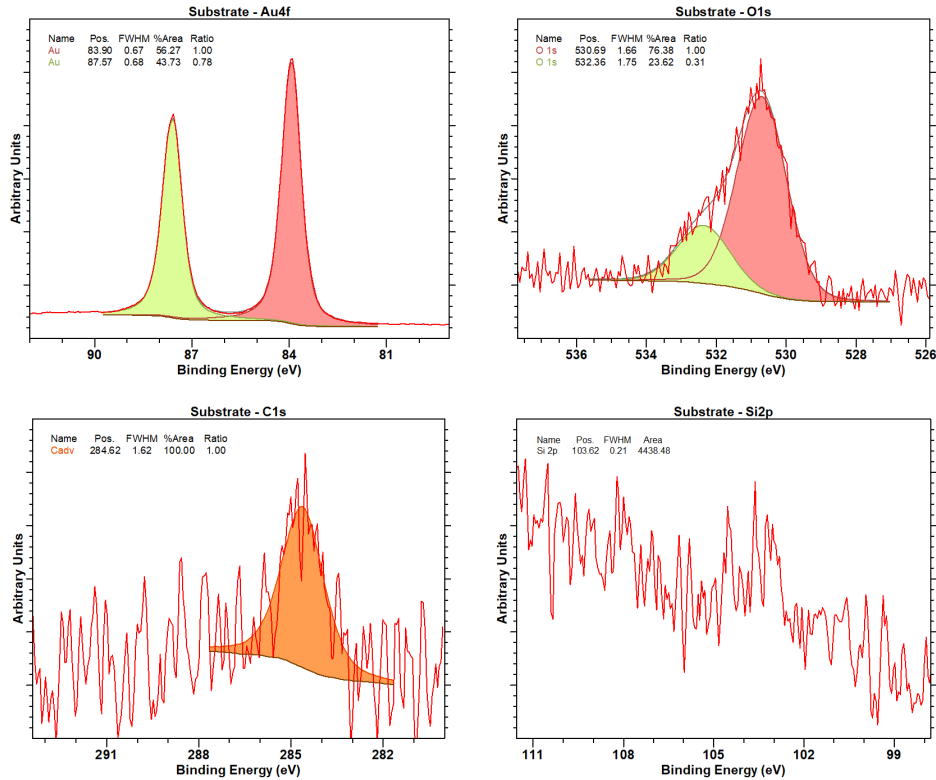


Figure 8.2. XPS local peaks of gold, oxygen, carbon, and silicon measured from the bare gold surface of the substrate.

material, the distances between the atoms are random, due to the absence of a lattice that provides a structural organization. As a matter of fact, the chemical state of each atom is slightly different and this is reflected in the binding energy of the electron states, which indeed depends on the chemical environment. With a FWHM equal to 0.67 eV, we can state that the surface is polycrystalline, thus characterized by several grains of different sizes, each with a proper crystal orientation. Additional considerations on the surface morphology can be acquired by microscopy techniques. Figure 8.3 shows the image of the bare gold substrate taken with the atomic force microscope in non-contact mode, from which we can measure the roughness of the substrate of ≈ 5 nm. From the phase image, we can determine that the black dots on the gold surface are contaminations that have been deposited during transport and manipulation. To improve the quality of any peak fitting of a metal, the asymmetry of the curve must be considered. However, in this case, the asymmetry is not so pronounced. A possible explanation is that the high intensity of the signal partially covers this feature. Moreover, it could be possible that the chromium and the oxygen atoms in the gold, interfere with the shake-up processes, thus suppressing the tails.

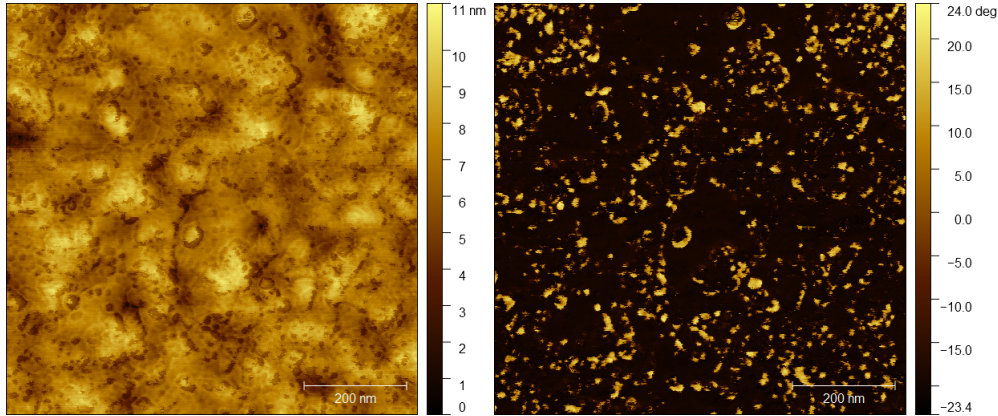


Figure 8.3. AFM images of the gold surface taken in the non-contact mode of the topography and phase. The sample belongs to Fabrizio Mo.

8.1.2 UPS results

From the UPS analysis, which is focused on the valence electrons of the sample, it is possible to investigate the very surface and to directly measure some electric properties of the system. In particular, the metal work function and the Fermi energy values are obtained. In figure 8.4 are plotted, on the left, the cut-off energy of the UPS spectrum and, on the right, the Fermi edge. The valuation of the Fermi level is conducted by setting the proper background type in *CasaXPS*, that is *Step Down*, which returns the value of the center of the step, that can be considered as the Fermi level. Indeed the smoothness of the edge is a consequence of the non-zero temperature during the measurement, thus expected. By definition, the Fermi level of a metal should be at 0 eV with an energy scale that refers to the binding energy, however, the shift at a positive energy of $E_F = 0.16$ eV is an instrumental error due to the non-perfect alignment of the Fermi levels between sample and detector. This offset must be considered when evaluating the other quantities, like the work function. In order to evaluate the work function, a linear interpolation of the curve is performed. From the graph in picture 8.4 the approximate value of the work function is $\phi_{Au} = 4.52$ eV, which is directly obtained by plotting the spectrum with respect to the kinetic energy of the electrons. However, the exact value is calculated by taking into consideration the offset of the Fermi level, therefore the work function of the bare gold substrate is $\phi_{Au}^* = 4.68$ eV.

The work function is a characteristic property of each material, nevertheless, it is affected by the crystal structure and the chemical composition of the material. Pure gold has a work function of $\phi_{Au}^{lit} = 5.1$ eV, with a possible variation of a few tenths of electronvolts. However, the value measured in my experiments, for all three substrates, is well below the expected value. The cause is traced back, once again, to the presence of the chromium adhesion layer. As said before, the chromium, during the gold deposition, inter-diffuses in the layer, and, due to the very high reactivity of chromium, the alloy Cr-Au is formed [85]. The properties of the metal alloys have intermediate values with respect to

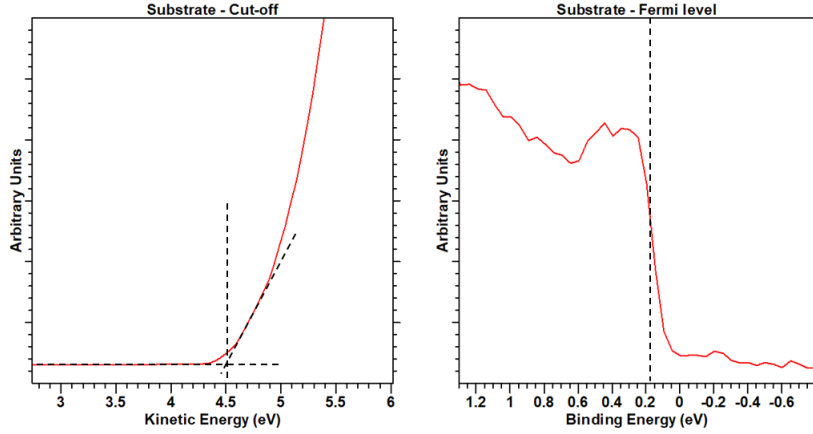


Figure 8.4. Plots of the cut-off energy (left) and Fermi edge (right) of the bare gold substrate of the first sample measured through UPS, the calculated values are $\phi_{Au} = 4.52$ eV and $E_F = 0.16$ eV.

the individual components. Moreover, according to the concentration of the components, the properties are tuned between the two limits. Therefore, the work function follows the same rule. Usually, for a binary alloy, the simplest model considers the linear interpolation expressed by the following equation:

$$\phi_{AB}(x) = x \cdot \phi_A + (1 - x)\phi_B \quad (8.1)$$

Where ϕ_A and ϕ_B are the two work functions while x and $(1-x)$ identify the concentrations of the respective components. However, for some specific alloys, a different model is required, therefore an accurate measurement of the composition of the alloy through the work function is a challenging task [86]. The substrate work function measured with UPS is in the expected range since the work function of pure chromium is $\phi_{Cr}^{lit} = 4.5$ eV. A deeper investigation of the substrate structure is not interesting for the purpose of this work. In fact, the shift of the work function, caused by the metal-organic interface, is independent of the substrate work function. To study the properties of the metal-organic interface one has to focus on the energy shifts rather than the absolute values.

8.1.3 Effects of the annealing

The annealing treatment of the samples before the introduction in the vacuum system was meant to reduce and increase the crystallographic order of the gold substrate, from a polycrystalline structure to a [111] directed surface. However, the process was not controlled at all, and the result was quite unpredictable. However, to prove the effects of the annealing, the comparison between the photoemission spectra of three samples subjected to an increasing intensity of the annealing process is discussed in the following. One sample did not undergo the annealing step, indeed, it has been already described in

the previous section. The other two samples have been annealed at the same temperature, but the processes last a different amount of time: 2 s and 40 s respectively. Even if the surface of the third sample, the one submitted to very long annealing, has been completely damaged by the thermal process, interesting considerations on the gold substrate can be deduced.

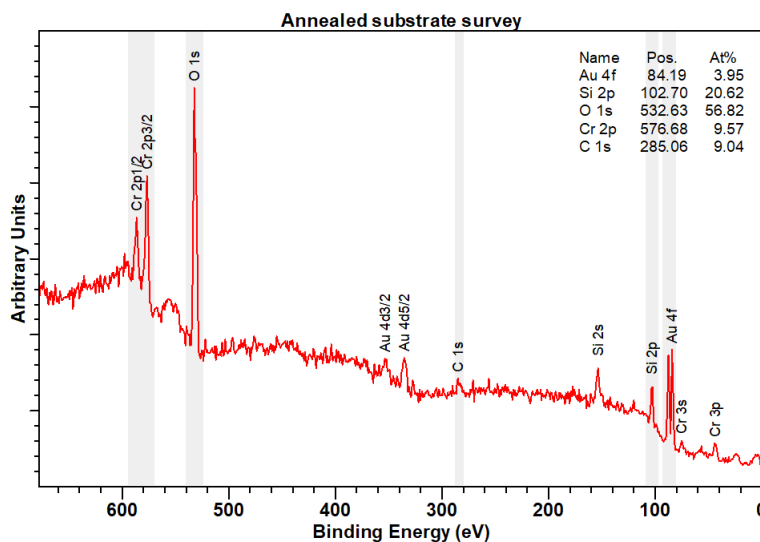


Figure 8.5. XPS full survey spectrum of the bare gold substrate after annealing at 700°C for 40 s.

As a starting point is interesting to discuss the main features of the XPS spectrum of the gold substrate after the 40 s annealing process, which is shown in figure 8.5, and point out the main differences with the data acquired from the not thermal treated sample of figure 8.1. The two spectra are indeed very different: the main peaks of the spectrum in 8.1 are characteristic of gold atoms, whereas, for the other sample in 8.5 the characteristic peaks of oxygen, silicon chromium, and gold are detected. The major peak corresponds to O_{1s} at 532.63 eV, figure 8.6 is focused on the analysis of this specific peak. The presence of several peaks for both chromium and silicon is evidence of their abundant amount at the surface, at the expense of the gold peak, which is considerably lower with respect to the other spectrum. It is clear that the annealing has a huge effect on the structure of the substrate and completely changes the chemical composition of the surface. The carbon C_{1s} peak, on the contrary, is low in both samples, which means that the annealing does not increase the amount of contamination, but rather it facilitates the removal of contaminations and the desorption of particles from the surface. The small amount of carbon can be connected to the exposure to the atmosphere after the annealing.

In figure 8.6 are shown the XPS spectra of the main peaks of each element of the substrate surface. Unfortunately, the chromium Cr_{2p} peak was not recorded during the analysis, still, the other peaks are sufficient to deduce the structure of the surface. The gold peak is once again split into two peaks due to the spin-orbit effect, however, after the

annealing, each peak is coupled to a secondary peak which can be connected to the Au-Cr alloy. Both secondary peaks are shifted with respect to the main one of $\Delta = 0.6$ eV, whereas the energy of the main peaks is identical to the value found in the literature. Concerning the FWHM of the main peak, it appears that it is reduced after the annealing, thus, the gold present at the surface has a better crystal organization. Looking at the oxygen O_{1s} spectrum, it is evident that the second peak at a binding energy of 532.76 eV has become the dominant one. The first peak, at a lower binding energy of 530.89 eV refers to the oxygen bonded to metal elements, like chromium in this case, moreover, it can also include the oxygen present in the contaminations of the surface, in any case, due to the very smaller amount of carbon, this component is negligible. Instead, the second peak at 532.76 eV is proper of the silicon oxide. Moreover, the wide FWHM of both peaks suggests that other peaks may be considered, nevertheless, the peak of oxides are usually characterized by a wider FWHM with respect to the respective pure metal. The predominant carbon C_{1s} has an energy of 285.32 eV, probably due to the bond with oxygen. For the spectrum of silicon, two components are individuated, the major at 103.56 eV and a very small one at 99.50 eV, which is almost comparable to the background noise. Nevertheless, the latter, a smaller binding energy, is proper of the silicon elements, whereas the other one indicates the presence, in large quantity, of silicon oxide at the surface [77, 76].

It is demonstrated that a heavy annealing process considerably alters the structure of the substrate. As a matter of fact, during the annealing, both the underlying layers, namely the chromium adhesion layer and the native silicon oxide, diffuse through the gold layer. This is evinced by the increasing signals characteristic of chromium, silicon, and oxygen. As already said, the chromium adhesion layer is partially oxidized and it is also bonded to the gold atoms, thus forming an alloy. A further step at high temperature, as the annealing, will undoubtedly enlarge the diffusion region, as a consequence, the inner layer will reach the surface. On the other hand, the drop of the gold peaks suggests that the gold sank into the substrate. As a result of the combination of these two processes, the surface is mainly made by silicon and chromium, partially oxidized, with some local regions where gold is crystallized, since the main peak of gold at 84.0 eV is still present, with a narrow FWHM. The accurate composition of the surface is difficult to determine, however, it cannot be excluded that the oxide at the surface is a mixture of both silicon and chromium. Figure 8.8 shows a picture of the annealed sample surface, the last one, on the bottom right. The picture is taken with an optical camera connected to the AFM, the one used to visualize the tip on the surface during the approach and the scanning process. The sample was covered by a very thin film, less than 2 nm, of ZnPc, which is not sufficient to cover the surface structure, in fact, it is possible to appreciate the chaotic and irregular surface.

The presence of silicon at the surface is also confirmed by the analysis of the UPS spectrum, by focusing, as always, on the onset and the Fermi level, which are displayed in figure 8.7. After the annealing, the onset energy is downshifted of almost half electronvolts, indeed it is at an energy of 4.058 eV, which corresponds to the electron affinity of silicon. Moreover, the semiconductive nature of the surface is confirmed by the position of the valence band edge, which stops at 1.475 eV, in fact, a metallic behavior, with a Fermi edge close to 0 eV is not measured. However, a valence band edge of 1.475 eV is quite high and

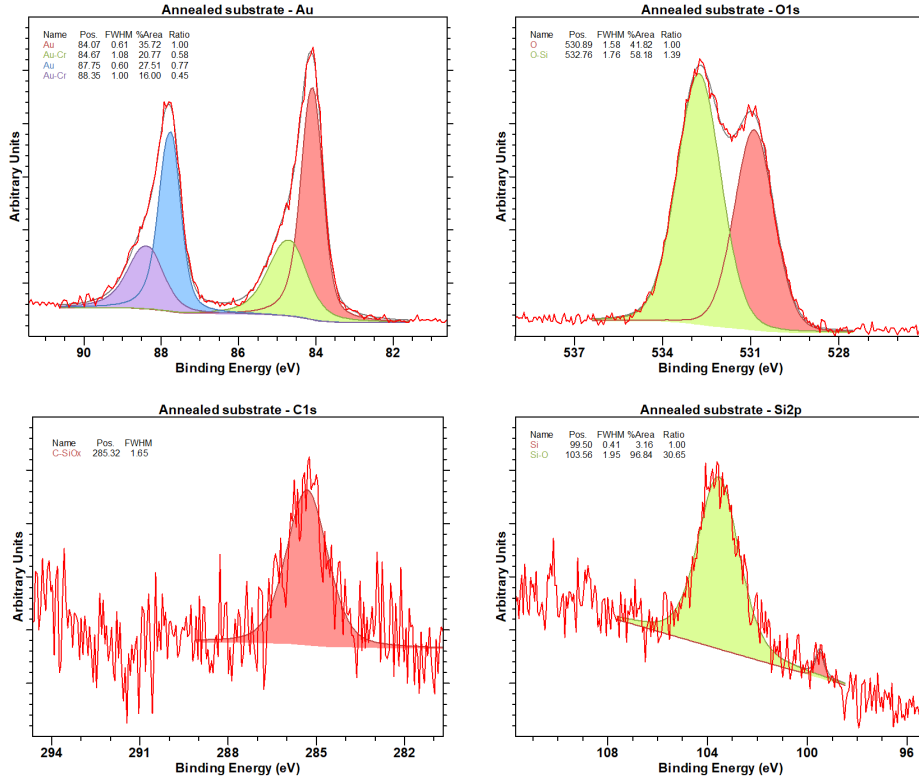


Figure 8.6. Local XPS spectrum of the main peaks of the annealed substrate at 700 °C for 40 s, in particular: Au_{4f} , O_{1s} , C_{1s} , and Si_{2p} .

cannot be connected to the silicon, since it has an energy gap of 1.12 eV. On the contrary, chromium oxide has a bandgap that varies between 3.00 eV and 3.40 eV depending on the stoichiometry of the compound. Thus, it may be the reason for the measured valence band edge.

In figure 8.8 are collected six pictures, taken with the AFM optical camera, of the sample surface. The sixth picture, the one in the bottom-right, refers to the 40 s annealed sample discussed before, whereas the other five pictures are taken from the sample where ZnPc has been deposited, thus it was annealed for just 2 s. The pictures show different regions of the same surface, thus the gradual effect of the annealing is clearly visible. The first one, on the top-left, is obtained from an almost not annealed region, where the gold layer is uniform and no particular features are visible with the AFM camera, except for the small black dots, which are the contaminations and the dust deposited on the surface after the exposure of the sample to the atmosphere. Moving on to the next picture, the consequences of the annealing start to be visible: circular features similar to bubbles appear at the surface without a specific organization, and the diameter goes from a few to tens of micrometers. The next pictures show successive regions where the annealing effect is increasing. There is a gradient in the bubbles' density and in addition,

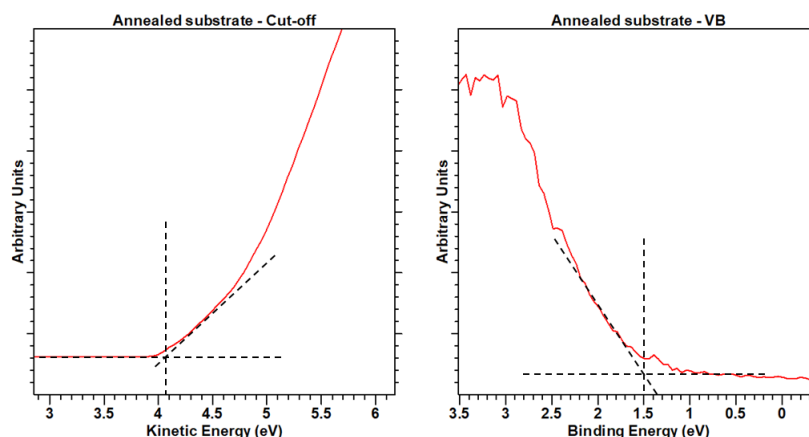


Figure 8.7. Plots of the electron affinity (left) and the valence band (right) of the oxidized surface of the annealed sample obtained through UPS.

they become larger and larger, at the expense of the gold. The third image shows a sort of "edge" where the bubbles start to merge and as a consequence, the surface is completely covered by silicon and oxides, as shown in the bottom-left image, where the bubbles are no longer visible, the surface is homogeneous and the gold concentration is heavily reduced. Moreover, the surface morphology after 40 s annealing shows additional features, like the dark dots (the last picture), which are holes that are probably caused by the sinking gold into the substrate or that is evaporated.

Anyway, both samples used for the deposition of ZnPc and MgPc show these surface features, however, the XPS and UPS analysis is conducted on a region similar to the one shown in the top-left image, where the annealing effect is almost negligible and, indeed, the surface is comparable to the not-annealed one, used for the CoPc deposition. As a matter of fact, both XPS and UPS spectra obtained before the deposition are very similar to the one described in 8.1, where the silicon and chromium peaks are much less intense and the oxygen second peak is less pronounced. Nevertheless, even if the surface appears to be not modified by the annealing, some effects of the thermal process seem to be detected by the XPS analysis, since the characteristic peaks of the oxides and silicon are a little bit more accentuated, suggesting an expansion of the chromium and oxide diffusion region towards the surface. However, the UPS spectrum is identical to the one in picture 8.4, this means that the composition of the very surface is almost completely made of gold. Thus, a comparison between the photoemission results of the three deposited samples (CoPc, ZnPc, and MgPc) will highlight the different properties of the organic layer only, since the substrate structure, in the analyzed regions, is almost identical.

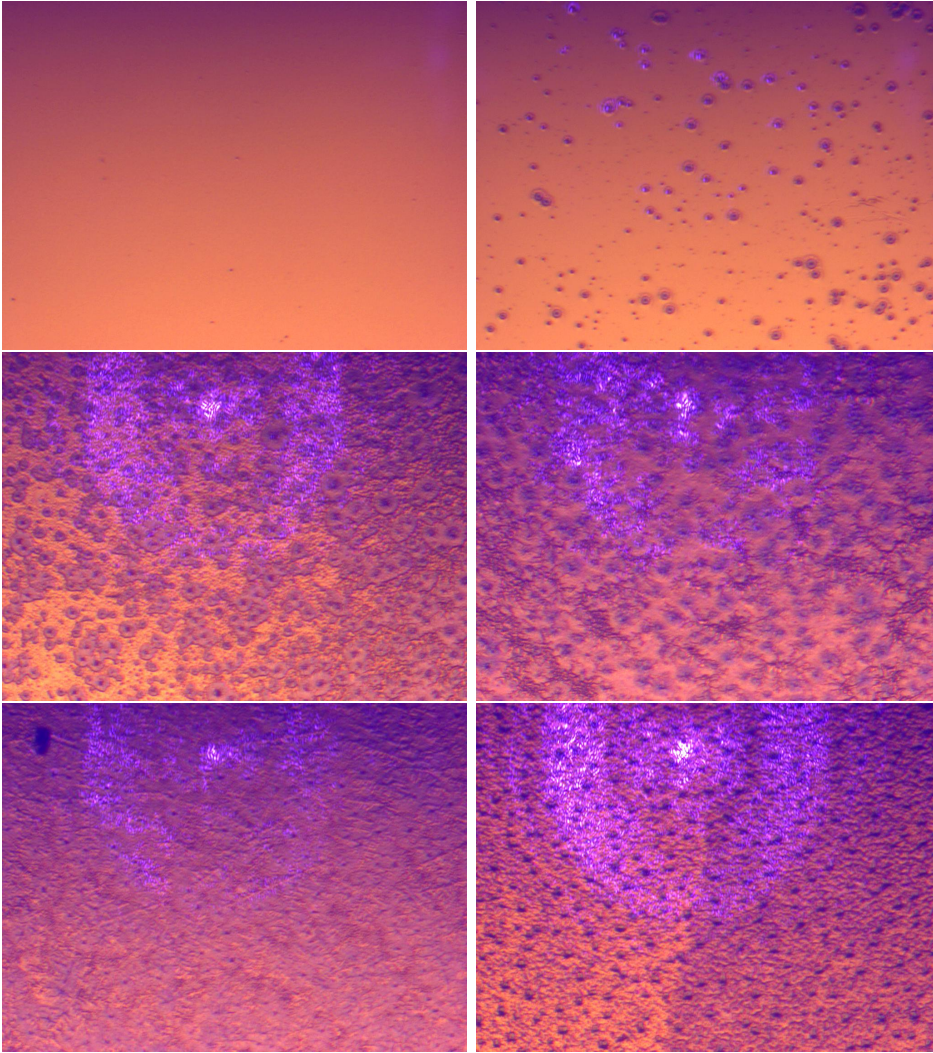


Figure 8.8. Pictures of the gold substrate after a 2s annealing process, showing a gradual damage of the surface taken with the AFM camera. The bottom-right image refers to a 40 s annealed sample.

8.2 CoPc on polycrystalline Au

The first phthalocyanine that has been deposited is CoPc, unfortunately, the deposition process ran into several complications that reduced the quality of the organic thin film. As a result, only four deposition steps have been conducted, thus the total expected thickness of the organic layer is $T = 2$ nm. After the fourth deposition process, in order to quickly reach the evaporation temperature, the heating of the source was so fast that burnt the powder in the crucible. As a consequence the CoPc molecules have been permanently damaged, in fact, it was necessary to change the source into ZnPc. For this reason,

the amount of collected data for Au/CoPc is less than the other two samples discussed in the following. Nevertheless, by comparing the measurements of the four depositions, we are able to discuss the structure of the organic layer. The step-wise deposition is conducted through PVD in a vacuum chamber at a pressure of 3×10^{-6} mbar with a source temperature of 300°C , providing a deposition rate between $0.01 - 0.03 \text{ \AA/s}$. At each step a layer of 0.5 nm is deposited, which is monitored with a quartz crystal microbalance.

From the analysis of the photoemission spectra, both qualitative and quantitative information about the metal/organic interface and the monolayer are obtained. According to the shifts in the characteristic binding energies, the chemical environment and the interface charge transfer can be determined, moreover, from the increase or reduction of the peak intensities measured at each deposition step, provides information on the evolution of the organic layer and on the structure of the thin film. In the following are presented and discussed the photoemission results, by separating the qualitative analysis from the quantitative one, obtained by combining the information gathered from different spectra.

8.2.1 Qualitative analysis

The analysis starts from the substrate signals, in particular, figure 8.9 shows the evolution of both Au_{4f} (on the left) and O_{1s} (on the right) peaks at each step, from the top to the bottom. Each plot is composed of five different curves obtained from the respective step, where "step 0" refers to the data acquired before the deposition, whereas, "step 1" is after the first deposition process, and so on... The offset between the curves is just for the sake of clarity, in such a way is possible to have a direct comparison of the spectra that preserves the characteristic features avoiding the overlapping of the curves, which may create confusion. The gold Au_{4f} peak is composed of two separate peaks due to the spin-orbit interaction and it is interesting to notice that the binding energies of both peaks do not vary during the deposition. The first peak is at a lower BE of $83.92 \pm 0.03 \text{ eV}$ whereas the second is at $87.60 \pm 0.03 \text{ eV}$, respecting the energy separation of $\Delta = 3.7 \text{ eV}$, as found in the literature [76, 77], and the intensity ratio of 4:3. This information is used to determine the type of adsorption process. As a matter of fact, since the gold peaks are fixed, the chemical interaction between the metal and the CoPc molecules is excluded. Thus, no chemical bonds are built between the two components, but rather the interaction is driven by weak van der Waals forces, which are not sufficiently strong to alter the chemical state of the surface gold atoms, which indeed are almost unaffected by the presence of the adsorbed molecule. This aspect is confirmed by the *ab initio* simulations 9.1.2. The oxygen peak is decomposed into two components, the main one at $530.69 \pm 0.05 \text{ eV}$ is associated with the generic O_{1s} orbital, whereas the second peak at $532.35 \pm 0.05 \text{ eV}$ can be connected to the chromium oxides present in the substrate. This is also confirmed by the detection of chromium, as shown in the survey spectrum in figure 8.12. This peak can also be associated with contaminations, however, the carbon peak of the bare gold surface is not so pronounced (figure 8.2) to justify such an intense oxygen peak. As expected, the intensities of the substrate signals are reduced as the organic layer gets thicker, since a smaller substrate volume is investigated. The intensities of the substrate peaks are exploited in the successive quantitative analysis.

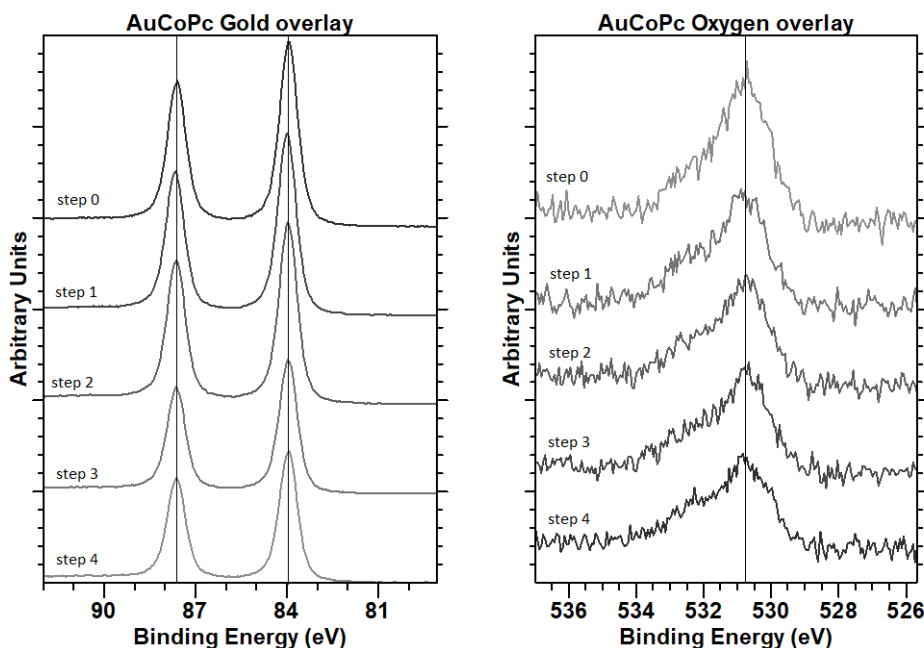


Figure 8.9. Gold Au_{4f} and oxygen O_{1s} peaks of the Au/CoPc sample measured after each deposition step.

The most important region of the XPS spectrum for the analysis of organic materials is the carbon C_{1s} peak. Here are presented the characteristic features of the carbon C_{1s} peak which are in common for the majority of metal phthalocyanines, as a matter of fact, the carbon backbone ring made of four pyrrole and four benzene groups is shared between all MPc. The typical peak fitting of the C_{1s} of a metal phthalocyanine is composed of a main peak (C1) followed by a second minor peak (C2) at higher binding energy. The former is characteristic of the sp^2 hybridization of the carbon orbitals involved in the benzene rings, whereas the latter is connected to the C-N bonds of the pyrrole groups. Indeed, an intensity ratio close to 3:1 that reflects the molecular stoichiometry is obtained. Both peaks are also followed by their own satellite peaks at higher binding energies. The satellite peaks are the result of the excitation of $\pi-\pi^*$ transitions, from HOMO to LUMO, as a matter of fact, the energy shift between the main peak and its satellite is the same for both couples. Moreover, the intensities of the satellites are around one-tenth of the respective main peak. However, the C-N satellite peak is superimposed on a resonance peak that arises from the stacking of the benzene rings, increasing its intensity and also providing additional information on the molecular organization. As a matter of fact, it is the main indicator of the stacking of benzene rings.

The characteristic features of the Au/CoPc carbon peak are shown in figure 8.10. On the left are collected, from the bottom to the top, the carbon C_{1s} peaks after each deposition step, by highlighting also the evolution of the several fitting components. Whereas,

on the right, there is a zoom of the peak fitting after the last deposition step, to focus on the features of the components. In order to accurately describe the carbon spectrum, the adventitious carbon must be considered by adding a fifth peak (C_{adv}), which is connected to the surface contamination buried at the metal/organic interface. Therefore, its intensity must decrease like gold and oxygen as the deposited layer becomes thicker. It is demonstrated that the binding energy of the adventitious carbon may vary on a wide energy range, however, these carbons are weakly bound to the surface and they feel the interface dipole between metal and CoPc. Therefore, after the deposition, the shift of the C_{adv} binding energy toward higher energies and the work function reduction are comparable, since caused by the interface dipole. Actually, the shift in the UPS cut-off is also caused by the interface charge transfer that, according to its direction, can accentuate or compensate for the work function reduction. However, from both the experimental and simulation results, the charge transfer between gold and the investigated phthalocyanines is small. Regarding the peak intensity, a rough estimation can be calculated by following the same reduction trend of both oxygen and gold peaks using the carbon peak of the bare gold surface as a reference. Indeed the contaminations can be considered as a part of the substrate since they are covered during the deposition.

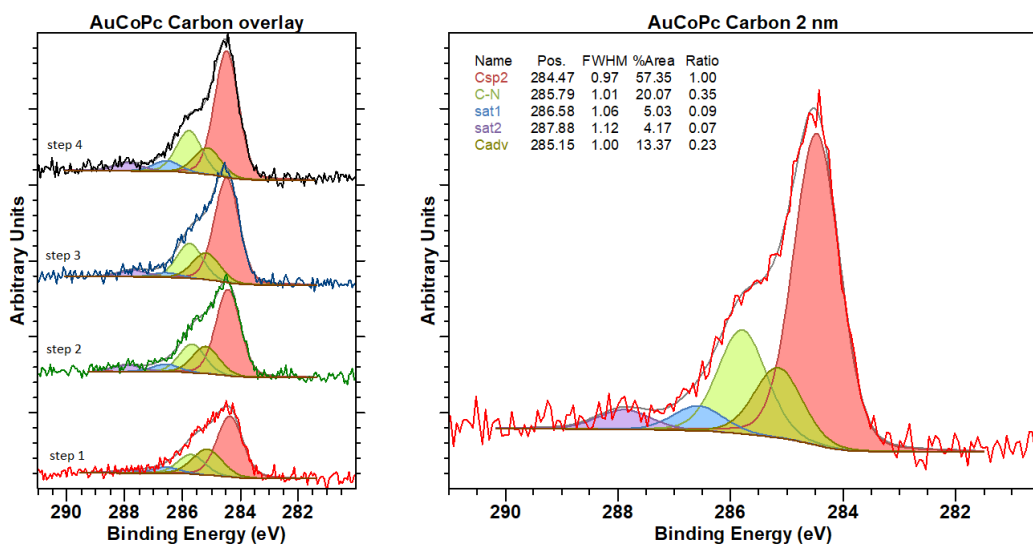


Figure 8.10. Au/CoPc carbon C_{1s} peaks, on the left the overlay of the spectra after each deposition step, while on the right the zoom of the carbon peak fitting for the last step, with an expected $d = 2$ nm.

The structure of the CoPc organic layer is discussed by analyzing the XPS spectrum of the thickest layer. As expected, the carbon C_{1s} peak is decomposed in five components, the main one, at 284.47 eV corresponds to the benzene rings carbon, thus with a sp^2 hybridization. The carbon involved in the N=C-N bond is subjected to the chemical shift, indeed the respective peak is at a binding energy of 285.78 eV, and the energy shift is exactly of 1.3 eV as demonstrated by other studies [18, 26]. The intensity ratio between

the two peaks should be close to 3:1 since 8 carbon over 32 is bonded to two nitrogen atoms, however, the second peak can be higher due to shake-up processes and a ratio of 35% is obtained. Both peaks are followed by their respective satellite peak, at a binding energy of 2.1 eV higher (286.58 eV and 287.88 eV), with an intensity that is below on tenth of the main peak. The last component at 285.15 eV takes into account the adventitious carbon detected from the bare gold substrate, as shown in figure 8.2, the shift in binding energy of 0.55 eV is caused by the interface dipole, measured from the UPS analysis as shown in table 8.1. On the contrary, the fact that the carbon peaks characteristic of the CoPc are not shifted during the deposition indicates that the polarization effect is localized at the interface and does not affect the organic layer.

The same peak fitting is performed for all the previous deposition steps, as shown in the overlay plot in figure 8.10. The thicker the layer, the more visible are the two main components of the CoPc molecule, whereas the contaminations become less significant. At the first deposition step, the amount of deposited molecules was so low that the satellite peaks were almost comparable to the background noise. Nevertheless, the presence of the satellite peaks is an indicator of the organization of the molecules, indeed, when there is a stacking of the benzene rings, the resonances generate a peak at an energy close to the satellite peak of C-N. This aspect is much more evident in the next two samples, where the deposited layer is much thicker and well-organized. The binding energies of the five carbon components are more or less stable during the whole deposition process. Interesting to notice that the energy separation between the C-N and the main peak is stable during the deposition. This aspect is an additional indicator of the absence of chemical bonds at the interface, that confirm the analysis of the gold peak [30].

Concerning the nitrogen and cobalt signals, the data are in accord with other studies [18, 26]. As shown in the right graph of figure 8.11, which describes the evolution of the cobalt $C_{O_{2p}}$ peak, the main component is at an energy of 780.5 ± 0.1 eV, indeed, with respect to the metal phase, a shift larger than 2 eV towards higher BE is detected, due to the particular chemical state of cobalt in the CoPc, that is bonded with four nitrogen atoms, characterized by a higher electronegativity [76]. Moreover, the satellite peak is characteristic of the unfilled electronic shell, the fact that it is populated after the deposition implies that there is an electron transfer from the metal to the molecule. The nitrogen peak energy is at 398.8 ± 0.1 eV in accord with the imine functional group [77], that have an identical chemical state as the nitrogen in metal phthalocyanines. Actually, it is better to decompose the peak into two components of similar intensities, as a matter of fact, half of the nitrogen atoms are bonded to the central metal, thus their chemical states are altered. However, in this case, the chemical shift is so small that the two peaks are almost superimposed and can be considered as only one. The single nitrogen peak suggests that the molecules are not bent during the adsorption, but rather they stay planar. As a matter of fact, if the deposition causes a deformation of the molecular structure, the bond lengths between the central metal and the four surrounding nitrogen are altered and, as a consequence, the nitrogen peak is broadened. A feature that is not detected for this sample. Indeed, the interaction between gold and CoPc is mainly due to weak interactions, like van der Waals forces, thus is very unlikely that the molecules are deformed. The weak interaction does not exclude an interface charge transfer, as a matter of fact, a slight shift of 0.2 eV toward higher binding energies is detected, which can be

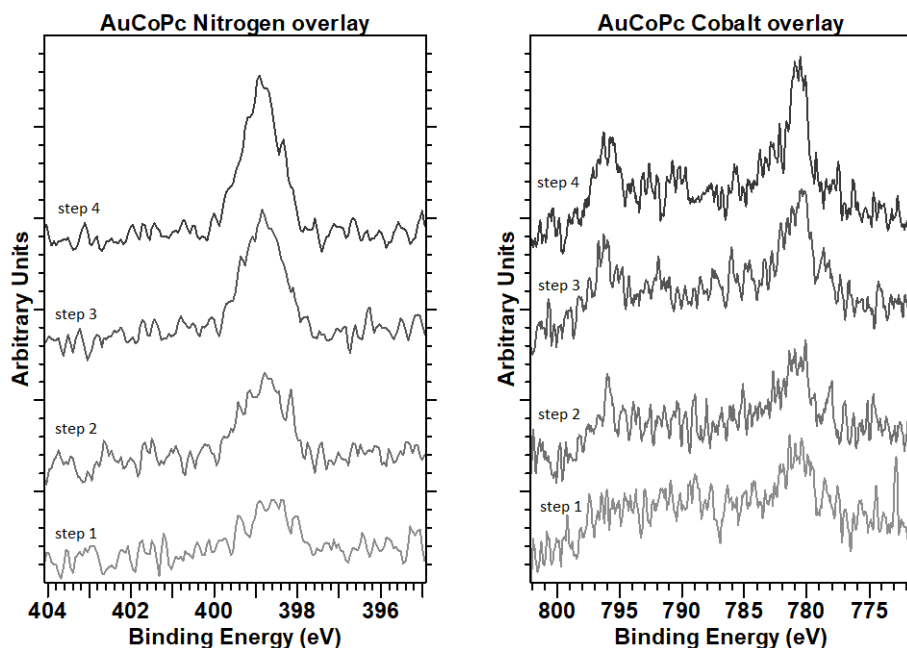


Figure 8.11. Nitrogen N_{1s} and cobalt Co_{2p} peaks of the Au/CoPc sample measured after each deposition step.

connected to positive charging of the nitrogen atoms after the adsorption.

From the UPS spectra the fundamental electronic quantities, like the work function and the HOMO level of the organic layer, are directly measured and they are collected in table 8.1. All the quantities in the tables are referred to as binding energies, thus a positive value means below the Fermi level. Moreover, there is an instrumental shift between the sample and the detector, as a consequence, the Fermi edge is not exactly at zero, but it is slightly shifted toward higher BE. Usually, after the deposition of organic molecules, the Fermi edge is no more visible, and the features of the molecules became more relevant, like the HOMO level. The fact that after the fourth deposition step, the Fermi level is still detected, gives us information on the thickness of the organic film, which is indeed much thinner than expected. The quantitative analysis will confirm this. All the values in the table are referred to the detector Fermi level, thus to calculate the work function ϕ of the system at each step, it is necessary to sum the cut-off energy and the Fermi edge. As already discussed in section 8.1, the ideal work function of pure gold is 5.1 eV, with slight variations depending on the crystal structure. The calculated value of $\phi_{Au} = 4.68$ eV is caused by the underlying chromium adhesion layer that alters the gold properties.

$\Delta\phi$ indicates the shift of the work function with respect to the bare gold reference after every deposition. As expected, the adsorption of CoPc reduces the work function of the system mainly due to the Pauli pushback effect, a repulsive interaction between the molecules and the metal that reduces the metal surface dipole. It is interesting to notice

that the energy shift of almost 0.55 eV happens right after the first deposition step, and then, with further deposition steps, no evident changes in the work function are observed. As a matter of fact, the Pauli pushback effect, and all the other mechanisms that occur at the metal/organic interface, depend only on the structure of the metal surface and the first organic monolayer. Thus, the additional deposition steps will not modify the interaction at the interface, indeed the work function is stable at $\phi = 4.15 \pm 0.05$ eV.

Table 8.1. Au/CoPc work function and work function shift at each deposition step.

Step	Cut-off (eV)	Fermi edge (eV)	ϕ (eV)	$\Delta\phi$ (eV)
0	4.52	0.16	4.68	/
1	3.97	0.17	4.14	0.54
2	3.93	0.23	4.16	0.52
3	3.90	0.19	4.09	0.59
4	3.95	0.19	4.14	0.54

The absence of additional features close to the Fermi edge after the first deposition processes, confirms the absence of chemical bonds and consequent charge transfer that can partially populate the LUMO level of the molecule. However, the slight reduction of the Fermi edge during the deposition may be caused by the occupation of the hybrid states, with energies within the HOMO-LUMO gap, that are generated as a consequence of the metal/organic interaction. With the UPS analysis, the characteristic features of the organic layer can be determined mainly from the energy and shape of the HOMO level. The HOMO intensity is proportional to the number of molecules on the substrate, thus thicker the layer, the more accurate the results. Thus, for the first two deposition steps, the HOMO peak is comparable to the background noise, and a proper measure is not provided.

However, with the successive analysis (step 3), the sharp HOMO peak at an energy of -1.45 eV with an FWHM of 0.54 eV is detected. Then, after the last deposition, the HOMO is slightly shifted towards lower energies and becomes less broadened. The presence of a well-defined HOMO level indicates that the cobalt phthalocyanine builds an organized structure on the gold surface, on the contrary, in the case of an amorphous material, the peak is broadened over a large energy interval. An FWHM of 0.5 eV indicates that the molecules nucleate forming organic grains with different orientations. The result is not surprising since the metal substrate is a rough polycrystalline gold. However, for a deeper analysis, other techniques are required, like XRD or Angle-Resolved XPS. In table 8.2 are collected the features of the HOMO peak just for step 3 and 4. In order to compare the experimental results with the simulations, it is more useful to measure the HOMO onset, rather than the HOMO peak, however, the low intensity of the signal makes the measurement challenging. Anyway, a value of -1.2 ± 0.05 eV is obtained for the final structure. Finally, from the obtained data we can build the energy band diagram of the interface, which is shown in figure 8.33.

Table 8.2. Energy features of the HOMO level of a CoPc thin film.

Step	HOMO (eV)	FWHM (eV)	Onset (eV)
3	-1.45	0.54	-1.1
4	-1.49	0.49	-1.2

8.2.2 Quantitative analysis

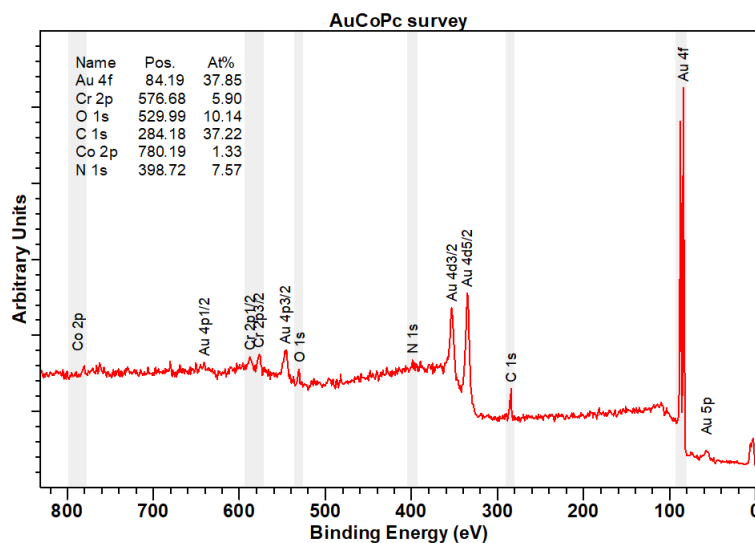


Figure 8.12. XPS survey of AuCoPc after step 4, at the maximum amount of deposited material. In the legend are collected the atomic percentage estimates of the different elements present at the surface.

Figure 8.12 shows the complete survey spectrum of the Au/CoPc sample after the final deposition. The binding energies are up to 800 eV because for higher values, up to 1486.6 eV, there are no characteristic peaks of the elements that compose the surface. For each element of the surface are indicated the binding energies of the main peaks, which are also highlighted by the grey regions. In addition, the atomic percentage of the surface elements is calculated from the peak intensities, by taking into account the Relative Sensitivity Factors (RSF) of each peak, which are already provided by *CasaXPS*. The atomic percentages of carbon, cobalt, and oxygen are respectively 37.22 %, 1.33 % and 7.57 %. These values reproduce almost perfectly the stoichiometry of the CoPc molecule, which, indeed, is made of 32 carbon, 8 nitrogen, and a single central cobalt atom. The resolution of a full spectrum is lower than the single peak analysis, therefore, the quantification of very small peaks is less accurate, still, it can be used to discuss the surface composition. Concerning the substrate elements like gold, oxygen, and chromium, the same intensity ratios of figure 8.9 are obtained once again, as a matter of fact, the substrate should keep

its structure during all the deposition and analysis processes.

As shown in figure 8.9, the intensities of both gold and oxygen peaks are slightly reduced after each deposition step, since the deposited organic layer becomes thicker and thicker. Thus, covering the substrate with molecules will limit the amount of photoemitted electrons characteristic of the substrate elements. On the other hand, after each step, the peaks associated with the elements composing the molecule become more and more evident. As a matter of fact, from the reduction of the gold Au_{4f} main peak, an estimate of the thickness of the deposited organic layer can be obtained, by exploiting the Lambert-Beer equation ???. The calculation takes into account an approximation of the mean free path of the electrons as a function of their kinetic energy, which is directly extracted from the position of the main gold peak $Au_{4f}7/2$, the density of the deposited molecules, which is $\rho = 1.667 \text{ g/cm}^{-3}$, and finally the ratio between the peak intensities before and after the deposition. By inverting the Lambert-Beer equation the thickness d is obtained. However, a crucial assumption of this method is that the deposited layer is homogeneous, which limits the applicability of the method. Uniformity is a quality that a thin organic layer deposited on a polycrystalline and rough gold substrate (8.3) is difficult to achieve. The graph in figure 8.13 displays the estimated thickness of the CoPc layer, at each deposition step, calculated with three different mean free paths approximations.

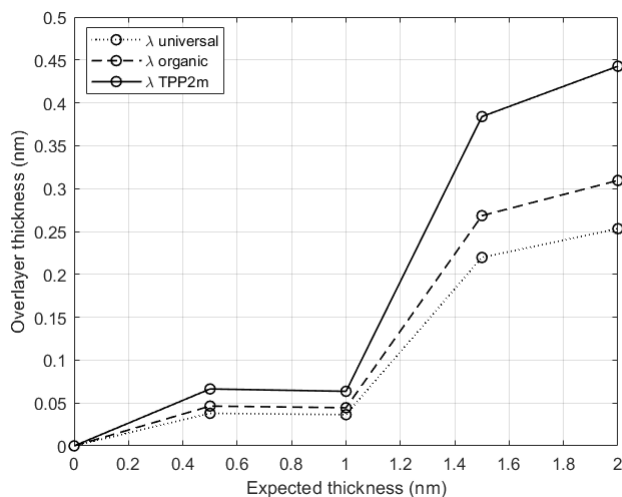


Figure 8.13. Estimate of the CoPc overlayer thickness through the Lambert-Beer law by using three different approximations of the electron mean free path.

It is evident that the calculated amount of deposited molecules is much below the expectations. The red and yellow lines use an analytical expression for the mean free path, however, the former is the less accurate since it does not consider the density of the CoPc, but it is universal for any overlayer (organic and oxides). Both approximations tend to underestimate the mean free path, which is respectively $\lambda_{uni} = 2.0225 \text{ nm}$ and $\lambda_{org} = 2.4714 \text{ nm}$, better results are usually obtained through the TPP2m approximation (solid line) with $\lambda_{TPP} = 3.535 \text{ nm}$. The thickness of the organic layer after two deposition

steps is below 1 Å, then the curve jumps to almost 4 Å after the third step with a small amount of additional deposited molecules during the final process. According to this graph, three over four deposition processes were a failure, since only the third one causes an increase of the layer thickness of 0.4 nm. However, the interpretation of these data may be misleading. As said before, an assumption of the Lambert-Beer method is the homogeneous coverage of the substrate which is far from the layer that is deposited, that rather is characterized by an island growth. In the following, by combining the data concerning the reduction of the gold peaks with the increasing intensities of the peaks characteristic of the CoPc, a more complete discussion on the layer growth and structure is provided.

By combining the peak intensities of both the substrate and the organic thin film a more accurate estimation of the layer thickness can be calculated. By analyzing the intensities of the CoPc characteristic peaks of carbon, nitrogen, and cobalt, it is observed that they increase in a linear fashion during the whole deposition process. The evolution of these peaks is interesting for the quantitative analysis of the sample, in particular, to determine the amount of deposited material at each step. The previous step-like results, shown in figure 8.13, are in contradiction with the linear evolution of the CoPc signals. As a matter of fact, a linear behavior indicates that the amount of deposited material is almost the same at each step. More accurate results of the film thickness can be obtained by exploiting the Hill method (??) or equation 6.15, which, differently from the Lambert-Beer method, depends on both the substrate and molecular peak intensities. However, there are some issues that make the evaluation more challenging. Firstly, the exact calculation of the deposited layer thickness requires the evaluation of the gold Au_{4f} and carbon C_{1s} attenuation lengths λ_s and λ_o . These quantities are connected to the mean free path, but they also take into account the elastic scattering of the electrons, thus they are a function of the electron kinetic energy and also depend on the experimental setup. Nevertheless, the mean free path can be used as an alternative at the expense of a higher uncertainty. Secondly, the more accurate methods require suitable reference signals for both the substrate and the molecule, which in our case could be gold Au_{4f} and carbon C_{1s} respectively. For the former, the peak of the bare gold substrate is perfect, but for the latter, the peak of the last deposition is not sufficiently pronounced, in fact, a thicker layer is necessary. In conclusion, these methods cannot be applied. However, a possible explanation of the different behavior of the substrate and molecular intensity peaks may be related to the type of growth model of the thin film, in particular, it can be associated with the island or layer plus island depositions, or more in general, in a non-uniform adsorption of molecules over the gold substrate. As a consequence, the sample surface is made by some regions covered with nucleated molecules and by exposed gold. The quantitative analysis of such a surface is a challenging task since both Lambert-Beer and Hill models require a homogeneous deposited layer, however, the steep increase of the CoPc layer thickness measured from the gold peaks after the third deposition step (8.13) may indicate that at that point, the full coverage of the gold surface is obtained, with no exposed gold regions. In addition, the lower increase after the last deposition may suggest a layer plus island growth, in this situation, after the deposition of the first monolayer, the molecules tend to nucleate around some energetically favorable spots, like defects of the organic lattice. Actually, the particular trend in figure 8.13 is not sufficient to determine

the growth mode of CoPc on polycrystalline gold because the non-uniform deposition may be caused by the roughness of the surface rather than the organic properties. A similar behavior is also obtained and discussed for the other two samples.

The previous considerations are just a hypothesis to explain the inconsistency of the XPS peaks, in fact, an exact quantitative analysis is not the main topic of this work and it is not strictly required. Nevertheless, it could be interesting to deeply investigate the XPS quantitative analysis of ultrathin films, because it could be an additional feature of the deposited layer that can be detected through XPS. The steep reduction of the substrate peak intensity during the deposition could indicate that the ultrathin layer has completely covered the substrate and this can be relevant during the fabrication of specific devices.

8.3 ZnPc on polycrystalline Au

The same qualitative and quantitative analyses are performed also for the ZnPc deposited on polycrystalline gold. For this specific sample, the number of deposition steps is seven, almost double with respect to Au/CoPc. As previously, at each step, a layer of 0.5 nm has been deposited through thermal PVD, in a high vacuum chamber, at a pressure of 2×10^{-6} mbar. The temperature of the source was around 350 °C with a deposition rate of 0.03 Å/s, which was monitored through a quartz crystal microbalance. From the analysis of the first steps, we are able to investigate the metal/molecule interface and study the different mechanisms that arise due to the adsorption. As a matter of fact, from the XPS and UPS spectra collected during the process, the reduction of the work function, mainly caused by the pushback effect, can be directly measured. Moreover, by studying the binding energy shifts of the characteristic peaks of ZnPc, information about the charge transfer between metal and molecule, the screening effect and the rearrangement of the molecular structure can be obtained. Moreover, the last deposition step add 3.0 nm to the organic overlayer rather than 0.5 nm, reaching a total thickness of 6.0 nm. From a thick layer, the characteristic features of the organic material are highlighted, mainly from the XPS analysis of the carbon C_{1s} peak, and from the features of the HOMO level. Further details on the deposition procedure are provided in section 7.2 and the steps are collected in table 7.1.

8.3.1 Qualitative analysis

The very first information that we can extract from the gold Au_{4f} peak is related to the type of adsorption mechanism of the ZnPc over the gold substrate. The chemisorption is a strong interaction that requires the formation of chemical bonds between the gold atoms and the molecule, as a consequence, there is a charge transfer between the two materials, and, in some cases, the molecule is also deformed. All these mechanisms cause a chemical shift in the elements involved in the bond. Therefore, the fact that the binding energy of the gold peak is the same before and after the first deposition step and that it does not change during the whole process, clearly indicates that the ZnPc molecules are physisorbed on the gold surface and that no chemical bonds are built during the adsorption. The stable evolution of the gold Au_{4f} peak is shown in the left panel of

picture 8.14: it is characterized by a main peak at 84.04 ± 0.02 eV and a secondary peak shifted towards higher bindings energies of 3.68 eV, caused by the spin-orbit interaction. The very slight variation of the binding energy is comparable with the resolution of the instrument. The result is not surprising, indeed gold is a noble metal, and chemical bonds are very unlikely. Moreover, an additional proof, that excludes chemisorption, is obtained from the analysis of the relative shift between the carbon C_{1s} main peak, related to the sp^2 hybridization characteristic of the benzene rings, and the C-N peak.

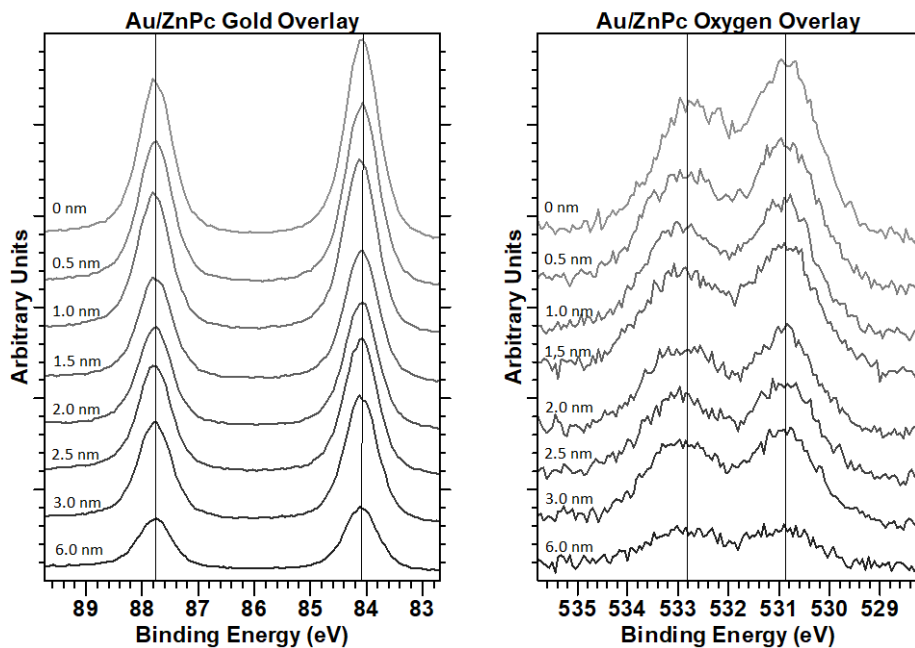


Figure 8.14. Gold Au_{4f} and oxygen O_{1s} peaks of the Au/ZnPc sample measured after each deposition step, indicating the expected thickness of the layer.

The oxygen O_{1s} is characterized by two peaks, the main one at a binding energy of 530.85 ± 0.05 eV and the secondary peak at 532.93 ± 0.03 eV. The first one is the general oxygen peak, whereas the other is the superposition of several chemical states that have comparable binding energies and are difficult to distinguish. However, considering the structure of the sample and the XPS database [77, 76], the peak takes into account the oxygen present in the silicon and chromium oxides underneath the gold, and the contaminations, thus C-O and C=O bonds. As shown in figure 8.14 (right panel), the oxygen peaks are subjected to a slight shift towards higher binding energies. However, the intensity of the effect is different for the two components. The main peak has a gradual shift of 0.1 eV, whereas the second one has a larger shift of 0.2 eV after the first deposition, then the position is almost fixed after the successive depositions. The fact that there is a significant shift after the first deposition indicates that additional mechanisms are involved during the adsorption of ZnPc on Gold. However, a hypothesis is connected

to the adventitious carbons. The fact that the gold peak is unaffected by the adsorption, excludes chemical bonds between the metal and the molecule, and even more so the oxides, buried in the substrate do not interact with the molecules. The other component of the secondary peak is from the carbon/oxygen bonds of the contaminations at the surface, which, are weakly bound to the metal and their binding energy is sensible to the interface dipole described by the pushback effect. As a consequence, the respective peak is shifted towards higher binding energies. The same effect is also considered in the fitting of the carbon C_{1s} peak as discussed in the following.

For this specific sample, the analysis of the carbon C_{1s} peak is particularly challenging, because of the high amount of contaminations at the gold surface, that have not been successfully removed by the argon-ion etching. Figure 8.15 shows the huge adventitious carbon signal that can be decomposed into four components, typical of the contaminations. The main peak at 284.71 eV, proper of the C-C and C-H bonds, is followed by three peaks related to different oxygen bonds at binding energies of 285.45 eV, 286.48 eV and 288.71 eV, respectively for C-O, C=O and O-C=O chemical state [76]. As a consequence, especially for the first deposition steps, the carbon peaks characteristic of the ZnPc are almost covered by the adventitious carbon, thus worsening the accuracy of the analysis. On the contrary, for the thicker layer, the ZnPc features are clearly distinguishable, providing information on the structure of the organic thin film.

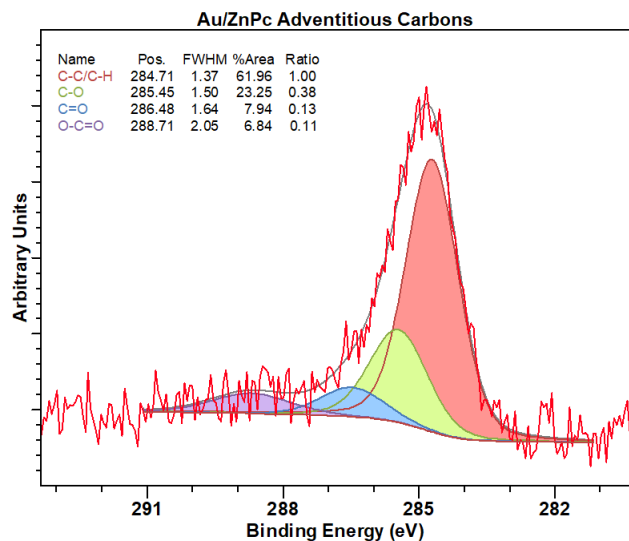


Figure 8.15. Carbon C_{1s} peak measured from the bare gold substrate. The signal originates from the adventitious carbon adsorbed at the surface that resisted the ion beam etching.

The information concerning the adventitious carbon C_{adv} measured before the deposition is fundamental to correctly analyze the successive photoemission spectra. The previous graph is used as a reference and, at each step, the contribution of the adventitious carbon to the total carbon spectrum should decrease. An estimation of the intensities of

these unexpected components is evaluated from the reduction of both gold and oxygen peaks, following the same trend. Moreover, the binding energy of the peaks is obtained by considering the dipole built at the interface, that shifts all the C_{adv} towards higher binding energies. The energy of the interface dipole is directly measured from the UPS spectra, by comparing the energy offsets before and after the deposition. The peak fittings of the carbon C_{1s} after each deposition step are collected in both panels of figure 8.16. Moreover, it is also possible to appreciate the evolution of each component. In particular, the red one refers to the sp^2 hybridization of the carbon composing the benzene ring, whereas the green one refers to the C-N bonds of the pyrrole groups. Both peaks are followed by their satellites, the blue and the purple peaks respectively. In addition, the orange curve represents the superposition of all the adventitious carbon components evaluated from the bare gold spectrum in figure 8.15.

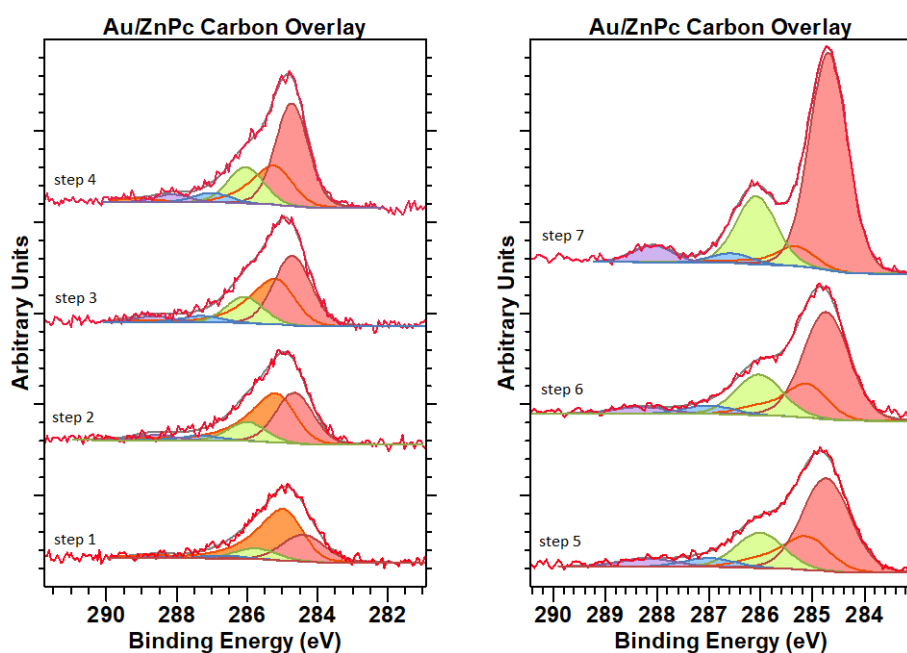


Figure 8.16. Carbon C_{1s} peaks of the Au/ZnPc sample measured after each deposition step.

The high amount of contaminations disturbs the analysis of the characteristic peak of the ZnPc, in particular, for the first and second depositions. The parameters of the characteristic components of the ZnPc are less accurate, thus making the investigation of the metal/molecule interface more challenging. However, from the third deposition, all the features of the organic layer are much more evident, thus providing information on the structure and morphology. All the spectra, except for the first one (step 1), are characterized by a main component at a binding energy of 286.70 ± 0.05 eV, with a slight decreasing behavior as the layer became thicker. The secondary peak has stable binding energy during most of the deposition process, and the chemical shift toward higher binding

energies is of 1.25 eV, with respect to the main peak. However, the energy separation measured from the last step is slightly higher and reaches 1.36 eV. Thus, denoting that something happens to the molecular structure while a thick organic layer is formed. The additional shift can be connected to a rearrangement of the molecules, or by a different charge transfer between the organic monolayer and the thin film. As already discussed in Au/CoPc, the charge transfer between gold and metal phthalocyanines is bi-directional, in the sense that the central metal atom and the carbon ring are both involved in the interaction with gold, but with opposite behavior. The zinc atom is positively charged, thus transferring electrons to the surface, whereas the carbon, especially the ones involved in the C-N bonds, receive electrons. Actually, due to the weak interaction, only fractions of electrons are transferred. This fact is also demonstrated by the *ab initio* simulations discussed in section 9.2.2, in par. The energies of the core electrons are thus affected by charge transfer, in particular, a reduction (increase) of the binding energy is measured for negatively (positively) charged atoms. Thus, since the C-N carbon atoms are negatively charged during the adsorption, their binding energy is reduced, and, since the charge transfer is more intense for the first monolayer and it fades out with the increasing distance from the gold surface, the C-N carbon atoms of the thin film are less charged, and their binding energies are slightly shifted towards higher values.

The satellite peaks start to be clearly distinguishable from the contaminations starting from the third deposition step. The binding energy shifts of both peaks with respect to their main component are not fixed during the whole deposition, but as the layer grows, the satellites move towards lower binding energies. Up to step 3, the energy separation is of 2.55 eV for both peaks, then it is reduced to 2.3 eV and reaches a minimum of 1.9 eV and 2.0 eV respectively after the last deposition. The displacement of the satellites can be attributed to the presence of adventitious carbon at the surface that can interfere with the adsorption, as a result, the molecular layer is less organized and the satellites are broadened on a wider energy range. On the contrary, for the last steps, the characteristic carbon C_{1s} components of ZnPc are prominent and the obtained values are close to previous works [32].

Particular attention is dedicated to the analysis of the carbon C_{1s} spectrum taken after the last deposition step, which is depicted in 8.17. In the legend are collected the features of each component, like the binding energy, the FWHM, and the intensity ratio, from which we can extract information on the structure and molecular organization of the organic thin film. The ratios between the ZnPc components are close to the expected, in particular, the C-N peak is 0.35 % of the main one, which is slightly higher than the ideal values due to shake-up processes, whereas the satellites are almost one-tenth of the main. The narrower broadening of the peaks, with respect to the previous steps, especially for the main one and the second satellite indicates that the molecules are well organised to form the organic thin film. In addition, the stacking of molecules is demonstrated by the high intensity of the satellite peak at 288.08 eV which is also connected to the resonance effects that are established when the benzene rings are vertically aligned. From the analysis of only the carbon peak is difficult to determine the molecular configuration (α , β or η) of the thin film. However, by analyzing the FWHM of the HOMO level (figure 8.18) and knowing that the gold surface is rough, it is probable that the thin film has several grains with different molecular orientations.

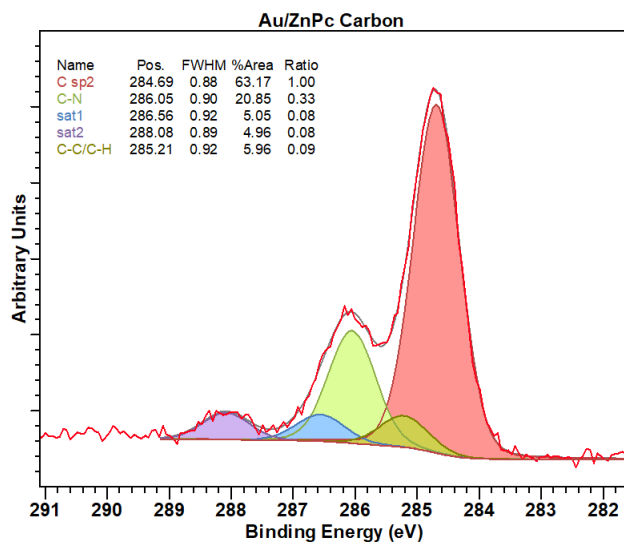


Figure 8.17. Carbon C_{1s} peak of Au/ZnPc after the final deposition step.

The analysis of the valence band allows further investigation of the metal/organic interface and the morphology of the organic layer. Figure 8.18 shows the evolution of the HOMO level with the deposition. From the UPS analysis of the bare gold surface (step 0), it is measured the shift of the Fermi level of 0.177 eV due to a non-ideal alignment between the sample and the detector. For the calculation, a linear interpolation is directly conducted in *CasaXPS* by using the *Step-Down* background type. The tail of the valence band edge is connected to the broadening of the Fermi function since the UPS is performed at a non-zero temperature. The Fermi offset is an experimental error that is identical for every measurement, thus all the energy values measured from the UPS must be corrected by using the non-zero Fermi level as a reference. In addition, the absence of additional features close to the Fermi edge at the early stages excludes an intense electron charge transfer from gold to ZnPc that populates the LUMO level, in accordance with the XPS analysis of C_{1s} .

As the amount of deposited molecules increases, the HOMO peak became more and more evident. The energy of the HOMO peak is equal to 1.70 eV up to the second to last measurement, then it is shifted towards a lower binding energy of 1.65 eV. In addition, the FWHM of the HOMO level is reduced during the process, reaching a final value of 0.518 eV. The low broadening of the peak indicates that there is a sort of organization of the molecules while forming the organic film, indeed, with such a value, the layer is characterized by many grains with a different molecular orientation. However, as already said, the most relevant quantity of the HOMO is not the energy of the peak, which is the result of a superposition of many curves, but the HOMO onset, which can be considered as the edge of the HOMO band of the organic semiconductor. The onsets are calculated only for the last four steps, where the HOMO has a well-defined shape and it is no more

comparable to the background. The data are collected in table 8.3. The slight shift towards higher binding energies as the layer grows can be caused by a better organization of the layer and/or a different metal/organic charge transfer, which is stronger for the first monolayer, thus the molecules far from the interface are less negatively charged. The HOMO onset measured after the final deposition is of 1.19 eV, then, after the correction of the Fermi level, a value close to 1 eV is calculated. With such a value, we can conclude that the organic layer has an intrinsic behavior since the HOMO-LUMO gap of the ZnPc is close to 2 eV [22]. The valence band of the last UPS analysis shows interesting features up to 8 eV, as depicted in the right panel of figure 8.18. The three peaks at 1.65 eV, 3.8 eV, and 7.2 eV are respectively the HOMO, HOMO-1 and HOMO-2, which can be visible only for non amorphous systems.

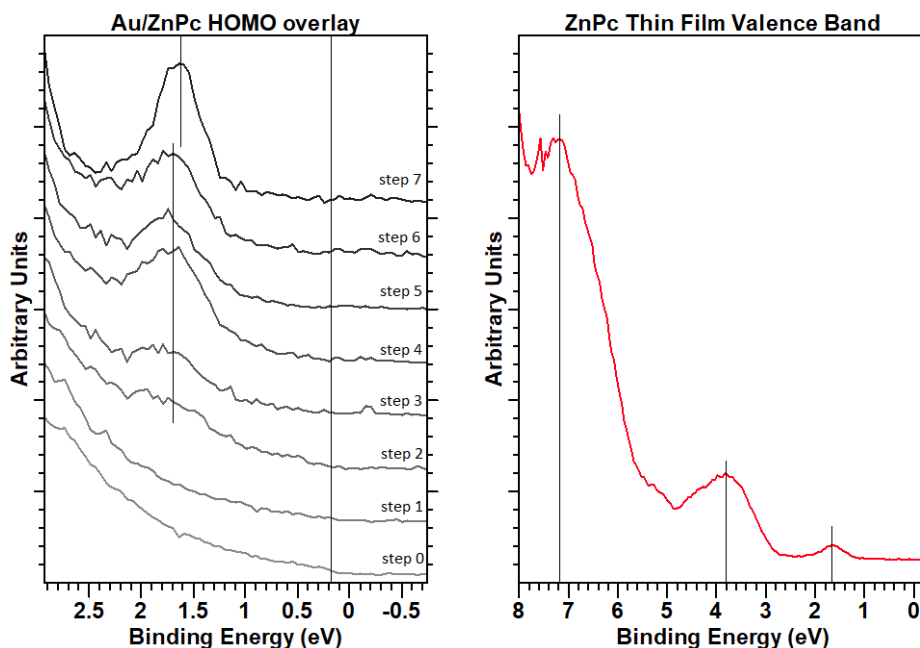


Figure 8.18. HOMO overlay and Thin film valence band.

The work function of the bare gold sample, which is directly measured from the cut-off energy of the UPS spectrum, is equal to 4.56 eV, due to the presence of the chromium adhesion. After the adsorption of the very first molecules, the work function is shifted toward lower values, as expected. The measures of the cut-off energies at each step are collected in table 8.3, where also the shifts with respect to the bare gold substrate are calculated. Different mechanisms may affect the reduction of the work function, and the identification is a challenging task. However, by combining the information gathered from UPS and XPS, which has been discussed previously, we can qualitatively picture the Au/ZnPc interface interaction. Indeed, since the charge transfer between metal and organic is low, the shift of the work function can be almost completely attributed to the

polarisation of the metal surface, caused by the Pauli pushback effect. A shift of 0.66 eV is measured just after the first deposition, which slightly increases as the layer becomes thicker, reaching 0.72 eV. The small correction of the work function may be caused by polarization screening [22]. With respect to Au/CoPc, the reduction of the work function is higher since the counter-effect caused by the positive charging of the central metal atom of ZnPc is lower, as demonstrated by the XPS analysis and *ab initio* simulations discussed in the following. The Work function of the thicker ZnPc layer is equal to 4.02 eV, this value takes into account the offset of the Fermi level, which adds 0.177 eV to the measured value. With the quantities measured from the UPS spectrum, we are able to draw the band diagram of the Au/ZnPc interface 8.33. The data concerning the LUMO band of the organic material are taken from another work [22], which shows very similar results.

Table 8.3. Au/ZnPc UPS results. The value indicated by (*) is the offset of the Fermi level measured from the UPS of step 0. All the values are referred to the zero energy of the detector. The missing data are due to the low signal.

Step	Cut-off (eV)	$\Delta\phi$ (eV)	HOMO (eV)	FWHM (eV)	Onset (eV)
0	4.56	/	/	/	0.177(*)
1	3.91	0.65	/	/	/
2	3.92	0.66	/	/	/
3	3.87	0.69	1.68	0.83	0.95
4	3.83	0.73	1.68	0.74	0.99
5	3.85	0.71	1.70	0.69	1.07
6	3.84	0.72	1.70	0.69	1.06
7	3.84	0.72	1.64	0.52	1.19

8.3.2 Quantitative analysis

In figure 8.19 are plotted the complete XPS survey of the sample before and after the deposition process, thus showing the features of the bare gold surface (on top) and of the organic layer (at bottom). In the legends are collected the data about the binding energies of the most relevant peak for each element and the respective atomic percentage, calculated by dividing the intensity of the peak by the respective sensitivity factor, as shown in table 8.4. In addition, some secondary peaks are labeled. The survey of the bare gold is similar to the one analyzed in section 8.1, however, here we can distinguish a carbon C_{1s} peak which indicates the high amount of contaminations at the gold surface that survived at the double solvent cleaning process and the ion beam etching. On the other hand, from the survey of the organic layer, the characteristic peak of the ZnPc molecules, in particular C_{1s} , N_{1s} , and Zn_{2p} are the most intense. In this case, the atomic percentages do not represent the stoichiometry of the ZnPc molecules, which are made of 32 carbon, 8 nitrogen, and a single zinc. However, a quantitative analysis based only on these quantities is affected by a large error, since an unknown fraction of the peak is dispersed in satellite peaks, which are indistinguishable from the background noise. Moreover, topographic samples may cause shadowing effects that alter the measurements. For metal/organic structures,

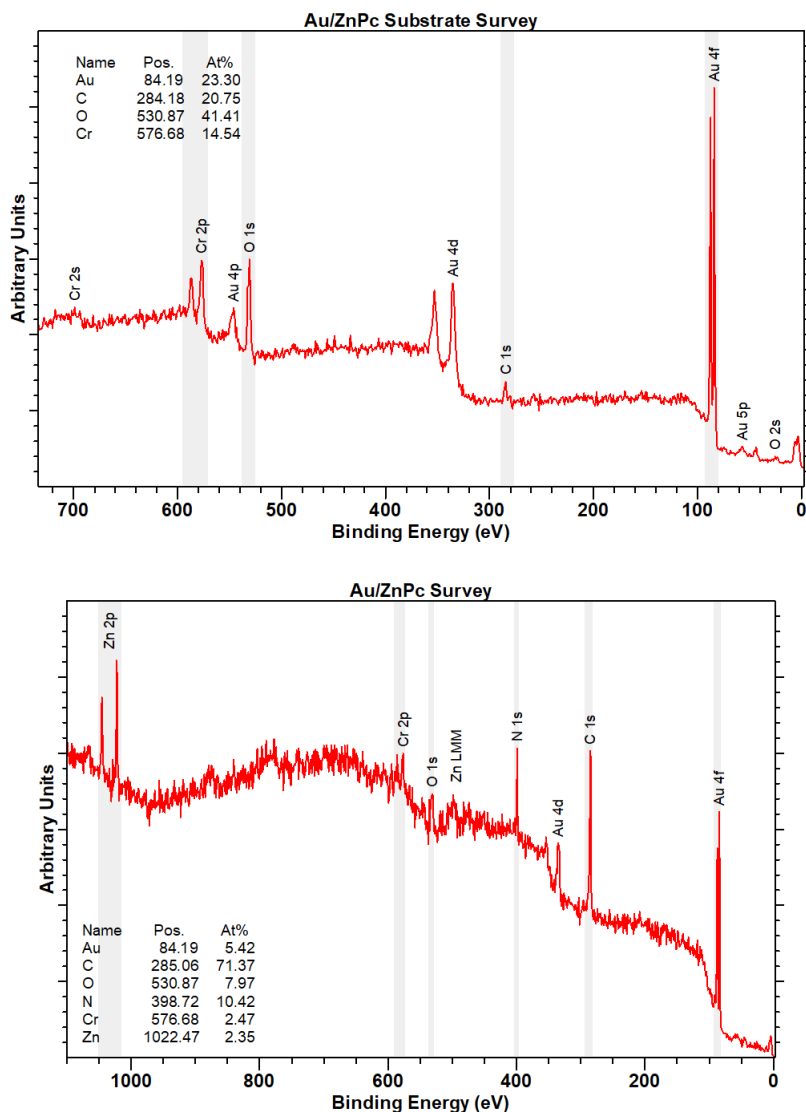


Figure 8.19. Full survey spectrum of Au/ZnPc before (top) and after (bottom) the deposition process. The first spectrum is plotted up to 730 eV since no characteristic peaks are detected for higher BE.

the error in determining the atomic concentration can reach the 40%, without a proper reference material. As a matter of fact, the full survey spectrum is used just to identify the elements composing the surface, nevertheless, it is always required for a complete analysis.

By comparing the full spectrum of the bare gold in figure 8.19, with the one of the Au/CoPc sample depicted in figure 8.1, we notice that the amount of chromium in is

much higher in Au/ZnPc. The reason for that is the diffusion of the chromium atoms due to the annealing during the preparation of the sample. Thus, the chromium and the relative oxide move toward the surface, and the respective XPS peaks are more intense. Indeed, the secondary peak of oxygen O_{1s} , which is connected to chromium oxide, is more intense in the Au/ZnPc sample. In any case, the absence of any sharp silicon peak and the presence of all gold peaks exclude high damage to the gold surface due to annealing.

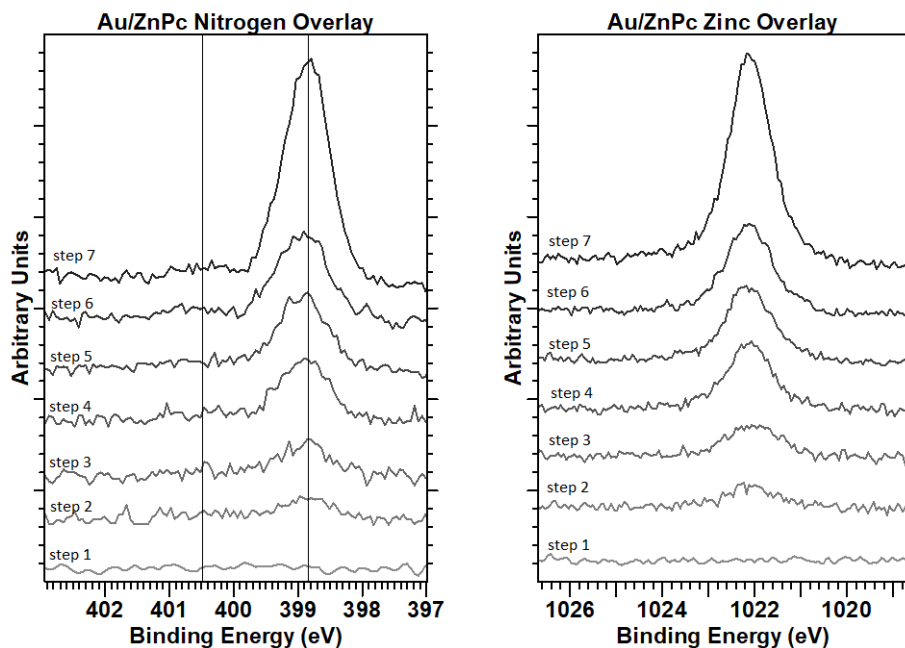


Figure 8.20. Nitrogen N_{1s} and zinc Zn_{2p} (primary) peaks of the Au/ZnPc sample measured after each deposition step.

The analysis of the last two characteristic peaks, namely N_{1s} and Zn_{2p} , is shown in figure 8.20, in which are collected the local spectrum after each deposition, from the bottom to the top. N_{1s} is characterised by a main peak at 398.90 ± 0.03 eV followed by a satellite peak shifted of about 1.6 eV toward higher binding energies. Other satellite peaks at even higher energies could be individuated around 403 eV and 405 eV, but their intensities are so low that they are almost indistinguishable from the background noise. Interesting to notice that the intensity of the main peak grows almost linearly with the deposition, whereas the variations of the first satellite are much lower, and the intensity is kept almost fixed during the deposition. The satellite peaks may have originated from resonance effects that arise in the organization of the organic layer, however, further analysis with other instruments, like atomic force microscopy (AFM), X-ray diffraction analysis (XRD), or angle-resolved XPS (ARXPS), should highlight the structure of the organic layer. Nevertheless, from the relatively low FWHM of the main nitrogen peak, which is equal to 0.84 eV at the last step, we can conclude that there is an organization

between molecules that improves with the deposition. Concerning the evolution of the zinc $Zn_{2p_{3/2}}$, nothing interesting happens, except for the almost linear increase of the intensity, as shown in figure 8.20. An intense interface charge transfer between gold and zinc is not expected, thus the binding energy of the zinc peak should not vary as a function of the layer thickness.

The XPS analysis of the first deposition step is quite strange, especially for nitrogen and zinc peaks. As is shown in the figure 8.20, at step 1, the peak is almost completely covered by the background noise. Moreover, the peak fitting of the carbon in figure 8.16 reveals that the amount of deposited material is very low, indeed the ZnPc components are still covered by the adventitious carbon. In conclusion, after the first deposition step, the amount of ZnPc molecules adsorbed at the gold surface is much lower than expected. Alternatively, it is also possible that the source was not sufficiently purified during the preparation steps, as a matter of fact, during the evaporation, both ZnPc and its fragments, like benzene and pyrrole rings, were deposited on the gold surface, explaining the higher increase of the carbon peak with respect to nitrogen and zinc.

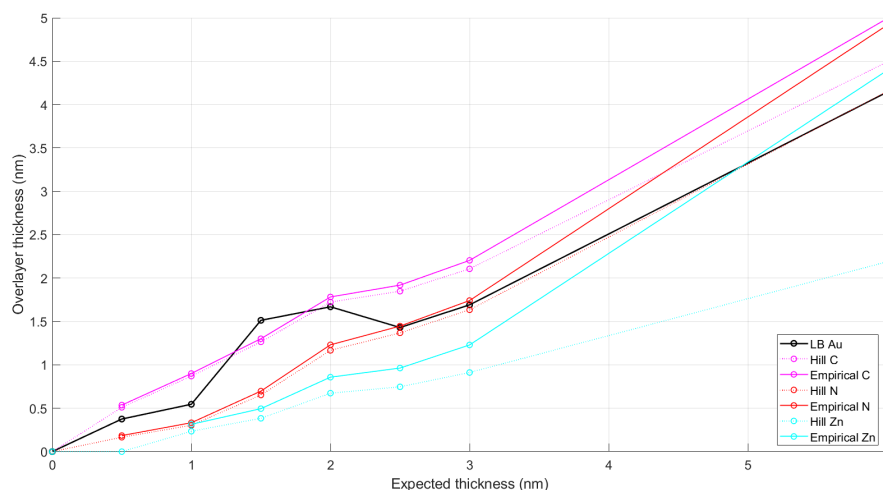


Figure 8.21. Comparison of the estimation results of the ZnPc overlayer thickness obtained through different methods and by considering different XPS signals.

An estimation of the organic thin film thickness at each step, based on the intensities of the main peaks is performed. The results are shown in figure 8.21. In the graph are plotted several curves, which have been calculated through different methods presented in 6.2.7, by referring to the specific XPS elemental peaks. All the methods for the overlayer thickness estimation are based on some assumptions, which are the exponential decay of the electron intensity with respect to the distance traveled through a material, the substrate must be flat, the thickness of the overlayer must be uniform and that the electrons have the same effective attenuation length, independently from their kinetic energy. The analyzed sample does not show the previous characteristic: the gold surface is rough and the deposited organic layer, especially in the first deposition steps is far from uniform. Moreover, for the

calculation of the thickness I used the electron mean free path, obtained from the TPP2m method rather than the effective attenuation length, as a consequence, the thickness is overestimated. The adopted parameters are collected in table 8.4. As a matter of fact, the thickness results are just approximations of the real thickness of the overlayer, indeed, the aim is not to provide a precise quantification of the layer but rather to discuss some trends and features of the organic film. Further details on the adopted methods are discussed in section 6.2.7.

Table 8.4. Parameters used for the calculation of the overlayer thickness.

Element	Orbital	E_{kin} (eV)	IMFP (nm)	RSF
Au	4f 7/2	1402.0	3.499	9.58
C	1s	1201.9	3.095	1
N	1s	1087.7	2.860	1.8
Zn	2p 3/2	464.5	1.508	18.92

The least accurate method for the calculation of the overlayer thickness is based on the Lambert-Beer equation (6.11). This method requires all the previous assumptions, thus it fails for the quantification of very thin layers, moreover, it considers the reduction of the substrate peak intensity due to the increasing deposition of organic material only. The result is shown by the black curve, which is characterized by a non-linear behavior, but, on the contrary, there is a strange behavior for the third and fourth steps, due to a surprisingly high reduction of the gold peak intensity. This peculiarity, unique for this curve, can be associated with the condition of full coverage of the gold surface. In the initial stages, the low amount of adsorbed molecules, combined with the roughness of the gold surface, the island growth of the organic material and even shadowing effects cause non-uniform deposition, thus there are regions covered by the organic material and other regions with exposed gold, characterized by a higher electron emission that make the quantification unreliable. Nevertheless, further investigations of this aspect should be conducted in future works, with a focus on the quantification of organic ultrathin films. The other curves are associated with quantification methods based on organic and substrate signals. The solid and the dashed curves are the results of different methods, respectively the Hill equation (6.14) and the empirical equation (6.16) [75]. Both methods combine the intensities of $Au_{4f7/2}$ and the molecular orbital taken into account (C_{1s} , N_{1s} or $Zn_{2p3/2}$), however, the second one consider the dependency of the effective attenuation length of the electron with respect to the electron kinetic energy. The applications of the Hill equation are limited, since it requires that substrate and deposited material have energetically close emission peaks. All three couples of curves have an almost linear behavior, thus, at each step, the amount of deposited material is more or less the same, with little process variability. That's the most important result we can extract from this rough estimation of the organic layer thickness. However, we can further analyze the data and notice that, as expected, the Hill equation fails in the calculation using the zinc peak, since the energy difference between the electron kinetic energies is almost 1000 eV. The Lambert-Beer method gives results comparable to the more accurate methods for thick layers, still, it seems to underestimate the value. The choice of the organic peak has a

huge impact on the result, which can differ up to 1 nm, this shift is mainly caused by two aspects: the non-perfect peak fitting, especially with carbon, which has a contamination component, that alter the intensities of the peaks, and the use of IMFP rather than the EAL, which depends also on experimental parameters, that overestimate the thickness. Anyway, with the adopted parameters, all the results are credible, none of them exceed the expected thickness of the layer, and provide a reasonable estimation of the organic layer thickness.

8.4 MgPc on polycrystalline Au

The last sample that we investigated consists of MgPc deposited on polycrystalline gold. Thanks to the better knowledge of the deposition process, we avoid accidentally altering or even damaging the powder source, as a consequence, the step-wise deposition process can be conducted up to nine steps. As for all the analyzed samples, at each step, a layer of 0.5 nm has been deposited through thermal PVD, in a high vacuum chamber, at a pressure around 2×10^{-6} mbar. The evaporation temperature of the source is close to 350°C , allowing a deposition rate of 0.03 \AA/s , which was monitored through a quartz crystal microbalance, accurately positioned. As for the Au/ZnPc sample, additional depositions of thicker layers are performed to highlight the characteristic XPS features of the organic material, the last deposition adds 3.0 nm, following two depositions of 1.5 nm. All the details are collected in table 7.1. The expected thickness of the final layer is of 10.5 nm, and, the final XPS data are used as a reference for the qualitative and quantitative analysis of the previous steps. From the analysis of an almost monolayer, we are able to investigate the metal/molecule interface and study the different mechanisms that arise due to the adsorption. The UPS spectra clearly show the reduction of the work function, mainly caused by the pushback effect and a slight charge transfer. Moreover, by studying the binding energy shifts of the characteristic peaks of MgPc, information about the charge transfer between metal and molecule, the screening effect and the rearrangement of the molecular structure can be obtained. As for Au/ZnPc the substrate has been annealed before the introduction to the vacuum system, moreover, it is also heated to a temperature of 60°C during each deposition, in order to favor the diffusion of the adsorbed molecule and improve the quality of the thin film.

8.4.1 Qualitative analysis

As previously said, the shift of the binding energy of gold Au_{4f} peak is related to the type of adsorption mechanism of the MgPc. Consequently to the formation of chemical bonds between the metal and molecules, the chemical states of the surface gold atoms change, thus a shift in the binding energy of the core levels should be detected, between the XPS measurements before and after the deposition. In the left panel of figure 8.22 is represented the overlay of the gold Au_{4f} XPS spectra acquired after each deposition. The vertical lines highlight the fact that the energy of the peak is always the same during the whole process. The gold peak is characterized by a main peak at $84.07 \pm 0.02 \text{ eV}$ and a secondary peak shifted towards higher bindings energies of 3.68 eV, caused by the

spin-orbit interaction. The stable BE excludes that MgPc is chemisorbed on gold, but rather, the deposition is driven by weak van der Waals interactions. Anyway, even in the case of physisorption, a non-negligible charge transfer at the interface, between the two materials is possible and must be investigated, by analyzing the other peaks. Moreover, we do not expect a huge deformation of the molecular structure during the adsorption, but, as shown in the literature for most metal phthalocyanine, the molecules lay horizontally to the surface, slightly bent. This is also confirmed by the *ab initio* simulations discussed in the next chapter.

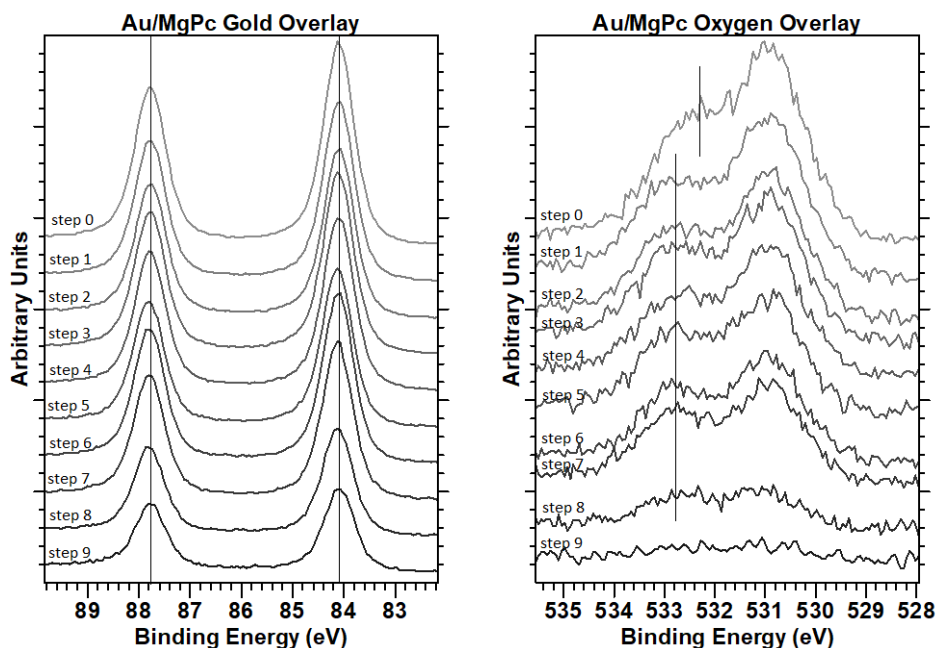


Figure 8.22. Gold Au_{4f} and oxygen O_{1s} peaks of the Au/MgPc sample measured after each deposition step.

Since the substrate was annealed, the oxygen O_{1s} peak shows the same features of Au/ZnPc. The peak is characterized by two components, the main one at a binding energy of 530.85 ± 0.05 eV, with slight variations at each step, and the secondary peak at 532.54 eV before the deposition, then it is shifted of about 0.3 eV toward higher BE just after the adsorption of the first molecules. As the layer gets thicker, the BE of the second peak is gradually reduced, reaching a final value of 532.68 eV. The energy separation between the two components increases to 1.8 eV. The main component is attributed to the general oxygen peak, whereas the other could be a superposition of several chemical states. One of them is characteristic of the C-O and C=O bonds present in the surface contaminations. Therefore, a possible explanation of the shift could be associated with the fact that the contaminations are loosely bonded to the metal, and their energy is sensible to the interface dipole that arises after the adsorption, which shifts the respective

electronic states toward higher binding energies. The same behavior is also detected for the carbon C_{1s} peak. The evolution of the oxygen peak is shown in the right panel of figure 8.22.

Contrarily to Au/ZnPc, the amount of contaminations that survived the cleaning processes was very low. Indeed, a short peak is measured from the full survey of the bare gold substrate (8.28), whereas a zoom is shown in the bottom curve of the left panel of figure 8.23 that collects the evolution of the C_{1s} peak, highlighting the different components. However, the non-negligible contaminations have to be considered for the analysis of the successive measurements and it must be included in the peak fitting. An estimation of the reduction of the adventitious carbon signal is obtained by following the same behavior of the gold and oxygen intensities during the step-wise process. On the other hand, the binding energy of the contaminations, which are affected by the energy shift caused by the interface dipole, is determined from the UPS spectrum. The colors in figure 8.23 are used to distinguish the carbon chemical state of the emitted electrons: the red one refers to the sp^2 hybridization of the carbon involved in the benzene ring, whereas the green one refers to the C-N bonds of the pyrrole groups. Both peaks are followed by their satellites, the blue and the purple peaks respectively. Finally, the orange curve encloses the two C_{adv} components associated with C-C/C-H and C-O/C=O bonds.

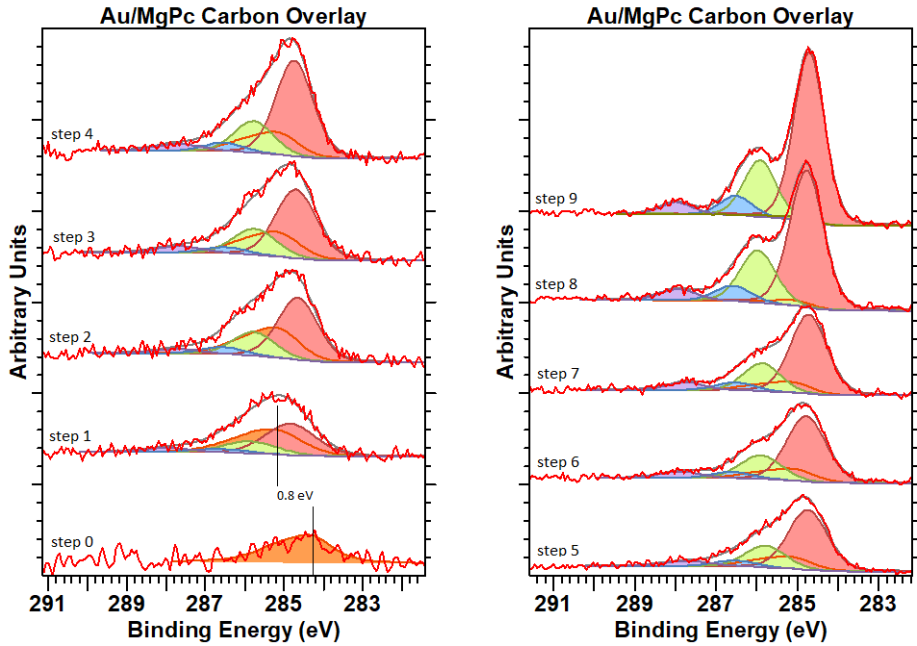


Figure 8.23. Carbon C_{1s} peaks of the Au/MgPc sample measured after each deposition step.

The peak fitting for all the spectra, except for the first one on the bottom left, is composed of five components, four of them are characteristic of the adsorbed MgPc, and the remaining one is associated with contaminations. Obviously, the spectrum obtained

from the bare gold substrate, the first one, shows only the latter. The spectra share some common features and, in addition, a sort of trend in the evolution of the binding energies of the MgPc peaks is measured. The intensity ratio between the main peak and the C-N is a little higher than the ideal value of 3:1, which can be explained by shake-up processes. However, as the layer grows, the ratio gets close to the ideal one, it starts from 40 % after the first two depositions, and then a better fit is obtained with a C-N peak of 35 % with respect the main one. Concerning the satellites, both the intensities are around one-tenth of the main one. The binding energy of the main peak is 284.75 ± 0.05 eV with slight variations at each step. However, the energy shifts of the satellites with respect to the main one are more interesting. The shift of the C-N peak gradually increases from 1.05 eV to 1.2 eV, thus it is slightly moved toward lower BE. The main peak satellite, on the other hand, is always at 1.8 eV from the main one, whereas, the other satellite also moves toward higher energies. Initially, it has a shift of 1.9 eV from the C-N peaks, which increases to 2.05 eV. All these variations in the binding energies may be connected to the low, but still present, charge transfer between gold and molecules.

As a result of the interaction, the molecules are charged with a very low negative charge of fractions of electrons, but the magnitude of the transfer depends on the distance from the gold surface. The simulation about the charge distribution of the adsorbed molecule (9.11) shows that the carbon atoms involved in the C-N bond are negatively charged, thus, the BE of the respective peak is lowered; the lower the charge transfer, the larger the shift to higher BE. For this reason, molecules farther from the gold are less charged, and the energy of the peak is lowered. Also for this sample, the measurements suggest that the layer is self-organizing and the order increases with the deposition. The FWHM of the main peak is of 0.89 eV for the last spectrum, denoting the presence of different molecular orientations, probably the island growth of the thin film generates several grains with proper features. The shapes of the satellites confirm the previous statement, indeed, they are sharp and clearly visible, in particular, the high intensity of the second satellite is due to resonance effects that arise when the benzene rings are stacked one over another, forming pillars of molecules. The organic layer is nano-structured. Figure 8.24 better shows the carbon spectrum of the organic layer, measured after the last deposition.

The nitrogen N_{1s} and magnesium Mg_{1s} spectra measured after each deposition are collected in figure 8.25, respectively on the left and right panel. The spectra relative to the bare gold substrate are not reported, since no peak is detected, as expected. Nitrogen is characterized by a main peak at 398.65 ± 0.05 eV followed by a secondary peak shifted toward higher BE of around 1.6 eV. Moreover, for some measurements, additional satellite peaks are detected at energies close to 403.5 eV and 405.5 eV. The origin of those peaks can be connected to the molecular organization, or to the excitation of other electrons during the emission. It is interesting to notice that the intensity of the secondary peak is more or less constant independent of the thickness of the organic layer. The explanation of this phenomenon is unknown and it requires additional investigations. A gradual shift of the main nitrogen peak toward higher binding is measured as the layer becomes thicker, the variations are small, as a matter of fact, the whole shift is of 0.1 eV, but they follow a sort of trend. It can be associated with a reduction of the charge transfer or deformation of the molecular structure following the organization. The same gradual shift is detected for the magnesium Mg_{1s} , but in this case is three times larger, reaching a maximum variation of

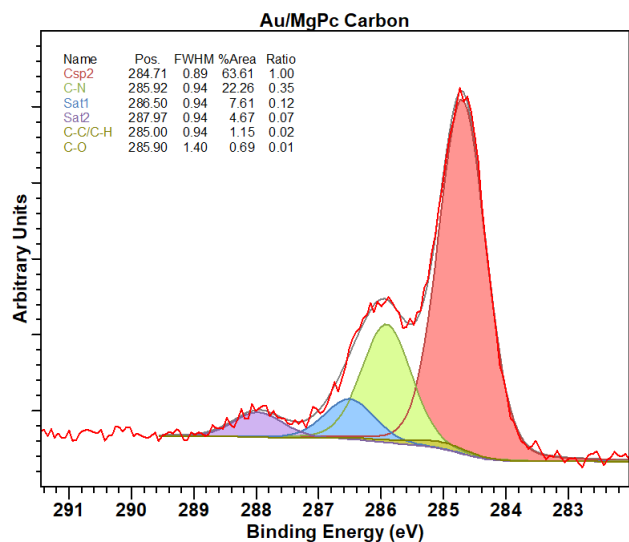


Figure 8.24. Carbon C_{1s} peak of Au/MgPc after the final deposition step.

0.3 eV. Likely, the reasons are the same. Through the overlay representation, the shifts previously discussed are highlighted.

From the UPS spectrum, highlighting the valence band of the structure, we can extract the most relevant electronic properties, moreover, additional information on the structure of the organic film is deduced. In figure 8.26 are collected the valence and edges measured after each deposition. It is possible to appreciate the HOMO level of the organic material, which becomes sharper as the thickness increases. As always, the analysis of the bare gold substrate is conducted to have a reference. Indeed, from the bottom curve in figure 8.26, the offset of the Fermi level with respect to the zero energy is measured, of about 0.155 eV. All the physical quantities, like the work function and the ionization potential, are evaluated with respect to the Fermi level as a reference. Thus it is crucial to take into account the energy shift caused by a non-ideal alignment between the sample and the detector. In table 8.5 are collected the measured values with respect to the zero energy. The cut-off energies and the HOMO onsets are determined by a linear interpolation of the spectrum performed with *CasaXPS* by selecting the proper background type. In particular, the *edge up/down*, whereas for the Fermi edge, the *step down* is used, since the UPS is conducted at non-zero temperature.

The very edge of the valence band provides information on the interface interactions, in particular, if there is a significant charge transfer between metal and molecules, we should detect some features at energies below 1 eV, which are connected to the population of originally empty molecular orbitals. However, as expected, no features are visible, confirming that the molecules are physisorbed and the charge transfer is weak, in accordance with the XPS results. In table 8.5 the HOMO energy refers to the position of the maximum of the interpolating curve, which has been fitted by selecting a *Tougaard*

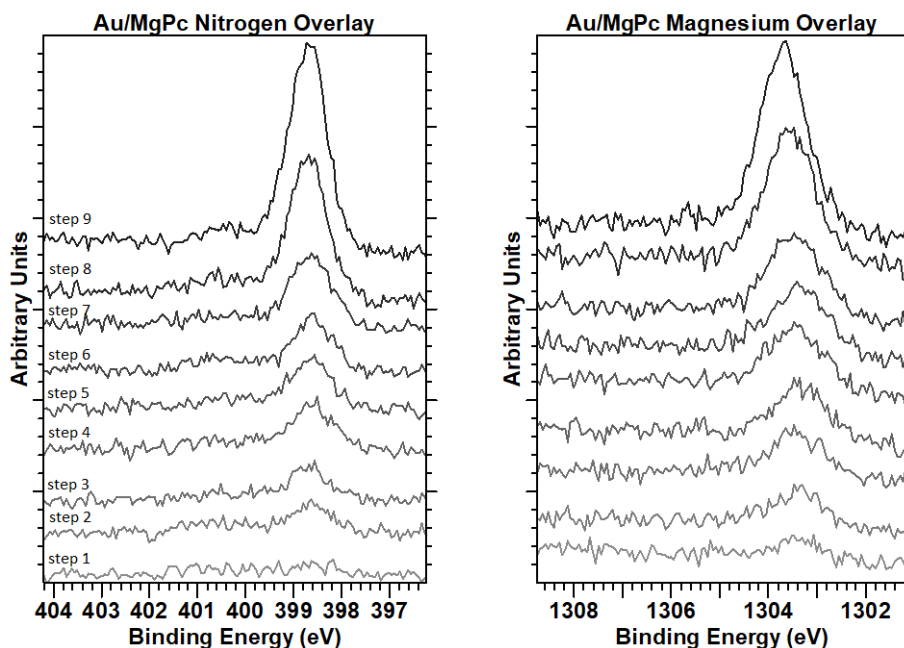


Figure 8.25. Nitrogen N_{1s} and magnesium Mg_{1s} peaks of the Au/CoPc sample measured after each deposition step.

background type, as usually do for low energy peaks. As the layer thickness increases, the peak becomes sharper and the estimations are more accurate. As a matter of fact, after the first deposition, the HOMO is not visible at all, but, surprisingly, just after the second deposition, the HOMO is well-defined with a low broadening. This indicates that the layer is well-organized. Compared to the Au/ZnPc samples, the HOMO is distinguishable from the background noise after more depositions. The reason is probably connected to the high amount of contaminations that worsen the quality of the monolayer. However, the crucial value used to build the energy band diagram is the HOMO onset, collected in the last column of the table, which indicates the real HOMO level of the molecules and can be compared to the simulation results. The onset shifts towards higher binding energies, thus moving away from the Fermi level, as the layer gets thicker. This is in accord with the theory and the previous results, and it is a consequence of the different charge transfer, that affects the molecular structure according to the so-called charging effect. Thus, a less-charged molecule has a larger HOMO-LUMO gap. As a matter of fact, in the final steps, the properties of the organic layer are less sensible to the interface, and they approach the bulk material. The HOMO-LUMO gap of MgPc cannot be determined, however, it should be comparable to ZnPc. With this assumption, we can conclude that the organic molecules have an intrinsic behavior since the Fermi level is in the middle of the energy gap. Figure 8.26 shows the evolution of the HOMO peak and the additional molecular orbitals that are visible after a few deposition steps. The peaks at 3.9 eV and

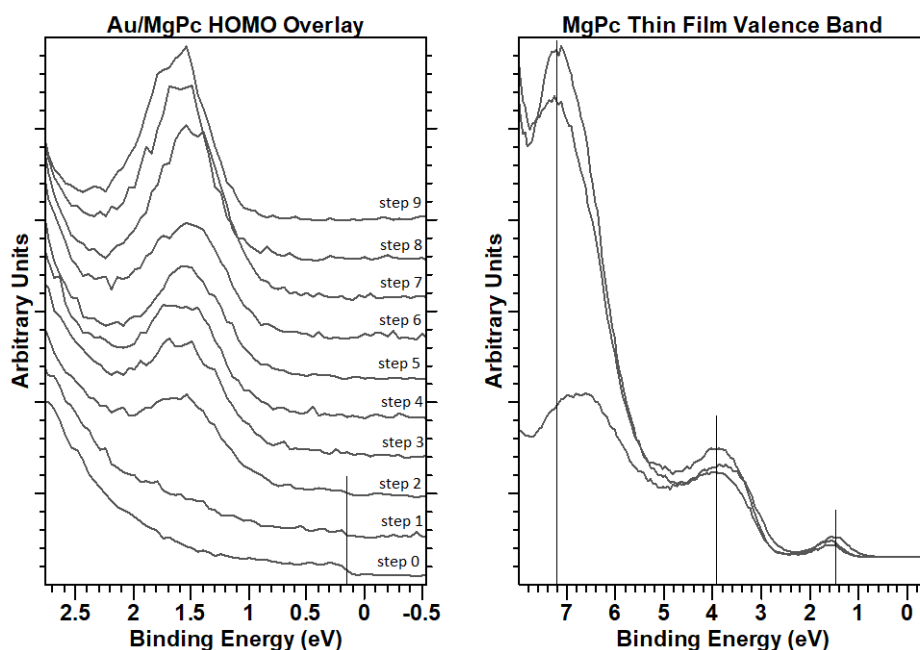


Figure 8.26. HOMO overlay and Thin film valence band.

7.2 eV are the HOMO-1 and HOMO-2. The latter shifts toward higher BE for the thick layer, nevertheless, the values are close to the ones of ZnPc, denoting similar electronic properties of the two organic materials.

Just after the adsorption of the first molecules, the interface dipole shifts down the work function of the system by a little more than 0.7 eV, as shown in table 8.5. Due to the previous considerations, the shift is mainly caused by the Pauli pushback effect and a minor contribution from the interface charge transfer. As a matter of fact, there is a slight increase in the work function for thicker layers, which can be once again attributed to the reduction of the charge transfer. To obtain the actual value of the work function, the cut-off must be corrected with the Fermi level offset, by summing the two quantities. The work function does not show a trend with respect to the film thickness, on the contrary, it appears that it reaches a stable value after a few steps, then it oscillates around 3.85 eV. As expected, the interface dipole does not depend on the thickness of the deposited organic layer.

8.4.2 Quantitative analysis

In figure 8.27 are plotted the complete XPS survey of the sample before and after the deposition process, thus showing the features of the bare gold surface (on top) and of the organic layer (at bottom). In the legends are collected the data about the binding energies of the most relevant peak for each element and the respective atomic percentage,

Table 8.5. Au/MgPc UPS results. The value indicated by (*) is the offset of the Fermi level measured from the UPS of step 0. All the values are referred to as the zero energy of the detector. The missing data are due to the low signal.

Step	Cut-off (eV)	$\Delta\phi$ (eV)	HOMO (eV)	FWHM (eV)	Onset (eV)
0	4.50	/	/	/	0.155(*)
1	3.77	0.73	/	/	/
2	3.79	0.74	1.56	0.78	0.85
3	3.82	0.68	1.54	0.74	0.85
4	3.86	0.64	1.55	0.70	0.88
5	3.86	0.64	1.52	0.68	0.86
6	3.83	0.67	1.52	0.73	0.87
7	3.82	0.68	1.50	0.66	0.91
8	3.87	0.63	1.59	0.59	1.08
9	3.85	0.65	1.62	0.61	1.07

calculated by dividing the intensity of the peak by the respective sensitivity factor, as shown in table 8.6. In addition, some secondary peaks are labeled. The bare gold surface shows a peak at 284.8 eV corresponding to the contaminations, however, in comparison to Au/ZnPc, the peak is much shorter and it does not interfere with the organic peaks of the successive measurements. On the other hand, from the survey of the organic layer, the characteristic peak of the MgPc molecules, in particular C_{1s} , N_{1s} , and Mg_{1s} are the most intense. In this case, the atomic percentages of these elements reflect the stoichiometry of the molecule, maybe the reason is related to the fact that we are analyzing the 1s orbital for each element. Nevertheless, a quantitative analysis based only on these quantities is affected by a large error, since an unknown fraction of the peak is dispersed in satellite peaks, which are indistinguishable from the background noise. The utility of the full survey spectrum is limited in the identification of the elements composing the surface, and it is always required for a complete analysis. As for Au/ZnPc, the annealing causes a diffusion of the chromium and oxygen atoms buried in the gold, as a result, the intensities of the respective peaks are increased. In particular, the second peak of O_{1s} is associated with metal oxides. No silicon is detected, meaning that there is no silicon oxide at the survey and that the effects of the annealing step are minor.

As for the previous sample, the large number of steps allows to estimate the thickness of the deposited organic film after each deposition, by analyzing the intensities of the main peaks. As for Au/ZnPc, three different methods of increasing accuracy are employed, the results are shown in figure 8.28. The line trait is used to indicate the method, whereas the color refers to the element exploited for the calculation, all the details are labeled in the legend. All the methods for the overlayer thickness estimation are based on some assumptions, which are the exponential decay of the electron intensity with respect to the distance traveled through a material, the substrate must be flat, the thickness of the overlayer must be uniform and that the electrons have the same effective attenuation length, independently from their kinetic energy. The analyzed sample, as all the structures analyzed in this thesis, does not show the previous characteristic, but the gold surface is

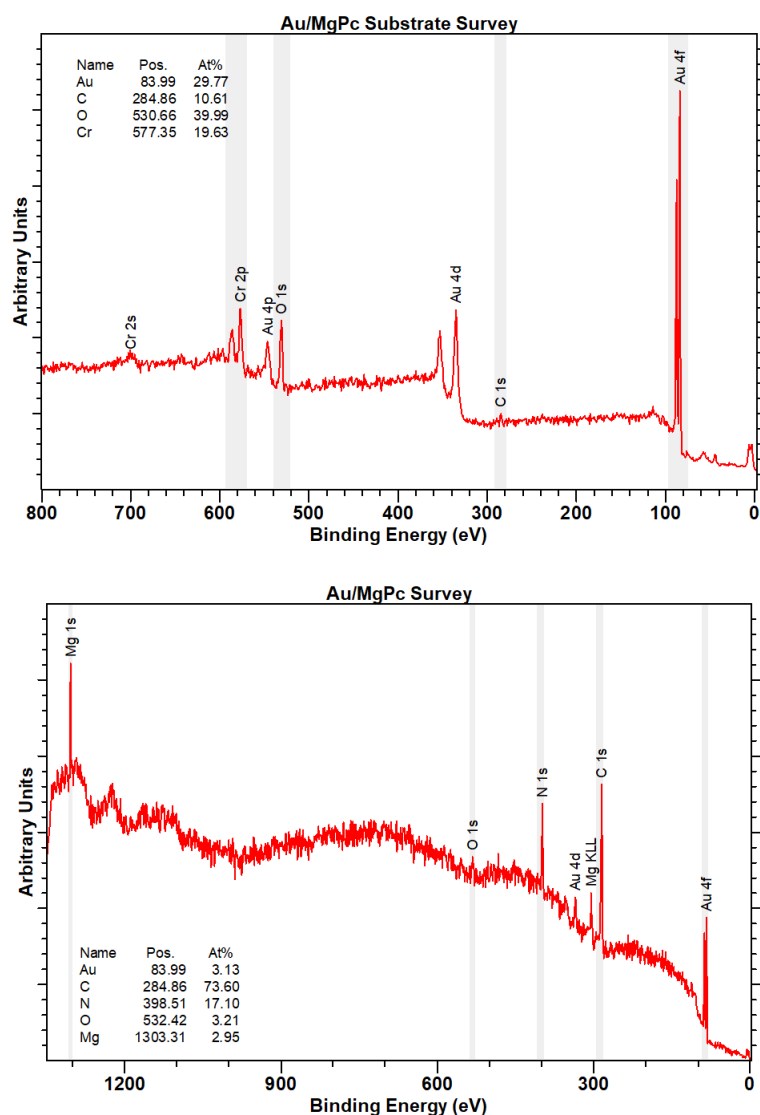


Figure 8.27. Full survey spectrum of Au/MgPc before (top) and after (bottom) the deposition process.

rough and the deposited organic layer, especially in the first deposition steps is far from uniform. Moreover, for the calculation of the thickness I used the electron mean free path, obtained from the TPP2m method rather than the effective attenuation length, as a consequence, the thickness is overestimated. The adopted parameters are collected in table 8.6. However, the results of the calculations are compared with the AFM image of the surface taken after the last deposition. Surprisingly, there is a good match between the theoretical values and the actual thickness, thus the adopted parameters are sufficiently

accurate.

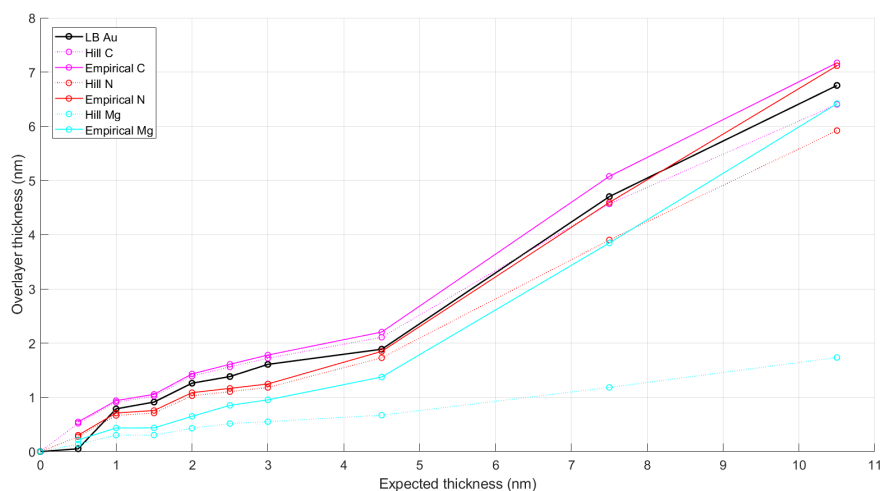


Figure 8.28. Comparison of the estimation results of the MgPc overlayer thickness obtained through different methods and by using different XPS signals.

The least accurate method for the calculation of the overlayer thickness is based on the Lambert-Beer equation (6.11). This method requires all the previous assumptions, thus it fails for the quantification of very thin layers, moreover, it considers the reduction of the substrate peak intensity due to the increasing deposition of organic material only. The result is shown by the black line. This method fails in the evaluation of very thin layers, as a matter of fact, we have an unrealistic step between the first and second depositions, as if the amount of MgPc adsorbed during the first deposition is almost null. That is in contrast with the XPS measurements since a Mg_{1s} signal is always detected. This can be connected, once again, with the condition of full coverage of the gold surface, as explained for Au/ZnPc, but here is even more evident. Nevertheless, except for the first step, the estimated values are not so different from the other more accurate methods.

The other curves are associated with quantification methods based on organic and substrate signals. The solid and the dashed curves are the results of different methods, respectively the Hill equation (6.14) and the empirical equation shown in 6.16 [75]. Both methods combine the intensities of $Au_{4f7/2}$ and the molecular orbital taken into account (C_{1s} , N_{1s} or Mg_{1s}), however, the second one consider the dependency of the effective attenuation length of the electron with respect to the electron kinetic energy. The applications of the Hill equation are limited, since it requires that substrate and deposited material have energetically close emission peaks. All the curves are almost superimposed, except for the curve based on the Hill method that exploits the magnesium peak, which has a binding energy significantly higher than the gold substrate. The same result was obtained for the Au/MgPc, showing the limit of the Hill equation. All the curves show different results, however, they are almost superimposed and, most importantly, they follow the same monotonic behavior. The low increase in the layer thickness between step 6 and

step 7, highlighted by all the curves, is connected to a lower control on the sixth deposition process, which was conducted with a higher deposition rate, around 0.06 \AA/s , almost the double than the usual. The higher rate reduces the amount of adsorbed molecules and worsens the quality of the thin film.

Table 8.6. Parameters used for the calculation of the overlayer thickness.

Element	Orbital	E_{kin} (eV)	IMFP (nm)	RSF
Au	4f 7/2	1402.5	3.528	9.58
C	1s	1201.9	3.121	1
N	1s	1087.9	2.886	1.8
Mg	1s	182.9	0.846	11.18

Figure 8.29 depicts the edge of the deposited organic layer obtained with an AFM in non-contact mode, on the right, whereas, on the left, are presented three profiles extracted from different lines. The image is post-processed with *Gwyddion* in order to remove the background and flatten the image. The edge shown in the figure is formed because of the clamping system that fixes the sample to the holder. Therefore, the brighter region on the right shows the deposited organic layer, and on the left side, there is the gold surface, which was completely covered by the clamps during the depositions. The edge is quite steep, indeed it is just $10 \mu\text{m}$ wide. The minor vertical offset between the three profiles is caused by the post-processing corrections. The results are almost perfectly matched to the theoretical calculations shown in figure 8.28, confirming that the thickness of the organic layer is about $6.0 \pm 0.2 \text{ nm}$. This means that the adopted theoretical parameters, like the inelastic mean free path, describe quite well the structure. The consideration can be extended to the other two samples, however, we don't have AFM images of their edges.

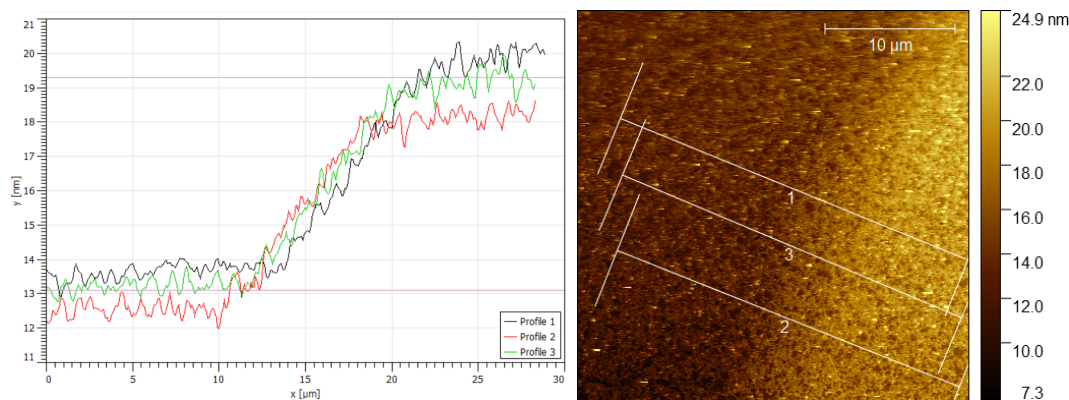


Figure 8.29. AFM image of the MgPc organic thin film edge. From the profiles measured across the edge, the measured final thickness is of 6 nm rather than the expected 10.5 nm.

Figure 8.30 shows both the topography image and the phase, taken with the AFM in non-contact mode, of a cluster of MgPc deposited on gold. From the phase image, we can

distinguish the molecular cluster from the gold substrate, in particular, the former is the dark region, whereas the latter is the large brown background. On the other hand, from the topography, we can measure the thickness of the molecular layer which is of ≈ 3 nm around the whole perimeter. The brighter areas in the phase are associated with regions where both metal and molecules are present at the surface, which can be caused by a non-uniform coverage. In the topography, the gold regions are characterized by grains due to the polycrystalline phase, the regions covered with the molecules show more smooth surfaces. On the other hand, in the partially covered regions, the gold grains are still distinguishable.

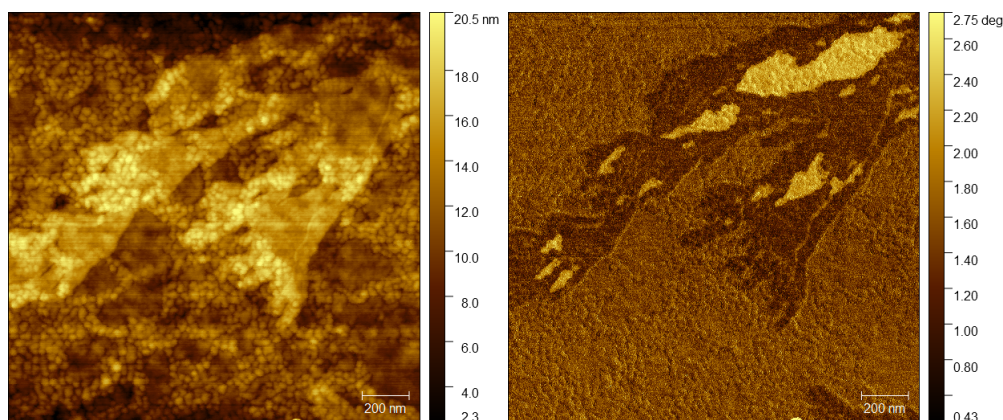


Figure 8.30. Topography and phase of a 3 nm thick cluster of MgPc deposited on gold. The sample belongs to Fabrizio Mo.

STM spectroscopy

The Au/MgPc is the only sample that was introduced in the vacuum Scanning Tunnel Microscope (STM) to better investigate the morphology of the deposited thin film of 6 nm. With this technology, the achievable resolution of the analysis is much improved with respect to the standard in-air AFM images, allowing for better investigation of the sample surface topography, reaching even the outstanding result of the imaging of single molecules and atoms. However, it is demonstrated that obtaining good-resolution images of a deposited layer of metal phthalocyanines on gold is very challenging since the tip dislodges and slightly moves the molecules while scanning and sensing the surface [87]. This is the result of the weak interaction between the gold and the phthalocyanine, as a matter of fact, to investigate the morphology of the phthalocyanine monolayer or thin films, other substrate materials, that strongly interact with the molecules, are exploited, providing a much more stable molecular organization during the scanning process [87].

Figure 8.31 shows three images of the MgPc deposited layer on gold taken with the STM. The central picture and the one on the right are extracted from the Au/MgPc sample presented and discussed in this chapter, whereas the picture on the left has been taken from another sample, belonging to Fabrizio Mo, consisting of a deposited MgPc

thin film of 3 nm on a polycrystalline gold substrate, thus very similar to the structures analyzed in this work. The purpose of the picture is limited to presenting the morphology of the deposited layer. In every image, the features of the surface topography, e.g. the roughness of the surface and the presence of grains are evident. The grains could be created by the nucleation of phthalocyanine molecules, thus forming localized regions where the molecules have the same orientation, or could be the grains of the polycrystalline gold which are covered by a thin film of phthalocyanines. Moreover, in support of the second hypothesis, in some regions, we can distinguish some terraces, like for example in the bottom of the right image, which is a characteristic feature of the gold surface. The low resolution of the picture is partially caused by the dragging of the molecules due to the tip, which is also demonstrated by the presence of fictitious horizontal lines. The pictures are shown uniquely to present the general features of the deposited thin film without a deep investigation of the sample surface which requires the analysis of the grains in order to determine the positioning and the distances between the deposited molecules.

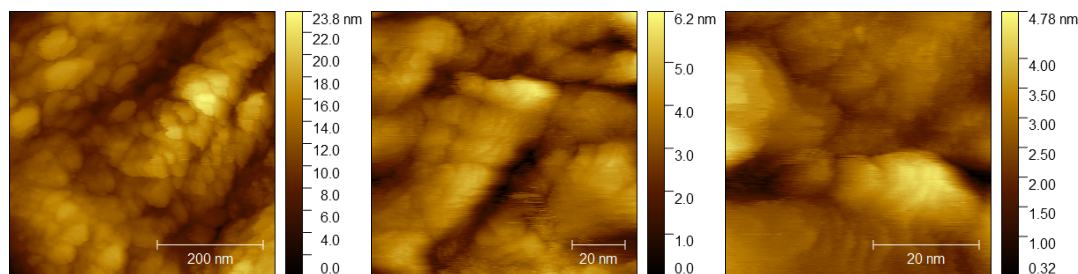


Figure 8.31. STM images of the MgPc thin film deposited on polycrystalline gold, showing a large number of grains. The left image belongs to Fabrizio Mo's sample.

In addition to the topography imaging, the STM can also perform local spectroscopy analysis of the sample, thus measuring the I-V characteristic in a single point. In addition, the normalized first-order derivative of the I-V characteristic with respect to the applied voltage corresponds to the density of states of the sample [88]. Figure 8.32 shows the results of the STM spectroscopy conducted in six different points of the Au/MgPC sample. For each point, both the I-V characteristic and the associated Density of States are plotted. In the first graph, the three measurements were taken from regions characterized by an uncovered gold surface. By comparing the results, we can understand the effect of the surface-tip distance on the measurements. As a matter of fact, the three spectroscopies are very different, apparently only the solid blue line shows the characteristic feature of metal since there is a huge and sharp increase of the current with small applied bias voltages, thus indicating that a large amount of electrons contribute to the current. The saturation of the current at $\pm 0.333 \mu\text{A}$ is an instrumental effect caused by the current amplifier that has reached the maximum current. Focusing on the respective DOS, indicated by the orange solid line, the typical metal features of the electron density of states are obtained, with a high concentration of states below the Fermi level, which is not set to zero due to an energy misalignment between sample and tip, representing the valence band, indicated by the negative energies. On the contrary, the different behavior of the other two dashed lines

is caused by the potential barrier that appears between substrate and tip as a result of the surface-tip distance. Therefore, the tunneling process between the two metals occurs with a larger applied voltage [88]. As a result, the I-V characteristics are similar to the ones of a semiconductor material, even if they are obtained from measuring gold. This aspect is crucial to correctly distinguish and thus analyze the sample surface. Moreover, from the respective density of states, indicated by the dashed orange lines of the top image, we can observe the gold electron density of both the valence band and conduction bands. The sharp peak exactly below the Fermi level is a characteristic feature of gold that coincides with the bump also so measured in the UPS spectroscopy in figure 8.4.

On the other hand, the second graph shows the I-V characteristics, in blue, and the respective density of states, in orange, of the MgPc layer obtained from three different points. The three curves show a similar trend, with a well-defined semiconductive behavior of the organic layer. Close to the Fermi level, the gold states are still visible, the reason is that in the case of a very thin layer, the gold electrons can still tunnel through the layer and reach the tip, thus contributing to the current. In addition to that, the gold-phthalocyanine interaction causes the formation of hybrid states that populate the forbidden band gap. As a result, the calculated DOS does not represent the MgPc electronic structure only, but it is superimposed on the gold one, making the analysis much more challenging. As a matter of fact, the sharp peak just below the Fermi level is not the HOMO, but, instead, it probably belongs to gold. The molecular HOMO can be one of the successive peaks in the energy range between -1 eV and 0 eV or is covered by the sharp gold peak. The same considerations are valid for the determination of the LUMO, which, however, should be easier to identify due to the absence of a very high gold contribution in the conduction band. Moreover, the strange behavior of the dashed I-V characteristic from 1 V to 2 V can be connected to the large contribution of the molecular states to the current, obtained when the LUMO peak enters in conduction. As a consequence, it is probable that the LUMO is in between that energy range and corresponds to one of the peaks in the DOS, probably the one at ≈ 1.5 eV. Finally, if we assume that the HOMO peak is included in the gold peak at ≈ -0.5 eV, a HOMO-LUMO gap of ≈ 2 eV is obtained, which is a plausible result. Nevertheless, a higher number of sampling points must be used to improve the quality of the analysis of the density of states, which a rough sampling of the features of the molecular states can be missed.

8.5 Conclusions

Here I want to summarize the information we have acquired from the photoemission analysis about both the interface interaction between the three investigated metal phthalocyanines adsorbed on a gold surface and the structure of the self-organized organic layer. All three molecules have a similar general behavior with respect to the gold (111) surface. In particular, the adsorption involves weak electrostatic interactions and no chemical bonds are formed. Nevertheless, a minor charge transfer at the interface is measured, with different intensities depending on the central metal atom of the molecule. Moreover, no evident deformation of the molecular structure is detected.

For the cobalt phthalocyanine, the charge transfer is more evident, and there is a

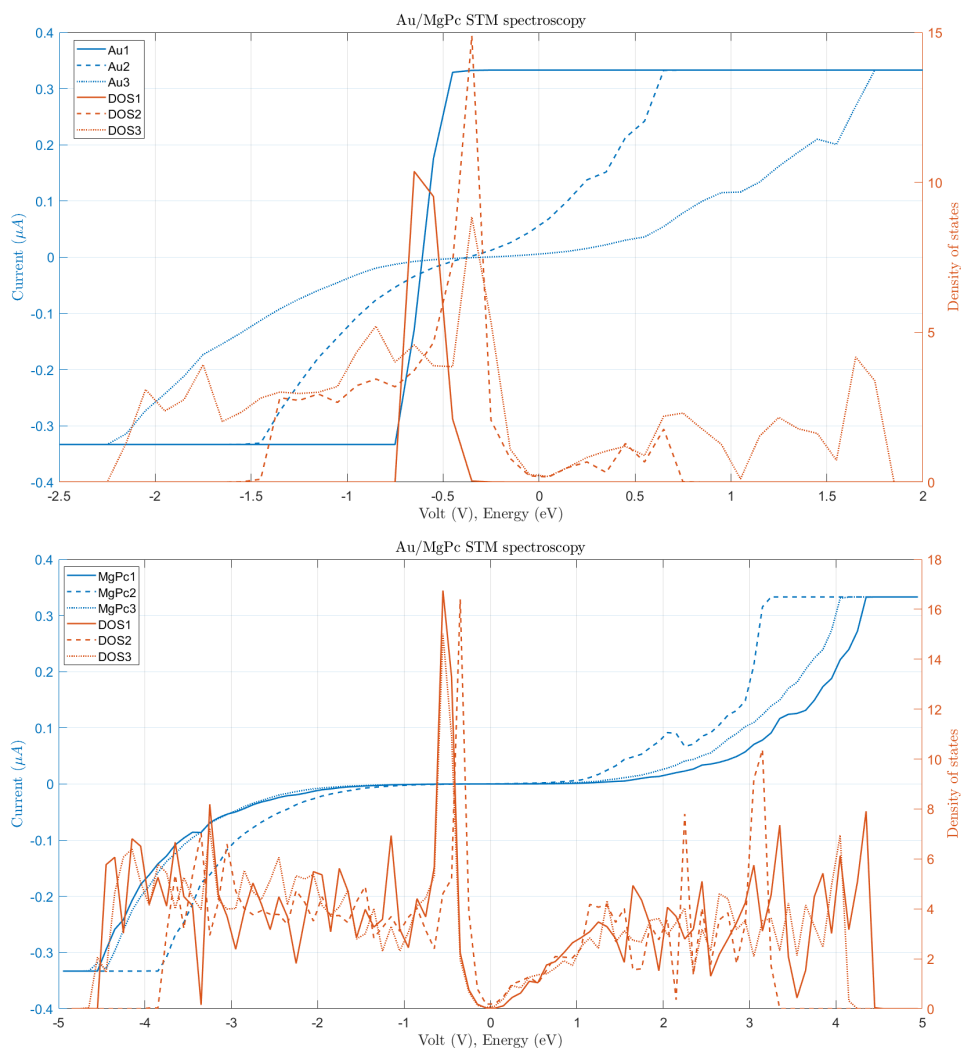


Figure 8.32. I-V characteristic and density of states calculated in six different points of the Au/MgPc sample. The first plot shows the uncovered gold surface, whereas the second plot is obtained from the organic thin film.

bi-directional transfer of charge that separately involves the central metal atom and the carbon ring backbone. In particular, the former donates electrons to the gold surface, whereas the latter takes electrons from the gold. As a result, the inner part is positively charged and the negative charge is mainly distributed in the surroundings. The previous consideration is obtained by analyzing the shifts of the characteristic peaks of carbon, nitrogen, and cobalt, which are sensible to the charging effect. Moreover, it also affects the reduction of the work function mainly caused by the Pauli pushback effect that arises at the metal/organic interface. As a consequence, Au/CoPc has a lower shift of the work function after the adsorption. Concerning Au/ZnPc and Au/MgPc, the contribution of

the charge transfer is lower. The reason for that could be connected to the filled atomic orbitals of the central metal atoms, whereas cobalt has an incomplete 3d shell that lacks of three electrons. That also provides interesting magnetic properties to CoPc, which can affect the interaction with the gold surface. However, this aspect was not investigated and it requires further analysis to understand the impact that has on the interface properties.

For all three samples, the properties of the mono-layer are slightly different with respect to the thin film. This is reasonable since the influence of the metal/organic interface is stronger for the adsorbed molecules and it fades with the distance from the gold surface. As a consequence, the binding energies of the characteristic XPS peaks have small corrections as the layer grows, approaching the features of the bulk organic material. The UPS analysis demonstrates that the adsorption of a few molecules highly affects the electronic properties of the system. As a matter of fact, the shift in the work function is measured just after the first deposition of less than 0.5 nm, which is not even sufficient to reach a full coverage of the gold surface. Thus, with a low amount of molecules is possible to tune the electronic properties of the substrate effectively. Additional information on the thin film structure is deduced from the photoemission analysis, which reveals the self-organization of the deposited molecules. Moreover, the steep reduction of the substrate peak intensities provides information on the coverage of the surface. As shown for Au/CoPc and Au/MgPc, the complete coverage is achieved with the third and second deposition steps respectively, and the calculated thickness is in between 0.4 eV and 1 eV, depending on the method used for the estimation. However, the morphology of the substrate surface has a high impact on the quality of the film, so the previous conclusions cannot be applied to any structure.

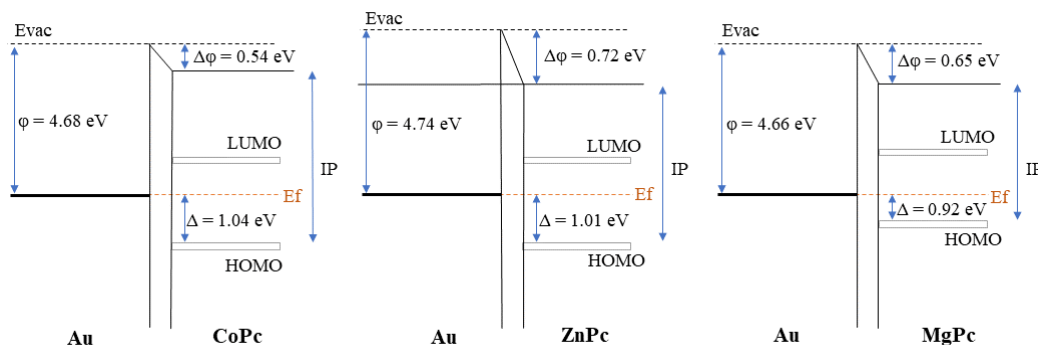


Figure 8.33. Band diagrams of the three samples, the energies are obtained from the XPS and UPS measurements.

In table 8.7 are collected the most relevant quantities that characterize the energy band structure of the three samples. The data are extracted from the UPS analysis of the last deposition step, showing the features of the thin film. With these quantities, we are able to build the energy band diagram at the interface for each sample. They are shown in figure 8.33. The direct measurements of the LUMO level are impossible with the employed instrumentation, however, for ZnPc, I use the value found in another article

[22], and I extend it to the other two samples, assuming a slight variation of the energy gap. Which are motivated by the similar electronic behavior of the molecules.

Table 8.7. Most relevant quantities to build the energy band diagram at the interface. In order: the work function of the bare gold surface, the shift of the work function after the adsorption, and the edge of the HOMO level, which coincides with the energy barrier.

Sample	ϕ_{Au} (eV)	$\Delta\phi$ (eV)	HOMO (eV)
Au/CoPc	4.68	0.54	-1.04
Au/ZnPc	4.74	0.72	-1.01
Au/MgPc	4.66	0.65	-0.92

Chapter 9

Simulation results

The investigation of the metal/organic interface is also performed through *ab initio* simulations, which are aimed at supporting the photoemission results. As a matter of fact, a part of the calculations is focused on the charge transfer between metal and molecule and the consequent charge distribution within the molecule. These aspects can be discussed also by analyzing the XPS and UPS spectra, as already done in the previous chapter, thus we can compare the simulations with the experiments. In addition, the *ab initio* simulations allow us to investigate other properties of the interface that are impossible to detect with the adopted instrumentation. In particular, we can better understand the adsorption mechanisms like how the molecules are deformed due to relaxation processes, and how the molecules are organized to form the monolayer. As a matter of fact, a huge part is dedicated to the study of the molecular geometry.

As already anticipated, the *ab initio* simulations exploit the density functional theory (DFT) approach in the Kohn-Sham framework, which is a simulation method developed for the calculation of the electronic structure of atomic systems. Further details on the method are discussed in chapter 5.2. All the simulations are performed with the commercial simulation tool *QuantumATK*, a powerful tool that allows the investigation of different aspects and properties of the system under study. However, for the purposes of this thesis, I focus my attention on the *OptimizeGeometry* tool and the calculations of the electric properties, like the charge and the potentials. Other interesting aspects, like the magnetic properties, fundamental for spintronic applications, are not investigated. Since the simulations are support material for the experiments, I avoid any analysis that does not have an experimental counterpart, which can be used as a reference. The investigation of the metal/organic interface is composed of two parts: firstly, the optimization of the atomic structure is performed, and then, the most relevant physical quantities are calculated on the already optimized system. The two parts are strictly connected, as a matter of fact, all the properties of the structure are functions of the arrangement of the atoms, thus, the optimization is fundamental, and must be conducted with particular care. This is valid for any atomistic simulation.

9.1 Geometry optimization

As the name suggests, geometry optimization tries to simulate the relaxation processes, as a result, the positions and the distances between the atoms are modified and corrected by the applied forces. The process is performed in different steps, at each step, the electronic structure of the system is calculated, then forces are applied, and as a consequence, the atoms are slightly moved. The successive step uses the previously obtained result as the initial configuration, and the cycle repeats until the force applied to each atom is lower than the selected threshold value [89]. The entire process can be quite time-consuming, as the majority of *ab initio* simulations. Many factors contribute to the duration of the optimization. As a matter of fact, it deeply depends on the system structure, in particular on the number of atoms, which normally, should not exceed 200 atoms, and on the specific elements involved [89]. The type of pseudopotential and basis set adopted to describe the atomic electronic structure of every single atom are surely one of the crucial aspects of every DFT simulation, indeed, a more complete basis set will provide more accurate results, but for systems with a large number of atoms, the solution becomes unmanageable. In addition, there are other simulation parameters that can be tuned to accelerate the simulation, like the threshold force and the maximum displacement. Thus, it is up to the operator to choose the proper parameters for a satisfactory balance of the speed-accuracy trade-off.

Another major aspect is how far is the initial configuration from the optimal one, because the employed software does not allow huge displacements of the atoms during the optimization step, but rather, the positions of the atoms are slightly corrected, and slowly approaching the optimized configuration. Therefore, in some cases, the simulation does not reach convergence, or even worse, the obtained result is nonphysical. Thus, the final optimized structure strongly depends on the initial configuration, and the result could be just a local minimum. Therefore, in order to achieve the best configuration, which means the system with the lower total energy, it is necessary to run several simulations, each one of them with a different initial condition, in order to cover the majority of cases, and then compare the total energies: the lowest is the most stable. However, for what concerns the adsorption, the symmetry of the structure can be exploited to reduce the number of simulated configurations. In addition, in *quantumATK* some constraints to the atomic structure can be imposed, involving different sets of atoms. For example, we can fix atoms in their original position, or we can select the set of atoms composing the molecule and allow only rigid displacement in the space, treating the entire molecule as a unique rigid body. Obviously, the constraints affect the final results, thus they must be appropriate for the system.

9.1.1 Methodology

The interface between gold and phthalocyanine is modeled through a simplified and idealistic structure composed of three layers of gold with a (111) surface orientation, and a single molecule placed parallel with respect to the metal surface. To properly model a bulk material, a high number of layers is required, however, due to the size of the supercell, defined by the geometry of the molecule, three layers allow running the simulation

in a reasonable amount of time and preserving the physics of the surface. The supercell is defined by the lattice vectors of the gold (111) surface, in such a way that each supercell hosts one molecule. As a result, the number of simulated atoms is reduced to the minimum. The lattice vectors are the following:

$$v_1 = 5 \cdot u_1 - 1 \cdot u_2 \qquad v_2 = 3 \cdot u_1 + 6 \cdot u_2$$

where u_1 and u_2 are the two unit vectors of the gold (111) surface, thus v_1 and v_2 define the lattice vectors (A and B) orthogonal to the surface normal (xy plane). Along the z direction (C), the lattice vector must be sufficiently long, around 40 Å, to have some void regions on top of the molecule, and below the first gold layer, in order to avoid any unwanted interatomic interactions. The molecule is then placed with the central metal atom in the middle of the supercell, at a distance of a few Å from the gold surface. The particular shape of the supercell, in combination with the periodic boundary conditions, allows a reasonable spacing between adjacent molecules, so that even the molecular interactions are taken into account in the optimization of the geometry. Moreover, with the so-defined v_1 and v_2 , we are able to reproduce the self-organized pattern that the phthalocyanine molecules create during the adsorption, which exploits the shape and symmetry of the molecule. The intent is to build a model that reflects the structure of the real monolayer since a single molecule cannot be experimentally analyzed. However, any ideal system is far from reality, especially in our cases, where the sample surfaces are not flat at all.

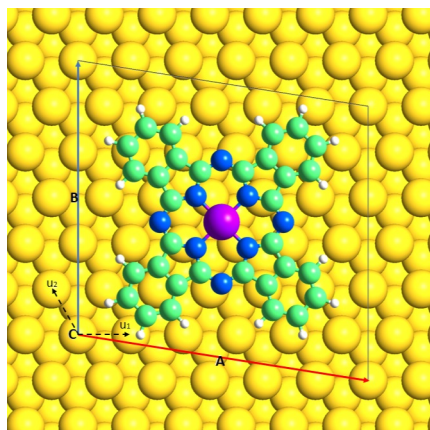


Figure 9.1. Representation of the supercell used in the simulations. The molecule is placed at the 0° rotation configuration. The gold (111) lattice vectors of the surface are indicated by the dashed black lines.

Several optimizations of the same system are performed in order to determine the best configuration, each one of them with a different initial condition, in order to overcome the limits previously mentioned. The phthalocyanine molecules lay horizontally on the gold surface during the adsorption, however, the angle with which they are disposed of with respect to the gold lattice has to be determined. To cover most of the cases and by exploiting the symmetry of both the molecule and the surface, six configurations with

different rotation angles are optimized, which are 0° , 15° , 20° , 30° , -15° , and -30° , considering the 0° the configuration that has the four benzene rings that resemble a cross ("X") and the positive angle identifies a clockwise rotation around the central metal atom (as shown in figure 9.1). The optimization at 20° is added following the results of the others. All the relevant data concerning the geometry optimization are collected in table 9.2. With such initial angles, the majority of cases are covered. Actually, to complete the 90° symmetry of the phthalocyanine, the 45° configuration is missing. However, it has been excluded due to the partial overlapping of the benzene rings, which forbid the planar structure of the molecule. Moreover, it is not reported in the literature. Every geometry optimization is performed with the same two-step method, composed of two consecutive simulations that differ in the type of applied constraints. By splitting the process, the optimization is faster. The first step is a preliminary calculation that is aimed at the identification of an approximate position of the molecule. As a matter of fact, the constraints are separately applied to both the substrate and the molecule. The former is kept fixed, whereas the latter is limited to a rigid displacement, avoiding any changes in the interatomic distances. In other terms, the relaxation of the system is forbidden. As a result, the molecule simply reaches the correct adsorption distance from the gold surface. The successive step simulates the relaxation of the structure as a consequence of the interaction of the two components. Therefore, all the atoms are free to move, except for the first gold layer, the one farther from the molecule, which is kept fixed to simulate the bulk material, which is unaffected by the presence of the molecule.

The geometry optimization, like any other operation, requires the calculation of the electronic structure of the system, which is obtained through the LCAO approach. The Poisson equation is solved with the two-dimensional fast Fourier transform (FFT2D), with periodic boundary conditions along the surface directions, and Dirichlet for the remaining one. The selected BCs are required to emulate the periodic behavior of the surface structure along the longitudinal directions and the surface discontinuity along the transversal one. Moreover, we used PBE functionals with pseudopotential of the FHI type, combined with the GGA exchange-correlation potential. Grimme DFT-D3 correction is adopted to take into account the van der Waals interactions. In order to obtain more accurate results, different basis sets are used depending on the element, as shown in table 9.1, which should provide better results, as indicated in the software manual [89]. In addition, to improve the description of the interface interaction, the counterpoise correction is used. The numerical accuracy of the solver is determined by the density of the k-points, set to [4,4,0] along the three directions of the supercell (A, B, and C), respectively, with a density mesh cut-off of 100 Hartree. Concerning the optimization tool, the maximum force tolerance is set to $0.05 \text{ eV}/\text{\AA}$, when lower values are reached, the simulation is over, and the maximum displacement per step is limited to 0.2 \AA for each atom. During the optimization, the lattice vectors (A, B, and C) are kept fixed, in order to apply the geometrical constraints.

Finally, after the relaxation of the structure, we can compare the total energies of all six configurations and determine the one with the lowest energy, which corresponds to the most stable configuration. In other terms, we can establish which is the most probable orientation and the deformations that the zinc phthalocyanine molecules assume while adsorbing on a gold (111) surface. The total energy of the system is calculated

Table 9.1. Employed FHI pseudopotentials for the specific element. For gold DZP is used for the geometry optimization and the analysis, whereas SZP is for the device calculations.

Element	Au	C	N	H	Mg	Co	Zn
PP	DZP (SZP*)	DZDP	DZP	DZP	DZDP	DZDP	SZP

according to the type of Poisson solver and the adopted set of parameters, listed before. Therefore, the contributions to the total energy are five: kinetic, electrostatic, entropy-term, exchange-correlation, and external field. The last one is zero since all the simulations are conducted in equilibrium conditions, moreover, each term has a specific counterpoise correction, whereas the van der Waals corrections are considered separately.

9.1.2 Monolayer organization

The two-step geometry optimizations of the six different configurations of a deposited ZnPc on a gold surface reveal interesting features that are discussed in the following. Most of the obtained simulation results are in agreement with both the XPS experiments and the literature [20, 23, 35]. Some remarkable considerations can be achieved just from the results of the first step of the optimization process, which is characterized by imposing a rigid displacement of the molecule and a fixed substrate. For every configuration, independently of the rotation angle, the molecule approaches the surface, reaching a distance in the range between 3.22 Å – 3.25 Å. Therefore, there is an attractive interaction between the phthalocyanine and the gold that moves the molecule in the most stable configuration, which is independent of the rotations around the z-axis. This demonstrates the ZnPc molecules are actually adsorbed on the gold (111) surface, moreover, the adsorption distance of a flat ZnPc is of 3.25 Å. As a matter of fact, if the initial surface-molecule distance is short, during the optimization the molecule is moved away because of the repulsive force characteristic of the adsorption potential (6.3), and it reaches again the same equilibrium position. Such a distance is typical of chemisorbed molecules, however, this is in contrast with the experimental results, since no chemical bonds are detected. Instead, it is more probable that, due to the large area of interaction, the adsorption is controlled by the superposition of several weak van der Waals forces that act both for the benzene rings and the central metal atom. Additional proofs are provided while discussing the adsorption energy calculations in section 9.1.3.

In the second optimization step the atoms are free to move, except for the lowest gold layer, which is kept fixed in order to model the effect of the bulk atoms on the surface relaxation. As a result, the deformation of the molecule as a consequence of the adsorption is calculated. For all the configurations, only small corrections are applied, except for the rotation angles of 30° and –30°, which are characterized by a rotation around the central metal atom. In general, the carbon backbone suffers a minor deformation that causes a slight concave bending of the structure with respect to the surface. On the contrary, a much more evident displacement is measured for the zinc atom, which approaches even more toward the surface. As a consequence, the interatomic distances between the central metal atom and the four nitrogen atoms increase, however, the molecular symmetry is

Figure 9.2. Animations of the relaxation process of ZnPc (15°) and gold substrate from the lateral and vertical view.

maintained, since the zinc atom is still in the central position. Concerning the gold substrate, the surface atoms slightly approach the molecule. However, a similar relaxation process is measured even without the presence of the adsorbed molecule. In conclusion, in accordance with the XPS analysis of the metal/organic interface, the interaction between gold and ZnPc is not sufficiently strong to cause a huge deformation of either of the two components. Moreover, the rotation angle does not affect too much the adsorption of the single molecule on gold, since none of the configurations shows a particular affinity with the substrate. In figure 9.2 are shown the relaxation process of the ZnPc with a rotation angle of 15° from the lateral and vertical sides. The former highlights the vertical displacement of the zinc atom and the overall bending of the molecule, whereas the latter reveals that the structure of the symmetry of the molecule is maintained. A similar minor relaxation happens for all the other cases, except for $\pm 30^\circ$, which deserves additional comment.

From the literature [20], we know that the phthalocyanine molecules are self-assembled onto the gold surface. The monolayer has a very specific periodic pattern that tends to fit in the molecules by exploiting the characteristic symmetry. The geometry optimizations reveal that the orientation of the molecules is the result of the repulsive interaction between the adjacent molecules, rather than a particular affinity with the gold substrate. This aspect is particularly evident in the optimizations with 30° and -30° as initial rotation angles. These configurations, in combination with the adopted lattice cell, are characterized by very close (but not overlapped) benzene rings, that make the optimization process much more interesting. After the first step (rigid molecule and fixed substrate), the molecule reaches an adsorption distance of ≈ 3.2 eV, like the other angles, however, during the second step, the molecules suffer a rigid rotation around the zinc atom in addition to the previous discussed relaxation mechanisms, as shown in figure 9.3. The cause of the rotation is connected to the repulsive forces that tend to separate the benzene rings of adjacent molecules. Remember that, thanks to the periodic boundary conditions, the system is not limited to a single cell, but the whole monolayer is modeled. Thus the intermolecular interactions between the molecule and its projections are considered.

Therefore, the -30° configuration is almost rigidly rotated clockwise, reaching the final angle of -20° . We can then deduce that for such an angle, the intermolecular forces that drove the deformation are negligible. This rotation is highlighted by the vertical view in figure 9.3.

Even more interesting is the information obtained from the lateral view, which shows that the molecule, during the rotation, is heavily deformed and loses its planar structure. Once again, as a consequence of the interatomic interactions, the adjacent benzene rings are bent in opposite directions, which reminds the tilted configuration characteristic of the thin film, as shown in figure 2.2. However, after this intermediate configuration, as the intermolecular forces become weaker, the phthalocyanine interatomic forces partially restore the planar structure of the molecule, which is expected from the monolayer and is in accordance with the other simulations, as shown in the lateral view of figure 9.3. However, it is important to specify that the geometry optimization is not a dynamic process that describes the time evolution of the molecular structure upon the adsorption, instead, it is a static process in which, step by step, the atomic positions are modified according to the calculations to find the energy minimum. Therefore, the actual temporal evolution does not coincide with the optimization trajectory, in fact, other simulations are required. Identical is the optimization of the 30° configuration, but it stops in the middle of the simulation since forces under the set threshold value are reached, and the molecule did not recover the planar structure. For this reason the additional simulation at 20° is performed, so that a full set of angles are analyzed. With these last optimizations, we have demonstrated that the orientation of the molecules is not driven by the interaction with the substrate, which has a minor role in the organization of the monolayer, as a matter of fact, the molecules do not align with the gold surface lattice and the substrate deformation are caused by the relaxation process. This indeed confirms the absence of chemical bonds at the interface between the two components. The gold, however, defines the adsorption distance and energy.

The most important quantities measured from the fully optimized structures are collected in table 9.2. In order to determine which one of them is the most stable, the total energies of systems must be compared. The one at 0° is the least stable, on the contrary, with rotation angles of 15° , 20° , and -20° the energy is minimum. Where the last one refers to the relaxed structure with an initial -30° angle. The fact that the results of three different configurations are close indicates that the monolayer organization is not unique, and different orientations are possible. Moreover, the energy difference between 15° and 20° is of 0.01 eV, which indicates that there is almost no difference between the two configurations. Thus, we can suppose that for any rotation in that interval, the results are similar. Thus, there is a set of directions with similar adsorption probability. In addition, the opposite direction at -20° is also equally possible, indeed there is almost no distinction between the two orientations. As a matter of fact, the monolayer organization with $\pm 20^\circ$ is very similar and in both of them, the molecular symmetry is exploited to reach the same pattern but mirrored, as shown in figure 9.6. Both angles better fit the gold (111) surface lattice, but this could be a coincidence obtained from the particular cell shape.

Concerning Au/CoPc and Au/MgPc, because of the previous results, the geometry optimization is performed only for a reduced set of rotation angles, in particular, three

Figure 9.3. Animations of the relaxation processes of a ZnPc that involve the rotation of the molecule around the central metal atom as a consequence of the intermolecular interactions. Initially, the ZnPc has a -30° rotation angle, which is reduced to -20° in the relaxed structure.

configurations (-12° , -20° , and 15°) for the former, and two for the latter ($\pm 15^\circ$). To be consistent, the substrate cell and the optimization parameters are kept identical to the previous Au/ZnPc model, as for the two-step optimization process. In general, the relaxation process is similar regardless of the central metal atom, however, there are some small differences concerning the central metal atom. The magnesium atom moves toward the gold surface by 0.5 \AA , whereas the cobalt is fixed on the molecular plane. In addition, the relaxation deformation of the CoPc backbone is negligible. In both cases the gold surface relaxation process is comparable, not showing particular affinity with any molecule. The optimal rotation angles are -12° and 15° respectively for Au/CoPc and Au/MgPc, as demonstrated by energies collected in table 9.2. Moreover, for Au/MgPc there is an energy difference of about 0.05 eV between the two configurations, whereas, once again, by comparing the two configurations at -12° and -20° of Au/CoPc, their energies are almost identical. Demonstrating that, according to the employed simulation model and parameters, the optimal configuration is not unique, but it belongs to a range of equal probable structures. Figure 9.4 shows the lateral and vertical views of the optimized structures to highlight the slight deformation of the molecule due to the adsorption and the orientation of the phthalocyanine on gold (111).

In table 9.2 are collected the most relevant quantities of the fully optimized structures, for Au/ZnPc, Au/CoPc, and Au/MgPc. The rotation angle in brackets indicates the configuration after the optimization process, as a consequence of the rigid rotation. The distances "Z1" and "Z2" refer to the z-position of the central metal atom with respect to the gold surface plane and the molecular plane, respectively. The calculated total energies do not directly provide any physical information on the interface properties, thus the single values are quite meaningless. But, by comparing them, we can determine the most probable configurations the adsorbed molecules should have. Moreover, they are

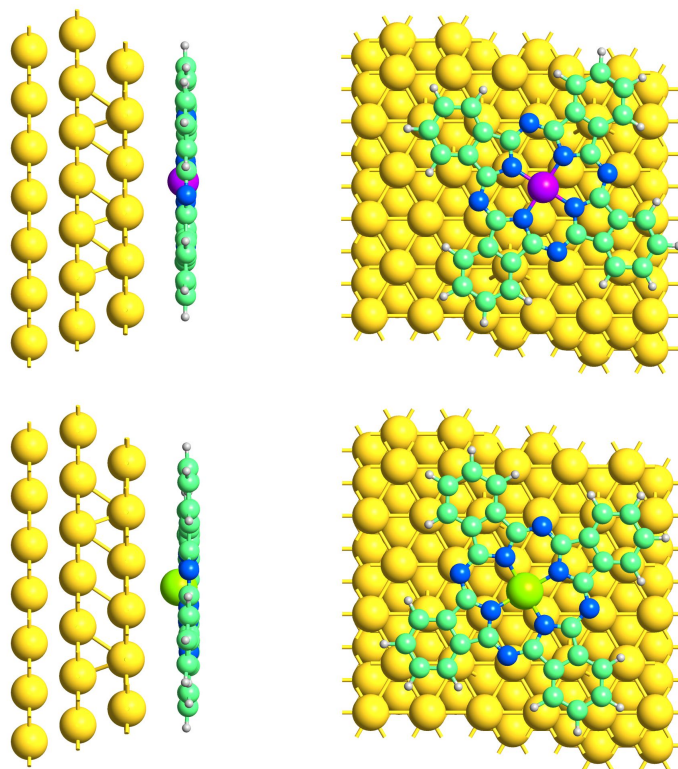


Figure 9.4. Lateral and vertical view of the fully relaxed Au/CoPc (top) and MgPc (bottom) in their respective best configuration (-12° and 15°).

fundamental for the calculation of the adsorption energies discussed in the next chapter. The last quantity ΔE is the energy difference with respect to the best configuration. The deformations of ZnPc and MgPc are quite similar, indeed the distances between the components are almost identical. On the contrary, CoPc is less deformed and the central metal atom is only slightly moved toward the gold surface. No configuration among the analyzed ones shows particular geometrical features. From the gathered results, the best adsorption configurations for ZnPc, CoPc, and MgPc on a gold (111) surface are characterized by the rotation angle of 20° , -12° , and 15° respectively. However, the energy difference between many configurations is very small, for example between 20° , 15° , and -20° for ZnPc. As a matter of fact, the calculated values of ΔE are small fractions of electronvolts. Thus indicating that the adsorbed molecule can assume different phases, that fit the molecular symmetry. Therefore, the two predominant angles are close to $\pm 15^\circ$.

All the structures analyzed are built in order to reproduce the periodic pattern of the metal phthalocyanine monolayer found in the literature [35]. However, there are two main constraints that limit the accuracy of the results. Firstly, since the periodic pattern of the monolayer is defined by the lattice vectors, the cell hosting the molecule must be

Table 9.2. Geometry optimization data: "Z1" and "Z2" are between the central metal atom and the gold surface (Z1) or the molecular plane (Z2) respectively. ΔE is the energy difference between the configurations. The angles in parenthesis refer to the fully optimized final structures.

Molecule	Rotation ($^{\circ}$)	Z1 (\AA)	Z2 (\AA)	Energy (eV)	ΔE (eV)
ZnPc	0	2.66	0.500	-10842.35989	0.154
	15	2.67	0.486	-10842.50175	0.012
	20	2.67	0.475	-10842.51342	/
	30 (25*)	2.64	0.415	-10842.3926	0.121
	-15	2.71	0.505	-10842.45549	0.058
	-30 (-20*)	2.69	0.500	-10842.50493	0.008
CoPc	15	2.95	0.121	-107813.00838	0.018
	-12	2.98	0.125	-107813.02644	/
	-20	3.01	0.125	-107813.02271	0.004
MgPc	15	2.63	0.500	-107005.91826	/
	-15	2.68	0.534	-107005.869	0.049

carefully shaped by selecting a proper linear combination of the gold (111) surface vectors u_1 and u_2 . Secondly, in order to reduce the simulation time, the number of atoms per cell should be reduced to the minimum, and only one molecule can be hosted. Despite that, the obtained results are quite promising and can be compared with other works and experimental results.

9.1.3 Adsorption energy

The most important physical quantity that can be extracted from the geometry optimization simulation is the adsorption energy E_{ads} , which can be related and compared to the experimental results. The adsorption energy is obtained by comparing the total energies of the fully optimized metal/organic structure with the total energies of the two separate components. In order to have consistent results, it is necessary that all the simulations are performed with identical parameters. As a matter of fact, the gold substrate and the ZnPc are both calculated by keeping the same supercell and boundary conditions, but, to increase the results' accuracy, the density mesh cut-off is reduced to 75 Hartree. Moreover, the substrate and the molecule undergo the same optimization process as the combined structure, in such a way the individual relaxation processes are not considered in the evaluation of the adsorption energy, which indeed takes into account only the effects involved in the adsorption. Thus, E_{ads} is calculated with the following equation:

$$E_{ads} = E_{S/O} - (E_S + E_O)$$

where E indicates the total energy and the subscripts S and O refer to the substrate and the organic molecule respectively. All the calculated energies are negatives, as shown in table 9.3. Actually, the previous equation determines the energy advantage of having a combined structure rather than two separate components, as a matter of fact, a negative

E_{ads} indicates that the adsorption is energetically favored, whereas a positive E_{ads} excludes any interactions between substrate and organic molecule, forbidding the adsorption. The adsorption energy is then the opposite since it is defined as a positive quantity (the energy stored in the interaction). From the intensity of the adsorption energy, we can determine the type of adsorption: typically, chemisorption energies are of some electronvolts, and the interaction is characterized by the formation of chemical bonds that support the structure, whereas in physisorption the forces are mainly of van der Waals, thus the adsorption energy is lower than 1 eV.

Benzene on Au(111)

Before the calculation of the adsorption energies of the gold(111)/phthalocyanine structure, a simpler metal/molecule interface is analyzed and the data are compared with the literature [90]. From this preliminary simulation, we are able to verify the reliability of the method and determine the accuracy of the results obtained with the employed set of parameters, which is then used for the gold/phthalocyanine structures. In order to speed up the simulations, the supercell built from the gold (111) surface is smaller than the one required by the ZnPc, nevertheless, for the sake of consistency, the substrate is modeled by three layers only and the optimization process is identical to Au/ZnPc. The structure is shown in figure 9.5, the optimal initial position of the benzene ring is obtained from the results of another work [90], which is also used to compare our results.

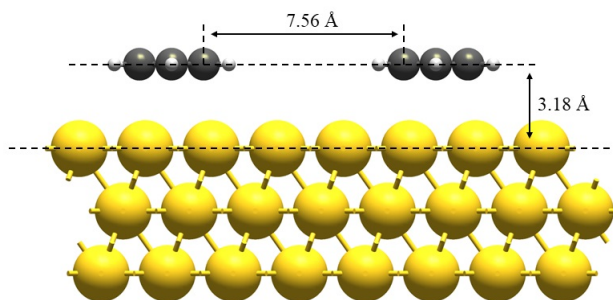


Figure 9.5. structure of the Au/benzene adsorption

With a distance of 7.56 eV between the adjacent benzene molecules, the effect of the intermolecular interactions can be neglected. The adsorption distance of 3.18 eV and the calculated adsorption energy is equal to 0.878 eV perfectly match the literature results. Moreover, the simulations are compared with the experimental results, and with the employed method, the adsorption energy is overestimated by about 0.2 eV. This difference should be considered while discussing the gold/phthalocyanine simulation results because an overestimation of the intensity is highly probable. The reason for that is connected to the type of functionals and the corrections used to solve the electronic structure of the system, which are less accurate in order to provide faster simulations. Moreover, elements like cobalt can be accurately modeled only by a few types of pseudo-potentials making

the simulations very time-consuming [89]. Nevertheless, with the adopted functional and basis sets, combined with the solver parameters, it is possible to achieve an acceptable accuracy.

Returning to the Au/MPc structures, the adsorption energies are calculated only for each best configuration. The results and the useful quantities like the total energies of the single components and the combined systems are collected in table 9.3. These results are obtained by using PBE functionals with FHI pseudopotentials, different for specific elements (table 9.1), with LCAO basis combined to GGA exchange-correlation. Further corrections are the Grimme DFT-D3 for the van der Waals forces and the counterpoise, to better represent the interface interaction. The adsorption energies of the three molecules on a gold (111) surface are comparable, they all have an E_{ads} higher than 5 eV, which indicates a quite strong interaction. At first glance, these results suggest a chemisorption of the molecule, however, from both the optimization and the experimental results, a strong physisorption is much more realistic. Such high values can be explained by the high interaction surface of the metal phthalocyanine, which indeed lays horizontally, allowing the four benzene rings and the pyrrole groups to interact simultaneously with the surface. Thus, several weak bonds, mainly van der Waals, are built at the surface that, as a whole, make the interaction quite strong. Moreover, the differences in the adsorption energies are connected to the central metal atom, which has a decisive role in the charge transfer at the interface. As shown by the successive analysis, CoPc has the highest binding energy and also the highest charge transfer, which in turn makes the adsorption stronger. On the contrary, ZnPc has the lowest charge transfer, thus the lowest E_{ads} . Nevertheless, all three systems are characterized by a charge transfer of fractions of electrons, and indeed, the adsorption energies are similar, indicating that the carbon backbone is the major responsible for the interaction with the metal. Concerning the single components, the three systems share the same gold substrate, thus the total energy of the relaxed gold is identical. On the contrary, the total energies of the three molecules differ due to the central metal atom, the heavier the atom, the higher the lowest the energy. It should be remembered that the absolute values of the total energies are difficult to interpret because they refer to an unknown energy reference. On the contrary, derived quantities like the adsorption energy are much more meaningful. Another important aspect is the fact that all the calculation results are overestimated, as demonstrated by the gold/benzene adsorption. Thus, the true adsorption energy of a metal phthalocyanine could be of few electronvolts. It could be interesting to investigate the adsorption energy of metal phthalocyanine of different substrates through experimental techniques, like thermal desorption spectroscopy because is an indicator of the stability and resistance of the thin film, qualities that are crucial for applications, like molecular sensors.

In conclusion, with the geometry optimizations and the associated adsorption energies, additional information on the morphology of the monolayer is acquired. Moreover, the

Table 9.3. Adsorption energy E_{ads} of the three metal phthalocyanine on polycrystalline gold evaluated for the best configuration.

System	θ ($^{\circ}$)	Au (eV)	MPc (eV)	Au/MPc (eV)	E_{ads} (eV)
Au/ZnPc	20	-99408.8856	-9009.04885	-108423.1158	5.18134
Au/MgPc	15	-99408.8856	-7591.71589	-107005.9183	5.3168
Au/CoPc	-12	-99408.8856	-8398.62083	-107813.0264	5.52004

simulations are in accordance with the experimental results, thus confirming the considerations on the photoemission results. In particular, we have demonstrated that the interaction between the analyzed metal phthalocyanines and the gold does not involve chemical bonds, which also prevents the marked deformation of both components upon the adsorption. As a matter of fact, the gold surface undergoes almost the same relaxation process as if the molecule were not present, whereas the molecules are only slightly bent, but they keep their structure and symmetry. According to the rotation angle simulations, the energetic advantage between the best and worst Au/ZnPc configurations is around 0.05 eV, a quite insignificant amount considering that the calculated adsorption energy is even higher than 5 eV. Thus, only a small fraction of the adsorption energy depends on the orientation of the organic molecule with respect to the gold. Therefore, the molecular organization of the monolayer is driven by the intermolecular forces, which arrange the molecules by exploiting their unique symmetry, as clearly visible from the optimization process in figure 9.3. The optimized pattern of the adsorbed zinc phthalocyanine on a gold (111) surface is depicted in figure 9.6, which highlights how the molecules are wedged.

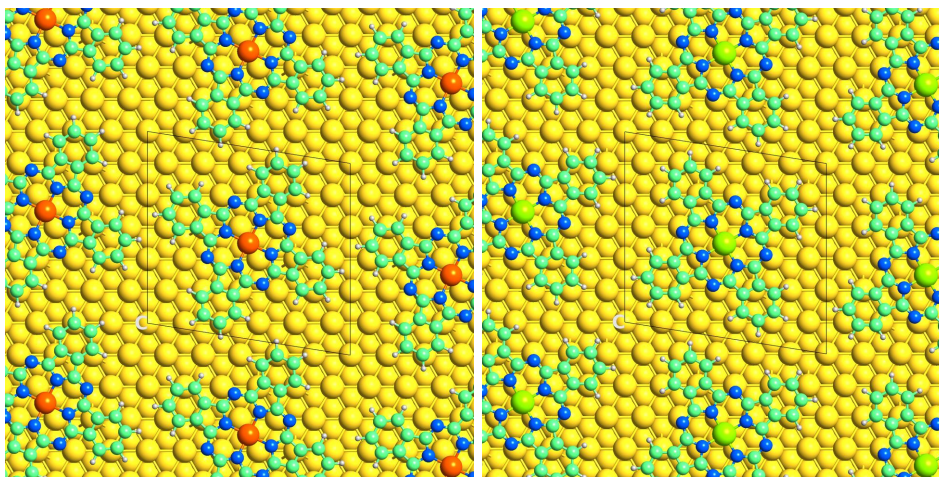


Figure 9.6. Representation of the molecular arrangement of the phthalocyanine monolayer that exploits the symmetry of the molecules. The two configurations have similar energies.

9.2 Analyses

QuantumATK has available several analysis tools that allow the calculations of different properties of the atomic structures and the molecular devices. However, for the purposes of this work, the attention is only focused on the electronic properties of the previously optimized structures, with particular interest in the density of states, how the charges are distributed in the single molecule, and the potentials at the interface. In order to highlight the effects of the adsorption on the molecular properties, the results of the interface are compared with single molecule simulations. Moreover, a comparison with the experimental results is conducted where available, like the calculated DOS vs. the experimental valence band. To be consistent with the geometry optimizations, the electronic structure of each system is obtained through the functionals (PBE), pseudopotentials (table 9.1), and exchange-correlation potential (GGA) presented previously, moreover, the same van der Waals and counterpoise corrections are applied.

In order to make the discussion clearer for the reader, the properties of the investigated metal/organic interfaces are presented by comparing the results obtained from the different structures, rather than analyzing the three models separately. In the first part (9.2.1) are presented the molecular energy spectra of the different models, which are directly compared with the photoemission results. Some quantities show some inconsistencies between the simulations and the experiments, like the HOMO-LUMO gap of the molecules and the work function, whereas, other aspects are incredibly matched, like the valence band. On the other hand, the second part (9.2.2) is focused on the calculation of the electron density, with particular attention to how the charge is distributed in the adsorbed molecule and on the interface charge transfer. These calculations cannot be directly compared with any experimental results, however, they match the charge transfer considerations discussed while analyzing the features of the photoemission spectra.

9.2.1 Molecular energy spectrum

The starting point of the simulation analysis is the discussion of the molecular electronic states obtained through the *DensityOfStates* tool of *QuantumATK*. For all the following calculations of the density of states, the k-points sampling density is increased to 12 Å along k_A and k_B in order to improve the results. Before proceeding with the comparison between simulation and experimental results, the effects of the adsorption on the electronic states of the molecules are investigated. The three graphs in figure 9.7 represent the electron states of each molecule (in order CoPc, MgPc, and ZnPc) calculated from different configurations. In each graph, the orange curve is the molecular projected density of states calculated from the optimized gold/phthalocyanine structure, whereas the blue curves refer to the gas phase. The dashes line has been obtained from the *molecular configuration*, by applying *Dirichlet* boundary conditions along all directions. Therefore, the system is composed of a single molecule and, by default, *quantumATK* applies a default broadening of the discrete energy levels that models the thermal agitation to better match the experimental results. On the contrary, the solid line is obtained from a *bulk configuration*, characterized by a united cell identical to one employed for the geometry optimization, and periodic boundary conditions along A and B. This structure models

the organic monolayer without the gold surface, but keeping the same periodicity. Thus, the effects of the adsorption on the electronic structures can be determined by comparing the blue and orange curves. First of all, as expected, the molecular electronic structure is characterized by localized peaks, however, there is not a complete match between the two blue curves, however, the most important peaks, the HOMO and the LUMO are superimposed.

After the adsorption, the molecules have different behavior. Concerning MgPc and ZnPc (respectively the second and third plot), the three different curves are more all less overlapped. The position of the HOMO and LUMO is stable after the deposition, actually, there is just a slight shift of the ZnPc LUMO towards lower energies, but it is lower than 0.1 eV. On the graphs, the HOMO-LUMO gaps are indicated, measured by considering both the peak maxima and the onsets. The latter is the one that should be compared with the experimental results. The calculated energy gaps are 1.07 eV and 1.13 eV for MgPc and ZnPc respectively. These values are in contradiction with other works [22], which provide twice our values. Moreover, our results do not match the experiments. As a matter of fact, with such a low energy gap, combined with the measured HOMO onsets, the Fermi level of the adsorbed molecule is close to the LUMO level, which indicates an important charge transfer at the interface. However, the low values of the forbidden energy gap are connected to the basis set employed in the DFT method, which are Gaussian curves that do not perfectly approximate the real orbitals, especially close to the nucleus, where they decay less than expected. Thus, causing an overestimation of the bond energies, with the consequent reduction of the energy gap. More interesting is the graph of CoPc, where a rigid shift of ≈ 0.4 eV toward lower energies is measured after the adsorption. Once again, for the same reason, the energy gap of 1.07 eV is too small, and the HOMO level of the gas phase is very close to the Fermi level. The reason behind the shift of the molecular electronic structure can be connected to physical explanations, like the more intense charge transfer between gold and CoPc, or the polarization effect due to the interface dipole. However, it could be also attributable to a simulation artifact generated by the bad modeling of the central cobalt atom. As a matter of fact, the employed basis sets are not suited for accurate results, thus simulations with other pseudopotentials, such as OMX high, are necessary [89].

The next step consists of the comparison between the calculated molecular electronic structure with the photoemission results, which have been already discussed and analyzed in the previous chapter 8. In figure 9.8 are collected six plots that represent the valence bands of the three samples, in order, from top to bottom, Au/CoPc, Au/MgPc, and Au/ZnPc. On the left, are shown the comparisons of the valence bands measured with the XPS with respect to the density of states of the whole structure calculated with *QuantumATK*. On the right, the focus is on the molecular properties, thus a comparison between the HOMO levels, measured by UPS, and the molecular electronic states is presented. The molecular states are calculated by projecting the density of states on the molecule only, thus, neglecting the substrate states. The blue curves refer to the experimental data, whereas the orange curves are the simulation results, obtained with the same k-points sampling density of 12 \AA along k_A and k_B . The UPS spectra have been calibrated in order to correct the Fermi level offset caused by a non-perfect alignment between the sample and the detector. In such a way, all plots refer to the same Fermi level (0 eV).

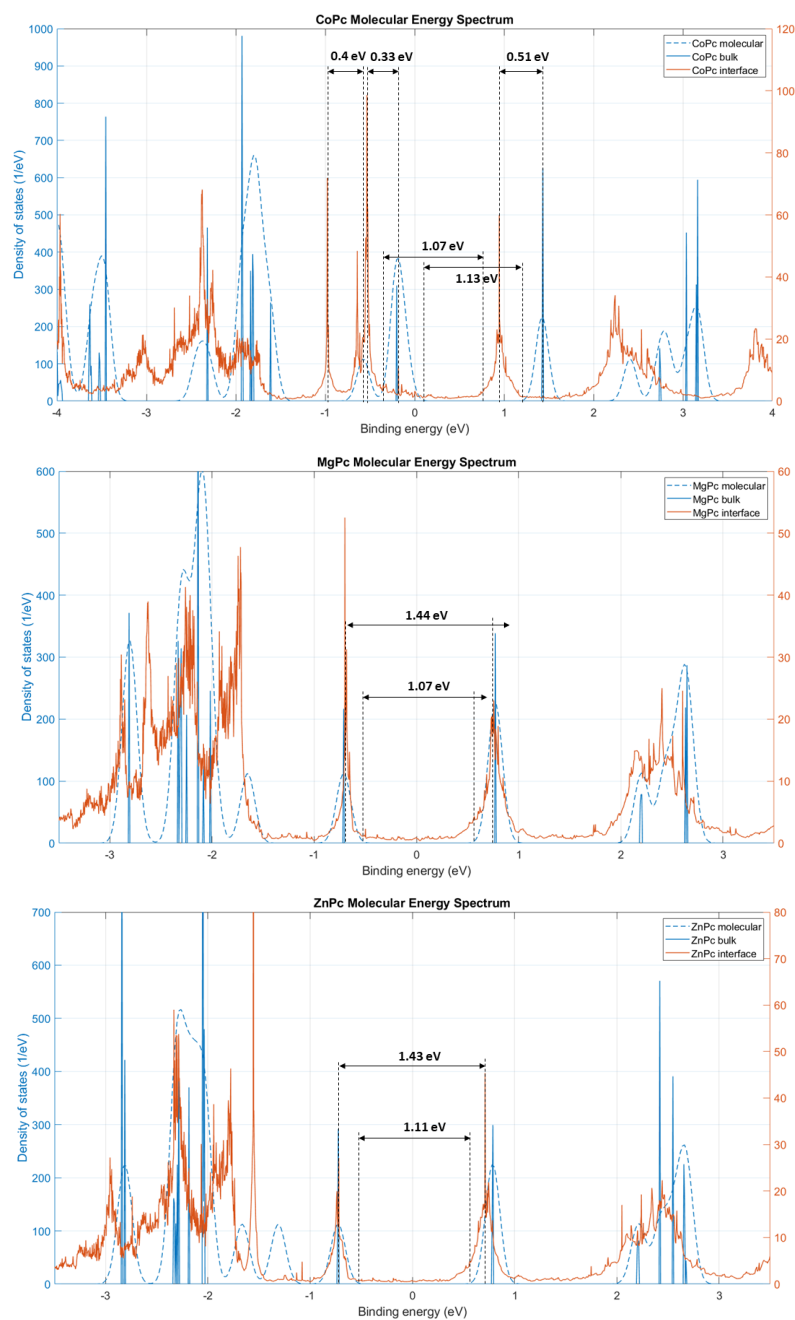


Figure 9.7. Molecular energy spectrum of the three molecules. the blue refers to the gas phase, calculated in both bulk and molecular configuration, and the orange is the projection of the DOS on the molecule after the adsorption.

Since the simulated models are composed of only a monolayer, the XPS valence bands shown in figure 9.8 (left) are taken from the analysis of the deposition steps that guarantee a full coverage of the gold surface, using the calculations of the layer thicknesses as a reference. The simulation results match almost perfectly the measurements. The general shape of the valence band is reproduced by the calculations, indeed, we can distinguish the three main peaks of the gold valence bands. However, there is a shift between the two results, and the calculated valence band is slightly moved toward higher energies. The reason for that is connected to a major aspect that makes challenging the comparison between measurements and calculations. As a matter of fact, the simulations are conducted on ideal models, whereas the real sample includes imperfections, defects, and contaminations, thus, there is never a perfect match between the two structures. Most importantly, here the comparison is between the calculated density of states and the electron photoemission spectrum. The latter is strictly connected to the material density of states since the emitted electrons carry information on their original binding energy. However, many electrons undergo scattering events, losing part of their kinetic energy and contributing to the background noise. As a result, moving toward lower binding energies, the noise necessarily increases, thus, making the mismatch even more evident. Moreover, the secondary electrons broaden the peaks toward lower energies, making the position of the maximum less reliable. For this reason, when comparing experiments and calculations, one has to refer to the onsets rather than the maxima. Thus, looking at the plots on the left, we can appreciate the almost perfect match between the offsets of both the first and third peaks, with a slight shift of fraction of electronvolts. Demonstrating that the density of states of the gold substrate is almost perfectly modeled by the simulation tool. Concerning the positive energies of the plots, the mismatch is easily explained. As already said, the simulations show the DOS, whereas with XPS we detect electrons, thus the available states above the Fermi level at 0 eV are not occupied.

The same consideration of the discrepancy between the position of the energy peaks between experiments and calculations can be extended to the plots on the right, which are focused on the molecular HOMO level. The blue curves are extracted from the UPS analysis of the last deposition step, where the intensity of the respective HOMO level is maximized. Thus, the spectra of the thin films are plotted. On the other hand, the orange curves are the projected densities of states of the single molecules composing the organic monolayer. Differently from the valence band plots, here the shift between the HOMO onsets is evident for all three samples. For ZnPc and MgPc, the shift between the onsets are respectively of 0.44 eV and 0.27 eV. For CoPc, the low intensity of the UPS HOMO peak makes the evaluation much more accurate, however, with a rough estimation, an energy shift close to 0.5 eV is obtained. The reasons behind the failure of the simulations in the calculation of the molecular energy spectrum can be various. Firstly, the adopted basis sets used to represent the atomic electronic structures could be not sufficiently accurate, and better results should be obtained by improving the simulation parameters, at the expense of the simulation time. Secondly, there is the possibility that the model fails in the calculation of the interface interactions and the surface electronic properties.

As a matter of fact, to correctly calculate the work function of a simple system, like a gold (111) surface, a specific configuration and simulation settings are required, moreover, some additional features must be added to the model [89]. In particular, with the adopted

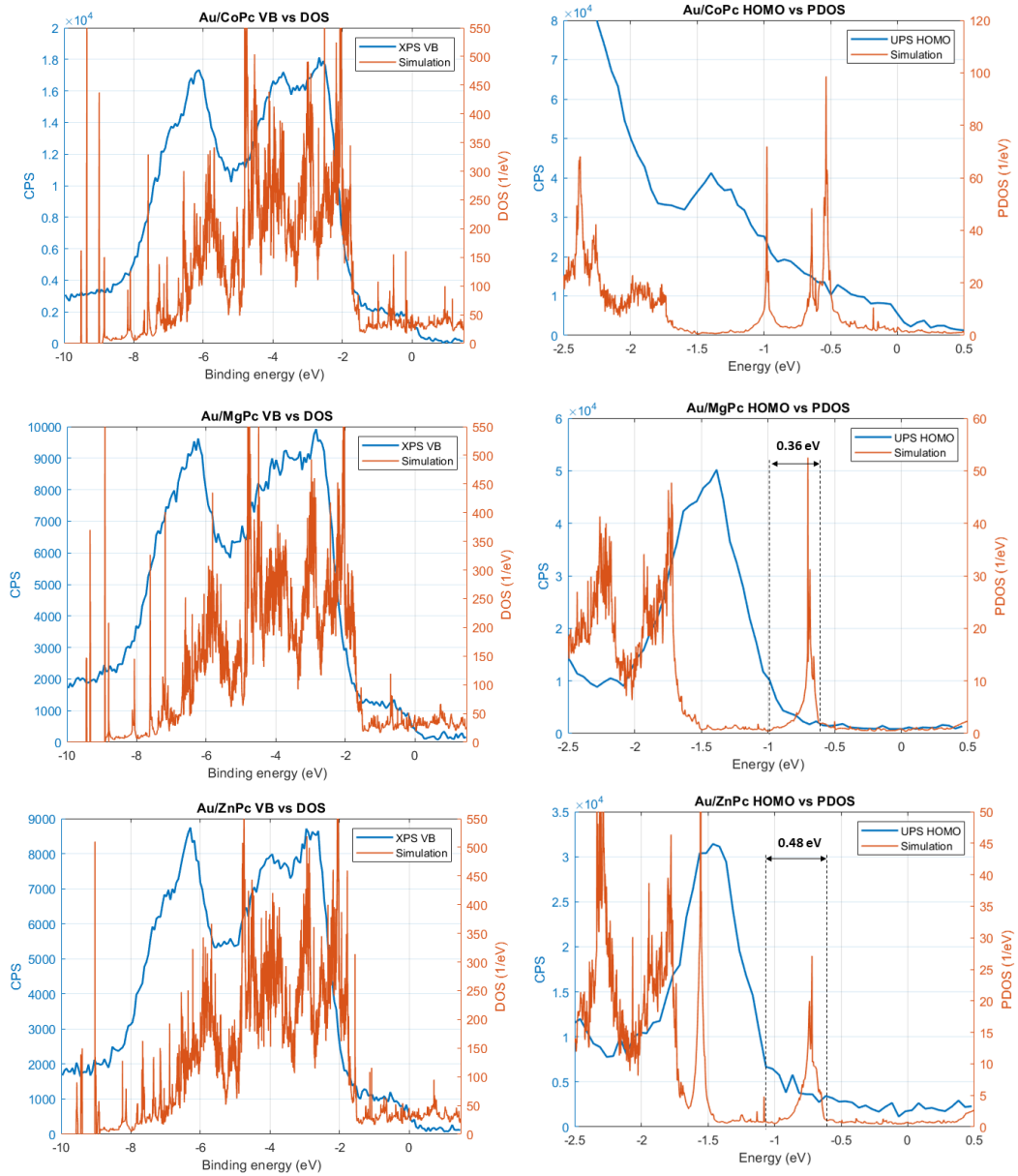


Figure 9.8. Comparison between the calculations and the photoemission measurements. On the left are plotted the valence bands of the Au/MPc vs. XPS, whereas on the right are plotted the PDOS vs. UPS.

FHI pseudopotentials and GGA exchange-correlation potential, the atoms of the last layer must be transformed into *ghost atoms*, and the boundary conditions of the Poisson solver must be Neumann (bottom) plus Dirichlet (top) along the z-direction. With these settings, the calculated work function of a gold (111) surface is of 5.26 eV, perfectly matching the

literature (5.30 eV). If the ghost atoms are not included, the work function drops to 3.95 eV. Thus, the inclusion of the final ghost atoms is crucial for the correct modeling on the metal surface. However, in a more complex structure, like the metal/organic interface, the ghost atoms cannot be applied. To investigate the work function of the Au(111)/ZnPc interface, the chemical potentials of the different components are calculated and compared. With always the same simulation settings, the work functions of the three systems (interface, molecule, and gold) are all close to 4 ± 0.05 eV. Denoting that the results are non-physical and, most importantly, that the expected reduction of the work function after the adsorption is not measured. One possible explanation is that the chemical potential is calculated with respect to an unknown reference energy, which should represent the vacuum level, making the resulting value difficult to be correctly interpreted. As a result, the calculated Fermi level is not reliable, and, as a consequence, the electronic density of states is shifted in energy. The most relevant consequence of the bad calculation of the work function is the wrong alignment of the energy level of the metal/organic interface. As a matter of fact, the interface and the single components share the same work function of 4 ± 0.05 eV, and the energy alignment between the gold surface and the molecule is probably performed by aligning the vacuum level, not taking into consideration the reduction of the work function caused by the interface dipole, mainly generated by the Pauli pushback effect. As a result, the calculated density of states is shifted in energy. As a matter of fact, the shift of the HOMO onset of ≈ 0.4 eV between the UPS spectra and the simulations, is similar to the energy reduction of the work function after the adsorption measured from the UPS analysis. In conclusion, the mismatch between the HOMO energies can be caused by a wrong energy reference in the calculations, which causes a shift in the whole density of states. Indeed, the valence band is also improved by this correction, since a similar shift was detected.

9.2.2 Charge transfer

The second part of the simulation calculations is focused on the charge density of the systems, with particular interest on how the charge transfer changes the charge distribution upon the adsorption. To be consistent with the previous results, always the same simulation parameters and configurations were adopted. For the investigation, the *ElectronDensity*, *ElectronDifferenceDensity*, and *MullikenPopulation* analysis tools provided by *quantumATK* were used, in order to analyze different aspects of the interaction [89]. The first tool calculates, as the name suggests, the electron density of the whole structure in the three-dimensional space. On the other hand, the second one calculates the electron density difference (EDD) between the self-consistent valence charge density and the superposition of the single atomic valence densities, thus indicating how the electron density of the whole structure differs from the single atomic components. In other terms, the following equation is applied:

$$\Delta n_e(\vec{r}) = n_e(\vec{r}) - \sum_i^{N_a} n_i(\vec{r}) \quad (9.1)$$

where $n_e(\vec{r})$ is the electron density of the whole system defined in the three-dimensional space, $n_i(\vec{r})$ are the single atomic electron densities and N_a is the total number of atoms.

As a result, through this calculation, the atomic charge redistribution caused by the formation of chemical bonds is obtained. In particular, a positive value of $\Delta n_e(\vec{r})$ indicates the accumulation of electrons, whereas a negative value is measured in case of a reduction of the electron density. Thus, with this analysis tool, we are able to determine the presence or not of chemical bonds at the interface. Figure 9.9 shows the three-dimensional isosurfaces of the *ElectronDifferenceDensity* calculated for the three different structures considering the isovalues of 0.05 and -0.05 , for the purple and blue surfaces respectively. The pictures show that the electron density difference is localized in the interatomic bonds of the molecules and gold only. Thus, confirming that no chemical bonds are formed between the gold surface atoms and the metal phthalocyanines under analysis, in accordance with the experimental results. The atomic structures are included in the picture to make the interpretation easier.

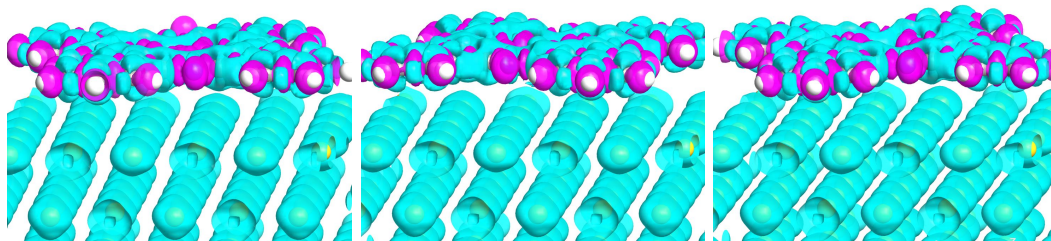


Figure 9.9. Electron difference density of the three structures (Au/CoPc, Au/MgPc, and Au/ZnPc) with isovalue 0.05 (purple) and -0.05 (blue).

With the previous calculations, we have analyzed the type of adsorption process that undergoes between the investigated metal phthalocyanines and the gold (111) surface. Demonstrating that the interaction is due to the superposition of weak electrostatic forces that do not involve a charge transfer between the two materials. However, in order to provide a complete description of the interface interaction, additional analyses focused on the effects of the adsorption are required. To investigate the charge redistribution upon adsorption, the electronic densities of the combined structures are compared with the results obtained from the single isolated components, which are the gold substrate and the metal phthalocyanines. In particular, the sum of the charge densities of the isolated components is subtracted from the charge density of the combined system, as indicated by equation 9.2 [29]. The *ElectronDensity* tool is used to calculate all the charge densities.

$$\Delta n_e(\vec{r})_{interface} = n_e(\vec{r})_{combined} - (n_e(\vec{r})_{substrate} + n_e(\vec{r})_{monolayer}) \quad (9.2)$$

Moreover, since the focus is on the interface effects only, the electronic densities of the isolated components are calculated starting from the fully optimized combined structure by removing the unwanted component. Thus, the geometry of the isolated molecule is identical to the one in the fully relaxed combined system, and the same for the gold substrate. As a result, all the other mechanisms that affect the charge distribution are removed from the calculation, in particular the atomic displacement caused by the relaxation processes.

The plots in figure 9.10 show the redistribution of the electron densities across the interface for the three different structures, thus $\Delta n_e(\vec{r})$. The black lines represent the average electron density along the z direction integrated over the xy plane. Whereas, the atomic structure is included in the graph just as a reference. A positive value of $\Delta n_e(\vec{r})$ indicates an accumulation of electrons, whereas negative values indicate a reduction of the electron density with respect to the isolated system. Thus, the electrons move from the negative to the positive regions. The results of the three different structures are very similar and they share the same behaviour. As expected, far from the interface, the electron distribution is not altered by the interaction, as a matter of fact, the difference is null. On the other hand, at the interface, some differences are calculated. In particular, there is a slight accumulation of electrons close to the adsorbed molecule and a reduction above the substrate surface, thus, indicating a small electron transfer from the gold to the molecule and, in addition, an interface dipole is formed. The vertical dashed lines in the plots indicate the most relevant atomic planes, which are the last gold layer, the central metal atom of the molecule, and the carbon backbone, from left to right. In correspondence to the last gold layer, electrons are accumulated after the adsorption. The reason for that can be attributed to the Pauli pushback effect that pushes the metal surface electron in the bulk, thus causing the formation of the interface dipole and also explaining the lower electron density just above the gold surface. On the molecule side, we can appreciate the different behavior of the central metal atom with respect to the carbon backbone for the three molecules. After the adsorption, the central metal atom loses electrons, thus it is positively charged, and, on the contrary, negative charges accumulate on the surrounding carbon ring. To further investigate the charge distribution within the molecule, the Mulliken population analysis is conducted and discussed in the following. If the charge distribution of MgPc and ZnPc are very similar, slight variations are obtained for CoPc, which is characterized by a lower accumulation of positive charge at the cobalt atom, and, on the contrary, the positive charging above the gold surface is enhanced. Which may indicate a larger charge transfer at the interface.

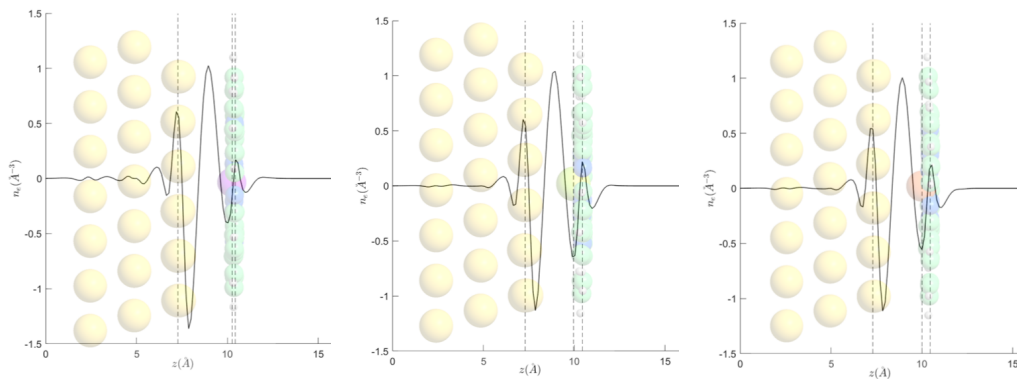


Figure 9.10. Profile of the electron density difference along the z -direction.

The charge distribution is also calculated through the Mulliken population, which is

defined by the different partition of the total number of electrons into atoms, orbitals, and bonds. The total number of electrons is calculated by the sum of the product between the density matrix (D) and the overlap matrix (S) over all the orbitals in the system, as expressed by the following equation.

$$N = \sum_{ij} D_{ij} S_{ij}$$

Thus, by restricting one index of the sum (i), the Mulliken population of one orbital (M_i) is calculated, moreover, the Mulliken population of the single atoms (M_μ) is calculated by summing all the respective orbital contributions, according to the equation:

$$M_\mu = \sum_{i \in \mu} \sum_j D_{ij} S_{ij}$$

As a result, the atomic charge calculation is provided, since the total charge of the system is separated and localized on the single atoms, thus, each atom is associated with a charge value. However, this calculation is not always the most suited method to measure the charge transfer, since it is just a limited trace of the density matrix of a set of orbitals, centered on the same atom. As a matter of fact, it strongly depends on the employed basis set to describe the atomic orbitals. The Mulliken population calculations are limited, and, in order to determine the charge transfer and the charge distribution, different methods should be used, and then, making an average of the results. For example, better results are obtained through the Bader charge analysis, in which each atom of the system is associated with a specific volume enclosed in the zero-flux surface, that individuates the minimum charge density perpendicular to the surface. Thus, the charge in the volume is a good approximation of the total electronic charge of the atom. However, *quantumATK* provides only the *MullikenPopulation* tool for the calculation of the atomic charge distribution of an electronic structure obtained through a pseudopotential DFT method. Nevertheless, the Mulliken calculation should provide a reasonable estimate of the charge transfer between weakly interacting systems, like the physisorption, where at least the direction of the charge transfer should be correct.

Figure 9.11 shows the three-dimensional representation of the Mulliken population for the three structures. Since the color scheme refers to the amount of charge localized on each atom, the accumulation of electrons, thus a negative charge, is indicated by the color blue, whereas the lack of electrons, resulting in a positive charge, is indicated in red. Moreover, the neutral atoms are represented in white, since the color bar is symmetric. The purpose of these graphs is to provide a qualitative representation of the charge distribution within the molecules and the gold substrate, further calculations of the single atomic charges are collected in table 9.4, where the charges of the most relevant components of the systems are calculated, like the whole molecule, the central metal atom, the nitrogen atoms, and the benzene rings.

The three adsorbed molecules have a similar charge distribution, with the negative charges localized on the carbon atoms bonded to the nitrogen atoms, whereas the central metal atom and the benzene rings are positively charged. The different properties of the central metal atoms are highlighted by the charge of the surrounding four nitrogen atoms,

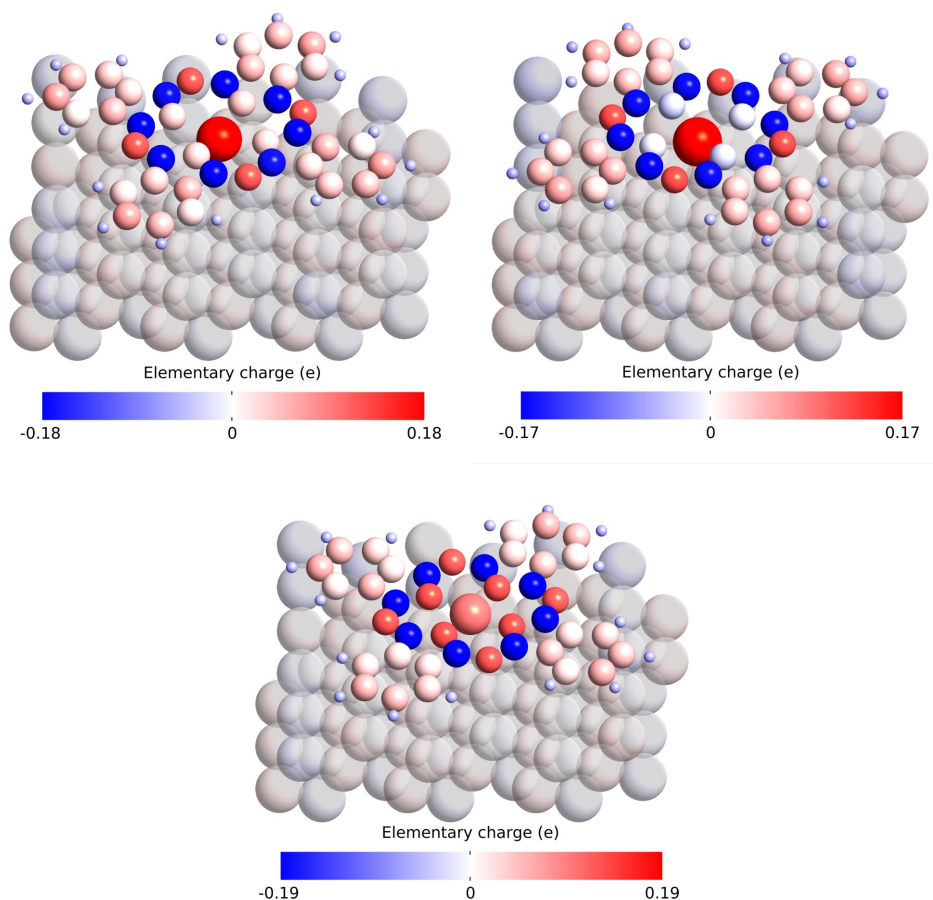


Figure 9.11. Representation of the Mulliken population on the three-dimensional model of the three interfaces, the scheme color indicates the charge, thus the positively charged atoms are in red, and the negatively charged in blue.

indeed, for MgPc and ZnPc the nitrogen atoms are almost neutral, thus indicating that all the inner positive charge is localized on the metal, whereas, for CoPc a larger amount of positive charge is localized on the nitrogen and the metal is slightly less oxidized. That can be explained by the larger electronegativity of the cobalt with respect to magnesium and zinc atoms. The whole negative charge is localized on the carbons bonded to nitrogen atoms, this is in accordance with the charge distribution of the pyrrole group, which is characterized by an oxidized nitrogen and the negative charge is localized within the ring. On the contrary, the benzene rings of the three molecules are all slightly positively charged and the electrons are localized around the hydrogen atoms, in contrast with the typical charge distribution of the single benzene molecule which has a concentration of electrons at the center of the ring. The pictures in figure 9.11 show the charge distribution of the adsorbed molecule, however, due to the slight charge transfer at the interface, the charge

distribution of the isolated molecules is very similar. Thus, just the plots of the Mulliken population are not sufficient to determine the charge transfer, and additional calculations are required. In order to determine the total amount of charge transferred between metal and molecule, the sum of the Mulliken population over all the gold atoms is compared with the total charge of the adsorbed molecule. Moreover, by comparing the charge of different sets of atoms before and after the adsorption, we can determine where the excess charge is localized within the molecule. The results are collected in table 9.4, where CMA stands for the central metal atom of the phthalocyanine, and with N, C-N, and C6 are respectively indicated as the sets of the eight nitrogen atoms, the 8 carbon atoms bonded to the nitrogen and the benzene carbon ring.

Table 9.4. Calculation of the charge localized in different regions of the system. The charge of the adsorbed molecules is compared with the isolated one to highlight the distribution of the excess charge upon adsorption.

Structure	Substrate	Molecule	CMA	N	C-N	C6
Au/CoPc	0.276	-0.276	0.106	1.048	-1.521	0.294
CoPc	/	$-2.1e^{-13}$	0.172	0.977	-1.393	0.313
Au/MgPc	0.190	-0.190	0.555	0.370	-1.312	0.312
MgPc	/	$5.5e^{-13}$	0.783	0.216	-1.263	0.320
Au/ZnPc	0.143	-0.143	0.419	0.662	-1.412	0.305
ZnPc	/	$5.2e^{-13}$	0.535	0.580	-1.369	0.310

The results shown in the table are in accord with the other simulations previously discussed and they can also be compared with the experimental results, showing some analogies. For each system, the total interface charge transfer is calculated, and the charge distribution of the adsorbed molecule is compared with the isolated one. The computational error of the calculation corresponds to the charge of the isolated molecules, which should be zero since the molecules are natural. Therefore, the expected error on the other results is of the order of 10^{-13} , which is negligible. First of all, from the sum of the Mulliken population of the substrate atoms and the molecule, it is demonstrated that all systems acquire a negative charge after the adsorption. In particular, a fraction of electrons is transferred from the metal surface to the molecule. The larger amount is calculated for the CoPc, with 0.276 e, followed by MgPc and ZnPc at 0.190 e and 0.143 e respectively. It is interesting to compare these results with the adsorption energies in table 9.3, the larger the charge transfer, the higher the adsorption energy, thus the interaction between substrate and molecule is stronger. As previously said, all phthalocyanine molecules are characterized by an inner part, composed of the central metal and the nitrogen atoms, which lack electrons, that are indeed localized on the surrounding carbon of the pyrrole rings. However, between the three molecules, the cobalt atom has the lowest positive charge, meaning that a larger amount of electrons are localized in the center of the molecule, which is also evident from the three-dimensional plot. By comparing the Mulliken population sums between the adsorbed and the isolated molecule, we can understand how the excess charge is distributed, thus defining the more active regions of the molecule. From the gathered results, the additional negative charge is shared between

more atoms, however, there is a huge distinction between the inner part of the molecule and the benzene rings. As a matter of fact, if the pyrrole rings and the metal atom acquire a small negative charge, the benzene rings are much less perturbed by the adsorption. By comparing the changes of the Mulliken population upon the adsorption with the profile of the electron density redistribution in figure 9.10, we notice that the results are inconsistent, especially for the central metal atom. As a matter of fact, the profiles of figure 9.10 indicate a positive ionization of the central metal atom, in contradiction to Mulliken. The reason, however, is probably connected to the fact that the large number of electrons localized at the interface (below the molecular plane) is erroneously attributed and almost equally distributed to all phthalocyanine atoms, resulting in a higher negative charge per atom. Nevertheless, the total amount of transferred charge calculated with the Mulliken population should be more reliable than the single atomic distribution, thus qualitatively describing the charge transfer. However, contrary to the XPS analysis, the bi-directional charge transfer is not measured with the Mulliken population. However, as already said, the employed method is very limited and does not provide accurate or even reliable results for all the systems. Thus, to better investigate the interface charge transfer, additional analyses with other methods are necessary.

9.3 Thin film and bi-layer analysis

The three ideal structures deeply analyzed previously represent the interface between the gold surface and a specific metal phthalocyanine. Due to the particular employed simulation configuration and boundary conditions, not a single molecule, but a periodic monolayer is modeled for each system. However, these structures are far from the real devices investigated through photoemission spectroscopy, which are characterized by a non-uniform organic thin film, necessary to obtain meaningful data. Therefore, in this section, both the morphological and electronic properties of the phthalocyanine thin film are analyzed and the results are compared with the respective monolayer. Actually, in order to model a thin film, several layers and thus a large number of atoms are required, making the simulations significantly time-consuming. Moreover, to determine the interface properties, the three gold layers used to represent the substrate surface are included, thus, the simulation of such a structure is unfeasible. As a consequence, the geometry optimization and the analyses are conducted on two different systems. For the former, since we are just interested in the molecule organization, in particular, to verify the stacking of the phthalocyanines, the system is made of four molecules only. On the contrary, for the latter, the number of molecules is reduced to two, thus the electronic properties of a bi-layer are investigated. At first glance, two layers could seem not sufficient to represent an organic thin film, however, as discussed in the following, we have obtained very interesting results that match the experimental results. Nevertheless, we do not exclude that with a higher number of layers, and a more accurate basis set, even better results could be achieved.

9.3.1 Geometry optimization

The main purpose of this first thin film analysis is to verify if our simulations are able to reproduce the characteristic molecular organization of the phthalocyanine organic thin film. As already discussed in chapter 2.2, the molecular organization changes according to the thickness of the deposited layer, for a few layers, indicatively up to a couple of nanometers, the molecules lay horizontally on the gold surface. On the contrary, by depositing additional layers, the molecules tend to establish a new stabler organization, which is obtained by tilting the molecules and keeping the central metal atoms aligned. As a result, the molecules are organized in stacks or columns. Moreover, depending on the deposition technique and parameters, three different configurations are possible, namely α , β , and η , which differ on the tilting angle and on the orientation of the stacks, that could be herringbone or brick-stone, as shown in figure 2.2. Figure 9.12 shows the optimization process (on the left) and the final configuration of the stack of four cobalt phthalocyanines. Differently from all the other simulations, this one is conducted with the molecular configuration, with the Dirichlet boundary conditions along every direction, thus the structure is not periodic and, as a result, the system is made by the four molecules only. The reason for that is to allow a free three-dimensional translation of the molecules, which is difficult to reproduce with a periodic structure since the cell puts constraints on the molecules' movements. Nevertheless, except for this only difference, the electronic structure of the system is calculated through the same FHI pseudopotentials indicated in table 9.1, GGA exchange-correlation potential, Grimme DFT-D3 correction and a density mesh cut-off of 80 Hartree. Since we are just interested in determining the molecular organization, the geometry optimization is conducted by applying the *Rigid* constraint to every molecule. As a result, each molecule is considered like a rigid body, and only rigid translations along the three directions are allowed. Then, the relaxation processes are simulated, however, the structure is only slightly modified, with no evident change in the configuration. The initial configuration does not follow a specific geometry, but it was built by placing the molecules in parallel without aligning the central metal atoms.

From the animation in figure 9.12 it is evident that the molecules are approaching during the optimization, by placing themselves at the same distance from one another. As indicated in the picture on the right, showing the final configuration, the molecular separation, measured between two cobalt atoms, is of 3.45 Å. Moreover, during the initial steps of the optimization, the alignment of the four cobalt atoms is lost, which is then recovered at the end of the process. Indeed, the final tilting angle measured between the normal of the molecular plane and the line crossing the four cobalt atoms is of $22.85 \pm 0.05^\circ$. Thus, from this simulation, it is demonstrated that the cobalt phthalocyanines tend to organize themselves into an ordered structure, that is characterized by the alignment of the central metal atoms, and by the overlapping of the benzene rings, which provide stability to the structure. By comparing these results with the literature, our structure is similar to the α or η configurations, which are shown in figure 8.24. The small variations could be connected to the adopted basis set, which is known to overestimate the interactions, thus reducing the intermolecular distance. Nevertheless, for the purposes of this work, which is focused more on the electronic properties rather than the morphology, the information obtained from this simulation is sufficient, and no further investigation of the molecular

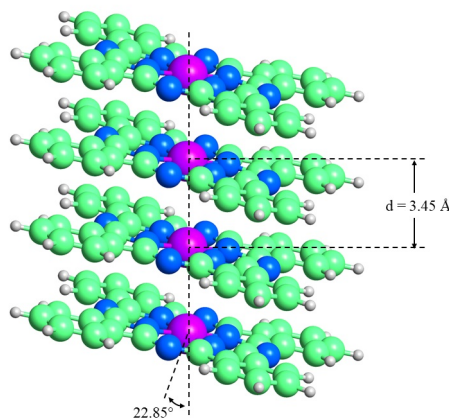


Figure 9.12. Animation and final configuration of the four cobalt phthalocyanine stack geometry optimization. The result is similar to the α and η configurations, with a tilting angle of 22.85° and molecular separation of 3.45 \AA .

organization of the phthalocyanine thin film is performed.

9.3.2 Charge transfer analysis

The simplest model that allows the investigation of the electronic properties of a metal phthalocyanine thin film deposited on gold is represented in figure 9.13, where the thin film is just represented by two molecules, one on top of the other, and the gold surface is made of three layers. With such a model, the number of atoms is reduced to the minimum, thus reducing the simulation time, but still providing meaningful results. The new structure is directly built starting from the fully optimized Au/ZnPc structure, where an additional ZnPc molecule has been placed above the other, at an initial distance of 3 \AA , with the central metal atoms and the benzene rings vertically aligned. Then, the geometry optimization has been conducted, following the two-step process, separating the large displacements from the deformation caused by the relaxation processes. However, this time, the gold substrate is kept fixed during both optimizations, since no major changes are expected and the simulations are significantly faster. The simulation setting and parameters are always the same. In the animations of figure 9.13, the first optimization process is shown since it already provides interesting results, that can be compared with the thin film organization discussed previously. As a matter of fact, during the optimization, both molecules are significantly moved and they reach a configuration that is very similar to the one in figure 9.12. Indeed, from a molecular perspective, the positions of the central metal atoms and the benzene rings are almost found again, with a slightly different overlapping direction. With a tilting angle of 24.02° and a distance between the zinc atoms of 3.71 \AA . surprisingly, these results are even more close to the ones found in the literature [35, 34, 20]. The second optimization is not shown since it just slightly corrects the position of the zinc atoms of the second molecule, which moves toward its molecular plane.

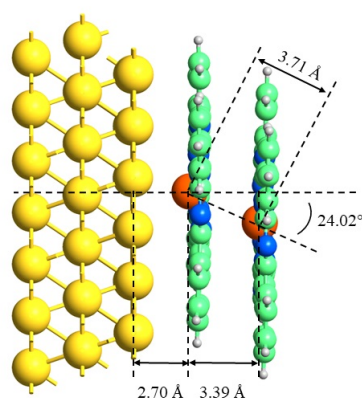


Figure 9.13. Animations of the geometry optimization from the lateral and vertical perspective of the bi-layer structure. In the picture are indicated the most relevant geometry parameters of the final structure.

As for the previous structures, the analysis of the electronic properties starts from the calculation of the molecular energy spectrum, which is obtained by projecting the density of states on the molecular part of the structure. The results are shown in figure 9.14, where the focus is on the HOMO and LUMO levels, and the zero energy reference is the Fermi level. The red curve belongs to the adsorbed molecule, whereas the blue one represents the electronic structure of the additional molecule, finally the black curve is the sum of the two, thus referring to the total organic system. The different behavior of the two molecules is reflected by the respective molecular energy spectrum, as a matter of fact, the HOMO and LUMO peaks are clearly distinguishable and the reason for that is due to the different interaction with the surface. In particular, the adsorbed molecule is characterized by a shift of both HOMO and LUMO toward lower energies of -0.16 eV and 0.20 eV respectively. As a result, the forbidden energy gap is also slightly reduced. Moreover, there is an evident broadening of the two peaks, reaching almost a double FWHM. These are consequences of

the metal/organic interaction that affects the adsorbed molecule. As a matter of fact, the adsorbed molecule is stabilized by the gold surface and the interface mechanisms, shifting the energy states, whereas the broadening is the result of the interface charge transfer. On the contrary, the second molecule is not affected by the gold surface, and the lower broadening indicates a negligible charge transfer between the molecules. The calculations demonstrate that the influence of the gold surface on the deposited molecules vanishes with the distance and that the effects of the metal/organic interaction are mostly localized at the interface, limiting them to the very first adsorbed molecules. As a consequence, the electronic properties of the monolayer could be substantially different with respect to the organic thin film.

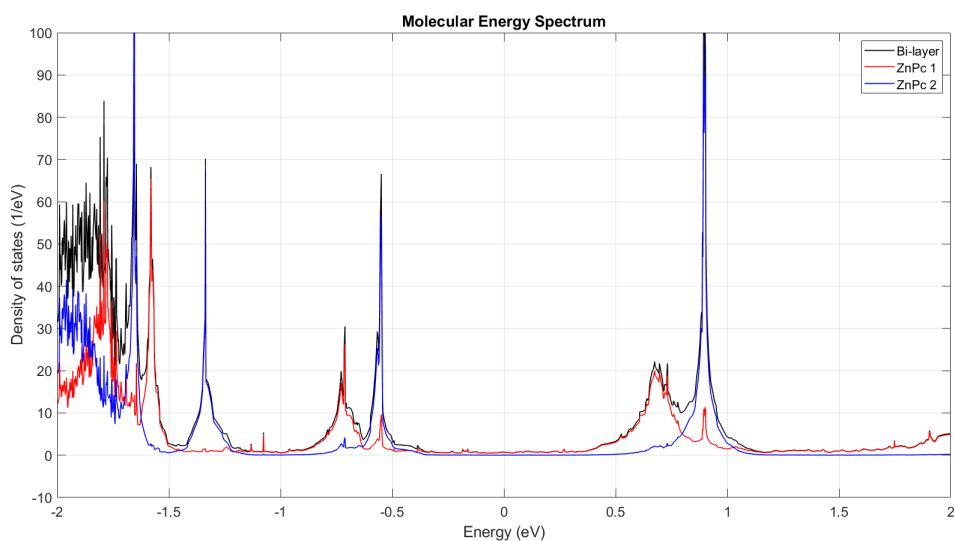


Figure 9.14. Molecular energy spectrum of the ZnPc bi-layer highlighting the splitting of the states caused by the interface interaction with the adsorbed molecule, indicated by the red curve (ZnPc 1).

The Mulliken population analysis is conducted to calculate the charge transfer between the three components. Therefore, to further investigate the effects of the metal/organic interface on the electronic properties of a thin film. The data collected in table 9.5 show the sum of the Mulliken population over different sets of atoms, in order to investigate the charge distribution within the molecules, where ZnPc1 stands for the adsorbed molecule and ZnPc2 is the additional one. Firstly, the total amount of transferred charge from the metal to the molecules is of 0.161 electrons, which is slightly larger than the single adsorbed molecule (0.143 9.4), denoting, however, that the larger number of molecules makes the metal/organic interaction even stronger. Moreover, looking at the total charge for each molecule, the excess charge is almost all localized in the first molecule, leaving the top one almost neutral. As a matter of fact, the charge distribution is almost identical to the one of the single ZnPc 9.4. These results perfectly describe the molecular energy spectrum discussed previously, with a gold surface that affects only the adsorbed molecule with

very low perturbation of the other one. These results indicate that the interface charge transfer almost depends uniquely from the first adsorbed layer and that the deposition of additional layers does not influence the properties of the interface. This is in accord with the photoemission results, where the reduction of the work function, caused by the combination of several interface mechanisms, is already measurable with the deposition of the very first molecules and it does not change with further deposition. The small corrections of the work function are probably caused by a rearrangement of the molecule, that alters the morphology of the first adsorbed layer. Thus, we can conclude that the properties of the deposited organic thin film on gold can be significantly different from the monolayer.

Table 9.5. Charge distribution in a ZnPc bi-layer deposited on Au(111) surface calculated for different atomic sets.

Structure	total	CMA	N	C-N	C6
ZnPc1	-0.151	0.421	0.531	-1.327	0.323
ZnPc2	-0.010	0.510	0.519	-1.284	0.314

9.4 Transport properties

9.4.1 Device structure

The devices analyzed in this work, for the investigation of the conduction properties, are very simple structures made of two gold electrodes with a phthalocyanine molecule in the middle that mediates the charge transport, as shown in figure 9.15. However, in order to make the simulation results comparable with the experimental measurements obtained with scanning tunneling microscopy (STM), the structures are built with some specific features. The positions of both the left electrode and the molecule are obtained from the geometry optimization results of the metal/organic interfaces, whereas the right electrode has a particular pyramidal shape that represents the characteristic single atomic tip of the scanning probe. Moreover, since the calculation results strictly depend on the distances between the molecule and the electrodes, the gold tip is kept at 3 Å from the molecular plane. In *quantumATK*, the calculation of the transmission spectrum and the I-V characteristic require the *device* configuration, which is indeed characterized by the definition of the electrode regions. Moreover, there are some differences in the settings for the calculation of the electronic structure. As for the other configurations, we used PBE functionals with FHI pseudopotentials, but, to speed up the calculations, gold is modeled by an SZP basis function rather than the usual DZP, as indicated by table 9.1. In the device configuration, the van der Waals correction is disabled, but the *Hubbard U Dual (Shell)* correction is employed. The numerical accuracy of the solver is determined by the density of the k-points, set to [4,4,150] and the density mesh cut-off of 75 Hartree. The default boundary conditions for the device configuration are Dirichlet below the left electrode and above the right electrode, and periodic for the other two directions. For further details on the device configuration consult the manual of the software [89].

In the specific, in this section are investigated the transport properties of the adsorbed CoPc and ZnPc molecules on a gold (111) surface. In addition, for ZnPc it is also investigated the bi-layer structure, in order to study the conduction between two vertically aligned phthalocyanines, which better represents the thin film structure. The three systems are shown in figure 9.15, where we can distinguish the electrode regions of the device configuration, and the pyramid-shaped right electrode, with the tip close to the center of the molecule.

9.4.2 Transmission spectrum and current

For every device, the transmission spectrum has been calculated at different bias voltages, from 0 V, the equilibrium condition, to 1 V equally spaced of 0.1 eV, with a total of 11 bias points. We stopped the calculations at 1 V to respect the technological limit. As a matter of fact, with higher voltages, the electric field generated in between the electrodes is so intense that the molecule will be damaged or even destroyed since the electrode separation is of 6 Å or 9 Å with two molecules. The transmission spectrum of each system is calculated at every bias point and the curves are plotted in a three-dimensional graph, as shown in figure 9.16. The energy is on the x-axis, the y-axis represents the applied bias, and the transmission probability is on the z-axis. The red part of each curve indicates the portion of the transmission spectrum that is included in the bias window for that specific applied voltage. Thus the portion that effectively contributes to the electric current, as shown by the model depicted in 3.9. The bias window is always centered on the molecular Fermi level, which behaves as the energy reference, thus with an applied bias voltage of 1.0 eV the electron states that enter in conduction are included in the energy range between -0.5 eV and 0.5 eV. The transmission spectrum and the density of states are strictly related, as a matter of fact, the two large peaks at the edges of the first plot are connected to the HOMO and LUMO of the CoPc molecule, whereas for ZnPc only the LUMO is represented. As evident from the plots, the transmission spectrum is not a unique function for a molecule, but it evolves depending on the device parameters, like for example the distance between molecule and electrodes, but also on the applied bias voltages that shift the position of the transmission peaks.

By comparing the transmission spectra of the single-molecule molecular devices, it is evident that the transmission properties of the two phthalocyanine molecules are very different. CoPc is characterized by a peak close to the Fermi level which enters in conduction even with short bias windows. As a result, the drain current has a significant increase for low voltages, as shown by the plot of the I-V characteristic in figure 9.17. Moreover, the transmission probability for energies within the HOMO-LUMO gap is not negligible, thus providing an overall linear behavior of the I-V characteristic for higher voltages. On the contrary, the transmission spectrum of ZnPc within the HOMO-LUMO gap is almost flat, with no relevant peaks. As a result, the drain current is much lower with respect to the previous molecule. However, it is interesting to notice that for a bias voltage of 0.9 V, the tail of the LUMO level enters into the bias window, and at 1.0 V a secondary peak of the LUMO is completely involved in the conduction, thus providing a significant increase to the drain current. Concerning the double-molecule molecular device, the transmission spectrum within the HOMO-LUMO gap is almost negligible, as expected (the spectra are

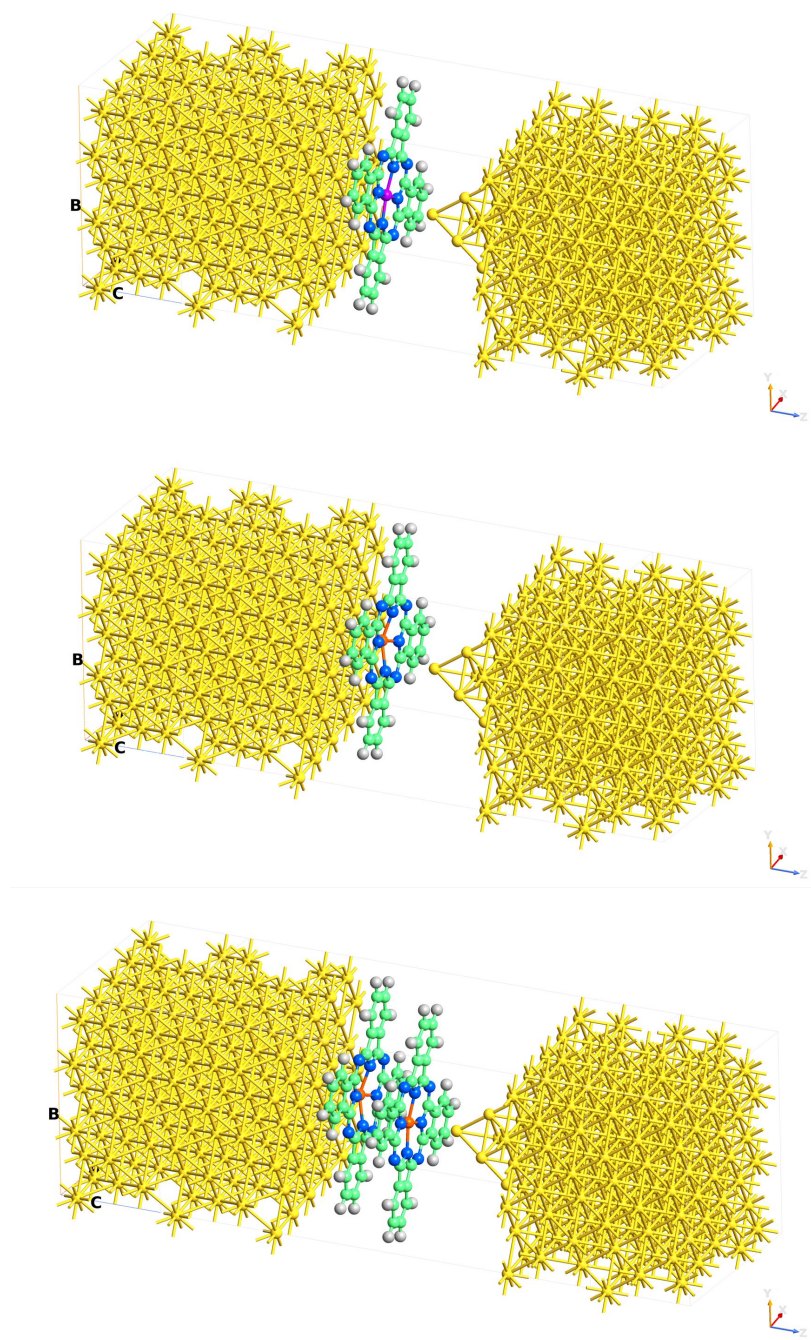


Figure 9.15. Representation of the device configuration of the three molecular structures. In order: CoPc, ZnPc, and ZnPc bi-layer, in each system the gold tip is close to the central metal atom, but not exactly on top.

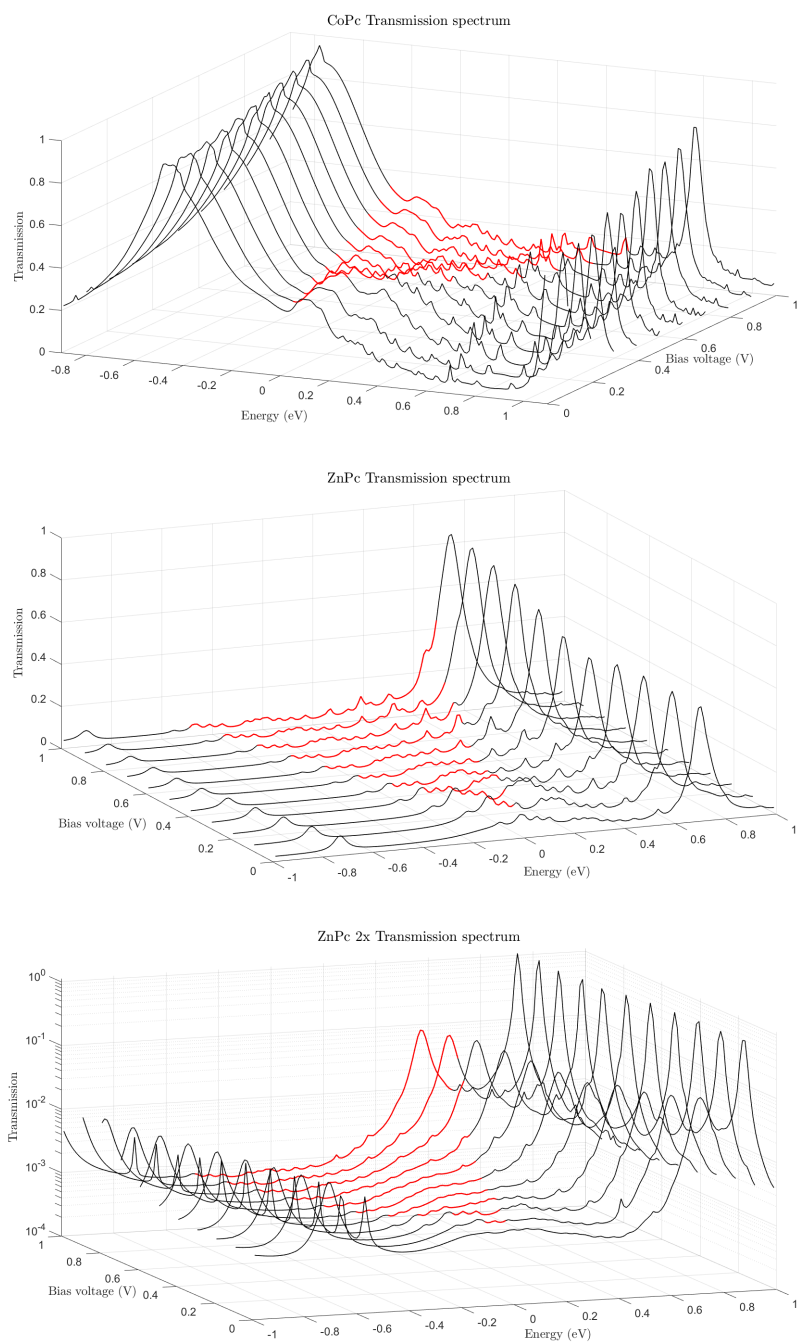


Figure 9.16. Transmission spectra of the three molecular devices for 11 bias voltages between 0 V and 1 V. The red part of the curves identifies the portion of the spectrum that is included in the bias window, thus that effectively contributes to the drain current.

indeed plotted in logarithmic scale). The reason for that is that molecular transport is characterized by tunneling processes between the electrodes and the molecule. By considering a very oversimplified description, with a single molecule, which acts like a transition state, the conduction requires two tunneling events, from the source to the molecule and from the molecule to the drain. With two molecules, the electrons must tunnel an additional time, from the first to the second molecule (assuming hopping transport between molecules), thus significantly reducing the transmission probability. As a result, the drain current of the last device is one order of magnitude lower than the single molecule device, with a maximum value of $0.535 \mu\text{A}$ with respect to the $6.47 \mu\text{A}$ with a bias of 1.0 V . With the applied bias voltages, no device exploits the HOMO or the LUMO for the conduction with a consequent limitation on the electric power. However, molecular devices can be engineered by providing the structure with additional electrodes, that allow the application of potentials along different directions. As a result, the simple structures presented in this work can be transformed into authentic molecular transistors [9, 10, 11]. As a result, depending on the application, by tuning the applied voltages it is possible to shift the bias window on different regions of the transmission spectrum, thus exploiting the HOMO and LUMO transmission peaks to improve the performances of the device.

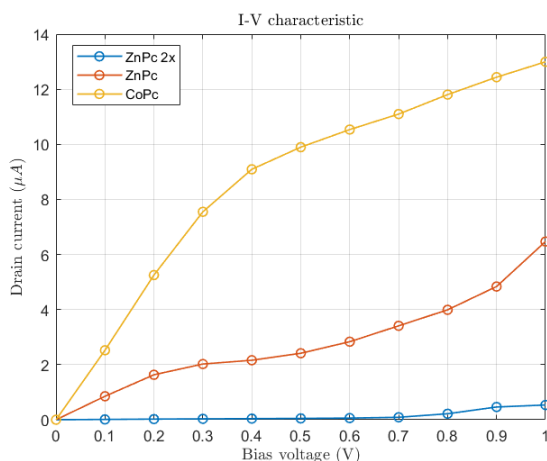


Figure 9.17. I-V characteristic of the three molecular devices.

From the transmission spectrum results of the different structures, it is evident that the central metal atom plays a central role in the conduction properties of the phthalocyanine. A deeper investigation of the transmission through the molecule is provided by the *TransmissionPathways* analysis tool, which separates the transmission coefficient into a sum of local bond contributions. The contributions can be positive, thus describing an electron that is moving from source to drain, or negative, which corresponds to a back-scattered electron along the bond. The results are plotted through arrows between atoms that point in the direction of the pathways. The magnitude of the pathway is illustrated by the volume of the arrow, whereas the color indicates the direction. In the specific, in the pictures of figure 9.18, the blue and the green arrows indicate the positive and the

negative transmission direction respectively (rotation angle of 0 and π). The transmission pathway is calculated for a single transmission energy for a specific bias voltage. As a matter of fact, pictures show the pathways of some significant transmission spectrum points like the maxima of the local peaks. Thus, due to the interesting features of CoPc, energies -0.29 eV and 0.32 eV are considered for an applied bias voltage of 0.8 V (on top). Whereas for both ZnPc devices, we have analyzed only one point from the transmission spectra with an applied 1.0 V bias. For the single molecule device, energy 0.45 eV indicates the peak of the LUMO shoulder, and for the other system, the peak is at 0.37 eV.

The transmission pathways indicate a substantially different conduction behavior between CoPc and ZnPc. The former exploits mainly the central metal atom, from which the majority of the electrons pass through, as indicated by the thick blue arrows that connect the molecule with both the substrate and the tip electrodes. On the contrary, the latter is characterized by a transmission that is mediated by the nitrogen and carbon atoms of the pyrrole groups below the tip, with a negligible contribution of the central metal atom. The fact that the pathways of the CoPc molecule are very similar, even if calculated at two opposite energies, indicates that the conduction mechanism does not depend on the electron energy and that the dominant pathway always involves the cobalt atom. Concerning the last picture, the one showing the bi-molecular device, the transmission properties between two aligned molecules can be discussed. If we focus on the molecule at the bottom, we notice that there is no substantial difference in the interaction with the gold substrate with respect to the single-molecule device. Therefore, the sharp decrease in the transmission spectrum is caused by a much less effective electron transfer between the two molecules, that, once again, does not involve the zinc atoms. As a result, only a small amount of electrons are transmitted to the tip thus contributing to the drain current.

9.5 Conclusion

From the gathered results, we can conclude that the *ab initio* simulations are an essential tool for the analysis of the structures investigated in this work. As a matter of fact, the electronic structure of the metal/organic interfaces is successfully calculated, providing comparable results with respect to the data collected through photoemission spectroscopy. Moreover, the results also demonstrate that it is possible to obtain additional information on the morphological properties of both the organic monolayer and thin film. However, because of the strong dependency on the simulation setting and employed parameters of the simulation results, a perfect match between simulations and experiments is very challenging to achieve. In fact, for some systems, a more accurate description of the atomistic structure is required, making the calculation significantly slower. Moreover, the idealized models are by definition different from the real samples, thus making the comparison even more complicated. Nevertheless, with our simple models and quite standard simulation settings, we have obtained interesting results that match the majority of the XPS and UPS data, at least qualitatively.

In conclusion, I want to point out which are the most relevant aspects and results of

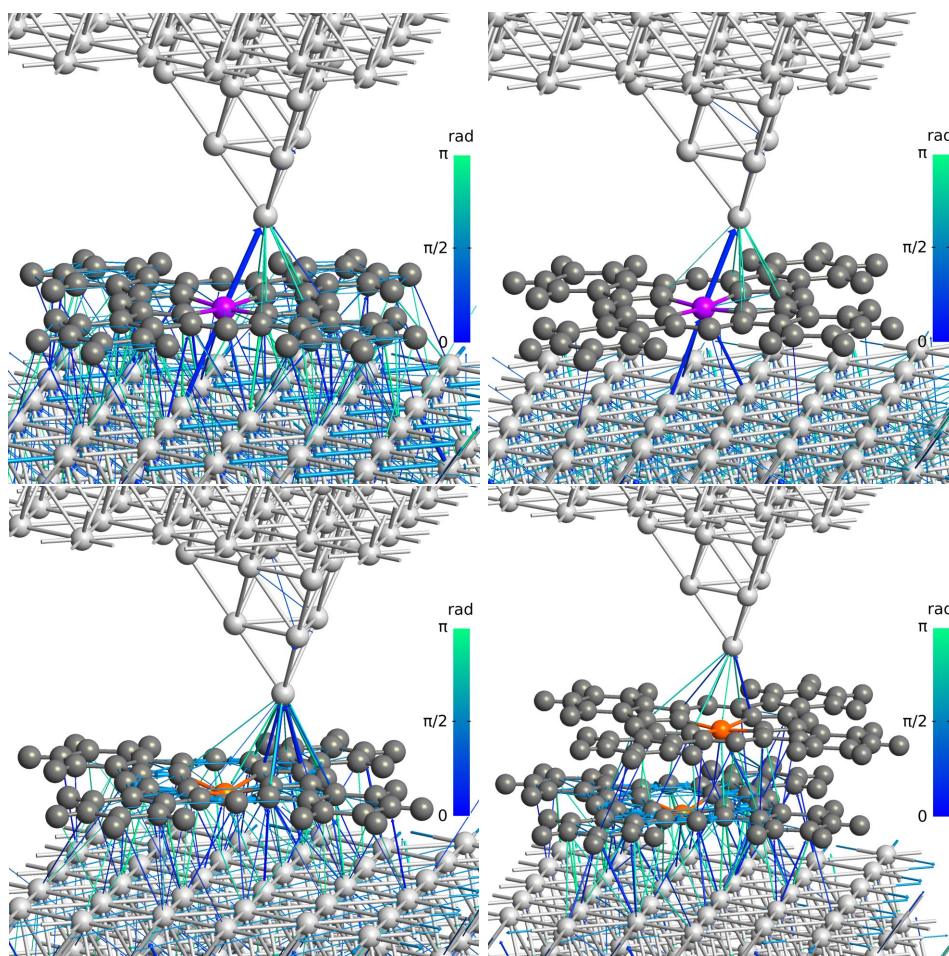


Figure 9.18. Transmission pathways of CoPc (violet) and ZnPc (orange) devices. The blue and the green arrows refer respectively to the forward and the backward electron transmission. The size of the arrow indicates the probability density.

our calculations. First of all, the geometry optimizations of all the investigated structures match the results found in the literature, in particular, we have obtained the planar configuration for the adsorbed molecules and a similar periodic pattern for the organic monolayer. In addition, the α -configuration is obtained for both the stack of four cobalt phthalocyanines and even for the bi-layer. Concerning the monolayer, the results indicate that the molecular organization is mainly determined by intermolecular interactions, rather than an affinity with the gold surface. As a consequence, two different configurations, that exploit the molecular symmetry, are almost equally probable. Secondly, the calculations of the electronic structures, and thus the interface charge transfer, mostly match the experimental results. In particular, no chemical bonds between metal and molecules are calculated, providing reasonable adsorption energies, but not excluding a small but still present charge transfer at the interface. The direction of the charge transfer

is in accordance with the experiments, indeed fractions of electrons are transferred from the metal to the molecule, which is slightly negatively charged after the adsorption. The electron density difference profiles across the surface demonstrate that the Pauli pushback effect is considered in the calculations, resulting in an accumulation of electrons in the substrate and a depletion just above the surface, with the consequent formation of the interface dipole. The molecular charge distribution has been calculated, showing that the excess of charge is localized in the inner part of the phthalocyanine (central metal atom and pyrrole rings), whereas the benzene rings are almost unaffected by the adsorption. Finally, the electronic structure of the bi-layer indicates that the interface effects are localized and limited to the molecules close to the metal surface, thus the deposition of additional layers does not alter significantly the interface properties. The only inconsistency between experiments and simulations regards the calculation of the work function reduction, causing a rigid energy shift in the energy states.

Chapter 10

Summary and conclusion

In this thesis, the electronic properties of the metal/organic interfaces and thin films are investigated, by combining the results obtained from photoemission analysis with the support of *ab initio* simulations in the KS-DFT framework. In the specific, the systems consist of three different metal phthalocyanines (CoPc, ZnPc, and MgPc) deposited on a polycrystalline gold-coated silicon substrate. The process consists of an alternation of deposition and analysis: at each step, the organic molecules are deposited through PVD, adding a thin film of 0.5 nm of thickness on the sample surface, then the sample is analyzed with photoemission spectroscopy (UPS and XPS). All these processes are conducted in a high vacuum system, with all chambers connected, so that the sample never leaves the vacuum conditions. Thus, the samples are never in contact with the external atmosphere, a crucial aspect to avoid any sort of unwanted contamination of the surface and organic thin film. With the collected measurements it is possible to investigate the evolution of the system properties as a function of the organic layer thickness. In particular, for very thin layers, the physical and chemical properties of the metal/organic interface are extracted, whereas information on the morphology and the organization of the organic molecules emerge from the photoemission analysis of the thicker layer. The simulations are conducted on simple ideal structures, which, despite that, are modeled in order to reproduce a real metal/organic interface. The simulations are limited to the investigation of the molecular organization of the adsorbed organic monolayer and to the calculation of the electronic properties, with a particular interest in the interface charge transfer that causes the metal/organic interaction.

By combining the experimental measurements with the simulation calculations, we are able to investigate different aspects of the metal/organic structure. In the following, the most important characteristics are pointed out, which are evinced from the gathered results. For all the investigated systems, the adsorption mechanism does not involve a strong interaction between the two components. Therefore, no chemical bonds are built and the molecules are physisorbed on the gold surface. As a consequence, there is no intense charge transfer between gold and phthalocyanines, and the deformation of the molecule upon adsorption is limited. Both measurements and calculations agree with the previous statement. In particular, for the former, it is confirmed by the absence of energy shifts for both the Au_{4f} peaks and the C-N component of C_{1s} peak. Whereas, the

latter shows that there is no electron density accumulation between the two components and that the metal and molecule orbitals are well separated. However, the calculated adsorption energies of $\simeq 5.0$ eV for the three molecules indicate a significant interaction strength comparable to a weak chemisorption. The reason can be attributed to the formation of several van der Waals interactions at the interface, indeed the molecules are adsorbed with a planar configuration, maximizing the interaction area with the gold surface. Moreover, an overestimation of the adsorption energies of $\simeq 30\%$ is expected by the simulations. Nevertheless, despite the absence of chemical bonds, a non-negligible interface charge transfer is detected in both experiments and calculations. As a matter of fact, the Mulliken population shows a negative charging of the molecules upon the adsorption, which indicates an electron transfer from the gold substrate to the phthalocyanine. The intensity of the charge transfer depends on the molecule's central metal atom, still, limited to a fraction of electron (0.15-0.25 e), determining CoPc as the most responsive. Furthermore, with the measurements, slight shifts of the characteristic peaks of the metal phthalocyanines toward higher binding energies are detected for the growing organic thin films. This indicates that there is a different charge transfer behavior for the monolayer and the thin film. In particular, the electrons are transferred mainly to the first layers and the charge transfer fades as the distance between metal and molecule increases. This is also confirmed by the calculation of the excess electron density of the bi-layer system, which is indeed almost entirely localized on the adsorbed molecule. Thus, the interface interaction is almost limited to the very first adsorbed layer. Moreover, through the UPS analysis, the localization of the interface interaction is also demonstrated by the significant reduction of the sample work function measured after the very first deposition step. As a matter of fact, with successive depositions, the work function of the combined structure is not affected by further shifts. Thus indicating that the thickness of the organic material does not alter considerably the gold/phthalocyanine interface interaction. For the specific systems, the reduction of the work function is mainly caused by the Pauli pushback, a repulsive effect, acting between the metal surface states and the molecular orbitals, that pushes the metal electrons toward the bulk, thus a dipole at the interface is generated. A small contribution is also attributable to the interface charge transfer. As a result, the measured reductions of the work functions are 0.54 eV, 0.65 eV, and 0.72 eV for CoPc, MgPc, and ZnPc respectively. Both mechanisms are calculated with the electron density redistribution caused by the adsorption. Moreover, it provides information on the molecular charge distribution, characterized by the delocalization of the electrons in the π -conjugated carbon backbone and leaving the central metal atom partially ionized. Finally, an initial investigation of the conduction properties of the metal phthalocyanine is conducted, with a focus on the transmission spectrum of simple molecular junctions with CoPc and ZnPc. The results show that the molecules have a different behavior. In particular, CoPc exploits the cobalt atom, characterized by an unpaired electron, thus improving the conduction. On the contrary, in ZnPc the current is limited since the zinc atom is not involved and the conduction is performed by the delocalized states of the carbon backbone.

The electronic properties of an organic or molecular device are strongly affected by the interface between the metal and the molecule. Therefore, the device's performance can be controlled and improved by engineering the interface. The information about the

gold/phthalocyanine interface, built upon the adsorption, can be exploited for the development of different devices. A direct application is the tuning of the metal electrode's work function, which determines the transport properties in the device. We have indeed demonstrated that a significant shift in the gold work function is obtained through the deposition of a single phthalocyanine monolayer and that the intensity of the shift depends on the central metal atom. Moreover, the metal phthalocyanines are self-assembled molecules, meaning that metal - ordered organic layers are possible. Well-defined molecular orientations are appealing not only for the potential high accuracy and yield in all the devices in which the metal-organic interfaces are used, but also for molecular Field Coupled Nanocomputing (FCN) applications. Since the phthalocyanines on gold are weakly physisorbed with low charge transfer they might present the FCN advantages of neutral molecules, e.g., low crosstalk [91]. In addition, the small charge transfer occurring at the interface makes phthalocyanine monolayer on gold even more interesting for FCN applications since it could enhance the performance by merging the whole molecular neutrality with some advantages of zwitterionic-like molecules, e.g., the easing of clock reset. The proven planarity of adsorbed phthalocyanine monolayers on gold can again be attractive for the usage of molecular crystallites for FCN applications if the crystallite presents group properties similar to the ones of isolated molecules.

Future works may focus on additional investigation of the potentiality of phthalocyanines for FCN applications. The focus might be on the analysis of the charge transfer with other substrates to tune the charging of phthalocyanine through the substrate interaction. Also, the functionalization of the benzene groups can be investigated for the same purpose. Both theoretical and experimental works might focus on the electrical transport through sub-monolayers, monolayers, and thin films of phthalocyanines on gold or different substrates, and relate the transport characteristics to the unique electronic properties of the interface, with particular attention to the role of the first molecular layers versus the total thickness of the organic layers. Finally, a deeper investigation of gold-phthalocyanine interfaces might reveal exclusive features in organic and molecular electronics, both for the fabrication of novel computing devices and for sensing applications, as the sensing features of phthalocyanines are already proven in literature [8]. In this standpoint, the different transport regimes between CoPc and ZnPc could be the initial basics for the design of devices governed by different current-voltage characteristics and integrated on the same chip, through masked deposition in specific areas of interest.

Bibliography

- [1] William Stallings. *Computer Organisation and Architecture. Designing for performance*. Pearson Education, 2016.
- [2] G. Moore. Cramming more components onto integrated circuits. *Proceedings of the IEEE*, 1998.
- [3] Y. Taur and T. H.Ning. *Fundamentals of Modern VLSI Devices*. Cambridge University Press, 2013.
- [4] International Roadmap for Devices and Systems. Executive summary. 2022.
- [5] N.R. Armstrong, W. Wang, D. M. Alloway, D. Placencia, E. Ratcliff, and M. Brumbach. *Macromolecular Rapid Communications*, 30.9-10, 2009.
- [6] M. Ling and Z. Bao. Copper hexafluorophthalocyanine field-effect transistors with enhanced mobility by soft contact lamination. *Organic Electronics* 7.6, 2006.
- [7] B. P. Rand, J. Genoe, P. Heremans, and J. Poortmans. Solar cells utilizing small molecular weight organic semiconductors. *Progress in Photovoltaics: Research and Applications* 15.8, 2007.
- [8] P. Powroznik, L. Grzadziel, W. Jakubik, and M. Krzywiecki. Sarin-simulant detection by phthalocyanine/palladium structures: From modeling to real sensor response. *Sensors and Actuators B: Chemical* 273, 2018.
- [9] H. Choi and C. Mody. The long history of molecular electronics: Microelectronics origins of nanotechnology. *Social Studies of Science* 39.1, 2009.
- [10] G. Cuniberti, G. Fagas, and K. Richter. *Introducing Molecular Electronics*. Springer, 2005.
- [11] James M. Tour. Molecular electronics. synthesis and testing of components. *Accounts of Chemical Research* 33.11, 2000.
- [12] James M. Tour. *Molecular Electronics. Commercial insights, chemistry, devices, architecture and programming*. World Scientific publishing, 2003.

-
- [13] H. Ishii, K. Sugiyama, E. Ito, and K. Seki. Energy level alignment and interfacial electronic structures at organic/metal and organic/organic interfaces. *Advanced Materials* 11.8, 1999.
- [14] N. Koch. Organic electronic devices and their functional interfaces. *ChemPhysChem* 8.10, 2007.
- [15] N. Koch, S. Duhm, J. P. Rabe, A. Vollmer, and R. L. Johnson. Optimized hole injection with strong electron acceptors at organic-metal interfaces. *Phys. Rev. Lett.* 95, 237601, 2005.
- [16] Egbert Zojer, Thomas C. Taucher, and Oliver T. Hofmann. The impact of dipolar layers on the electronic properties of organic/inorganic hybrid interfaces. *Adv. Mater. Interfaces*, 6, 1900581, 2019.
- [17] Susi Lindner. Charge transfer at phthalocyanine interfaces. *Technischen Universität Dresden*, 2014.
- [18] V.V. Maslyuk, V.Y. Aristov, O.V. Molodtsova, D.V. Vyalikh, V.M. Zhilin, Y.A. Ossipyan, T. Bredow, I. Mertig, and M. Knupfer. The electronic structure of cobalt phthalocyanine. *Applied Physics A*, 2009.
- [19] F. Petraki, H. Peisert, I. Biswas, and T. Chasse. Electronic structure of co-phthalocyanine on gold investigated by photoexcited electron spectroscopies: Indication of co ion-metal interaction. *J. Phys. Chem. C*, 114, 17638–17643, 2010.
- [20] Rosemary R. Cranston, , and Benoit H. Lessard. Metal phthalocyanines: thin-film formation, microstructure, and physical properties. *RSC Adv.*, 11, 21716, 2021.
- [21] P. Peumans and S. R. Forrest. Very-high-efficiency double-heterostructure copper phthalocyanine/ c_{60} photovoltaic cells. *Appl. Phys. Lett.* 79, 126, 2001.
- [22] W. Gao and A. Kahn. Electronic structure and current injection in zinc phthalocyanine doped with tetrafluorotetracyanoquinodimethane: Interface versus bulk effects. *Organic Electronics* 3.53-63, 2002.
- [23] M. Kato, M. Nakaya, and Y. Matoba et al. Morphological and optical properties of α - and β -phase zinc (||) phthalocyanine thin films for application to organic photovoltaic cells. *J. Chem. Phys.* 153, 2020.
- [24] C. Barraud, K. Bouzehouane, C. Deranlot, D. J. Kim, R. Rakshit, S. Shi, J. Arab-ski, M. Bowen, E. Beaupaire, S. Boukari, F. Petroff, P. Seneor, and R. Mattana. Phthalocyanine based molecular spintronic devices. *Dalton Trans.*, 45, 16694-16699, 2016.
- [25] W. Brutting and Ch. Adachi. *Physics of Organic Semiconductors*. Wiley-VCH, 2005.
- [26] F. Petraki, H. Peisert, J. Uihlein, U. Aygöl, and T. Chassé. Copc and copcf₁₆ on gold: Site-specific charge-transfer processes. *Beilstein J. Nanotechnol.* 5, 524–531, 2014.

-
- [27] Pierluigi Gargiani, Giorgio Rossi, Roberto Biagi, Valdis Corradini, Maddalena Pedio, Sara Fortuna, Arrigo Calzolari, Stefano Fabris, Julio Criginski Cezar, N. B. Brookes, and Maria Grazia Betti. Spin and orbital configuration of metal phthalocyanine chains assembled on the au(110) surface. *Physical Review B* 87, 165407, 2013.
- [28] Leeor Kronik and Yoshitada Morikawa. *The Molecule–Metal Interface*. WILEY-VCHVerlag GmbH 'I&' Co, 2013.
- [29] Oliver T. Hofmann. Structure-to-property relationships in metal/organic interfaces. *Graz University of Technology*, 2010.
- [30] Qi Wang, Jiacheng Yang, Alexander Gerlach, Frank Schreiber, and Steffen Duhm. Advanced characterization of organic–metal and organic–organic interfaces: from photoelectron spectroscopy data to energy-level diagrams. *J. Phys. Mater.* 5 044010, 2022.
- [31] D. Kolacyak, H. Peisert, and T. Chassé. Charge transfer and polarization screening in organic thin films: phthalocyanines on au(100). *Applied Physics A* 95, 2008.
- [32] S. Dick, H. Peisert, and D. Dini et al. Influence of the alkyl-chains length on the electronic structure and interface properties of 1,4-octasubstituted zinc phthalocyanines on gold. *J. Appl. Phys.* 97, 2005.
- [33] F. Schreiber. Structure and growth of self-assembling monolayers. *Progress in Surface Science* 65.5-8,, 2000.
- [34] Taoyu Zou, Xiaoyan Wang, Haidong Ju, Li Zhao, Tingting Guo, Wei Wu, and Hai Wang. Controllable molecular packing motif and overlap type in organic nanomaterials for advanced optical properties. *Crystals*, 8, 22, 2018.
- [35] T.J.Z. Stock and J. Nogami. Copper phthalocyanine thin films on cu(111): Submonolayer to multi-layer. *Surface Science* 637–638, 132–139, 2015.
- [36] H. Peisert, I. Biswas, L. Zhang, M. Knupfer, M. Hanack, D. Dini, M.J. Cook, I. Chambrier, T. Schmidt, D. Batchelor, and T. Chasse. Orientation of substituted phthalocyanines on polycrystalline gold: distinguishing between the first layers and thin films. *Chemical Physics Letters* 403 1–6, 2005.
- [37] Wei Wu, A. Kerridge, A. H. Harker, and A. J. Fisher. Structure-dependent exchange in the organic magnets cu(ii)pc and mn(ii)pc. *Phys. Rev. B* 77, 184403, 2008.
- [38] N. Ashcroft and N. Mermin. *Solid State Physics*. Holt-Saunders, 1976.
- [39] Hans Luth. *Solid Surfaces, Interfaces and Thin films*. Springer-Verlag, 2010.
- [40] H. Vazquez, Y.J. Dappe, J. Ortega, and F. Flores. A unified model for metal/organic interfaces: Idis, ‘pillow’ effect and molecular permanent dipoles. *Applied Surface Science* 254 378–382, 2007.

- [41] Michele Penna, Alberto Marnetto, Francesco Bertazzi, Enrico Bellotti, and Michele Goano. Empirical pseudopotential and full-brillouin-zone $k \cdot p$ electronic structure of $cdte$, $hgte$, and $hg_{1-x}cd_xte$. *Journal of Electronic Materials volume 38, pages1717–1725*, 2009.
- [42] Richard Tran, Xiang-Guo Li, Joseph H. Montoya, Donald Winston, Kristin Aslaug Persson, and Shyue Ping Ong. Anisotropic work function of elemental crystals. *Surface Science 687, Pages 48-55*, 2019.
- [43] Robert J. Silbey, Robert A. Alberty, and Mounji G. Bawendi. *Physical Chemistry, 4th Edition*. John Wiley 'I&' Sons, 2005.
- [44] Robert S. Mulliken. Spectroscopy, molecular orbitals, and chemical bonding. *Science, 157, 3784*, 1967.
- [45] James E. House. *Fundamentals of Quantum Mechanics*. Elsevier Inc. All, 2018.
- [46] Nir Tessler, Yevgeni Preezant, Noam Rappaport, and Yohai Roichman. Charge transport in disordered organic materials and its relevance to thin-film devices: A tutorial review. *Advanced Materials 21(27):2741 - 2761*, 2009.
- [47] Allen Miller and Elihu Abrahams. Impurity conduction at low concentrations. *Phys. Rev. 120, 745*, 1960.
- [48] R. A. Marcus. On the theory of electron-transfer reactions. unified treatment for homogeneous and electrode reactions. *J. Chem. Phys. 43, 679–701*, 1965.
- [49] H. Vazquez, F. Flores, and A. Kahn. Induced density of states model for weakly-interacting organic semiconductor interfaces. *Organic Electronics 8.2-3*, 2007.
- [50] L. Romaner, G. Heimel, J. Brédas, A. Gerlach, F. Schreiber, R. L. Johnson, J. Zegenhagen, S. Duhm, N. Koch, , and E. Zojer. Impact of bidirectional charge transfer and molecular distortions on the electronic structure of a metal-organic interface. *Physical Review Letters 99.25*, 2007.
- [51] Supriyo Datta. *Quantum transport: atom to transistor*. Cambridge University Press, 2005.
- [52] Cesare Rossetti. *Rudimenti di meccanica quantistica*. Levrotto 'I&' Bella, 2008.
- [53] Frank Jensen. *Introduction to computational chemistry*. John Wiley 'I&' sons, 2007.
- [54] Jack Simons. *An introduction to theoretical chemistry*. Cambridge University Press, 2003.
- [55] M. Born and R. Oppenheimer. Zur quantentheorie der molekeln. *Annalen der Physik 389.20*, 1927.
- [56] T. A. Albright, J. K. Burdett, and M. Whangbo. *Orbital interactions in chemistry*. John Wiley 'I&' sons, 2013.

- [57] W. Kohn and L. J. Sham. Self-consistent equations including exchange and correlation effects. *Physical Review* 140, 1965.
- [58] P. Hohenberg. Inhomogeneous electron gas. *Physical Review* 136, 1964.
- [59] C. Yang, J. C. Meza, B. Lee, and L. Wang. Kssolv - a matlab toolbox for solving the kohn–sham equations. *ACM Transactions on Mathematical Software* 36.2, 2009.
- [60] John P. Perdew, J. A. Chevary, S. H. Vosko, Koblar A. Jackson, Mark R. Pederson, D. J. Singh, and Carlos Fiolhais. Atoms, molecules, solids, and surfaces: Applications of the generalized gradient approximation for exchange and correlation. *Phys. Rev. B* 46, 6671, 1992.
- [61] Theodore L. Brown, H. Eugene LeMay Jr., Bruce E. Bursten, Catherine Murphy, Patrick Woodward, Steven Langford, Dalius Sagatys, and Adrian George. *Chemistry: The Central Science*. 14th. Pearson College Div., 2018.
- [62] Tro Nivaldo. *Chemistry: A Molecular Approach*. 4th. Pearson Education, 2017.
- [63] P. Atkins and J. de Paula. *Physical Chemistry*. Oxford University Press, 2006.
- [64] Ilya G. Kaplan. *Intermolecular Interactions: Physical Picture, Computational Methods and Model Potentials*. John Wiley 'I&' sons, 2006.
- [65] M. Waller and S. Grimme. Weak intermolecular interactions: A supermolecular approach. *Handbook of Computational Chemistry*, 2016.
- [66] Frans B. van Duijneveldt, Jeanne G. C. M. van Duijneveldt-van de Rijdt, , and Joop H. van Lenthe. State of the art in counterpoise theory. *Chemical Reviews* 94.7, 1994.
- [67] Krishna Seshan. *Handbook of Thin-film Deposition Processes and Techniques*. Noyes Publications, 2002.
- [68] Andresa Baptista, Francisco Silva, Jacobo Porteiro, José Míguez, , and Gustavo Pinto. Sputtering physical vapour deposition (pvd) coatings: A critical review on process improvement and market trend demands. *Coatings*, 8(11), 402, 2018.
- [69] H. Busse and B. Koel. *Surface Processes*. Wiley-VCH, 2009.
- [70] VAC Aero International Inc. The fundamentals of vacuum theory.
- [71] Fred A. Stevie and Carrie L. Donley. Introduction to x-ray photoelectron spectroscopy. *J. Vac. Sci. Technol. A* 38, 063204, 2020.
- [72] Teignmouth Science and Technology Centre. Introduction to surface analysis using xps.
- [73] Prevac. User manual.

- [74] D. Roy and D. Tremblay. Design of electron spectrometers. *Rep. Prog. Phys.* 53 1621, 1990.
- [75] Alexander G. Shard. Practical guides for x-ray photoelectron spectroscopy: Quantitative xps. *J. Vac. Sci. Technol. A* 38, 041201, 2020.
- [76] ThermoFisher Scientific. X-ray photoelectron spectroscopy of atomic elements.
- [77] XPSfitting. X-ray photoelectron spectroscopy (xps).
- [78] Sven Tougaard. Practical guide to the use of backgrounds in quantitative xps. *J. Vac. Sci. Technol. A* 39, 011201, 2021.
- [79] George H. Major, Neal Fairley, Peter M. A. Sherwood, Matthew R. Linford, Jeff Terry, Vincent Fernandez, and Kateryna Artyushkova. Practical guide for curve fitting in x-ray photoelectron spectroscopy. *J. Vac. Sci. Technol. A* 38, 061203, 2020.
- [80] Hiroshi Shinotsuka, Shigeo Tanuma, Cedric J Powell, and Dave R Penn. Calculations of electron inelastic mean free paths. xii. data for 42 inorganic compounds over the 50 ev to 200 kev range with the full penn algorithm. *Surf Interface Anal.* 51,4, 2018.
- [81] Hideo Iwai, John S. Hammond, and Shigeo Tanuma. Recent status of thin film analyses by xps. *Journal of Surface Analysis* 15,3, 2009.
- [82] Peter J Cumpson. The thickogram: a method for easy film thickness measurement in xps. *Surf. Interface Anal.* 29,403–406, 2000.
- [83] A. Jablonski and C. J. Powell. Effective attenuation lengths for different quantitative applications of x-ray photoelectron spectroscopy. *ournal of Physical and Chemical Reference Data* 49, 2020.
- [84] Y. F. Chen, C. M. Kwei, and C. J. Tung. Electron inelastic mean free paths versus attenuation lengths in solids. *J. Phys. D: Appl. Phys.* 25 262, 1992.
- [85] Matteo Todeschini, Alice Bastos da Silva Fanta, Flemming Jensen, Jakob Birkedal Wagner, and Anpan Han. Influence of ti and cr adhesion layers on ultrathin au films. *ACS Appl. Mater. Interfaces*, 9,42,37374–37385, 2017.
- [86] Ryusuke Ishii, Katsunori Matsumura, Akira Sakai, and Toyo Sakata. Work function of binary alloys. *Applied Surface Science Volumes 169–170*, 2001.
- [87] H. J. Guntherodt and R. Wiesendanger. *Scanning Tunneling Microscopy I*. Springer-Verlag, 1992.
- [88] V. L. Mironov. *Fundamentals of Scanning Probe Microscopy*. Institute for physics of microstructures, The Russian Academy of Sciences, 2004.
- [89] Inc. Synopsys. Quantum atk manual, 2023.

- [90] Jose A. Garrido Torres, Benjamin Ramberger, Herbert A. Fruchtl, Renald Schaub, and Georg Kresse. Adsorption energies of benzene on close packed transition metal surfaces using the random phase approximation. *Phys. Rev. Materials* 1, 060803, 2017.
- [91] Yuri Ardesi, Giuliana Beretta, Marco Vacca, Gianluca Piccinini, and Mariagrazia Graziano. Impact of molecular electrostatics on field-coupled nanocomputing and quantum-dot cellular automata circuits. *Electronics*, 11(2), 276, 2022.